

Universität Stuttgart

# **A single electron sensor assisted by a quantum coprocessor**

Von der Fakultät Mathematik und Physik der Universität Stuttgart zur Erlangung der Würde eines Doktors der Naturwissenschaften (Dr. rer. nat.) genehmigte Abhandlung.

vorgelegt von

**Sebastian Felix Zaiser**

aus Vaihingen an der Enz

Hauptberichter: Prof. Dr. Jörg Wrachtrup  
Mitberichterin: Prof. Dr. Gisela Schütz

Tag der mündlichen Prüfung: 28. März 2019

3. Physikalisches Institut  
Universität Stuttgart  
2019







# Abbreviations

<b>AWG</b>	arbitrary waveform generator
<b>APD</b>	avalanche photo diode
<b>CVD</b>	chemical vapor deposition
<b>CSH</b>	coherent stimulated echo
<b>DCT</b>	discrete cosine transform
<b>DFT</b>	discrete Fourier transform
<b>DD</b>	dynamical decoupling
<b>EPR</b>	electron paramagnetic resonance
<b>ESLAC</b>	excited state level anti-crossing
<b>FID</b>	free induction decay
<b>FWHM</b>	full width half maximum
<b>GeV center</b>	germanium-vacancy center
<b>GSLAC</b>	ground state level anti-crossing
<b>HBAC</b>	Heat-bath algorithmic cooling
<b>HPHT</b>	high pressure high temperature
<b>iQFT</b>	inverse quantum Fourier transform
<b>MW</b>	microwave

## *Abbreviations*

**NMR** nuclear magnetic resonance

**C<sub>n</sub>Pi<sub>e</sub>-gate** nuclear spin controlled electron  $\pi$ -gate

**NV center** nitrogen-vacancy center

**NV<sup>-</sup>** nitrogen-vacancy center in the negative charge state

**NV<sup>+</sup>** nitrogen-vacancy center in the positive charge state

**NV<sup>0</sup>** nitrogen-vacancy center in the neutral charge state

**ODMR** optically detected magnetic resonance

**P1 center** substitutional nitrogen center

**QDTC** quantum discrete cosine transform

**QFT** quantum Fourier transform

**QND measurement** quantum nondemolition measurement

**RF** radio frequency

**SNR** signal-to-noise-ratio

**SiV center** silicon-vacancy center

**SSR** single-shot readout

**SIL** solid immersion lense

**z-axis** connecting line between nitrogen atom and vacancy

**ZFS** zero field splitting

**ZPL** zero-phonon line

# Symbols

$a_{\text{iso}}$  proportionality constant describing the Fermi contact interaction

$\mathbf{B}_0$  external magnetic field

$B_{0,z}$  z-component of the external magnetic field

$\mu_{\mathbf{B}}$  Bohr magneton

$D_{\text{es},z}$  excited state zero field splitting parameter

$D_{\text{gs},z}$  ground state zero field splitting parameter

$D_z$  zero field splitting parameter

$\epsilon$  polarization, expressed as population difference of a two-level system

$\mathbf{S}$  electron spin-1 angular momentum operator (spin 1)

$\hat{S}_z$  z-component of electron spin-1 angular momentum operator (spin 1)

$F_{\mathbf{r}}$  single-shot readout readout fidelity

$\tilde{\gamma}_{\mathbf{C}}$  reduced  $^{13}\text{C}$  gyromagnetic ratio

$\tilde{\gamma}_{\mathbf{e}}$  reduced electron gyromagnetic ratio

$\tilde{\gamma}_{\mathbf{n}}$  reduced nuclear gyromagnetic ratio

$\tilde{\gamma}_{\mathbf{N}}$  reduced  $^{14}\text{N}$  gyromagnetic ratio

$\hat{H}_{\mathbf{e}}$  NV center Hamilton operator

$\mathbf{A}$  hyperfine tensor describing the coupling between electron and nuclear spin

## Symbols

$A_{zz}$   $zz$ -component of the hyperfine tensor  $\mathbf{A}$

$\hat{H}_{\mathbf{n}}$  NV center Hamilton operator

$\hat{H}_{\mathbf{NV}}$  NV center Hamilton operator

$k_{\mathbf{B}}$  Boltzmann constant,  $1.380\,648\,52 \times 10^{-23} \text{ m}^2\text{kg s}^{-2}\text{K}^{-1}$

$m_{\mathbf{C}}$   $^{13}\text{C}$  spin quantization number along the  $z$ -axis

$m_{\mathbf{N}}$   $^{14}\text{N}$  spin quantization number along the  $z$ -axis

$m_s$  electron spin quantization number along the  $z$ -axis

$\mu_0$   $4\pi \cdot 10^{-7}$ , vacuum permeability

$\mathbf{I}$  nuclear spin angular momentum operator

$\hat{I}_z$   $z$ -component of nuclear spin angular momentum operator

$Q$  electric quadrupole splitting of the nuclear spin

$\mathbf{r}$  positional vector connecting the NV electron spin and a nuclear spin

$T_1$  longitudinal relaxation time

$T_{1,e}$  longitudinal relaxation time of the NV center electron spin

$T_2$  transverse spin relaxation time

$T_2^*$  inverse inhomogeneous broadening

$\mathbf{e}_r$   $\mathbf{r}/|\mathbf{r}|$

# Zusammenfassung

Die Quantenmechanik begann vor mehr als hundert Jahren als ein kontraintuitives mathematisches Konstrukt, dessen Auswirkungen selbst von ihren Begründern kaum zu glauben waren. Während das Wissen über die Gesetze der Quantenmechanik in zahlreichen Bereichen der modernen Technologie, wie z.B. beim Bau von Lasern, Atomuhren oder modernen Computern, unerlässlich ist, bleibt die Kontrolle über mehrere interagierende Quantensysteme bis heute eine große Herausforderung. Viele Jahre lang schien die Bewältigung dieser Herausforderungen von rein wissenschaftlichem Interesse zu sein, ohne dass die Gesellschaft unmittelbar davon profitieren würde. Im Jahr 1982 änderte sich dies durch die Idee des Nobelpreisträgers Richard P. Feynman einen Quantencomputer mit bisher unvorstellbarer Rechenleistung zu bauen, der in der Lage ist, selbst komplexeste Quantensysteme zu simulieren [1]. Nach Feynman wurden neue Quanteninformationsverarbeitungsalgorithmen entdeckt, von denen der bekannteste der Shor-Algorithmus für die Faktorisierung großer Zahlen ist [2–4]. Als sich die Nachricht verbreitete, dass moderne Kryptographie innerhalb von Sekunden geknackt werden könnte, wurde das enorme Potenzial quantenmechanischer Instrumente einem breiteren Publikum bekannt. Heutzutage wird die quantentechnologische Forschung an einem breiten Spektrum von Themen wie Quantencomputer und Quantenkommunikation sowie Quantenmetrologie durchgeführt. Seit mehr als zwei Jahrzehnten gewinnt die Forschung auf diesen Gebieten ständig an Schwung und es gibt einen Wettlauf zwischen zahlreichen vielversprechenden physikalischen Systemen wie zum Beispiel Photonen [5], eingefangenen Ionen (trapped Ions) [6], supraleitenden Schaltungen [7], Quantenpunkten [8] und Spindefekte in Feststoffen [9].

**Das Stickstoff-Fehlstellenzentrum im Diamanten** Das Stickstoff-Fehlstellenzentrum (NV Zentrum) in Diamant ist eines der technologisch fortschrittlichsten Spindefekte, bestehend aus einem Stickstoffatom und einer angrenzenden Fehlstelle. Dieses paramagnetische, atomartige Defektzentrum hat mehrere herausragende Eigenschaften, die es von anderen kontrollierbaren Quantensystemen unterscheiden. Das negativ geladene NV Zentrum hat ein Elektronen-Spin-1-System im Grundzustand, dessen Spinzustand optisch in-

initialisiert und ausgelesen werden kann. Einerseits ist dieser Elektronenspin sehr gut von der Umgebung isoliert und erreicht auch unter Normalbedingungen longitudinale Relaxationszeiten sowie Kohärenzzeiten von mehr als einer Millisekunde. Andererseits stellt das NV Zentrum mehrere Schnittstellen für die Kommunikation mit anderen Quantensystemen zur Verfügung, wie z.B. die Kopplung über die photonische Schnittstelle, Magnetfelder, elektrische Felder oder Phononen [10–13]. Diese Schnittstellen bieten dem NV Zentrum hervorragende Perspektiven im Bereich der Quantenkommunikation, aber auch im Bereich der Quantenmetrologie, wo eine hohe Suszeptibilität für Messgrößen gefordert ist. Auf dem Gebiet der Quanteninformationsverarbeitung ist die Kopplung an andere Quantensysteme besonders wichtig, da nur bei hinreichender Skalierbarkeit und der Möglichkeit zur Kommunikation mit anderen Systemen das volle Potential eines Quantensystems ausgeschöpft werden kann.

In dieser Arbeit wird der Elektronenspin des NV Zentrums als Zentralspin verwendet, der mit dem  $^{14}\text{N}$  Stickstoff Kernspin und mit mehreren  $^{13}\text{C}$  Kohlenstoff Kernspins innerhalb des Diamantgitters gekoppelt ist. In einem solchen hybriden Spinsystem erhöhen Synergien zwischen den beiden verschiedenen Spinspezies die Vielseitigkeit eines einzelnen NV Zentrums. Der Elektronenspin dient zur Repolarisierung und zum Auslesen der Kernspinzustände, aber auch des eigenen Spinzustandes. Es überträgt die Wechselwirkungen zwischen den Kernspins und kommuniziert mit der Außenwelt. Kommunikation wird hier in Bezug auf die Kopplung an andere Quantensysteme für die Erweiterung des quantenmechanischen Systems verstanden, aber auch in Bezug auf die Quantenmetrologie, wo Informationen über Messgrößen erfasst werden müssen. Die Kernspins hingegen sind extrem robust und haben longitudinale Relaxationszeiten von weit mehr als einer Sekunde [14]. Sie können kohärent kontrolliert und zu Kernspinregistern für die Speicherung und Verarbeitung von Quanteninformation kombiniert werden [15–17]. Die Robustheit der Kernspinzustände bleibt auch dann erhalten, wenn der Zustand des Elektronenspins optisch ausgelesen wird. Dadurch wird die zerstörungsfreie Messung (quantum non-demolition measurement) von Quanteninformationen möglich, die ein wichtiger Bestandteil der Quanteninformationsverarbeitung ist. Stark gekoppelte  $^{14}\text{N}$  und  $^{13}\text{C}$  Kernspins (d.h. solche, die stärker gekoppelt sind als die inverse inhomogene Verbreiterung der Elektronenspinübergänge) können mit einer Technik, für die der Begriff Single Shot Readout geprägt wurde, zerstörungsfrei ausgelesen werden [18, 19]. Die vorliegende Arbeit wurden vollständig bei Raumtemperatur durchgeführt.

**Diese Arbeit** stellt wichtige Ergebnisse an der Schnittstelle zweier wichtiger Bereiche der modernen Quantenwissenschaft vor, nämlich der Quantenmetrologie und der Quanteninformationsverarbeitung. Dafür werden zwei unterschiedliche Subsysteme kombiniert. Das eine Subsystem besteht aus einem einzigen Elektronenspinsensor, der mit dem Zielsystem interagiert und Phaseninformationen über die zu messenden Größen sammelt. Das andere Subsystem besteht aus mehreren Kernspins, die als kleiner Quantenpro-

zessor zusammenwirken. In einem ersten Schritt wird die effiziente Initialisierung des Quantenregisters dargestellt. Anschließend wird der Kernspin-Quantenprozessor verwendet, um die vom Quantensensor erhaltene Quanteninformation zu speichern und zu verarbeiten, in dem die Techniken der Quantenphasenschätzung (quantum phase estimation) und der Quantenkorrelationsspektroskopie kombiniert werden. Zu diesem Zweck wird der Quanten-Fouriertransformations-Algorithmus (QFT) auf dem Quantenprozessor implementiert. Es wird gezeigt, dass der Quantenprozessor die spektrale Auflösung des Quantensensors durch die verlängerte Speicherzeit der Metrologiedaten verbessert. Es erhöht auch die Empfindlichkeit der Messung und die Messbandbreite der detektierbaren Feldamplituden durch die Verwendung des Quantenphasenschätzalgorithmus. Diese Arbeit legte den Grundstein für Anwendungen in der hochauflösenden Magnetresonanzspektroskopie (NMR) [20]. Die Funktionsfähigkeit des Sensorsystems bei Raumtemperatur macht diesen durch einen Quantenprozessor verbesserten Sensor interessant für Anwendungen beispielsweise in der Biosensorik.

**Gliederung** In Kapitel 1 werden die Aspekte des NV Zentrums in Diamant vorgestellt, die für die Quantenmesstechnik und die Quanteninformationsverarbeitung mit Kernspinunterstützung wichtig sind. In Kapitel 2 werden wichtige Methoden zur Kernspinkühlung und Kernspininitialisierung diskutiert, wobei ein besonderer Schwerpunkt auf der Wärmebadalgorithmischen Kühlungstechnik (heat-bath algorithmic cooling) liegt. In den weiteren drei Kapiteln werden verschiedene Aspekte des Quantenphasenschätzalgorithmus im Rahmen von Korrelationsspektroskopieverfahren diskutiert. Kapitel 3 verbessert bestehende Korrelationsspektroskopieverfahren durch einen Quantenspeicher, um die spektrale Auflösung zu erhöhen und eine kohärente Kopplung an schwach gekoppelte Kernspins zu ermöglichen. Kapitel 4 kombiniert dann die Quantenspeicher gestützte Korrelationsspektroskopie-Methode mit Lock-in-Detektionsverfahren. Es wird gezeigt, dass dadurch zuvor spektral nicht auflösbare Kernspins nun adressierbar werden. Folglich werden die Prinzipien der Einzel-Qubit-Phasenschätzung auf den Quantenphasenschätzalgorithmus in Kapitel 5 erweitert. Zu diesem Zweck wird ein theoretischer Rahmen für die Implementierung der Quanten-Fouriertransformation und des Quantenphasenschätzalgorithmus auf hybriden Qudit-Systemen beliebiger Größe entwickelt. Dann wird die Implementierung des Quantenphasenschätzalgorithmus zuerst auf einem einzelnen Qutritspeicher und dann auf einem Quantenregister aus einem Qutrit und zwei Qubits vorgestellt.

**Kernspinkühlung und Kernspinpolarisation** Eine zentrale Herausforderung in der Quantentechnologie ist die Vorbereitung des Ausgangszustandes der verwendeten Quantensysteme. Insbesondere die Quantenfehlerkorrektur benötigt eine konstante Zufuhr an initialisierten Qubits. In der Quantenmetrologie werden die Sensitivitäten durch die Spinpolarisation begrenzt, weshalb Sensoren in der klassischen NMR aus sehr vielen Spins bestehen müssen,

um trotz ihrer oft schlechten Spinpolarisation hohe Empfindlichkeiten zu ermöglichen. Daher sind Spinpolarisation und insbesondere Spinpolarisationstransfertechniken ein sehr intensiv untersuchtes Thema [21–23]. Aufgrund seines effizienten optischen Spinpolarisationsmechanismus in Kombination mit der kohärenten Spinkontrolle ist das NV Zentrum ein nützliches Werkzeug für die Übertragung der Spinpolarisation auf Kernspins.  $^{13}\text{C}$  Kohlenstoff Kernspins innerhalb des Diamanten können als gut charakterisiertes Testfeld für die Untersuchung solcher Polarisationsübertragungstechniken dienen. Der größte Teil des zweiten Kapitels behandelt die Wärmebadalgorithmische Kühlungstechnik (HBAC), die es ermöglicht, den Quantenzustand einiger Zielqubits zu bereinigen (purify), indem sie wiederholt einige andere Qubits (die Resetqubits) polarisiert und eine Quantengatteroperation zwischen den Zielqubits und den Resetqubits durchführt. Der Schritt für die Repolarisierung der Resetqubits wird üblicherweise durchgeführt, indem man sie in Kontakt mit einem Wärmebad bringt, das eine Temperatur hat, die niedriger ist als die der Zielqubits. Interessanterweise ermöglicht dieses Verfahren, die Zielqubits unter die Temperatur des Wärmebads zu kühlen. Experimentelle Implementierungen von HBAC erfordern eine sehr gute Kontrolle über Qubits sowie die Möglichkeit, diese neu zu initialisieren. Bisher wurden HBAC Experimente in NMR Experimenten durchgeführt, bei denen nur konzeptbestätigende Messungen durchgeführt wurden, welche nur mit wenige Wiederholungen möglich waren oder die nur begrenzte Zielspin-Polarisationen von  $\Delta p \sim 10^{-2}$  erreichten. Insbesondere eine Schlüsselprognose, die asymptotische Grenze von HBAC, war noch nicht nachgewiesen. An dieser Grenze erlauben wiederholte Anwendungen des HBAC-Algorithmus nicht mehr, weiter Entropie aus dem Zielqubitsystem zu extrahieren, und es kann deshalb nicht mehr weiter gekühlt werden [24]. In dieser Arbeit können zwei  $^{13}\text{C}$  Kohlenstoff Kernspinqubits durch den Elektronenspin, der die Rolle des Wärmebades übernimmt, zurückgesetzt werden, während ein  $^{14}\text{N}$  Stickstoff Kernspinqubit gekühlt werden soll. Zuerst wurde ein Algorithmus zur partiellen Polarisationsübertragung eingeführt, der eine individuelle Steuerung der Polarisation der beiden Resetspins ermöglicht. Der Maximalwert der Polarisationen der beiden Resetspins ist aufgrund der unterschiedlichen Hyperfeinstrukturkopplungen und der daraus resultierenden unterschiedlichen Qualität der experimentellen Kontrolle über die beiden Spins nicht identisch. Die Polarisation der beiden Resetspins mit dieser Spin-Polarisationsübertragungstechnik kann von Null aus um bis zu mehr als drei Größenordnungen über der Boltzmann-Verteilten Polarisation frei eingestellt werden. Die Quantengatteroperation, die zur Kühlung des Ziel-Kernspins verwendet wird, muss als nicht-lokales Quantengatter zwischen den drei beteiligten Kernspins implementiert werden, welche aufgrund ihrer kleinen gyromagnetischen Verhältnisse nicht selbst miteinander interagieren. Dazu wurde eine Quantengattersequenz entworfen, die den Elektronenspin und dessen Hyperfeinstrukturkopplung zu den drei Kernspins nutzt. Der Elektronenspin dient als Vermittler zwischen den Kernspins und die für das HBAC-Kühlgatter erforderliche Gatteroperation wird mit einer Sequenz realisiert, die aus 15 einzelnen Elektronen- und Kernspin-Gattern zusammengesetzt ist. Das Kühlgatter

ist unitär und führt die Operation  $|trr\rangle = |100\rangle \leftrightarrow |011\rangle$  zwischen dem Zielqubit  $t$  und den beiden Resetqubits  $r$  aus. Aus klassischer Sicht ändert dabei der Zielspin nur dann seinen Zustand, wenn beide Resetqubits in die dazu entgegengesetzte Richtung zeigen. Da die beiden Resetqubits in den Zustand  $|rr\rangle = |11\rangle$  polarisiert sind und daher eine bevorzugte Orientierung haben, existiert die Vorzugsrichtung  $|100\rangle \rightarrow |011\rangle$ . Es soll beachtet werden, dass dies nur bis zu einer maximalen Zielspinpolarisation gilt, ab der die beiden Richtungen gleich wahrscheinlich werden und der Kühlvorgang deshalb stoppt. Der Kühlvorgang der Resetspin-Repolarisation mit anschließender Anwendung der Wärmebadalgorithmischen Kühlung (Heat-bath algorithmic cooling (HBAC)) wird bis zu 23 Mal wiederholt. Die asymptotische Grenze von HBAC wurde für verschiedene Resetspin-Polarisationen nachgewiesen  $\Delta p = p(|0\rangle) - p(|1\rangle)$ .  $\Delta p$  wird als Differenz der Wahrscheinlichkeiten, für das Auffinden des Kernspinqubits in einem der beiden Eigenzustände  $|0\rangle$  und  $|1\rangle$  angegeben. Für die maximal getesteten Resetspin-Polarisationen von  $\Delta p = 0,59$  und  $\Delta p = 0,42$  erreichte die Zielspin-Polarisation  $\Delta p = 0,8$ , was eine Erhöhung der Zielspin-Polarisation um den Faktor 1,35 über die Polarisation des Bades (d.h. über der Reset-Polarisationen der Resetqubits) zeigt. In einem weiteren Experiment wurden die Polarisationen der beiden Resetspins einzeln von  $\Delta p = 0$  auf ihre individuellen Maximalwerte variiert und die Ziel-Spinpolarisation überwacht. Zur weiteren Demonstration der Kühlung schwach gekoppelter Kernspins wurde mit dem PulsePol-Framework eine Pulssequenz entworfen, die mit der Hyperfeinstruktur-Kopplungskomponente  $A_{zz}$  einen künstlichen Flip-Flop-Hamiltonian zwischen dem Elektronenspin des NV Zentrums und einem oder mehreren  $^{13}\text{C}$  Kohlenstoff Kernspins erzeugt. Kernspins mit Kopplungen von  $A_{zz} = 12.3\text{ kHz}$  und  $A_{zz} = 5.8\text{ kHz}$  können jeweils zu  $\Delta p > 90\%$  polarisiert werden.

**Quantenphasenschätzung** In Kapitel 3 bis 5 wird der Elektronenspin als zentraler Spin-Sensor mit Kopplung an die Umgebung verwendet, während ein  $^{14}\text{N}$  Kernspinquartit und zwei  $^{13}\text{C}$  Spinqubits zur Speicherung, Verarbeitung und zum effizienten Auslesen der Sensordaten verwendet werden. Mit diesem Aufbau wird der Quantenphasenschätzalgorithmus mit verschiedenen Registergrößen von zwei bis zwölf Speicherzuständen implementiert. Die Phaseninformationen werden mit einer Korrelationsspektroskopie-Messung gesammelt, die hochfrequente Auflösungen ( $\approx 200\text{ Hz}$ ) als Folge langer Phasenkorrelationszeiten ermöglicht. Letzteres kann in der Größenordnung der longitudinalen Relaxationszeit des Elektronenspins des NV Zentrums liegen ( $\approx 5\text{ ms}$ ). Bei Korrelationsmessungen werden die Ergebnisse von zwei einzelnen Quantenmessungen korreliert und dieses Korrelationssignal ist dann das eigentliche Ergebnis. Dabei liegen die zu korrelierenden Messergebnisse idealerweise als Quanteninformation vor, z.B. könnten das die beiden Messphasen  $\phi_1 = \tilde{\gamma}B_1$  und  $\phi_2 = \tilde{\gamma}B_2$  sein. Das gyromagnetische Verhältnis  $\tilde{\gamma}$  ist eine Proportionalitätskonstante, die bestimmt, wie viel Phase ein Quantensensor für ein bestimmtes Magnetfeld  $B$  aufammelt. Wenn sehr hohe Frequenzauflösungen erforderlich sind, speichern bestehende Techniken die Messphasen auf der Spinpopulation des Elektronenspins, wo sie

der Dekohärenz unterliegen. Dadurch gehen wertvolle Sensorinformationen verloren und die erforderlichen Messzeiten werden erhöht. Ein wichtiger Vorteil der Verwendung des  $^{14}\text{N}$  Kernspins als Quantenspeicher zeigt sich in einer Reduzierung der Messzeit um den Faktor vier bei gleichem Signal-Rausch-Verhältnis. Die Verwendung des Quantenspeichers führt zu einer vernachlässigbaren Erhöhung der Sequenzdauer um 0.083 %. Die mit Quantenspeicher verbesserte Korrelationssequenz wird verwendet, um ein Spektrum der  $^{13}\text{C}$  Hyperfeinstrukturkopplungen  $A_{zz}$  mit einer Frequenzauflösung von 210 Hz (FWHM) aufzunehmen. Kohärente Wechselwirkungen zwischen dem Quantenspeicher und einem schwach gekoppelten Kernspin werden auch mit der genannten Frequenzauflösung realisiert, so dass einzelne Qubits in einem sehr dichten Spektrum adressiert werden können. Dabei werden als schwach gekoppelte Kernspins diejenigen bezeichnet, welche Kopplungen in der Größenordnung der inhomogenen Verbreiterung des Elektronenspins aufweisen. Es wurden zwei Möglichkeiten zur Erzeugung eines maximal verschränkten Zustands zwischen dem Quantenspeicher und dem schwach gekoppeltem Probenspin gezeigt. Durch die Fähigkeit, schwach gekoppelte Kernspins zu detektieren und selektiv anzusprechen, wird die Anzahl der nutzbaren Qubits drastisch erhöht, was die Möglichkeiten von NV Zentren für die Informationsverarbeitung verbessert.

In Kapitel 4 wird aufgezeigt, wie im  $A_{zz}$  Hyperfeinspektrum nicht auflösbare Kernspins dennoch adressiert werden können. Daher wird die quantenverstärkte Korrelationssequenz mit einer dynamischen Entkopplungssequenz kombiniert, die die Probenspins mit einer Rate ihrer Hyperfeinkomponenten  $A_{zx}$  [25] manipuliert. Die kombinierte Sequenz ermöglicht es, ein  $A_{zx}$  -Spektrum mit Auflösungen zu erhalten, die durch die longitudinale Relaxationszeit des Elektronenspins begrenzt sind, während bei existierenden Techniken die kürzere Elektronenspin-Kohärenzzeit relevant ist [25]. Die  $A_{zz}$  und  $A_{zx}$  Hyperfeinkopplungskomponente von sechs Kernspins wurden mit dieser neuartigen Technik experimentell bestimmt. Zwei dieser Kernspins mit Hyperfeinkopplungen  $A_{zz}$ , die sich um deutlich weniger als ein kHz unterscheiden, sind nun durch die Addressierung über ihre Hyperfeinkopplungskomponenten  $A_{zx}$  gut auflösbar geworden. Eine Erweiterung auf eine dritte Hyperfeinkopplungskomponente  $A_{zy}$  ist möglich.

In Kapitel 5 wird der Quantenphasenschätzalgorithmus experimentell auf einem Speichersystem eines einzelnen Elektronenspinsensors und außerdem auf einem hybriden Quditspeicherregister mit bis zu zwölf Speicherzuständen implementiert. Die Quantenphaseninformation wird vom Elektronenspinsensor erfasst und in das Speicherregister geschrieben, wo sie vom der inversen Quanten-Fouriertransformation (iQFT) verarbeitet wird. Anschließend wird sie durch Auslesen der Speicherzustände in klassische Information umgewandelt.

Um diese Aufgabe erfüllen zu können, wird eine allgemeine und instruktive Theorie entwickelt, die zur Konstruktion des Quanten-Fouriertransformationsalgorithmus und des Quantenphasenschätzalgorithmus auf Quantenregistern genutzt werden kann. Diese Quantenregister können aus Qudits mit einer unterschiedlichen Anzahl an Speicherzu-

ständen bestehen. Bestehende Theorien für Speicherregister, die aus Qudits gleicher Multiplizitäten zusammengesetzt sind, werden für die Implementierung des Quanten-Fouriertransformationalgorithmus auf Speicherregister erweitert, die aus Qudits beliebiger Multiplizitäten  $d = \{d_1 d_2 \dots d_n\}$  bestehen. Als erstes Ergebnis wird eine Gattersequenz für die experimentelle Implementierung der Quanten-Fouriertransformation auf einem Quantenregister, bestehend aus einem Qutrit und zwei Qubits, hergeleitet. Die Quanten-Fouriertransformation auf einem einzelnen Qutrit wurde als Chrestenson-Gatter identifiziert. Eine entsprechende Gattersequenz für die Implementierung der iQFT kann einfach hergeleitet werden, indem die Gatter-Reihenfolge der Sequenz für die QFT invertiert wird und jedes beteiligte Quantengatter konjugiert wird. Als zweites Ergebnis wurde eine Prozedur zur Bestimmung der Phasen  $\Delta\phi^{(l)}$  gefunden, die auf die unterschiedlichen Qudits geschrieben werden muss. Nur wenn dieses Verfahren befolgt wird, kann der Quantenphasenschätzalgorithmus eine sinnvolle Annäherung an eine beliebige zu messende Phase  $\Delta\phi$  finden. Für ein Register mit einem Qutrit und zwei Qubits müssen die geschriebenen Phasen ein Verhältnis von 1 und 2, 1 und 4 sowie 1 und 8 haben.

Für die experimentelle Implementierung des Quantenphasenschätzalgorithmus wird zunächst ein Qutrit-Speicherregister verwendet, auf das eine von einem einzelnen Elektronenspinsensor gemessene Phase  $\Delta\phi$  geschrieben wird. Zu diesem Zweck misst der Elektronenspinsensor das Magnetfeld, das durch einen einzelnen  $^{13}\text{C}$  Kernspin mit Hyperfeinkopplung  $A_{zz} \approx 90 \text{ kHz}$  erzeugt wird. Dies wird durch eine Quantenkorrelationsmessung erreicht, bei der zwei Phasenerfassungsschritte durch eine lange Korrelationszeit  $T_c$  getrennt sind. Die Kombination des Quantenphasenschätzalgorithmus mit der Quantenkorrelationspektroskopie ermöglicht es, Messungen durchzuführen, die aufgrund der langen Korrelationszeiten  $T_c$  eine hohe Frequenzpräzision aufweisen und gleichzeitig die Signalamplitude mit hoher Präzision und auch hoher Bandbreite bestimmen lassen. Ein Speicher mit drei Speicherzuständen (Qutrit) erhöht den möglichen Informationsgehalt der Messung um den Faktor 1,58 im Vergleich zu dem oft verwendeten zweistufigen (Qubit) Speicher. Die Qutrit-Sensorsequenz wird im Experiment verwendet, um die Amplitude und das Vorzeichen der Magnetisierung eines einzelnen  $^{13}\text{C}$  Kernspins zu bestimmen.

Anschließend wird der Quantenphasenschätzalgorithmus erstmals experimentell auf einem nativen Hybrid-Spinsystemregister implementiert, das aus einem Qutrit und zwei Qubits besteht (vgl. [26], wo ein Qutrit von zwei Qubits emuliert wird). Ein Speicher mit zwölf möglichen Zuständen kann einen Faktor von 3,58 mehr Phaseninformation erhalten als ein Speicher mit zwei möglichen Zuständen, wodurch beispielsweise die Bandbreite einer Amplitudenmessung um diesen Faktor erhöht werden kann.

In zukünftigen Experimenten kann die Größe des Speicherregisters durch den Einsatz von schwach gekoppelten Kernspins erhöht werden. Daher kann es notwendig sein, das NV Zentrum auf niedrigere Temperaturen herunterzukühlen, bei denen die longitudinale Relaxationszeit des Elektronenspins des NV Zentrums gegenüber der bei Raumtempe-

## *Zusammenfassung*

ratur drastisch verlängert werden kann. Die Quantenphasenschätzalgorithmen können im bestehenden Register der Größe  $N = 12$  durchgeführt werden, um externe Magnetfelder zu messen oder die Erkennung und kohärente Kopplung an Kernspins im und außerhalb des Diamanten zu verbessern. Grundlegende Quantenalgorithmen wie der Shor-Algorithmus sind ebenfalls ein interessantes Forschungsgebiet. Insbesondere auf dem sich aktuell entwickelnden Gebiet des Quantenmaschinenlernens ergeben sich neue Einsatzmöglichkeiten für die Quanten-Fouriertransformation.

# Acknowledgements

Many people directly or indirectly contributed to the work which is presented in this thesis and made the years of my PhD pleasant and interesting.

First of all I want to thank Prof. Jörg Wrachtrup for giving me the freedom, the means and also guidance for the investigation of many interesting projects. I would like to thank Prof. Gisela Schütz for promptly accepting to be the second referee to my thesis and Prof. Maria Daghofer for chairing the PhD exam.

Extraordinary thanks go to Dr. Philipp Neumann, who inspired and supervised major parts of this thesis. His enormous commitment and personal dedication combined with a deep understanding of physics helped me greatly and it was a pleasure to work with him. Mentioned in the same breath shall be Dr. Gerald Waldherr, who introduced me to the experimental setup and who helped me to find my way into the field of nitrogen-vacancy center physics. I was very lucky to work together with the very talented student Nikolas Abt during his master thesis and also thereafter and want to thank him for the very fruitful collaboration. Dr. Nabeel Aslam and Dr. Matthias Pfender were great office mates, and I want to thank them for many interesting discussions which were not only about physics. Further thanks go to Dr. Durga Dasari, who supported me on theoretical issues about algorithmic cooling and also the quantum Fourier transform and who talked a lot with me about physics. I am also glad that Dr. Vadim Vorobev continues the experiments on the setup that I spent so many hours with and wish him best luck with his experiments. I also thank Nikolas Abt, Dr. Nabeel Aslam, Dr. Durga Dasari, Jonas Meinel, Dr. Matthias Pfender, Farida Shagieva, Dr. Vadim Vorobev, Dr. Boris Yavkin, and Dr. Ingrid Zaiser for proof-reading of my thesis.

Then I want to thank Mrs. Claudia Unger, Stephan Hirschmann and Dr. Andrea Zappe for forming the firm rock on which PI3 is built and as the go to address for all the small and big questions that come up during the course of the day. Mrs. Ivanka Spajic did a great job in preparing snacks in the afternoon, which helped me through some late stays in the lab. A big thank you also for all the used coffee cups that have miraculously vanished from my desk over night. Generally speaking, I want to thank all the colleagues from PI3 and in particular all members of Grup Pneumann for the great

## *Acknowledgements*

atmosphere. I really enjoyed being a part of this institute with preparing the Christmas parties (including the choir), the volleyball tournament and the preparation for the many after defense examinations.

Last but definitely not least, I am extraordinarily thankful for my beloved family, who always supported me!

# Contents

<b>Abbreviations</b>	<b>v</b>
<b>Symbols</b>	<b>vii</b>
<b>Acknowledgements</b>	<b>xvii</b>
<b>Summary</b>	<b>1</b>
<b>1 The nitrogen-vacancy center and the nuclear spins surrounding it</b>	<b>9</b>
1.1 Defects in diamond . . . . .	10
1.2 Electronic configurations of the nitrogen-vacancy center . . . . .	12
1.3 The optical and spin properties of the nitrogen-vacancy center . . . . .	14
1.4 The nitrogen-vacancy center as a hybrid quantum system . . . . .	18
1.4.1 The intrinsic nitrogen nuclear spin . . . . .	20
1.4.2 $^{13}\text{C}$ nuclear spins surrounding the nitrogen-vacancy center (NV center) . . . . .	22
1.4.3 Electron and nuclear spin eigenstates and eigenvalues . . . . .	23
1.5 Experimental setup . . . . .	23
1.5.1 Used NV center . . . . .	23
1.5.2 Optical path . . . . .	25
1.5.3 External magnetic field . . . . .	26
1.5.4 Electron and nuclear spin driving . . . . .	26
1.6 Single spin manipulation . . . . .	27
1.6.1 The Rabi formula . . . . .	28
1.6.2 Electron Rabi . . . . .	29
1.6.3 Optically detected magnetic resonance . . . . .	31
1.6.4 Nuclear spin manipulation . . . . .	32
1.6.5 Local spin phases . . . . .	34
1.6.6 Non-local spin operations . . . . .	35
1.6.7 Implementation of common quantum gates in NMR . . . . .	37

1.7	Storage times of quantum information . . . . .	38
1.8	Quantum nondemolition measurement of nuclear spins . . . . .	42
1.9	The neutral electron charge state unraveled by single shot readout . . . . .	46
<b>2</b>	<b>Nuclear spin cooling</b>	<b>49</b>
2.1	Cooling by postselection . . . . .	51
2.2	Full and partial polarization transfer . . . . .	52
2.2.1	Increasing the $^{14}\text{N}$ nuclear spin polarization . . . . .	54
2.2.2	Increasing the $^{13}\text{C}$ nuclear spin polarization . . . . .	56
2.3	Heat-bath algorithmic cooling . . . . .	59
2.3.1	Cooling principle and asymptotic limit . . . . .	60
2.3.2	Representation of the cooling gate . . . . .	61
2.3.3	HBAC scaling with iterations and bath polarization . . . . .	64
2.4	Pulsed polarization . . . . .	67
2.4.1	Using average Hamiltonian theory for the generation of a flip-flop Hamiltonian . . . . .	68
2.4.2	Experimental determination of the coupling constant . . . . .	69
2.4.3	Polarization measurements . . . . .	70
2.4.4	Effective interpulse distance for long microwave pulses . . . . .	71
2.5	Summary and outlook . . . . .	72
<b>3</b>	<b>Quantum enhanced correlation spectroscopy</b>	<b>75</b>
3.1	Measurement protocol with and without quantum memory . . . . .	76
3.1.1	Entanglement free correlation measurement with classical memory . . . . .	77
3.1.2	Quantum memory enabled by sensor-memory entanglement . . . . .	80
3.1.3	Performance comparison of quantum and classical memory . . . . .	82
3.1.4	Transition between classical and quantum memory . . . . .	84
3.2	Applications of the quantum enhanced correlation spectroscopy sequence to carbon nuclear spins . . . . .	86
3.2.1	Quantum correlations between memory qubit and sample spin . . . . .	89
3.2.2	Enhanced high resolution correlation spectroscopy . . . . .	91
3.3	Fixed sensing scheme for the detection of variable fields at high resolution . . . . .	93
3.4	Summary and outlook . . . . .	99
<b>4</b>	<b>High resolution hyperfine tensor analysis</b>	<b>101</b>
4.1	Quantum enhanced correlation spectroscopy combined with a dynamical decoupling sequence . . . . .	102
4.2	Determination of hyperfine component $A_{zx}$ . . . . .	104
4.3	Resolving $^{13}\text{C}$ nuclear spins by their $A_{zx}$ coupling. . . . .	105
4.4	Summary and outlook . . . . .	106

<b>5</b>	<b>The quantum Fourier transform in a hybrid qudit quantum phase estimation algorithm</b>	<b>109</b>
5.1	Basic principles of quantum phase estimation . . . . .	110
5.2	The hybrid qudit quantum Fourier transform . . . . .	111
5.3	The quantum phase estimation algorithm . . . . .	115
5.4	Experimental three level quantum phase estimation with quantum correlation spectroscopy . . . . .	122
5.5	Experimental implementation of the quantum phase estimation algorithm on a twelve level register . . . . .	126
5.6	Summary and outlook . . . . .	128
	<b>Appendices</b>	<b>131</b>
<b>A</b>	<b>Calibration of electron Rabi oscillations</b>	<b>131</b>
<b>B</b>	<b>Temperature tracking via the NV center electron spin double quantum transition</b>	<b>132</b>
<b>C</b>	<b>Additional experimental parameters</b>	<b>133</b>
<b>D</b>	<b>Effective sensing time for quantum enhanced stimulated echo</b>	<b>135</b>
<b>E</b>	<b>Trigonometrical similarities: <math>\sin(\sin)</math> and <math>\sin(\cos)</math></b>	<b>138</b>
<b>F</b>	<b>The Chrestenson gate implemented on the nuclear spin qutrit</b>	<b>139</b>
<b>G</b>	<b>State evolution during quantum phase estimation on a qutrit memory</b>	<b>141</b>
	<b>Bibliography</b>	<b>145</b>
	<b>Eidesstattliche Erklärung</b>	<b>163</b>

*O Diamond, Diamond, thou little knowest the mischief  
thou hast done.*

Sir Isaac Newton

# Summary

Quantum mechanics started out more than one hundred years ago as a counter-intuitive mathematical construct, whose implications could hardly be believed even by its founders. While knowledge about the laws of quantum mechanics is essential in numerous fields of modern technology, such as for the construction of lasers, atomic clocks or modern computers, control over multiple interacting quantum systems to this day remains tremendously challenging. For many years, overcoming these challenges seemed to be of purely scientific interest with no immediate reward for society. In the year 1982, Nobel laureate Richard P. Feynman changed that, when he came up with the idea to build quantum computers with previously unimaginable processing power, capable of simulating even most complex quantum systems [1]. Following Feynman, new quantum information processing algorithms were discovered, of which the most prominent one is Shor's algorithm for the factoring of large numbers [2–4]. As the word spread, that modern cryptography could be cracked within seconds, the enormous potential of quantum mechanical devices became known to a broader audience. Nowadays, quantum technological research is performed on a broad range of topics such as quantum computing and quantum communication as well as quantum metrology. For more than two decades, research on these fields has now been constantly gaining momentum and there is an ongoing race between numerous promising physical systems such as photons [5], trapped ions [6], superconducting circuits [7], quantum dots [8] and impurity spins in solids [9].

**The nitrogen-vacancy center in diamond** The NV center in diamond is one of the most advanced impurity spin systems, consisting of a nitrogen atom and an adjacent vacancy. This paramagnetic, atom like defect center has several outstanding properties, which distinguish it from other controllable quantum systems. The negatively charged NV center has a ground state electron spin-1 system, whose spin state can be initialized and read out optically. On one hand, this electron spin is very well isolated from the environment and reaches longitudinal relaxation times as well as coherence times beyond one millisecond even at ambient conditions. On the other hand, the NV center provides several interfaces for communication to other quantum systems, such as coupling via the

## Summary

photonic interface, magnetic fields, electric fields or phonons [10–13]. These interfaces give the NV center excellent perspectives in the field of quantum communication but also in the field of quantum metrology, where high susceptibilities to measured quantities are required. On the field of quantum computation, coupling to other quantum systems is particularly important, as only those who can gain control over multiple interacting quantum systems can unleash the full potential.

In this thesis, the NV center electron spin is used as a central spin, which couples to the  $^{14}\text{N}$  nuclear spin and to multiple  $^{13}\text{C}$  nuclear spins within the diamond lattice. In such a hybrid spin system, synergies between the two different spin species increase the versatility of a single nitrogen-vacancy center. The electron spin serves for repolarization and readout of the nuclear spin states but also of its own. It mediates the interaction between the nuclear spins, and communicates with the outside world. Communication here is understood in terms of coupling to other quantum systems for the upscaling of the quantum mechanical system but also in terms of quantum metrology, where information about measured quantities need to be acquired. The nuclear spins on the other hand are extremely robust with longitudinal relaxation times well above one second [14]. They can be controlled coherently and combined to nuclear spin registers for information storage and processing [15–17]. The robustness of the nuclear spin states persists, when the electron spin state is read out by laser illumination. Thereby, the quantum non-demolition measurement of quantum information becomes possible, which is an important ingredient in quantum information processing. Strongly coupled  $^{14}\text{N}$  and  $^{13}\text{C}$  nuclear spins (i.e. those coupled stronger than the inverse homogeneous broadening of the electron spin transitions) can be non-destructively read out with a technique for which the term single shot readout was coined [18, 19]. The present work has been executed entirely at room temperature.

**This thesis** presents pioneering work at the interface of two important fields of modern quantum science: quantum metrology and quantum information processing. Therefore, two subsystems are combined. One subsystem comprises of a single electron spin sensor which interactions with the target system and collects phase information about the measured quantities of interest. The other subsystem is formed by several nuclear spins, which work together as a small quantum processor. In a first step, the efficient initialization of the quantum register is shown. Then, the nuclear spin quantum processor is used to store and process the quantum information which is acquired by the quantum sensor in a measurement scheme, in which quantum phase estimation and quantum correlation spectroscopy is combined. Therefore, the quantum Fourier transform (QFT) algorithm is implemented on the quantum processor. The quantum processor is shown to improve the spectral resolution of the quantum sensor by the elongated storage time of the sensing information. It also increases the sensitivity of the measurement and the measurement bandwidth of detectable field amplitudes by use of the quantum phase

estimation algorithm. This work laid the foundation for applications in high-resolution nuclear magnetic resonance (NMR) spectroscopy [20]. The room temperature operability makes this quantum processor enhanced sensor interesting for applications in biosensing.

**Outline** In chapter 1, the aspects of the nitrogen-vacancy center in diamond which are important for quantum metrology and quantum information processing with nuclear spin support are introduced. In chapter 2, important methods for nuclear spin cooling and nuclear spin initialization are discussed, with a special focus on the Heat-bath algorithmic cooling technique. The remaining three chapters discuss different aspects of Kitaev's quantum phase estimation algorithm in the context of correlation spectroscopy methods. Chapter 3 improves existing correlation spectroscopy methods by a quantum memory to enhance spectral resolution and allow for coherent coupling to weakly coupled nuclear spins. Chapter 4 then combines the quantum memory enhanced correlation spectroscopy method with lock-in detection methods. It is shown, that thereby spectrally unresolvable nuclear spins become addressable. Consequentially, the principles of single qubit phase estimation are extended to the quantum phase estimation algorithm in chapter 5. A theory framework for the implementation of the QFT and the quantum phase estimation algorithm on hybrid qudit systems of arbitrary size is developed. Then the implementation of the quantum phase estimation algorithm is shown for a single qutrit memory and then on a quantum memory register of one qutrit and two qubits.

**Nuclear spin cooling** A key challenge in quantum technology is the initial state preparation of the used quantum systems. In particular quantum error correction needs a constant supply of fresh ancilla qubits. In quantum metrology, sensitivities are limited by spin polarization, due to which classical nuclear magnetic resonance sensors must be composed of very many spins to allow for high sensitivities despite their often poor spin polarization. Therefore, spin polarization and in particular spin polarization transfer techniques are a hugely investigated topic [21–23]. Due to its efficient optical spin polarization mechanism in combination with coherent spin control, the NV center is a convenient tool for spin polarization transfer to nuclear spins. Internal  $^{13}\text{C}$  nuclear spins can serve as a well characterized testbed for the investigation of such polarization transfer techniques. The major part of chapter 2 discusses the Heat-bath algorithmic cooling technique, which allows to purify the quantum state of some target qubits by repeatedly polarizing some other qubits (the reset qubits) and performing a gate operation between the target qubits and the reset qubits. The repolarization step of the reset qubits is commonly performed by bringing them in contact with a heat-bath with a temperature that is lower than that of the target qubits. Interestingly, this procedure allows to cool the target qubits below the temperature of the heat-bath. Experimental implementations of HBAC requires very good control over qubits as well as the ability to reset them. So far, HBAC experiments were performed in NMR experiments, where no more than

## Summary

proof-of-concept measurements were possible, which did not go beyond a few iterations or in which only very limited target spin polarizations  $\Delta p \sim 10^{-2}$  were reached. In particular, one key prediction, the asymptotic limit of HBAC had not yet been proven. At this limit, repeated applications of the HBAC algorithm do no more allow to extract entropy from the target system and it can not be cooled any further [24]. In this work, two  $^{13}\text{C}$  nuclear spin qubits can be reset by the electron spin which serves as the bath, while one  $^{14}\text{N}$  nuclear spin qubit is the cooling target. First a partial polarization transfer algorithm was introduced, which allows for individual control over the polarization of the two reset spins. The maximum value for both the two reset spins is not identical due to the different hyperfine couplings and the resulting different degrees of control over the two spins. The polarization of the two reset spins with this spin polarization transfer technique can be freely tuned from zero up to more than three orders of magnitude above the Boltzmann distributed polarization. The quantum gate operation which is used to cool the target nuclear spin has to be implemented as a non-local gate between the three involved nuclear spins, which due to their small gyromagnetic ratios do not interact with each other. Therefore, a quantum gate sequence was designed, which makes use of the electron spin and its hyperfine coupling to the three nuclear spins. The electron spin serves as a mediator between the nuclear spins and the gate operation required for the HBAC cooling gate is implemented with a gate sequence that consists of 15 individual electron and nuclear spin gates. The cooling gate is unitary, and performs the operation  $|trr\rangle = |100\rangle \leftrightarrow |011\rangle$  between the target qubit  $t$  and the two reset qubits  $r$ . From a classical point of view, thereby the target spin is flipped only, if the two reset qubits are pointing in the opposite direction. Since the two reset qubits are polarized into the state  $|rr\rangle = |11\rangle$  and therefore have a preferred orientation, the direction  $|100\rangle \rightarrow |011\rangle$  has a higher probability. Please note, that this is true only up to a certain target spin polarization, beyond which the two directions become equally probable and the cooling procedure stops. The cooling procedure of reset spin repolarization with subsequent application of the HBAC cooling gate is repeated up to 23 times. The asymptotic limit of HBAC was proven for different reset spin polarizations  $\Delta p = p(|0\rangle) - p(|1\rangle)$ .  $\Delta p$  is given as differences of the probabilities to find the nuclear spin qubit in either of its two eigenstates  $|0\rangle$  and  $|1\rangle$ . For the maximally tested reset spin qubit polarizations of  $\Delta p = 0.59$  and  $\Delta p = 0.42$ , the target spin polarization reached  $\Delta p = 0.8$ , which shows an increase of the target spin polarization by a factor of 1.35 over the polarization of the bath (i.e. the reset polarizations of the reset qubits). In a second experiment, the polarizations of the two reset spins were varied individually from  $\Delta p = 0$  to their individual maximum values and the target spin polarization was monitored. For further demonstration of the cooling of weakly coupled nuclear spins, a pulse sequence was designed with the PulsePol framework, which uses the hyperfine coupling component  $A_{zz}$  to generate an artificial flip-flop Hamiltonian between the NV center electron spin and one or multiple  $^{13}\text{C}$ . Nuclear spins with couplings of  $A_{zz} = 12.3\text{ kHz}$  and  $A_{zz} = 5.8\text{ kHz}$  could both be

polarized to  $\Delta p > 90\%$ .

**Quantum phase estimation** In chapters 3 to 5 the electron spin is used as central spin sensor with coupling to the environment, while one  $^{14}\text{N}$  nuclear spin qutrit and two  $^{13}\text{C}$  spin qubits are used for storage, processing and efficient readout of the sensing data. With this setup, the quantum phase estimation algorithm is implemented, with different register sizes from two to twelve levels. The phase information is collected with a correlation spectroscopy measurement, which allows for high frequency resolutions ( $\approx 200$  Hz), as a consequence of long phase correlation times. The latter can be on the order of the longitudinal relaxation time of the NV center electron spin ( $\approx 5$  ms). In correlation measurements, the results of two individual quantum measurements are correlated and this correlation signal is then the actual result. Thereby, the measurement results that are correlated ideally exist as quantum information, e.g. the two measurement phases  $\phi_1 = \tilde{\gamma}B_1$  and  $\phi_2 = \tilde{\gamma}B_2$ . The gyromagnetic ratio  $\tilde{\gamma}$  is a proportionality constant, which determines how much phase a quantum sensor acquires for a given magnetic field  $B$ . When very high frequency resolutions are required, existing techniques store the measurement phases on the spin population of the electron spin, where it is subject to decoherence. Thereby, valuable sensing information is lost and the required measurement times are increased. A first but important advantage of the use of the  $^{14}\text{N}$  nuclear spin as a quantum memory is shown to be a factor of four reduction in measurement time for the same signal-to-noise ratio. The use of the quantum memory leads to an increase of the overall sequence duration of only 0.083%. The quantum memory enhanced correlation sequence is used to acquire a spectrum of the  $^{13}\text{C}$   $A_{zz}$  hyperfine coupling with a frequency resolution of 210 Hz (FWHM). Coherent interactions between the quantum memory and one weakly coupled nuclear spin are shown with the same frequency resolution, allowing to address individual qubits in a very dense spectrum. Thereby, weakly coupled nuclear spins are those, that have couplings on the order of the inhomogeneous broadening of the electron spin. Two ways to generate a maximally entangled state between the quantum memory and weakly coupled sample spin were shown. By the ability to detect and selectively address weakly coupled nuclear spins, the number of usable qubits is drastically increased, which improves the NV center capabilities for information processing.

In chapter 4 a path is shown, to address nuclear spins unresolvable in the  $A_{zz}$  hyperfine spectrum. Therefore, the quantum enhanced correlation sequence is combined with a dynamical-decoupling sequence, which manipulates the sample spins at a rate of their hyperfine components  $A_{zx}$  [25]. The joint sequence allows to acquire an  $A_{zx}$  spectrum with resolutions that are limited by the longitudinal relaxation time of the electron spin, whereas in existing techniques the shorter electron spin coherence time is relevant [25]. The  $A_{zz}$  and  $A_{zx}$  hyperfine coupling components of six nuclear spins have been experimentally determined with this novel technique. Two of those nuclear spins with

## Summary

hyperfine couplings  $A_{zz}$ , which differ by well below one kHz are shown to be now well resolvable via their hyperfine coupling components  $A_{zx}$ . An extension to a third hyperfine coupling component  $A_{zy}$  is possible.

In chapter 5, the quantum phase estimation algorithm is experimentally implemented on a sensor-memory system of a single electron spin sensor and a hybrid qudit memory register of up to twelve levels. The quantum phase information is acquired by the electron spin sensor and written to the memory register, where it is processed by the inverse quantum Fourier transform (iQFT) before it is converted to classical information by readout of the computational basis states.

To be able to accomplish this task, a general and instructive theory for construction of the QFT and the quantum phase estimation algorithm on hybrid multiplicity quantum systems is given. Existing theories for memory registers which are composed of qudits of equal multiplicities are extended for the implementation of the QFT to memory registers which are composed of qudits of arbitrary multiplicities  $d = \{d_1 d_2 \dots d_n\}$ . As a first result, a gate sequence for the experimental implementation of the QFT a register of one qutrit and two qubits is found. The QFT on a single qutrit was identified as the Chrestenson gate. A corresponding gate sequence for the implementation of the iQFT can be straightforwardly obtained by reverting the sequence for the QFT and conjugating each involved quantum gate. As a second result, a procedure was found for the determination of the sensing phases  $\Delta\phi^{(l)}$  that need to be written to each qudit. Only when this procedure is followed, the quantum phase estimation algorithm can find a meaningful approximation of an arbitrary sensing phase  $\Delta\phi$ . For a register of one qutrit and two qubits, the written phases must have ratios of 1 and 2, 1 and 4, and 1 and 8.

For the experimental implementation of the quantum phase estimation algorithm, firstly a qutrit memory register is used, to which a sensing phase  $\Delta\phi$  is written by a single electron spin sensor. Therefore, the electron spin sensor detects the magnetic field which is produced by single  $^{13}\text{C}$  nuclear spin with hyperfine coupling  $A_{zz} \approx 90$  kHz. This is achieved by a quantum correlation measurement, where two phase acquisition steps are separated by a long correlation time  $T_c$ . The combination of the quantum phase estimation algorithm with the quantum correlation spectroscopy allows to perform measurements which have high frequency precision due to long  $T_c$  and at the same time allow for determination of the signal amplitude with high precision and also high bandwidth. A three level memory increases the information content by a factor  $\log_2 3 \approx 1.58$  compared to a commonly used two-level memory. The qutrit sensing sequence is used to determine the amplitude and sign of the magnetization of a single  $^{13}\text{C}$  nuclear spin.

Secondly, the quantum phase estimation algorithm is experimentally implemented for the first time on a native hybrid spin system register consisting of a qutrit and two qubits (cf. [26], where a qutrit is emulated by two qubits). A twelve-level memory can obtain a factor of  $\log_2 12 \approx 3.58$  more phase information than a two-level memory and thus for example increase the bandwidth of an amplitude measurement by this factor.

In future experiments, the size of the memory register can be increased by the use of weakly coupled nuclear spins. Therefore, it may be necessary to go to lower temperatures, where the longitudinal relaxation time of the NV center electron spin is longer. The quantum phase estimation algorithms can be performed on the register of size  $N = 12$  to measure external magnetic fields or to improve the detection and coherent coupling to nuclear spins within the diamond. Proof of principle quantum algorithms such as Shor's algorithm are also an interesting application. In particular on the evolving field of quantum machine learning, new potential applications for the QFT are arising.



# The nitrogen-vacancy center and the nuclear spins surrounding it

The NV center has several extraordinary properties, making it well suited for the use in quantum devices in the fields of quantum metrology, quantum information processing and quantum communication. Research is performed in various directions ranging from single-photon source [27, 28] and devices built for quantum teleportation and quantum key distribution [29–32] over quantum computing devices [14, 16, 17, 33–35] to quantum sensors of many kinds. The NV center is highly susceptible to measure quantities such as magnetic fields [36–38], electric fields [12, 39, 40], temperature [41–44] and pressure [42, 45] and can be used for their detection. Moreover the spin nature of the NV center allows for the construction of gyroscopes [46]. Furthermore, the small size and the high susceptibility to magnetic fields makes the NV center well suitable for the detection of single or multiple spins inside or outside the diamond [20, 25, 47–53]. This chapter highlights the aspects of the NV center which are important for quantum sensing and quantum information processing at ambient conditions and high magnetic fields. Section 1.1 discusses the properties of the host material, diamond, along with the properties of some common impurities. Section 1.2 gives a quick overview about the very important but often overlooked fact, that one NV center can exist in different charge states at different times. Section 1.3 covers the optical readout and initialization of the NV center electron spin as well as the energy level structure and the ground state and excited state Hamiltonian. As the intrinsic  $^{14}\text{N}$  nuclear spin and additionally the  $^{13}\text{C}$  spins around the NV center are particularly important for the present work, section 1.4 discusses these two nuclear spin species and their hyperfine coupling to the NV center electron spin. Section 1.6 then explains basic principles and experimental implementation of electron and nuclear spin manipulations including non-local operations between the

spins. The longitudinal and transversal relaxation times of electron and nuclear spins are found in section 1.7. Finally, section 1.8 covers the quantum nondemolition measurements (QND measurements) readout of single  $^{14}\text{N}$  and  $^{13}\text{C}$  nuclear spins and the requirements thereof.

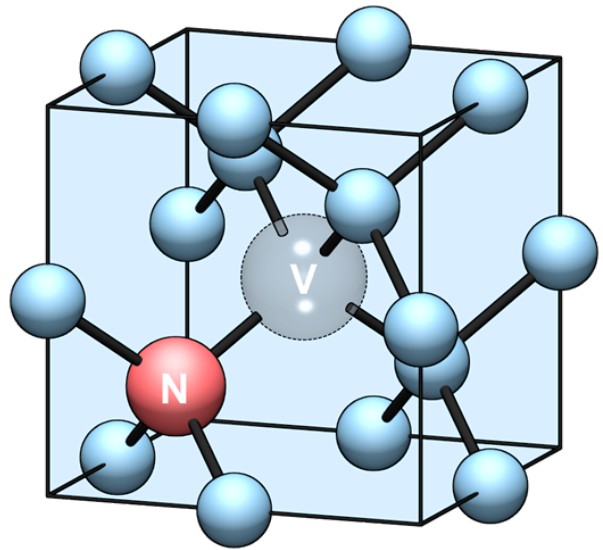
## 1.1 Defects in diamond

Diamond consists of carbon atoms with a face-centered cubic crystal structure and a two atomic basis. There is a shift of one fourth of a unit cell between the two sublattices [54]. Each carbon shares electrons with four other carbon atoms to which it is covalently bonded. The atom orbitals are  $sp^3$  hybridized and are arranged in a tetrahedral structure with interior angles of  $109.5^\circ$ . The covalent bond is strong and the carbon-carbon bonding length is only  $1.54 \text{ \AA}$ . This structure is the reason for several extraordinary properties making diamond stand out from other materials. As the covalent bond has to be broken, diamond is very stable in terms of thermal stress, physical stress and when treated with chemicals. Almost any substance can be brought in contact to a diamond based quantum sensor for chemical, physical or biological analysis. Diamond is the hardest naturally occurring material with a very high Debye temperature of  $1860 \text{ K}$  [55]. As a result, the phonon density is extremely low. The high thermal conductivity makes diamond suitable as a heat sink material or as a detector material in high energy physics [56]. In quantum applications, the measurement apparatus itself may produce large amounts of heat due to laser or microwave control fields, which with diamond as base material can be cooled away efficiently and passively. Diamond has one of the largest band gaps of all materials ( $5.5 \text{ eV}$  at room temperature) and thus is, in its pure form, transparent as well as an electrical insulator [57]. The refractive index of diamond is  $\sim 2.4$  in the visible and infrared, but reaches values up to  $\sim 3.5$  in the ultraviolet region. In nature, diamond rarely exists in its pure form of only carbon, with a natural concentration of  $98.9\% \text{ }^{12}\text{C}$  and  $1.1\% \text{ }^{13}\text{C}$ . Instead, there exist a large number of different impurities and lattice defects, making the physical properties of diamond such as heat conductivity, electrical conductivity and optical properties tunable in a wide range [58, 59]. The most prominent tunable property is the color of diamond making it an important gemstone. Nitrogen built into the lattice changes the appearance of diamond to yellow, and boron to blue, while a high concentration of NV centers lets diamond appear dark red or even close to black [60]. Some prominent examples of optically active impurities other than the NV center are the silicon-vacancy center (SiV center) and the germanium-vacancy center (GeV center). Countless numbers of other luminescent lattice defects may be the cause for brown, green, purple, pink, orange or red color [61].

In nature, diamonds are formed deep inside the mantle of the earth under high pressures and high temperatures. In quantum technology, often artificial diamonds are used. New

fabrication techniques provide diamond in almost arbitrary purity and concentration ratio of  $^{12}\text{C}$  and  $^{13}\text{C}$  isotopes. The isotope  $^{12}\text{C}$  does not possess a nuclear spin and thus diamond can provide an environment with ultra low magnetic field noise. This good control over the exact isotope composition of created diamonds allow for spin noise environments with very long coherence times. The high pressure high temperature (HPHT) method resembles the natural formation process of diamonds and is for example used for the generation of nanometer sized diamond fragments (nanodiamonds) and in industrial applications. The chemical vapor deposition (CVD) method uses a carbon-containing vapor in a plasma chamber, which is treated by electromagnetic radiation. The thereby generated free carbon atoms are deposited on a diamond substrate and the diamond grows homoepitaxially. If enough nitrogen is in the plasma, NV centers are generated during the growth process, usually followed by high temperature annealing. In general, only a small fraction of nitrogen is converted to NV centers, the rest remains as substitutional nitrogen centers (P1 centers) within the diamond lattice. P1 centers are the reason for a yellow color of diamond but also for magnetic noise, as they have a single electron spin ( $S = 1/2$ ). Other impurities like silicon or boron can also be deposited out of the gas phase. Isolated vacancies, created during growth or later by bombardement with molecules or atoms can be optically active and behave as deep electron donors or acceptors depending on their charge state. At high temperatures, vacancies become mobile, leading to two different, relevant scenarios. Either an NV center is formed together with a nitrogen atom or a divacancy is formed, when two vacancies find each other. Divacancies are stable and can exist in different charge states. They are mostly a source of noise and can be analyzed via electron paramagnetic resonance (EPR) measurements [62, 63]. The orientation of the grown diamond depends on the provided diamond substrate. Orientations are (1 0 0), where the C-C bonds form an angle of  $54.75^\circ$  with the surface and (1 1 1), where the possible angles are  $90^\circ$  and  $19.5^\circ$ . The greater hardness of (1 1 1) diamond makes it more difficult to cleave and even more difficult to polish. Thus it is less often used compared to (1 0 0) diamond, although some orientations of NV center in (1 1 1) diamond tend to shine brighter due to a more favorable orientation of the optical dipole perpendicular to the diamond surface [64].

**Fig. 1.1: NV center inside a diamond unit cell.** One atom is replaced by a nitrogen (N) atom while next to it, one carbon atom is removed (V) [65]. The tetrahedral diamond structure with bond angles of  $109.5^\circ$  allows four different orientations of NV center with respect to the diamond surface. The direction of the NV center bond (N-V or V-N) is another degree of freedom, which is hard to detect and in most applications plays a minor role [40]. The NV center has  $c_{3v}$  symmetry with a symmetry axis as the  $z$ -axis falling together with the  $(\langle 111 \rangle)$  direction of the diamond lattice. Image by Ingmar Jakobi



## 1.2 Electronic configurations of the nitrogen-vacancy center

The NV center is a deep level defect in diamond, which was first detected optically in the year 1976 by Davies et al. The real potential of the NV center for quantum technology was unravelled in 1997, when single NV centers have been detected for the first time by Gruber et al. [66]. The NV center can exist in different charge states.

The  $NV^0$  charge state involves a total of five electrons attributed to the dangling bonds of the nitrogen atom and the vacancy site, see figure 1.2a [67, 68]. In the  $NV^0$  charge state, the NV center has one unpaired electron and is paramagnetic with  $S = 1/2$  in the ground state and  $S = 3/2$  in the optically excited state [69]. The  $NV^0$  ground and excited states are separated by a zero-phonon line (ZPL) of 2.156 eV (575 nm), see figure 1.3.

A large bias gate voltage and a resulting shift of the diamonds Fermi level can lead to ionization of  $NV^0$  and bring the NV center to its positive charge state  $NV^+$ , see figure 1.2b.  $NV^+$  is spinless and not optically active, making it useful to store information [14]. Optical excitation with energies on the order of the  $NV^0$  ZPL and above can lead to the capture of an electron and thus to the formation of the  $NV^-$  with two unpaired electrons ( $S = 1$ ) [70–72]. The ZPL of  $NV^-$  is found at an energy of 1.945 eV, equivalent to a wavelength of 637 nm (see figures 1.3 and 1.4). Both  $NV^-$  and  $NV^0$  charge states can be stable at room temperature, depending on the local chemical environment around the NV center [73].

The laser induced conversion from  $NV^-$  to  $NV^0$  happens predominantly at wavelengths well below the  $NV^-$  ZPL [74]. Consequently, at wavelengths around 637 nm, the  $NV^0$  charge state is stable, however pumping to  $NV^0$  occurs at a rather small rate. The wavelength and power dependent ionization and recombination processes between  $NV^0$  and  $NV^-$  lead to applications such as super-resolution microscopy and new readout

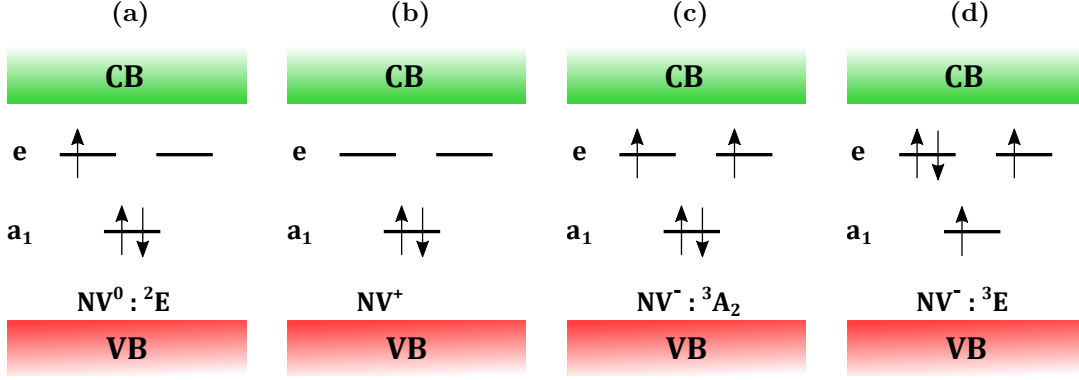
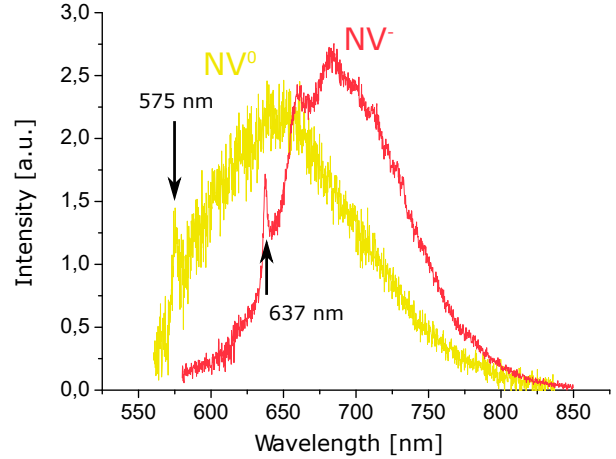


**Fig. 1.2: Electronic configurations of the NV center for different charge states.** (a) The nitrogen-vacancy center in the neutral charge state (NV<sup>0</sup>) has a total of five electrons and one unpaired electron ( $S = 1/2$ ). Two electrons are in the valence band. (b) The nitrogen-vacancy center in the positive charge state (NV<sup>+</sup>) has a total of four electrons and no unpaired electron. Ground (c) and excited state (d) of the nitrogen-vacancy center in the negative charge state (NV<sup>-</sup>) both have six electrons with two unpaired electrons ( $S = 1$ ).

**Fig. 1.3: Fluorescence emission spectrum of the NV center in diamond in two different charge states NV<sup>0</sup> and NV<sup>-</sup>.** Phonon sideband emission is dominant for both charge states, ZPL emission is only a very small fraction of the overall emission ( $\sim 4\%$  for NV<sup>-</sup>). The NV<sup>-</sup> spectrum is redshifted compared to the NV<sup>0</sup> spectrum, allowing for optical discrimination of the two charge states.



techniques for the electron spin state [75, 76]. For the present work, the presence of NV<sup>0</sup> has exclusively negative effects and at best, lowers the maximally achievable measurement contrast but in the worst case, makes experiments impossible to perform. Fermi level engineering allows to increase the probability to be in the NV<sup>-</sup> charge state to  $p(\text{NV}^-) \gtrsim 99\%$  even under optical illumination [77]. Unfortunately, this technique has unfavorable effects on other properties of the produced NV centers and is not widely applied. Without Fermi level engineering, the NV<sup>-</sup> concentration under optical illumination can not be increased above  $p(\text{NV}^-) \approx 80\%$ , which is also true for the present work (see section 1.8). Dependent on necessity and feasibility, either the reduced measurement contrast due to NV<sup>0</sup> is accepted, or alternatively, methods for the post selection are applied [17, 74, 78]. Fortunately, the NV<sup>-</sup> charge state is stable without

laser illumination beyond common experimental timescales of a few ms.

Throughout this thesis, charge states  $NV^0$  and  $NV^+$  play only a minor role, while charge state  $NV^-$  is the actual resource. Thus, outside section 1.2, the term NV center refers exclusively to  $NV^-$ , while any mentioning of the other two charge states is indicated separately.

### 1.3 The optical and spin properties of the nitrogen-vacancy center

The level structure of the NV center is very feature rich, involving numerous transitions in the optical and microwave ( $\sim$  GHz) regime [65]. At room temperature and when diamonds with low crystal strain are used, the complexity in particular of the excited state triplet  ${}^3E$  is drastically reduced [79–82]. This reduced level structure, which is sufficient for the present work, is shown in figure 1.4.

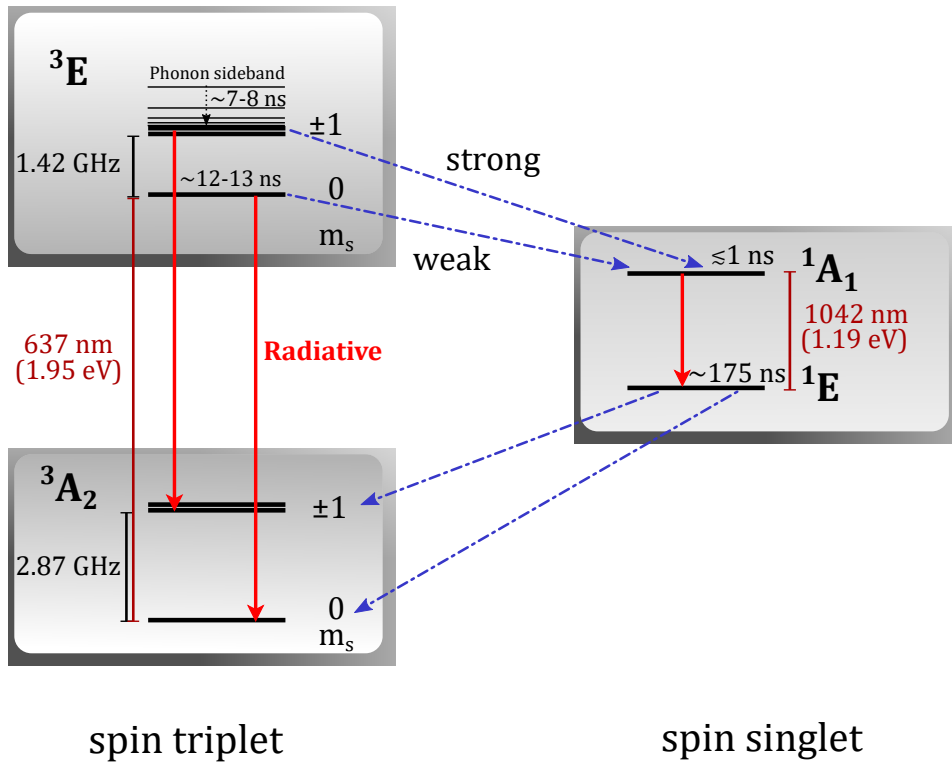


**Fig. 1.4: Reduced structure of the electron spin and optical transitions of the NV center in charge state  $NV^-$ .** The optical ground state  ${}^3A_2$  and the optical excited state  ${}^3E$  are separated by a ZPL of 637 nm. Electron spin magnetic quantum states  $m_s = \pm 1$  are shifted to positive energies by a zero field splitting (ZFS) of 2.87 GHz (1.47 GHz) compared to  $m_s = 0$  in optical ground (excited) state. The decay rates from excited to the metastable singlet state  ${}^1A_1$  are strongly spin state dependent. This mechanism allows for optical readout and polarization of the NV center electron spin.

### 1.3 The optical and spin properties of the nitrogen-vacancy center

The NV center has two unpaired electron spins, forming a triplet system ( $S = 1$ ) [70] in the optically excited and ground state. The electric dipole axes are perpendicular to the  $z$ -axis of the defect, making optical excitation and fluorescence detection most efficient along this axis [65]. The radiative transition between ground and excited state happens almost exclusively with conservation of the NV center electron spin [82]. The excited state lifetime is on the order of 10 ns (see figure 1.4) [33, 83, 84]. Very efficient optical excitation is possible with green laser light ( $\approx 500$  nm to 540 nm) into the phonon side band, which rapidly relaxes into the ground vibrational level of the optically excited state [74]. As most of the fluorescence ( $>95\%$ ) is emitted into the phonon sideband, which is red shifted to the ZPL, efficient separation of NV center fluorescence and the laser light used for excitation is possible [85]. One of the most prominent properties of the NV center can be understood, by taking into account the metastable singlet state, to which a non-radiative decay path exists from the optically excited state [65]. With 150 ns to 450 ns, the lifetime of this metastable singlet state is one order of magnitude larger than that of the optically excited state [79, 86]. The electron spin state not only determines the decay rate into the ground state ( $\sim 10$  ns) but also into the metastable singlet state. While the electron spin state  $m_s = 0$  undergoes many optical cycles before being trapped, spin states  $m_s = \pm 1$  decay from the optically excited state into the metastable singlet state with a probability exceeding 50% [84]. This spin selective trapping mechanism leads to approximately 30% to 40% higher NV center fluorescence in spin state  $m_s = 0$  compared to  $m_s = \pm 1$  and thus allows for optical spin readout (cf. figure 1.5).

After only a few optical cycles equivalent to 0.1  $\mu$ s to 1  $\mu$ s, the electron spin is found in the electron spin state  $m_s = 0$  with a probability exceeding 90% [67, 79, 87]. Excitation with red laser light with intensities well below saturation suppresses  $NV^0$  and allows for polarization efficiencies exceeding 98% (cf. figure 1.8 and section 1.8).

The twofold effect of laser illumination on the NV center electron spin comes with a downside. Spin initialization during the readout limits the possible readout time before the information is destroyed. Thus, an average of  $\lesssim 0.1$  signal photons is acquired per readout laser pulse (0.15  $\mu$ s to 3  $\mu$ s) and a measurement typically has to be repeated millions of times until the signal-to-noise-ratio (SNR) is sufficiently large. When the photon collection efficiency is increased by use of specialized photonic structures (e.g. solid immersion lenses (SILs)), the number of signal photons per laser pulse can, at least in principle, be increased above 1, however due to the limited measurement contrast of 30% to 40%, even then many repetitions are required [57, 88].

Both in the optically excited and ground states the two electrons experience spin-spin coupling leading to a  $D_{gs,z} = 2.87$  GHz and a  $D_{es,z} = 1.42$  GHz [89–91]. At ambient

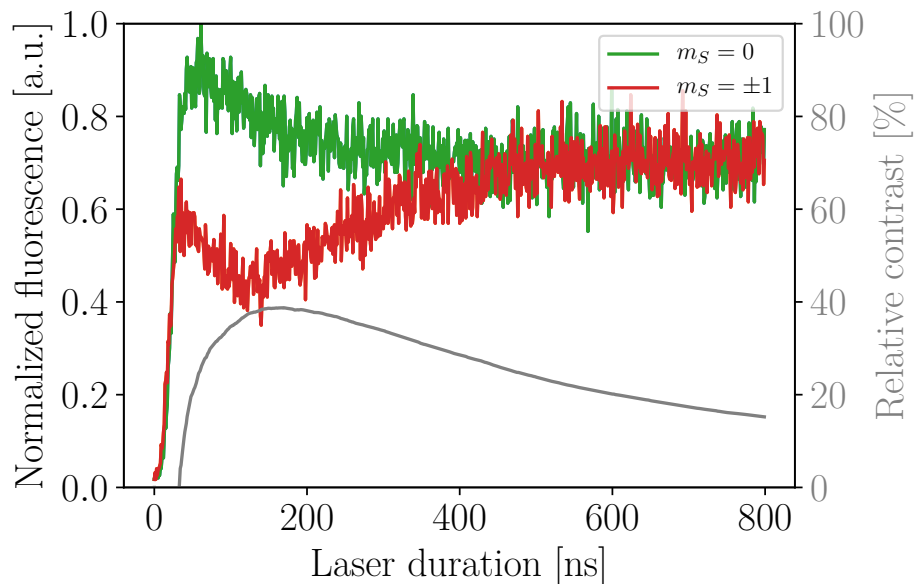


**Fig. 1.5: NV center fluorescence timetrace for preparation in electron spin states  $m_s = 0$  (green)  $m_s = \pm 1$  (red) and resulting relative fluorescence contrast.** The electron spin is prepared in either  $m_s = 0$  or  $m_s = -1$  and then read out via a green laser pulse of  $1.5 \mu\text{s}$  duration. For both curves, the experiment is repeated  $8e5$  times, during which all photons are detected along with the time of their arrival at a binning of  $1 \text{ ns}$ . The maximal achievable measurement contrast of  $30\%$  to  $40\%$  is found at approximately  $150 \text{ ns}$ , a value very close to the lifetime of the metastable singlet state. After somewhere near  $500 \text{ ns}$ , the number of acquired photons is almost independent of the initial  $m_s$  state and the incoming photons carry no information about the electron spin state. Thus, it is common to use the photon count rate at  $t \rightarrow \infty$  as a reference point for the counts received in the first  $250 \text{ ns}$  to  $500 \text{ ns}$ .

### 1.3 The optical and spin properties of the nitrogen-vacancy center

conditions,  $D_{\text{es},z}$  experiences a temperature dependence [43]

$$\frac{\partial}{\partial T} D_{\text{es},z} = -74.2 \frac{\text{kHz}}{\text{K}} \quad (1.1)$$

On one hand, this behaviour makes use of the NV center as a temperature sensor possible, for a large temperature range of 120 K to 700 K [41, 92, 93], however for the presented work it mostly increases the necessity for recalibration of the NV center electron transition (section 1.6.3 and appendix B).

The gyromagnetic ratio of the NV center electron spin is  $g = 2.0028 \pm 0.0003$ , deviates only very slightly from that of a free electron (2.0023) [67, 68]. The equivalent to a reduced electron gyromagnetic ratio is

$$\begin{aligned} \tilde{\gamma}_e &= g \frac{\mu_B}{h} \\ &= -28.031(4) \frac{\text{GHz}}{\text{T}} \end{aligned} \quad (1.2)$$

with  $\mu_B = 9.274\,009\,94 \times 10^{-24} \text{ J T}^{-1}$  and  $h = 6.626\,070\,04 \times 10^{-34} \text{ m}^2\text{kg/s}$ .

When the coupling to other spins (e.g.  $^{14}\text{N}$  or  $^{13}\text{C}$  nuclear spins) is ignored, in the optical ground state, the  $\hat{H}_{\text{NV}}$  comprises of the ZFS resulting from spin-spin coupling of the two electron spins and the Zeeman effect, i.e the splitting due to an external magnetic field  $\mathbf{B}_0$  is

$$\hat{H}_e = H_{\text{ZFS}_e} + H_{\text{zeemann}} \quad (1.3)$$

Due to constraints further specified in sections 1.4 and 1.8, for the present work all static external magnetic fields are applied along the  $z$ -axis, i.e.  $\mathbf{B}_0 = (0, 0, B_{0,z})^T$ . Additionally, the electron spin density forms a disk with the  $z$ -axis as a symmetry axis [67] and as a consequence, the ZFS is highly anisotropic and can be safely reduced to its  $z$ -component. For this scenario, the electron energies are described by the Hamiltonian

$$\hat{H}_e = D_z \hat{S}_z^2 - \tilde{\gamma}_e B_{0,z} \hat{S}_z \quad (1.4)$$

Since the zero field splitting parameter  $D_z$  and the electron transition frequency can be determined with accuracies far better than 10 kHz, equations 1.2 and 1.4 allows for the determination of the magnetic field  $B_{0,z}$  with a precision of

$$\begin{aligned} \Delta B_{0,z} &= -\frac{\Delta \tilde{\gamma}_e}{\tilde{\gamma}_e} B_{0,z} \\ &= 0.0001 B_{0,z} \end{aligned} \quad (1.5)$$

Figures 1.6a and 1.6c show the electron energy levels for different magnetic fields in ground and excited state according to equation 1.4. Spin states  $m_s = 0$  and  $m_s = -1$

are crossing for external magnetic fields  $B_{0,z} = \tilde{\gamma}_e/D_{\text{gs},z} \approx 0.1$  T in the ground state and  $B_{0,z} \approx 0.05$  T in the excited state, respectively. Since in reality, the NV center electron spin is coupled to its intrinsic  $^{14}\text{N}$  or  $^{15}\text{N}$  nuclear spin, some of the levels are in fact not crossing but rather have an avoided crossing. These two points are called ground state level anti-crossing (GSLAC) (cf. figure 1.6d) and excited state level anti-crossing (ESLAC) (cf. figure 1.6b). The behaviour at these special points has some drastic implications on the energy level scheme for a wide range of magnetic fields(cf. section 1.4).

## 1.4 The nitrogen-vacancy center as a hybrid quantum system

Two different nuclear spin isotopes have particular importance for the present work:  $^{13}\text{C}$  and  $^{14}\text{N}$ . The latter is important, as the NV center electron spin is always associated with its intrinsic nitrogen nuclear spin, and while there exist other nitrogen isotopes, only  $^{14}\text{N}$  ( $I = 1$ ) is found with high probability (natural concentration 99.63 %)(see table 1.1). The  $^{15}\text{N}$  ( $I = 1/2$ ) generally plays a role in NV center based research, however in natural diamonds, the probability of finding an  $^{15}\text{N}$  NV center is low. Other nitrogen isotopes are unstable with half-lives of no more than a few minutes [94] and play no role at all. The second widely important nuclear spin species in diamond is  $^{13}\text{C}$  ( $S = 1/2$ ) with a natural abundance of 1.1 %. Each  $^{13}\text{C}$  replaces a spinless  $^{12}\text{C}$  and thus can be found at any position in the diamond lattice. In artificially created diamond, both  $^{13}\text{C}$  and  $^{14}\text{N}$  concentrations are freely variable with techniques described in section 1.1.

**Hamiltonian of isolated nuclear spins** The Hamiltonian  $\hat{H}_n$  of any isolated nuclear spin consists, just like that of the NV center electron spin, of a potential ZFS with the associated constant  $Q$  and the Zeeman energy of the spin in an external magnetic field (equation 1.6).

$$\hat{H}_n = Q\hat{I}_z^2 - \tilde{\gamma}_n B_{0,z} \hat{I}_z \quad (1.6)$$

with the nuclear Larmor frequency  $f_L = -\tilde{\gamma}_n B_{0,z} \hat{I}_z$ . The  $^{14}\text{N}$  has an electric quadrupole moment  $Q = -4.946$  MHz [95], making the  $^{14}\text{N}$  nuclear spin transition energies susceptible to changes in the local electric field.  $^{13}\text{C}$  do not have a quadrupole splitting and thus  $Q = 0$ . Their reduced gyromagnetic ratios are  $\tilde{\gamma}_{n\text{C}} = 10.705$  for  $^{13}\text{C}$  and  $\tilde{\gamma}_{n\text{N}} = 3.0766$  for  $^{14}\text{N}$  resulting in a by  $\tilde{\gamma}_e/\tilde{\gamma}_{n\text{C}} \approx -2600$  times and  $\tilde{\gamma}_e/\tilde{\gamma}_{n\text{N}} \approx -9100$  times lower susceptibility to magnetic fields compared to the electron spin. The relevant nuclear spin parameters except for the hyperfine splitting are summarized in table 1.1.

Isotope	Natural abundance (%)	Nuclear spin $I$	$\tilde{\gamma}_n$ [MHz T <sup>-1</sup> ]	Quadrupolar splitting $Q$ [MHz]
<sup>14</sup> N	99.63	1	3.0766	-4.96
<sup>15</sup> N	0.37	1/2	-4.3156	0
<sup>13</sup> C	1.1	1/2	10.7051	0
<sup>12</sup> C	98.9	0	0	0

**Table 1.1:** Most abundant isotopes in the diamond lattice. <sup>14</sup>N and <sup>13</sup>C are the important isotopes for the present work. They both have a spin and a rather high natural abundance. The isotopes <sup>12</sup>C and <sup>15</sup>N are listed here for the sake of completeness.

**Full system Hamiltonian** The full NV center Hamiltonian  $\hat{H}_{\text{NV}}$  also involves the hyperfine coupling between the NV center electron spin and nuclear spins.

$$\hat{H}_{\text{NV}} = \hat{H}_e + \sum_i \left[ -\tilde{\gamma}_{n_i} B_{0,z} \hat{I}_{z,i} + Q \hat{I}_z^2 + \mathbf{S} \mathbf{A} \mathbf{I}_i \right] \quad (1.7)$$

The associated hyperfine tensor  $\mathbf{A}$  is described by the matrix

$$\mathbf{A} = \begin{pmatrix} A_{xx} & A_{xy} & A_{xz} \\ A_{yx} & A_{yy} & A_{yz} \\ A_{zx} & A_{zy} & A_{zz} \end{pmatrix} \quad (1.8)$$

The hyperfine coupling is composed of the isotropic Fermi contact interaction and the anisotropic dipolar interaction [65], thus

$$\hat{H}_{\text{hf}} = \hat{H}_{\text{Fermi}} + \hat{H}_{\text{dip}} \quad (1.9)$$

The isotropic Fermi contact interaction is proportional to the NV center electron spin density at the location of the nucleus and described by the proportionality constant describing the Fermi contact interaction  $a_{\text{iso}}$ .

$$\hat{H}_{\text{Fermi}} = a_{\text{iso}} \mathbf{S} \mathbf{I} \quad (1.10)$$

The spin density distribution is non-trivial, making it generally hard to find good theoretical estimates for hyperfine tensor describing the coupling between electron and nuclear spin. It can, for example, be extracted from density functional theory calculations [96].

The dipolar coupling is described by the Hamiltonian

$$\hat{H}_{\text{dip}} = \frac{\mu_0}{2} \hbar \tilde{\gamma}_e \tilde{\gamma}_n \frac{\mathbf{S} \mathbf{I} - 3(\mathbf{S} \mathbf{e}_r)(\mathbf{I} \mathbf{e}_r)}{|\mathbf{r}|^3} \quad (1.11)$$

Changes in temperature do change the lattice distances within the diamond lattice and thus have an effect on the hyperfine coupling.

Direct interaction between two nuclear spins is very weak due to the small values of  $\tilde{\gamma}_n$  and hence not considered in equation 1.7. The special case of two  $^{13}\text{C}$  nuclear spins positioned at adjacent lattice sites is very rare, and even then the dipolar coupling is no larger than a few kHz [97]. Nonetheless, such  $^{13}\text{C}$  dimers can be interesting quantum systems of their own, e.g. for robust storage in a decoherence free subspace [97–99].

### 1.4.1 The intrinsic nitrogen nuclear spin

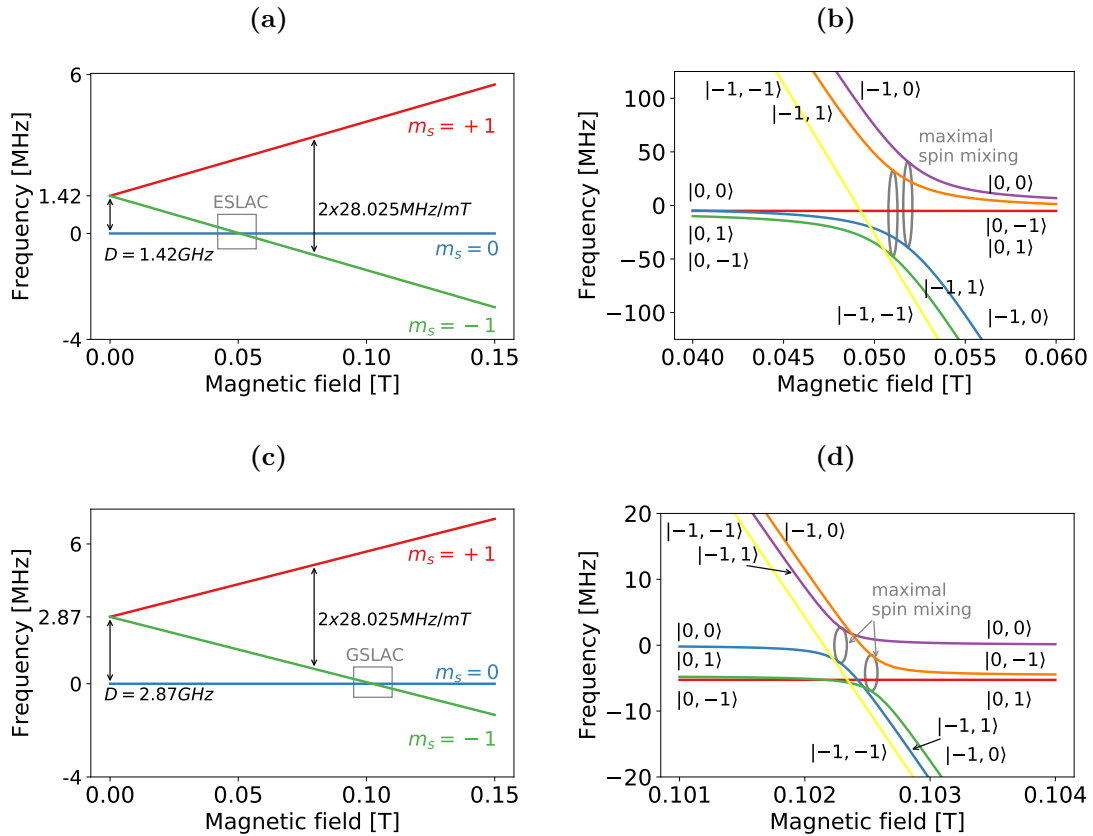


**Fig. 1.6:** Dependence of NV center energy levels on magnetic field  $B_{0,z}$  in optical excited ((a) and (b)) and optical ground state ((c) and (d)). While the reduced electron gyromagnetic ratio  $\tilde{\gamma}_e$  and thus the slope is identical in (a) and (c), the spin-spin coupling of the two electron spins is different and thus  $m_s = 0$  and  $m_s = -1$  are crossing at different magnetic fields. The six individual hyperfine levels are labeled as  $|m_s, m_N\rangle$ .

The location  $\mathbf{r}$  of the nitrogen atom relative to the NV center is fixed, and thus the  $^{14}\text{N}$  hyperfine parameters vary only by a few kHz from NV center to NV center. Due to the

### 1.4 The nitrogen-vacancy center as a hybrid quantum system

NV centers  $c_{3v}$  symmetry,  $\mathbf{A}$  in case of  $^{14}\text{N}$  is diagonal with respect to the  $z$ -axis, both in optical ground and excited state with components  $A_{xx} = A_{yy} = A_{\perp}$  and  $A_{zz} = A_{\parallel}$ .

$$\mathbf{A} = \begin{pmatrix} A_{\perp} & 0 & 0 \\ 0 & A_{\perp} & 0 \\ 0 & 0 & A_{\parallel} \end{pmatrix} \quad (1.12)$$

While in the optical ground state, the electron spin density is concentrated at the dangling bonds towards the carbon atoms, in the excited states it is shifted towards the nitrogen nuclear spin [67, 68]. Thus, the  $^{14}\text{N}$  hyperfine interaction is more than one order of magnitude larger in the optical excited state ( $A_{\parallel} = -60$  MHz,  $A_{\perp} = -40$  MHz) compared to the optical ground state ( $A_{\parallel} = -2.165$  MHz,  $A_{\perp} = -2.7$  MHz) having some drastic implications on  $^{14}\text{N}$  nuclear spin lifetimes (cf. section 1.8). The  $^{14}\text{N}$  and  $^{15}\text{N}$  hyperfine parameters are summarized in table 1.2.

Isotope	Electron	$A_{\parallel}$ [MHz]	$A_{\perp}$ [MHz]
$^{14}\text{N}$	ground state	-2.165	$-2.7 \pm 0.07$ [69]
$^{14}\text{N}$	excited state	-60 [90]	-40 [96]
$^{15}\text{N}$	ground state	$3.03 \pm 0.03$	$3.65 \pm 0.03$
$^{15}\text{N}$	excited state	$\pm 61 \pm 6$ [90]	$\pm 61 \pm 6$ [90]

**Table 1.2:** Nitrogen hyperfine parameters in optical ground and excited states.

In the case of a diagonal hyperfine tensor  $\mathbf{A}$ , the hyperfine interaction term  $\hat{H}_{hf}$  can be rewritten to

$$\hat{H}_{hf} = A_{\parallel} \hat{S}_z \hat{I}_z + \frac{A_{\perp}}{2} (\hat{S}_+ \hat{I}_- + \hat{S}_- \hat{I}_+) \quad (1.13)$$

Consequently, the electron and nuclear spin states  $|m_s, m_N\rangle$  experience a mixing (cf. figures 1.6b and 1.6d) which is maximal at GSLAC and ESLAC. In the basis of the low field energy eigenstates the mixing states are

$$\begin{aligned} |0, 0\rangle &\leftrightarrow |-1, 1\rangle \\ |0, -1\rangle &\leftrightarrow |-1, 0\rangle \end{aligned} \quad (1.14)$$

At magnetic fields far from GSLAC and ESLAC, the mixing behaviour is suppressed [16]. Also, in the ground state, this behaviour rarely plays a role as the coupling is very weak compared to the electron energy splitting ( $\sim$  GHz) (cf. table 1.2).

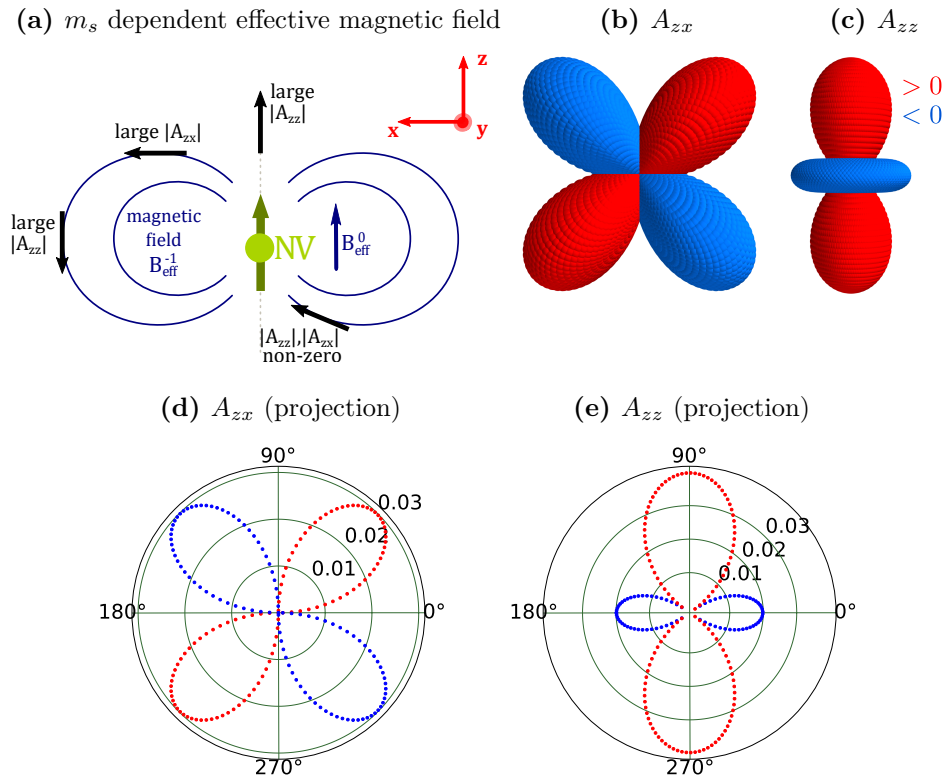


**Fig. 1.7: Dipolar hyperfine coupling components  $A_{zx}$  and  $A_{zz}$  for a  $^{13}\text{C}$  positioned 1 nm away from the NV center.**  $A_{zy}$  is not shown, as it is equivalent to  $A_{zx}$  due to the NV centers rotational symmetry. For each angle pair  $(\vartheta, \varphi)$ , the hyperfine tensor  $\mathbf{A}$  was calculated from equation 1.11 at a constant distance  $|\mathbf{r}| = 1$  nm. The resulting values  $A_{zx}(|\mathbf{r}| = 1$  nm,  $\vartheta, \varphi)$  and  $A_{zz}(|\mathbf{r}| = 1$  nm,  $\vartheta, \varphi)$  are shown schematically in (b), (c) and as a cut along the  $x$ - $z$ -plane in (d) and (e).

#### 1.4.2 $^{13}\text{C}$ nuclear spins surrounding the NV center

For  $^{13}\text{C}$  spins, the hyperfine tensor is diagonal only in special cases. More importantly, though, the term  $A_{\perp}$  is small for the majority of possible  $^{13}\text{C}$  positions relative to the NV center [100]. The relevant dynamics are described by the simplified hyperfine tensor

$$\mathbf{A} = \begin{pmatrix} 0 & 0 & 0 \\ 0 & 0 & 0 \\ A_{zx} & A_{zy} & A_{zz} \end{pmatrix} \quad (1.15)$$

For individual  $^{13}\text{C}$ , the NV centers  $c_{3v}$  symmetry allows to find a basis in which  $A_{zy} = 0$  and thus the  $^{13}\text{C}$  hyperfine tensor  $\mathbf{A}$  can be described by just two components  $A_{zx}$  and  $A_{zz}$ . The reduced structure of  $\mathbf{A}$  takes into account  $^{13}\text{C}$  effects on the electron spin eigenenergies but neglects those on its eigenstates. This so called “secular approximation” again is justified by the large energy difference between electron and nuclear spins.

Throughout this thesis,  $^{13}\text{C}$  will be used as a major resource, and their position relative to the NV center and consequently their hyperfine tensor associated with each  $^{13}\text{C}$  is crucial. Different locations of  $^{13}\text{C}$  can be detected, polarized and possibly used as a resource for quantum computing or quantum sensing with different techniques. Some techniques, such as nuclear QND measurements (cf. section 1.8) are only applicable, when  $|A_{zz}|$  is large compared to the inhomogeneous broadening of the NV center electron spin (cf. section 1.7) and  $|A_{zx}|$  is negligible compared to the  $^{13}\text{C}$  Zeeman splitting. These  $^{13}\text{C}$  are found mostly along the NV center  $z$ -axis and on a ring around the NV center with the  $z$ -axis as normal (cf. figure 1.7a-e). A second category of techniques provides selectivity to only those  $^{13}\text{C}$  with a certain  $A_{zz}$ , while the dynamic implemented via these techniques is happening on timescales of  $A_{zx}$ . This category of techniques can address weakly coupled  $^{13}\text{C}$  with  $A_{zz} > T_{2,e}$  but has larger restrictions on  $\mathbf{A}$ , as two hyperfine components are important.

### 1.4.3 Electron and nuclear spin eigenstates and eigenvalues

Unless noted otherwise, the external magnetic field throughout this thesis is applied along the  $z$ -axis and with  $B_{0,z} = 0.65$  T is rather large. Therefore, the eigenstates of NV center electron spin as well as of  $^{14}\text{N}$  and  $^{13}\text{C}$  nuclear spins are quantized along the  $z$ -axis with a very small tilt due to the hyperfine interaction. The electron spin eigenstates are  $|+1\rangle, |0\rangle, |-1\rangle$  with associated quantum number  $m_s = +1, 0, -1$ . The  $^{14}\text{N}$  nuclear spin eigenstates are  $|+\rangle, |0\rangle, |-\rangle$  with associated quantum number  $m_N = +1, 0, -1$ . The  $^{13}\text{C}$  nuclear spin eigenstates are  $|+\rangle, |-\rangle$  with associated quantum number  $m_C = +1/2, -1/2$ .

## 1.5 Experimental setup

Figure 1.8 shows the experimental setup consisting of a homebuilt confocal microscope, a permanent magnet for the creation of the external magnetic field  $B_{0,z}$  and equipment for electron and nuclear spin manipulation (cf. figure 1.10). The setup operates at ambient conditions, i.e. room temperature and atmospheric pressure and is used exclusively to work with single NV centers. The diamond sample is embedded into a sapphire waver of 2 mm thickness and a diameter of 50 mm. The sapphire waver is mounted on a 3-axis piezoelectric scanner with a travel range of  $100\ \mu\text{m} \times 100\ \mu\text{m} \times 25\ \mu\text{m}$  and sub nanometer resolution.

### 1.5.1 Used NV center

The diamond used for the most part of this thesis is a type IIa CVD layer with  $[100]$  surface orientation and a  $^{13}\text{C}$  concentration of 0.2% [101]. The size of the diamond is  $1.6 \times 1.2 \times 0.9\ \text{mm}^3$ . Within this diamond, among thousands of searched NV centers

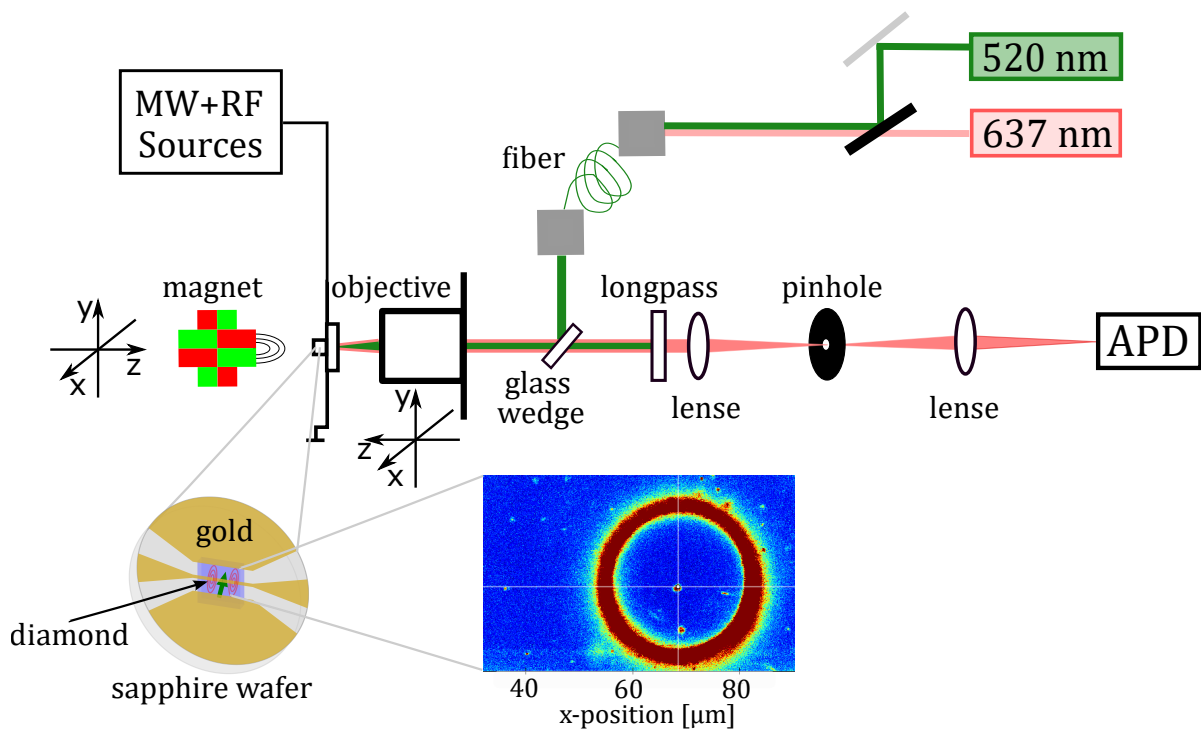
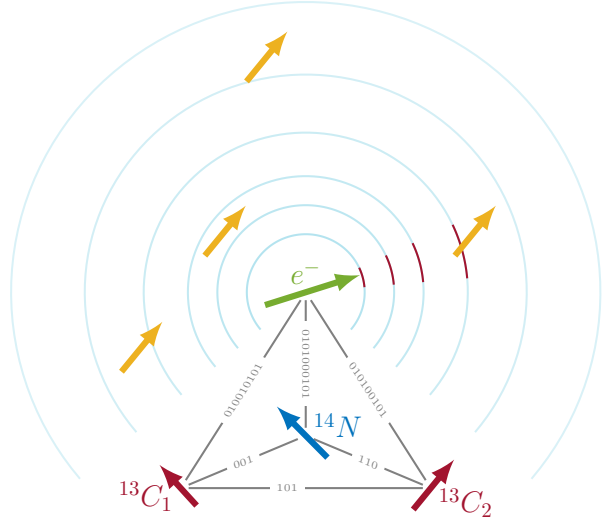


**Fig. 1.8: Sketch of the experimental setup.** The setup consists of a homebuilt confocal microscope, a permanent magnet and microwave (MW) and radio frequency (RF) sources. The 520 nm laser is operated at a power close to NV center saturation (0.1 mW to 0.5 mW before the objective). The 637 nm laser is used for electron spin repolarization and thus has a power of less than 10  $\mu$ W.

there was found one with three nuclear spins allowing for high fidelity QND measurement of their spin state (cf. figure 1.9 on page 25). This NV center was used for all experiments presented in this work, if not noted otherwise. It is located approximately  $15\ \mu\text{m}$  below the diamond surface and a solid immersion lens has been carved around it via focused ion beam milling [102]. The maximum count-rate measured was 1050 ks with a background of 18 ks. One of the three nuclear spins is the intrinsic  $^{14}\text{N}$  nuclear spin (details, cf. section 1.4 on page 18). The other two nuclear spins are both  $^{13}\text{C}$  nuclear spins, with  $A_{zz} = 0.089\ \text{MHz}$  and  $A_{zz} = 0.413\ \text{MHz}$  [17]. The electron spin optically detected magnetic resonance (ODMR) spectrum of transition  $m_s = 0 \leftrightarrow -1$  for this NV center is shown in figure 1.13 on page 32. The characteristic decay times can be found in section 1.7 on page 38. Additional details about this NV center have been unraveled with techniques described throughout this thesis, for example about other components of the hyperfine tensor  $\mathbf{A}$  or nuclear spins with weaker  $A_{zz}$  couplings. These results are presented in the respective chapters. To give the reader an overview about the experimental conditions, appendix C on page 133 lists some calibration data.

**Fig. 1.9: Used NV center electron spin (green) with its three nuclear spins  $^{14}\text{N}$  (blue),  $^{13}\text{C}_1$  and  $^{13}\text{C}_2$  (red).** The  $^{14}\text{N}$  nuclear spin is coupled with  $A_{zz} = -2.16\ \text{MHz}$ ,  $^{13}\text{C}_1$  with  $A_{zz} = 0.089\ \text{MHz}$  and  $^{13}\text{C}_2$  with  $A_{zz} = 0.413\ \text{MHz}$ . There are also other  $^{13}\text{C}$  nuclear spins (yellow) which are weaker coupled than  $^{13}\text{C}_1$  and  $^{13}\text{C}_2$ .



### 1.5.2 Optical path

The excitation laser beam generated by green (520 nm) and a red (637 nm) laser is combined with a beam splitter, guided through a single mode fiber and then reflected into a microscope objective by a glass wedge (cf. figure 1.8). The two lasers can be pulsed on time scales  $< 10\ \text{ns}$ . The oil microscope objective with a working distance of  $300\ \mu\text{m}$  and a numerical aperture of 1.3 focuses the excitation beam onto the NV center. To correct for potential drifts, e.g. due to thermal expansion, the fluorescence beam emitted by the NV center then again passes the glass wedge with a transmission  $> 99.5\%$  and is focused through a pin hole with a diameter of  $50\ \mu\text{m}$ . Fluorescence not coming

from an emitter in the focal plane of the objective is effectively filtered out. Then it passes a 650 nm long-pass filter, to block the excitation beam, which is multiple orders of magnitude stronger than the actual fluorescence. Finally, the fluorescence is detected by an avalanche photo diode (APD) with a collection efficiency  $> 70\%$  and a dead time of 7 ns. The total collection efficiency for fluorescence emitted by the NV center is much lower and can be estimated to be less than 0.2% to 2%. Onto the diamond used for most part of this work, there is a semispherical SIL fabricated with a size of 30  $\mu\text{m}$  diameter, to enhance the collection efficiency. The maximally measured count rate with the SIL was  $1050 \text{ kcts s}^{-1}$  with  $\approx 20 \text{ kcts s}^{-1}$  of background fluorescence. Over time, fluorescent particles on the sample increase the background fluorescence and most experiments are performed with only  $750 \text{ kcts s}^{-1}$  and  $\approx 80 \text{ kcts s}^{-1}$  background fluorescence.

### 1.5.3 External magnetic field

The external magnetic field is created by a permanent magnet, mounted on a 3-axis stage with a travel range of 30 cm and an additional rotational degree of freedom. The positioning is used, to align the field of the neodymium based magnet parallel to the  $z$ -axis with a precision of a few degrees. The magnet can produce magnetic fields of up to  $\approx 0.75 \text{ T}$ , equivalent to a transition frequency of the NV center electron transition  $m_s = 0 \leftrightarrow -1$  of  $\omega_0 \approx 18 \text{ GHz}$ . The chosen permanent magnet has a large magnetic field gradient and thus needs to be placed within a few hundred micrometers to the diamond. Therefore, both the thickness of the sample holder ( $\approx 2 \text{ mm}$ ) and the thickness of the diamond play a role. For the most part of this work, the distance between the magnet and the NV center was  $\approx 1 \text{ mm}$ . Unfortunately, a large magnetic field gradient comes with a very high sensitivity to thermal expansion of parts of the setup or any other positional drift of the magnet versus the position of the NV center. Since high fidelity operation of the setup can only be provided, when the NV center electron transition frequency is known with an accuracy better than the smallest hyperfine frequency to be addressed (here 89 kHz) (cf. sections 1.5.1 and 1.6.3 on pages 23 and 31), ODMR measurements are done at least every minute.

### 1.5.4 Electron and nuclear spin driving

A coplanar waveguide structure fabricated onto the diamond is used to focus the MW and RF fields onto the NV center. Electron spin energy splittings are typically on the order of GHz both in the optical ground and excited states [103]. Nuclear spins like  $^{13}\text{C}$ ,  $^{14}\text{N}$  or  $^{15}\text{N}$  however have gyromagnetic ratios multiple orders of magnitude lower compared to the NV center electron spin. Thus, their energy splittings are on the orders of MHz (cf. section 1.4 on page 18). This commonly large frequency separation makes use of MW as electron driving field and RF as nuclear spin driving field advisable throughout this work.

The circuit used for spin manipulation is shown in figure 1.10. Both the MW and the RF fields are generated by three of four channels of a single four channel arbitrary waveform generator (AWG). The used AWG has a sampling frequency of  $12 \text{ Gsamples}^{-1}$  but a bandwidth of 3.5 GHz, which is sufficient to directly generate RF fields but not sufficient to generate the required electron driving frequencies of 12 GHz to 18 GHz. Thus, the MW signal is upconverted with a second MW source and an IQ mixer. MW and RF fields are amplified and combined before they are sent through the sample for spin manipulation.

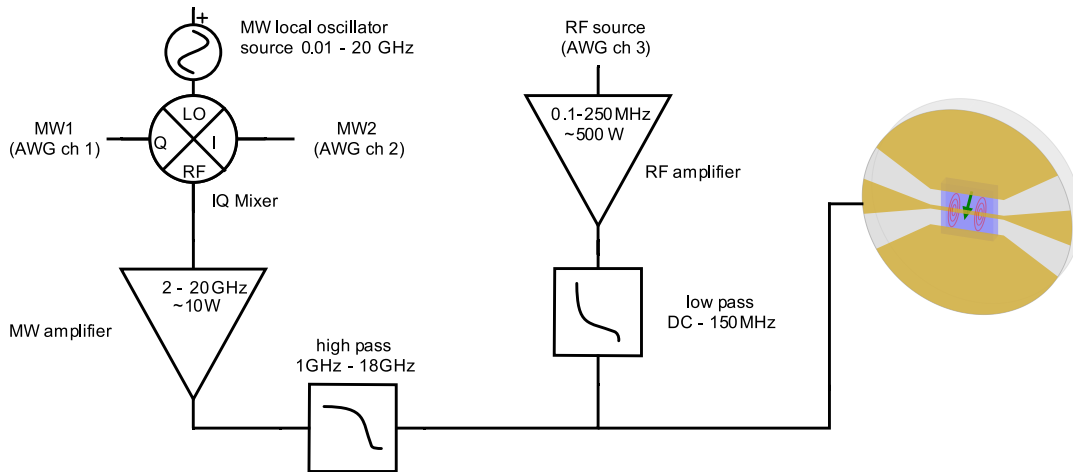


**Fig. 1.10: MW and RF circuit connected to sample holder.** The MW part consists of the Anritsu MG37929A signal generator as a high frequency local oscillator which is fed into an IQ mixer (Markimicrowave MMIQ-0626L). The intermediate (I) and quadrature (Q) signals are generated by two channels of a four channel Keysight M8190A AWG with 12 GHz sampling frequency and a bandwidth of 0 GHz to 3.5 GHz. The RF output of the IQ mixer is amplified to up to 10 W. The RF side is formed by the third AWG channel, amplified to up to 500 W. The amplified MW and RF signals are combined with a diplexer formed by a high pass and a low pass filter and then guided through a coplanar waveguide structure. The coplanar waveguide structure was fabricated on top of the diamond sample, for minimum separation to the NV center and thus maximum strength of the driving field.

## 1.6 Single spin manipulation

There are many spin manipulation techniques, e.g. the implementation of cavity mediated non-local quantum interactions, interactions mediated via strain or the environment and measurement based approaches [18, 104–107]. The most common spin manipulation technique both for the NV center electron spin as well as for the nuclear spins surrounding it, is performed via time dependent magnetic fields  $B_1(t)$ , applied along an axis perpendicular to the NV center axis [15, 108]. Without the loss of generality, this axis

for now is referred to as the y-axis. The resulting time dependent Hamiltonian reads

$$\hat{H}(t) = \hat{H}_0 + \tilde{\gamma}B_1(t)\hat{S}_y \quad (1.16)$$

Both, the availability of technical equipment and the availability of simple mathematical formalisms make use of cosine shaped fields feasible (cf. equation 1.17)

$$B_1(t) = B_{1,\text{amp}} \cos(2\pi\omega t + \varphi) \quad (1.17)$$

### 1.6.1 The Rabi formula

In the simplest case,  $\hat{H}(t)$  describes a two-level system and the driving is weak compared to the energy splitting  $\omega_0$  of the addressed transition ( $B_{1,\text{amp}}\tilde{\gamma}_e \ll \omega_0$ ). Then, transformation to the rotating frame and application of the rotating wave approximation [109, 110] leads to

$$\hat{H}_{RWA} = \begin{pmatrix} -\frac{\Delta}{2} & \Omega \\ \Omega & \frac{\Delta}{2} \end{pmatrix} \quad (1.18)$$

with the detuning  $\Delta = \omega - \omega_0$  and the Rabi frequency  $\Omega = \tilde{\gamma}B_{1,\text{amp}}$ . Conveniently,  $\hat{H}_{RWA}$  is time independent, but still gives a sufficiently good approximation for the full dynamics of the driven system according to

$$|\psi(t)\rangle = \underbrace{e^{-i\hat{H}_{RWA}t}}_U |\psi_0\rangle \quad (1.19)$$

One result of equation 1.18 is the so called Rabi Formula equation 1.20, which gives the probability  $p_{|1\rangle}$  to find a two level system which was initially prepared in state  $|0\rangle$  then after the pulse in state  $|1\rangle$ .

$$\begin{aligned} p_{|1\rangle}(t) &= |\langle 1|U(\Omega, t)|0\rangle|^2 \\ &= \frac{\Omega^2}{\Omega^2 + \Delta^2} \sin\left(\frac{\sqrt{\Omega^2 + \Delta^2}}{2}t_{\text{Rabi}}\right)^2 \\ &= \frac{\Omega^2}{\Omega_{\text{eff}}^2} \sin\left(\frac{\Omega_{\text{eff}}}{2}t_{\text{Rabi}}\right)^2 \end{aligned} \quad (1.20)$$

with  $\Omega_{\text{eff}} = \sqrt{\Omega^2 + \Delta^2}$ . Equation 1.20 can already provide a deep understanding of the manipulation of spin systems with multiple levels, multiple individual spins and even different spin species. When spectra are dense and thus transition frequencies are close, only this understanding makes high fidelity spin manipulation in complex systems possible.

### 1.6.2 Electron Rabi

At external magnetic fields  $B_{0,z}$  above the ground state level anti-crossing, the two NV center electron spin transitions  $m_s = 0 \leftrightarrow +1$  and  $m_s = 0 \leftrightarrow -1$  have a constant transition frequency difference of  $2D_{gs,z} \approx 5.74$  GHz (cf. figure 1.6c on page 20). Thus, for common Rabi frequencies  $\Omega < 100$  MHz  $\ll 2D_{gs,z}$  either of the two transitions can be individually treated as a two-level system according to equation 1.20. Figure 1.11c shows a Rabi experiment addressing the NV center electron spin subspace given by  $|0\rangle \equiv m_s = 0$  and  $|1\rangle \equiv m_s = -1$ .

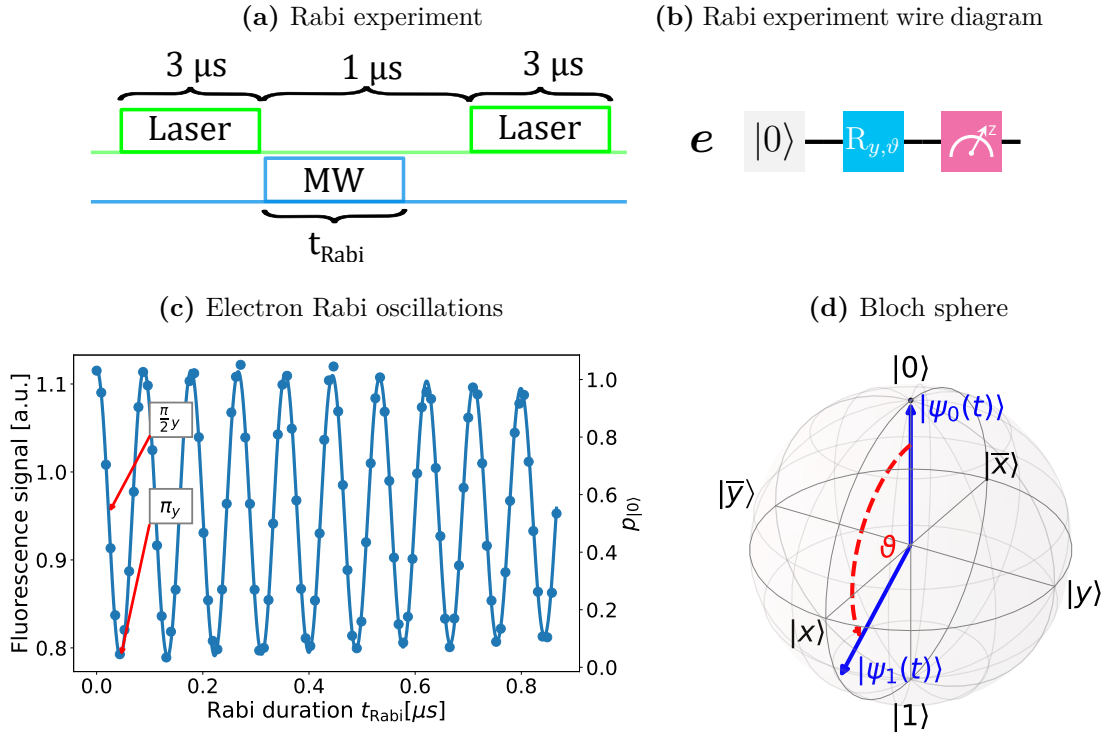


**Fig. 1.11: Electron Rabi oscillations at maximum MW driving power.** The pulse sequence is presented (a) schematically and (b) as a quantum wire diagram. Initially the electron spin is polarized into the spin state  $|0\rangle \equiv m_s = 0$  by a green laser pulse of duration  $3\mu\text{s}$ . Then the MW is turned on for a time  $t_{\text{Rabi}}$ , rotating the spin for an angle  $\vartheta = 2\pi\Omega t_{\text{Rabi}}$  around the  $y$ -axis of the Bloch sphere. The state after a time  $t_{\text{Rabi}}$  is  $|\psi(t)\rangle = \cos(\vartheta/2)|0\rangle + \sin(\vartheta/2)|1\rangle$ . A second green laser pulse finally reads out the electron spin population  $p_{|0\rangle}$ , which oscillates according to equation 1.20. The fluorescence signal shows a contrast of 31% and the oscillation frequency is 11.3 MHz at a driving power of  $-10$  dBm. The total time between the two laser pulses is constant, such that the experimental result is not falsified by electron spin decay (section 1.7).

The Rabi sequence consists of two green laser pulses for electron spin initialization and

readout, separated by a resonant MW pulse of duration  $t_{\text{Rabi}}$  (cf. figure 1.11a). The MW field is applied resonantly and  $t_{\text{Rabi}}$  is swept from  $0 \mu\text{s}$  to  $1 \mu\text{s}$ . The detected fluorescence signal shows oscillations resulting from the coherent electron spin manipulation. In figure 1.11c, the second y-axis gives the probability  $p_{|0\rangle}$  to be in  $m_s = 0 \equiv |0\rangle$  for different Rabi durations  $t_{\text{Rabi}}$ . Please note, that the values on this axis can only give an estimate for the actual value  $p_{|0\rangle}$ , as readout here is not a QND measurement (cf. sections 1.3 and 1.8 on pages 14 and 42).

Besides  $t_{\text{Rabi}}$ , defining the rotation angle  $\vartheta \propto t_{\text{Rabi}}$  on the Bloch sphere (figure 1.11d), the experimenter can also set the phase  $\varphi$  of the microwave (cf. equation 1.17), defining the axis around which the rotation occurs. For the important special case of resonant excitation ( $\Delta = 0$ ), the resulting operation can be expressed as

$$\mathbf{R}_{\varphi, \vartheta} = e^{-i\vartheta[\hat{S}_x \cos\varphi + \hat{S}_y \sin\varphi]} \quad (1.21)$$

Instead as an angle  $\varphi$ , the rotation axis sometimes is given as Cartesian axis label, which is shown in (cf. figure 1.11d).

$$\begin{aligned} x \equiv \varphi = 0 & & y \equiv \varphi = \pi/2 \\ \bar{x} \equiv \varphi = \pi & & \bar{y} \equiv \varphi = -\pi/2 \end{aligned} \quad (1.22)$$

There is a Rabi duration  $t_\pi = 1/2\Omega$ , for which the spin population is fully inverted and thus  $p_{|1\rangle} = 1$ . In the experiment presented in figure 1.11c, this happens after  $t_\pi \approx 44 \text{ ns}$ . This operation plays a major role in NV center experiments and thus has a special name,  $\pi$  - pulse:

$$\begin{aligned} \mathbf{R}_{\pi, y} &= \mathbf{R}_{y, \pi} \\ &= \begin{pmatrix} \cdot & -1 \\ 1 & \cdot \end{pmatrix} \end{aligned} \quad (1.23)$$

Another important point on the Rabi curve is at  $t_{\text{Rabi}} = .25/\Omega$ , corresponding to a  $\pi/2$  - pulse:

$$\begin{aligned} \mathbf{R}_{\pi/2, y} &= \mathbf{R}_{y, \pi/2} \\ &= \frac{1}{\sqrt{2}} \begin{pmatrix} 1 & 1 \\ 1 & -1 \end{pmatrix} \end{aligned} \quad (1.24)$$

The resulting state is an equal superposition of  $|0\rangle$  and  $|1\rangle$

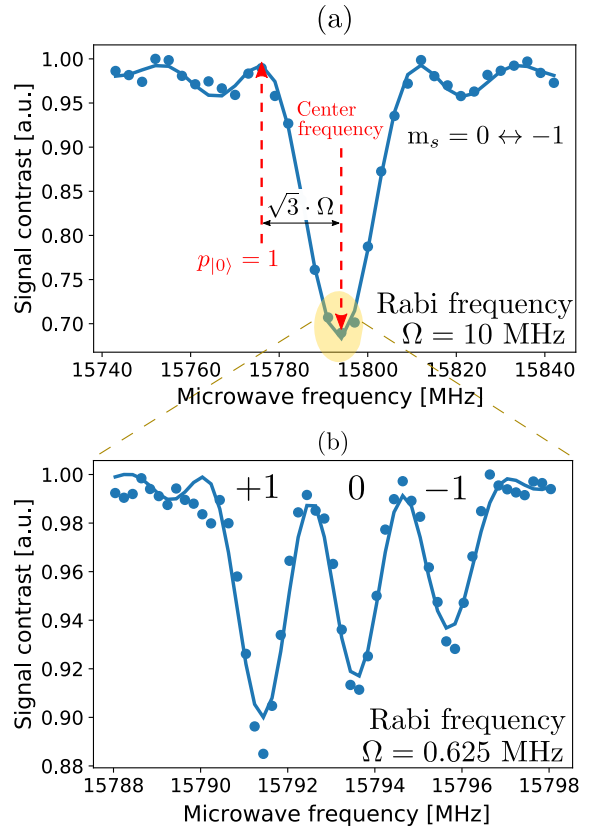
$$|\psi_{\pi/2}\rangle = \frac{(|0\rangle + |1\rangle)}{\sqrt{2}} \quad (1.25)$$

### 1.6.3 Optically detected magnetic resonance

The EPR spectrum of the NV center electron spin transitions is obtained, when the MW frequency  $\omega$  is swept while keeping the MW duration  $t_{\text{Rabi}} = t_\pi$  constant (cf. figure 1.11a). This type of experiment is called optically detected magnetic resonance, since unlike in standard EPR and NMR, the spin state is not determined by magnetic field measurements with magnet coils but optically, via detection of the NV center fluorescence [111].

Figure 1.12 shows two ODMR spectra taken of the NV center transition  $m_s = 0 \leftrightarrow -1$  at a magnetic field  $B_{0,z} \approx 0.66$  T. At a Rabi frequency  $\Omega = 10$  MHz, which is large compared to the  $^{14}\text{N}$  hyperfine component  $A_{zz} = -2.165$  MHz, the individual  $^{14}\text{N}$  are not visible due to power broadening. When the Rabi frequency is reduced to 0.625 MHz, the three individual hyperfine lines can be resolved.

**Fig. 1.12: ODMR spectra of NV center electron transition  $m_s = 0 \leftrightarrow m_s = -1$ .** The sequence is identical to figure 1.11a, however, here not the pulse duration but the pulse modulation frequency is swept. (a) was taken with a Rabi frequency  $\Omega = 10$  MHz resulting in a sinc function with the first minimum offset by  $\sqrt{3} \cdot \Omega \approx 8.7$  MHz to the center. The spectral linewidth is determined exclusively by the large Rabi frequency. (b) was taken with  $\Omega = 0.625$  MHz. There, the individual  $^{14}\text{N}$  hyperfine lines become visible at a separation of  $-2.165$  MHz. The population contrast is higher for higher  $^{14}\text{N}$  magnetic quantum numbers, due to the flip-flop processes resulting from equation 1.13 on page 21.



When the Rabi driving frequency is further reduced to  $\Omega = 25$  kHz, the spectral resolution improves further and the hyperfine couplings to all three strongly coupled nuclear spins  $^{14}\text{N}$ ,  $^{13}\text{C}_1$  and  $^{13}\text{C}_2$  are resolved (cf. section 1.5.1). The qutrit and the two qubits split the electron transition into twelve transitions, as shown in figure 1.13. Although there are nuclei coupled weaker than the coupling of nuclear spin  $^{13}\text{C}_2$  ( $A_{zz} = 89$  kHz), a further reduction of  $\Omega$  will not resolve any nuclei with smaller couplings, as the resolution of the ODMR spectrum is limited by the NV center  $T_2^*$  time (cf. section 1.7).

Taking an ODMR spectrum with sufficiently good resolution and width to resolve all features visible in figure 1.13 requires a lot of measurement time, and potential drifts need to be continuously refocused. Therefore, here a simulation with realistic  $A_{zz}$  and  $T_2^*$  values was made.

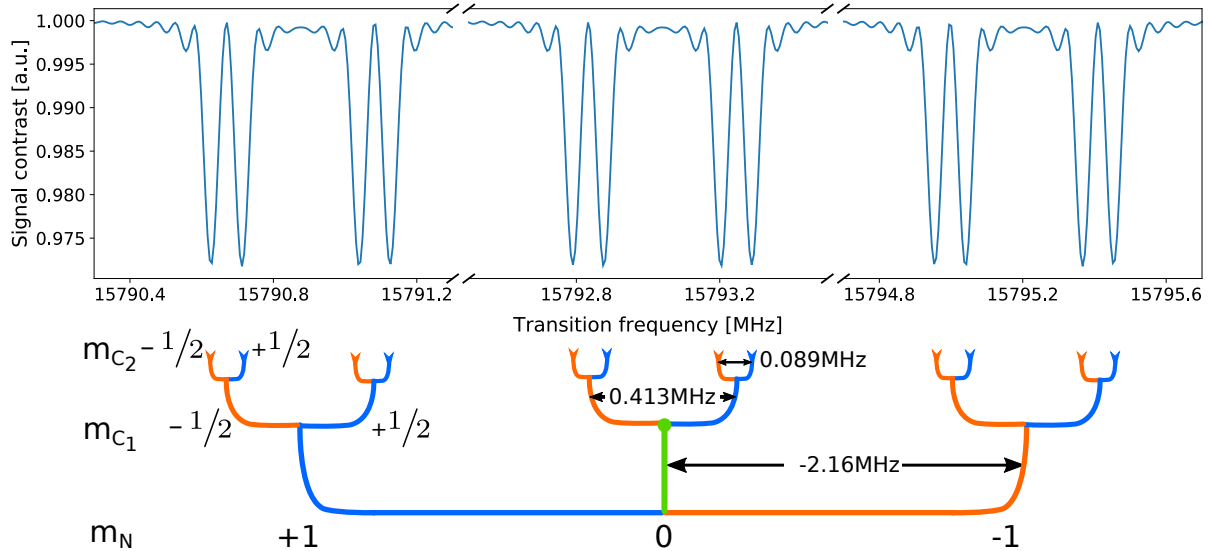


**Fig. 1.13: ODMR spectrum of electron transition  $m_s = 0 \leftrightarrow -1$ .** The electron is coupled to one  $^{14}\text{N}$  ( $I = 1$ ) and two  $^{13}\text{C}$  ( $I = 1/2$ ) nuclear spins, resulting in a twelve-fold split electron transition. The spectrum is simulated with experimental values  $A_{zz} = -2.16$  MHz, 0.413 MHz and 0.089 MHz determined from NMR experiments. The linewidth is a combination of inhomogeneous broadening and power broadening and was determined experimentally.

#### 1.6.4 Nuclear spin manipulation

The basic principles of electron spin manipulation that have so far been covered in this chapter can straightforwardly be transferred to nuclear spin manipulation. The main differences are the lower transition frequencies on the order of a few MHz as well as the lower Rabi frequencies on the order of kHz due to lower  $\tilde{\gamma}_n$ . Nuclear spin operations are often time consuming and can easily require hundreds of microseconds to be performed, which is long even on timescales of  $T_{1,e}$  (cf. section 1.7 on page 38). Therefore, the number of nuclear spin operations is usually limited to the minimum possible number. Nuclear spin Rabi frequencies can be hyperfine enhanced, which means that their Rabi frequency  $\Omega$  does not follow the simple formula  $\Omega = B_{1,\text{amp}}\tilde{\gamma}_n$  [112]. This is the case, when electron and nuclear spin states mix (cf. figure 1.6d on page 20), and therefore the nuclear spins effective reduced gyromagnetic ratio  $\tilde{\gamma}_n$  is increased [113]. The same effect does not play a role for electron spins, due to the orders of magnitude larger  $\tilde{\gamma}_e$  compared to  $\tilde{\gamma}_n$ .

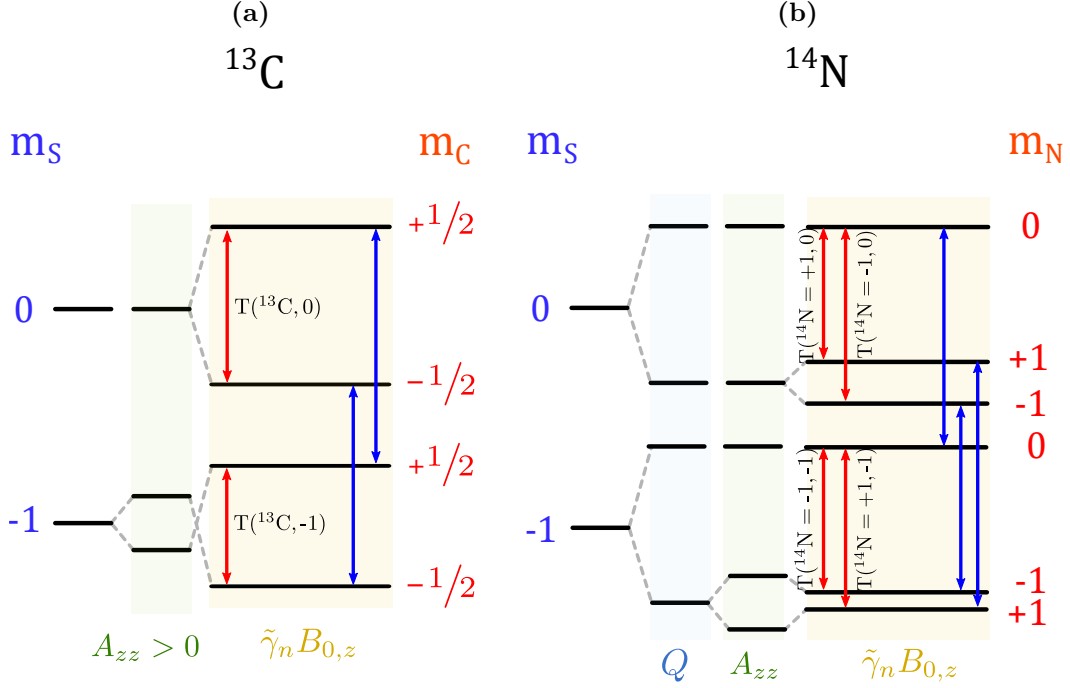


**Fig. 1.14: Energy levels of  $^{14}\text{N}$  and  $^{13}\text{C}$  nuclear spins for electron spin states  $m_s = 0$  and  $m_s = -1$  according to equations 1.26 and 1.27.**  $^{13}\text{C}$  energy levels are determined by the Zeeman and the hyperfine component, while the  $^{14}\text{N}$  energy levels are shifted by an additional quadrupole splitting  $Q$ . Allowed transitions are indicated by blue (electron) and red (nuclear) arrows. The transition frequencies are in the GHz range for electron spins and in the MHz range for nuclei.

The nuclear spin energy levels and spin transitions are shown in figures 1.14a and 1.14b for external magnetic fields  $B_{0,z}$  above the GSLAC. Since off-diagonal elements in the NV center Hamiltonian (equation 1.7 on page 19) can be neglected for the description of most phenomena, the  $^{14}\text{N}$  eigenenergies can be expressed as

$$f_N = m_N^2 Q - m_N \tilde{\gamma}_N B_{0,z} - m_N m_C A_{zz} \quad (1.26)$$

while the  $^{13}\text{C}$  eigenenergies are expressed by

$$f_C = -m_C m_s A_{zz} - m_C \tilde{\gamma}_C B_{0,z} \quad (1.27)$$

Local and non-local gates involving manipulation of one or more  $^{13}\text{C}$  nuclear spins are selective to one particular  $^{13}\text{C}$  only, if the electron is in the  $m_s = \pm 1$  subspace and hence the hyperfine interaction makes the  $^{13}\text{C}$  distinguishable. When the electron is in spin state  $m_s = 0$ , all  $^{13}\text{C}$  have the same transition frequency.

The labeling of  $^{14}\text{N}$  nuclear spin transitions is shown in figure 1.14b. Since the  $^{14}\text{N}$  is a spin triplet, two numbers are required, where  $T[^{14}\text{N} = +1, m_s]$  labels the

transition  $m_N = +1 \leftrightarrow 0$  and  $T [^{14}\text{N} = -1, m_s]$  labels the transition  $m_N = 0 \leftrightarrow -1$ . Spin operations on the  $^{14}\text{N}$  nuclear spin are labeled with a superscript  $+$  when the transition  $T [^{14}\text{N} = +1, m_s]$  is addressed and a superscript  $-$  when the transition  $T [^{14}\text{N} = -1, m_s]$  is addressed.  $^{13}\text{C}$  nuclei are spin doublets and thus, in principle, they have only one transition  $m_C = 1/2 \leftrightarrow -1/2$  per  $m_s$  - state. However, as there are many of them, the value of the  $A_{zz}$  coupling component is added to uniquely identify each  $^{13}\text{C}$  spin. As an example, the strongly coupled nuclear spin  $^{13}\text{C}_2$  has a hyperfine coupling frequency  $A_{zz} = 89$  kHz. The nuclear spin transitions of this nuclear spin are labeled  $T [^{13}\text{C} (A_{zz} = 89 \text{ kHz}), m_s]$ .

Table C.1 on page 134 lists Rabi driving calibration data for the individual  $^{14}\text{N}$  and  $^{13}\text{C}$  nuclear spin transitions in the different electron spin subspaces  $m_s$ .

### 1.6.5 Local spin phases

Local spin phases affect only a single spin and thus are never the cause for entanglement. A  $Z_\varphi$  operation can imprint a local spin phase  $\varphi$  onto a superposition state

$$\text{---} Z_\varphi \text{---} = \begin{pmatrix} 1 & \cdot \\ \cdot & e^{i\varphi} \end{pmatrix} \quad (1.28)$$

In free induction decay (FID) experiments,  $Z_\varphi$  is generated from a mismatch  $\Delta f$  of the addressed transition frequency, leading to a phase accumulation  $\varphi = 2\pi\Delta f \cdot \tau$  during a phase accumulation time  $\tau$ . This principle is also the foundation for quantum metrology performed with the NV center, as  $\Delta f$  may be generated by an offset magnetic field  $\Delta B_{0,z}$ . An FID is implemented via sequence Seq1.1.

$$\mathbf{e} \quad |0\rangle \text{---} \left[ \frac{\pi}{2} y \right] \text{---} Z_\varphi \text{---} \left[ \frac{\pi}{2} y \right] \text{---} \left[ \text{readout} \right] \text{---} \quad (\text{Seq1.1})$$

Here,  $\varphi$  contains the metrology information and thus is not known prior to spin readout. Not only external magnetic fields can cause a mismatch  $\Delta f$ , but also hyperfine coupling of another spin, that can be turned on and off. The borders to non-local spin operations here are fluent. Sometimes, a predefined local spin phase is supposed to be set on one or multiple nuclear spins, for example when a specific algorithm needs to be tested. Energy mismatches are in this case impractical to generate, and the situation gets more complicated, when multiple spins with different values of  $\tilde{\gamma}$  are supposed to be assigned different local spin phases  $\varphi_1, \varphi_2, \dots$ . However, there is a significantly simpler way to experimentally generate an effective representation of  $Z_\varphi$ , which works equally well for all spin types. Therefore, the phase  $\varphi$  of the MW field is changed according to equation 1.17

on page 28. The presence of a local spin phase in any FID type experiment can be efficiently mimicked according to

$$\text{---} \boxed{Z_\varphi} \text{---} \boxed{\frac{\pi}{2}_y} \text{---} = \text{---} \boxed{\frac{\pi}{2}_{\varphi'}} \text{---} \quad (1.29)$$

with  $\varphi' = \varphi + \pi/2$ . This is possible, as  $\varphi$  is a relative phase between the current spin state and the rotating frame of the MW. Both rotating the spin state on the Bloch sphere as well as counter-rotating the MW phase have the same effect. This technique is used widely in this thesis, for example in chapter 5, to benchmark the quantum phase estimation algorithm without actually performing the sensing step.

### 1.6.6 Non-local spin operations

As a rule of thumb, non-local spin operations require more experimental effort and have lower fidelities than local spin operations. Since there are three different spin species involved, there are several combinations of controlled gates and for some of them, there exists more than one straightforward experimental implementation.

**Electron controlled nuclear spin rotations** The simplest non-local gates are nuclear spin rotations  $R_{\varphi,\vartheta}$ , which are controlled by the electron spin state  $|m_s\rangle$ .

$$\begin{array}{c} e \text{---} \bullet \text{---} \\ | \\ \mathbf{n} \text{---} \boxed{R_{\varphi,\vartheta}} \text{---} \end{array} \quad (1.30)$$

These operations are performed by frequency selective driving the correct nuclear transition, which is valid for the respective electron spin subspace (cf. section 1.6.4 on page 32). Interestingly, for seemingly simple local nuclear spin rotations  $R_{\varphi,\vartheta}$  which act independently of the electron spin state, more than one transition needs to be addressed (cf. red arrows in figures 1.14a and 1.14b on page 33). Therefore, local nuclear spin rotations  $R_{\varphi,\vartheta}$  are harder to implement than their non-local counterpart.

**Nuclear spin controlled electron rotations** Rotations of the electron spin  $R_{\varphi,\vartheta}$ , which act only when the correct nuclear spin state  $|m_N\rangle$  or  $|m_C\rangle$  is present are another very important building block for experiments performed in this work. They can be implemented straightforwardly, if the nuclear spin hyperfine lines are resolvable in the ODMR spectrum (cf. figure 1.13 on page 32) [15, 114].

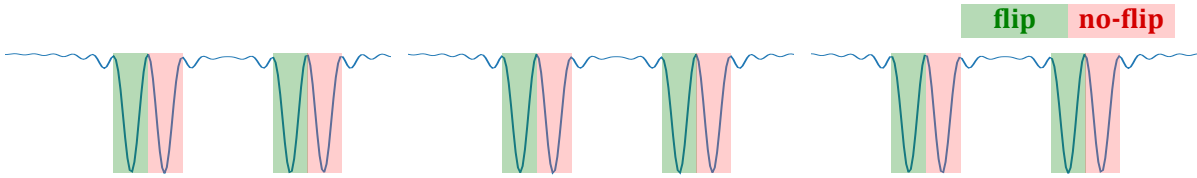


**Fig. 1.15: Selectivity of nuclear spin controlled electron pulse for the case of a dense, broadened electron spin spectrum.** The description of the individual lines is found in figure 1.13 on page 32. The line width is broadened by  $T_{2e}^*$  to approximately 30 kHz, while the closest hyperfine lines are only 89 kHz apart, corresponding to  $A_{zz}$  of  $^{13}\text{C}_2$ . A  $\pi$ -pulse intended to flip the electron spin selective to  $^{13}\text{C}_2$  nuclear spin state  $m_C = -1/2$  would require driving the electron spin in the parts of the spectrum which are marked in green, but not in the parts marked in red. A pulse performing this operation with a fidelity equal to one would take infinite time. Reasonably good fidelities can be achieved for pulses of 20  $\mu\text{s}$  duration.

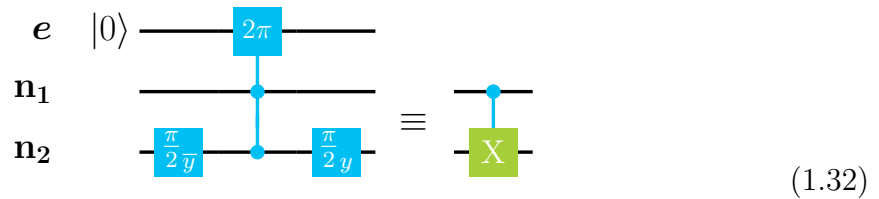
$$\begin{array}{c}
 e \text{ --- } \boxed{R_{\varphi, \nu}} \text{ ---} \\
 | \\
 \text{n} \text{ --- } \bullet \text{ ---}
 \end{array}
 \tag{1.31}$$

One example of such an operation would be an electron  $\pi$ -pulse, which is only performed, if the  $^{14}\text{N}$  nuclear spin is in state  $|+\rangle$ . The hyperfine resolved ODMR spectrum shown in figure 1.12 on page 31 proves, that the  $^{14}\text{N}$  hyperfine coupling  $A_{zz}$  is resolvable in the electron spin spectrum. The Rabi frequency needs to be set to  $\Omega \approx 0.625$  MHz and the MW frequency to approximately 15.792 GHz. With this parameter set, a  $^{14}\text{N}$  controlled electron spin  $\pi$ -pulse is performed after  $t_{\text{Rabi}} = 0.8 \mu\text{s}$ . Arbitrary operations  $R_{\varphi, \nu}$  can be implemented by setting the MW phase  $\varphi$  and the duration (cf. section 1.6.2 on page 29). The same principle can be applied for other nuclear spins coupled to the electron spin with  $A_{zz} \gtrsim 1/T_{2e}^*$  as well as for electron rotations which are simultaneously controlled by the spin states of multiple nuclear spins (cf. figure 1.13 on page 32). Thereby, implementation of the NMR equivalent of CNOT and Toffoli gates is possible [115]. For dense electron spin spectra involving many coupled nuclear spins, or weak couplings  $A_{zz}$  on the order of  $T_{2e}^*$ , this type of operation can be very challenging, as figure 1.15 shows. While the  $T_{2e}^*$ -broadened transitions require a spectrally broad pulse, the next hyperfine transition is very close and should not be affected by the pulse. The only pulse being able to fully satisfy this condition is a sinc-pulse, which has an ideal square as a signal spectrum [116]. Unfortunately, a sinc-pulse has an infinite temporal width and therefore can not be performed efficiently. To bring the efficiency of the pulses to the maximum and use the resources most efficiently within the experimentally exploitable parameter space, often the application of optimal control theory is required, to be able to perform high fidelity quantum operations [117]. For the present work,

optimal control theory was an important building block.

**Nuclear spin controlled electron phases** For phase accumulation, the electron spin first needs to be brought into a superposition state. Then, any offset magnetic field will immediately lead to a phase offset on the electron spin. This is also true for any nuclear spin with a hyperfine coupling  $|A_{zz}| > 0$ , which makes this method unsuitable for electron phase accumulation selective to one particular nuclear spin. The solution here generally is decoupling from all magnetic offset fields in a certain frequency range and selective recoupling of one or multiple of these offset fields (cf. section 1.7 on page 38). One very common technique is, to design the spectral filter function of the dynamical decoupling (DD) sequence to match Larmor and  $\mathbf{A}$  of some nuclear spins. For nuclear spins with hyperfine couplings stronger than  $A_{zz} > 1/T_{2e}$  but  $A_{zx} > 0$ , DD sequences can be used [17, 25, 48].

**Non-local gates between nuclear spins** As the hyperfine coupling amongst nuclear spins is negligible for all but very next neighbors, non-local gates between nuclear spins can only be performed if the NV center electron spin acts as a mediator for the interaction. Therefore, the electron spin needs to be in a predefined state. One possible implementation for a CNOT gate between a nuclear spin  $n_1$  and another nuclear spin  $n_2$  is via a nuclear spin state selective  $2\pi$  - rotation on the electron spin.



Interestingly, although all the gates in sequence 1.32 are NMR gates, the resulting gate is a CNOT gate (X) and not a controlled  $\pi$  - rotation. A high fidelity implementation of sequence 1.32 requires optimal control theory, when the electron spin spectrum is dense. There are various implementations for non-local gates between nuclear spins.

### 1.6.7 Implementation of common quantum gates in NMR

In quantum information science, the  $X$  (NOT) and Hadamard gates are the basic building blocks. In EPR and NMR, though, these gates can not be straightforwardly implemented. Luckily,  $\pi$  - and  $\pi/2$  - pulses are similar to NOT and Hadamard gates and in most experiments one can replace them without further implications for the experiment. Additionally, when the actual  $X$  or Hadamard gate needs to be performed, this can be done by a sequence of gates implementable in EPR and NMR (while neglecting global phases). A NOT gate can be expressed by

$$\text{---} \boxed{X} \text{---} = \text{---} \boxed{\pi_y} \text{---} \boxed{Z_x} \text{---} \quad (1.33)$$

A Hadamard gate can be expressed by

$$\text{---} \boxed{H} \text{---} = \text{---} \boxed{Z_{\frac{\pi}{2}}} \text{---} \boxed{\frac{\pi}{4}_y} \text{---} \boxed{\pi_x} \text{---} \boxed{\frac{\pi}{4}_y} \text{---} \quad (1.34)$$

The same logic also applies to all non-local spin manipulations, which are implemented as both as NMR gates and (with a little more effort), as gates commonly used in quantum information science, such as CNOT or CPHASE.

## 1.7 Storage times of quantum information

Quantum systems tend to be hard to isolate from the environment and thus information stored on them and also information acquired with them is fragile. Figure 1.16b on page 39 shows the most important lifetimes of electron and nuclear spins, which are discussed in this chapter in more detail. They have been taken for one specific NV center, which has already been introduced in section 1.5.1 on page 23.

Longitudinal relaxation times  $T_1$  denote population decay, i.e. the decay of the diagonal elements of the density matrix. Transversal relaxation times  $T_2^*$  and  $T_2$  denote the decay of coherences, i.e. the decay of the off-diagonal elements of the density matrix. The mechanisms inducing transversal relaxation are fundamentally different from those inducing longitudinal relaxation [118]. Transversal relaxation times can only be understood in the context of the respective experiment. As an example, the  $T_2^*$  gives a measure for coherence loss without any experimental countermeasures, while the  $T_2^{\text{KDD}}$  is a very advanced dynamical decoupling technique, which spectrally filters most noise sources. The available sensing time is generally limited by the sensor coherence time  $T_{2e}$ , which then sets a bound for the best achievable sensitivity with this sensor [119].

The time over which a quantum system can store quantum information fundamentally limits the interaction time to other quantum systems and its performance as a quantum sensor both regarding frequency resolution and sensitivity. Figure 1.16a on page 39 shows the classification of hyperfine  $^{13}\text{C}$  nuclear spins according to their hyperfine component  $A_{zz}$ . Strongly coupled nuclear spins are those with a coupling  $A_{zz} > 1/T_{2e}^*$ . They can appear as individual lines in the ODMR spectrum (cf. figure 1.13 on page 32). Weakly coupled nuclear spins are all those, that can be detected with the NV center electron

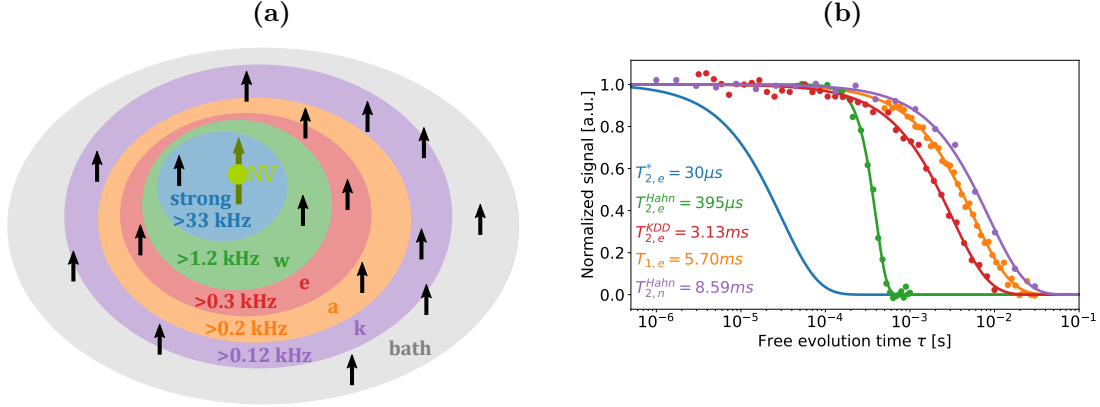


**Fig. 1.16: Summary of characteristic electron and nuclear spin decay times and nuclear spin classification according to coupling strength.** (a) Classification of nuclear spins around the NV center in strongly coupled, weakly coupled and bath spins according to their hyperfine coupling. Strongly coupled nuclear spins have  $A_{zz} > 1/T_{2,e}^* = 33 \text{ kHz}$ . Weakly coupled nuclear spins can be addressed on timescales faster than  $T_{2,n}^{\text{Hahn}}$  and thus need to be coupled stronger than  $A_{zz} = 0.12 \text{ kHz}$ . All nuclear spins coupled weaker than that are classified as bath spins. (b) Various decay curves of longitudinal and transversal lifetime measurements for electron spin and  $^{14}\text{N}$  nuclear spin. For disambiguation of  $T_2$  measurement sequences, the respective measurement sequence is given as superscript (Hahn or KDD). All curves were fitted to the function  $a \cdot \exp[-(t/T_{\text{dec}})^p] + c$ . The nuclear spin coherence time  $T_{2,n}^{\text{Hahn}}$  is limited by the  $T_{1,e}$  time and has a value of  $\approx 1.5T_{1,e}$  [14]. The curve showing the  $T_{2,e}^*$  decay is a simulation with realistic parameters.

spin sensor but are not strongly coupled. In the context of this work, weakly coupled nuclear spins are all those coupled with  $A_{zz} > 1/T_{2,n}^{\text{Hahn}}$ . The bath then denotes all nuclear spins that can not be individually detected but “disappear in the crowd” of all the other nuclear spins. As new sensing techniques are discovered, the boundary between weakly coupled nuclear spins and the bath may shift.

**Electron spin sensor  $T_{1,e}$  time** Diamond is a very stiff material, and thus the number of phonons is very low compared to other materials leading to long longitudinal relaxation times  $T_{1,e}$  (cf. section 1.1, [120, 121]). At room temperature, the interaction with phonons limits the  $T_{1,e}$  to values of 10 ms [122]. The  $T_{1,e}$  time can be measured with a green laser pulse for initialization into  $|m_s = 0\rangle$ , a waiting time  $T$  and finally another green laser pulse for electron spin readout.

$$\begin{array}{c}
 e \\
 |0\rangle \\
 \hline
 \xrightarrow{T} \\
 \hline
 |+\rangle \\
 {}^{14}\text{N}
 \end{array}
 \begin{array}{c}
 \xrightarrow{\pi^+} \\
 \xrightarrow{\text{QND}}
 \end{array}
 \begin{array}{c}
 \text{---} \\
 \text{---} \\
 \text{---}
 \end{array}
 \quad (\text{Seq1.2})$$

This sequence measures  $T_{1,e}$  of spin state  $m_s = 0$ . To decrease measurement time, the electron spin subspace  $m_s = 0 \leftrightarrow \pm 1$  was transferred to the  $^{14}\text{N}$  subspace  $m_N = +1 \leftrightarrow 0$  which allows for a more efficient QND measurement readout compared to standard electron spin readout (cf. section 1.8 on page 42). The measured value here is  $T_{1,e} = 5.7$  ms. At low temperatures, the relaxation time  $T_{1,e}$  is increased by multiple orders of magnitude and consequentially also the electron spin and nuclear spin coherence times can be longer. Electron  $T_{1,e}$  times up to 8 h have been reported [123]. In charge state  $\text{NV}^0$ ,  $T_{1,e}$  is drastically reduced to 13  $\mu\text{s}$  [78].

**Electron spin sensor  $T_{2,e}^*$  time** The inverse inhomogeneous broadening,  $T_{2,e}^*$ , is measured with an FID experiment, where the electron spin is brought into a superposition state and left there for a time  $\tau$ . Finally, the remaining coherence is read out with a  $\pi/2$  - pulse.



(Seq1.3)

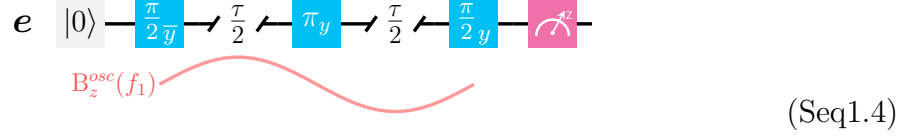
FID type sequences do not decouple from any magnetic field source, which can either be nuclear spins including the  $^{13}\text{C}$  and the intrinsic  $^{14}\text{N}$  nuclear spin or external offset fields. The  $T_{2,e}^*$  curve in figure 1.16b on page 39 is simulated with experimentally determined parameters ( $T_{2,e}^* \approx 30 \mu\text{s}$ ) and under the assumption that all strongly, ODMR resolvable nuclear spins are initialized, i.e. throughout the sensing time  $\tau$ , the  $^{14}\text{N}$  and  $^{13}\text{C}$  all are in spin states  $|m_N = +\rangle$  and  $|m_C = +\rangle$ , respectively. When the strongly coupled nuclear spins are not initialized, the curve oscillates rapidly with a superposition of the  $A_{zz}$  couplings [112, 124].

In general, the main contribution to magnetic field noise in diamond are long-lived  $^{13}\text{C}$  nuclear spins and P1 centers [125, 126]. For this particular NV center, the major contribution to this inhomogeneous broadening ( $\text{FWHM} \approx 1/T_{2,e}^*$ ) can be exclusively explained by the nuclear spins that have been found near the presented NV center, which alone produce a maximal field of 25 kHz to 30 kHz (cf. figures 3.9 and 3.11a on pages 94 and 98).

A reduction of  $^{13}\text{C}$  concentration in the diamond compared to the present 0.2% is possible, however there is a trade-off between inhomogeneous broadening due to  $^{13}\text{C}$  nuclear spins and the probability to find usable  $^{13}\text{C}$  nuclear spins to be used as qubit resource.

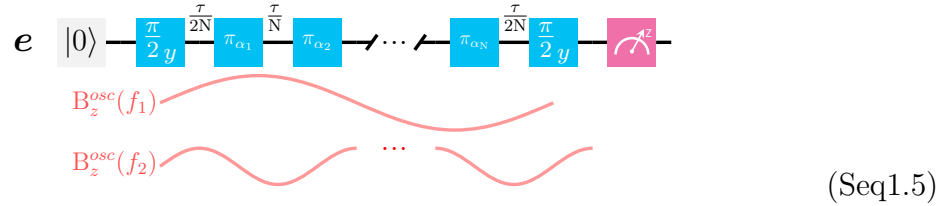
**Electron spin sensor  $T_{2e}$  time** Unlike  $T_{2,e}^*$  measurements, during  $T_{2e}$  measurements generally a part of the noise spectrum is refocused. Usually, larger experimental effort leads to sequences with better decoupling from noise. To decouple from static magnetic fields,

the Hahn-echo DD sequence Seq1.4 is suitable, which, compared to an FID measurement involves one additional  $\pi$  - pulse for refocusing [127].



When a static magnetic field  $B_z^{\text{stat}}$  is applied, phases  $\varphi_1$  and  $\varphi_2 = -\varphi_1$  are accumulated during the sensing times  $\tau_1$  and  $\tau_2$ , respectively. As the net phase is zero, the electron spin state will not be altered by the sequence, independent of the value of  $B_z^{\text{stat}}$ . This filtering of static and low frequency noise leads to an increase in coherence time of  $T_{2,e}^{\text{Hahn}} = 395 \mu\text{s}$ , which is more than one order of magnitude longer compared to an FID measurement.

However, a Hahn echo can not decouple from all signals. The filter function of the Hahn-echo sequence has a maximum for sine signals  $B_z^{\text{osc}}(f_1)$  with a frequency  $f = 1/\tau$ . This means that a Hahn-echo sequence does not decouple from  $B_z^{\text{osc}}(f_1)$  but magnifies the signal. Please note, that in this special case an FID sequence would completely decouple from  $B_z^{\text{osc}}(f_1)$ . The immediate approach to further increase the NV center electron spin coherence time towards the expected maximum of  $T_{1,e} = 5.7 \text{ ms}$  is, to add more  $\pi$  - pulses to the DD sequence. Thereby, the selectivity of the filter function is increased [128]. sequence Seq1.5 shows a general version of such a higher order DD sequence.



sequence Seq1.5 has a total number of  $N$   $\pi$  - pulses and filters all frequencies except for  $f = k \cdot N/2\tau$  with  $k \in 1, 3, 5, \dots$ . The width of the resonance decreases with  $N$  as  $\Delta f = 1/N\tau$ . For  $N = 1$  (which then again is a Hahn-echo), the DD sequence Seq1.5 decouples from  $B_z^{\text{osc}}(f_1)$  but not from  $B_z^{\text{osc}}(f_2)$ , which would be the case both for an FID and a Hahn-echo sequence. The phases  $\{\alpha_i\}$  in principle can be identical for all  $\pi$  - pulses. Then sequence Seq1.5 will provide only very low protection against mis-calibration of the respective  $\pi$  - pulse amplitudes and against frequency detunings. The choice of  $\{\alpha_i\}$  is an art of its own and there exists a huge amount of DD sequences differing only by the number of  $\pi$  - pulses and the phases  $\{\alpha_i\}$ . Commonly used phase combinations  $\{\alpha_i\}$  are found as KDD and XY type sequences [129–131]. When a spin-locking type effect is required, which protects one spin component better than the others, even having all phases  $\{\alpha_i\}$  the same can be an option despite the reduced robustness [132].

The resulting decay constant  $T_{2,e}^{\text{KDD}} = 3.13 \text{ ms}$  from a measurement using a KDD sequence with 80  $\pi$  - pulses is almost one order of magnitude larger than  $T_{2,e}^{\text{Hahn}}$ .  $T_{2,e}^{\text{KDD}}$  is

likely to be limited by the  $T_{1,e}$  time, as using more than 80  $\pi$  - pulses does not significantly increase the coherence time.

**Nuclear spin  $T_1$ ,  $T_2^*$  and  $T_2$  time** Nuclear spins in diamond do barely interact with the environment or with each other and hence can have exceptionally long lifetimes, which at the here prevalent magnetic fields  $B_{0,z} \approx 0.65$  T can reach  $T_{1N}^{\text{dark}} > 100$  s and up to 240 s at  $B_{0,z} \approx 1.5$  T [14]. Please note, that  $T_{1n}^{\text{dark}}$  is the  $^{14}\text{N}$  nuclear spin lifetime without laser illumination or any other manipulation of the NV center electron spin. The longitudinal relaxation time of nuclear spins coupled to the NV center electron spin under optical illumination is discussed in section 1.8 on page 42. The longitudinal relaxation time  $T_{1C}^{\text{dark}}$  of  $^{13}\text{C}$  nuclear spins has not been measured, but under the assumption that  $T_{1C}^{\text{dark}} > T_{1C}^{\text{bright}}$ , a lifetime of  $T_{1C}^{\text{dark}} > 10$  s can be deduced from figure 1.17 on page 43.

The relation of  $T_{2,e}^{\text{Hahn}}$  to  $T_{1,e}$ , may give rise to the hope, that for nuclear spins a similar relation holds, and that the nuclear spin coherence time largely exceeds that of the electron spin. Unfortunately, the nuclear coherence time  $T_{2,n}^{\text{Hahn}}$  is not limited by  $T_{1C}^{\text{dark}}$  but by  $T_{1,e}$ . Any spin flip of the NV center electron changes the effective magnetic field felt by the nuclear spin and then induces decoherence at a rate of its hyperfine coupling to the electron spin. Therefore, the nuclear spin coherence time is limited to  $T_{2,n}^{\text{Hahn}} \approx 1.5T_{1,e}$ , which for the present NV center is  $T_{2,n}^{\text{Hahn}} = 8.57$  ms [14]. Another consequence of this special nuclear spin decoherence mechanism is, that  $T_{2,N}^*$  and  $T_{2,n}^{\text{Hahn}}$  are equal. Only  $^{13}\text{C}$  nuclear spins with couplings  $A_{zz} < 1/T_{1,e}$  may profit from motional averaging effects and hence have longer coherence times.

## 1.8 Quantum nondemolition measurement of nuclear spins

Fast, reliable measurement of a quantum state is crucial both for quantum computation and quantum metrology. The traditional spin readout discussed in section 1.3 on page 14 yields a qualitative statement about the NV center electron spin state from the photons received in the first 300 ns of optical illumination. Qualitative here refers to the fact, that no clear statement about the spin state can be made but only about the difference between a higher and a lower number of photons corresponding to less and more contribution of  $m_s = 0$ . A SNR of 1 is reached only after many readout cycles for which, since the electron spin state does not survive even one cycle, the measurement needs to be repeated many times [133]. For short measurements, such as electron Rabi experiments a repetition of the experiment may be acceptable, for long measurements such as that performed for the determination of  $T_{1,e}$ , however, repeating an experiment becomes largely inefficient.

**Repetitive readout** A first approach to increase the SNR without having to repeat the experiment is the repetitive readout technique [134]. Thereby, the electron spin state is

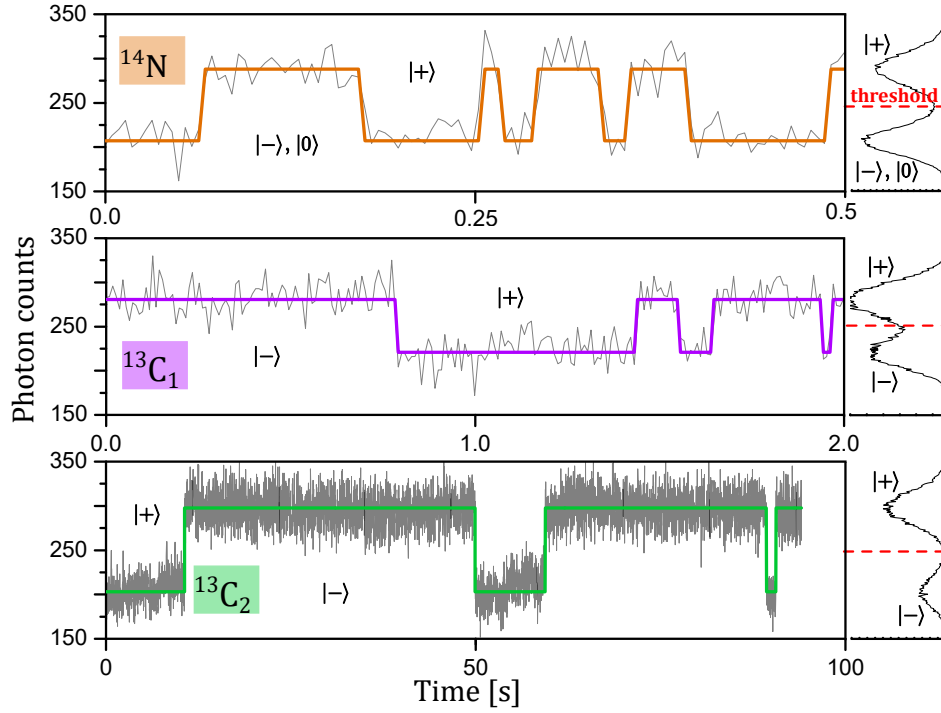


**Fig. 1.17: Single shot readout timetraces for three different nuclear spins under optical illumination.** Experiment was performed according to sequence Seq1.6. A photon histogram for each timetrace is shown on the right, along with a red dashed line indicating the photon threshold separating the two read out nuclear spin subspaces. The  $^{14}\text{N}$  nuclear spin flips between spin subspaces  $|0\rangle$  and  $|\pm 1\rangle$  on timescales below 1 s due to its strong hyperfine component  $A_{\perp}$  (cf. section 1.4.1 on page 20). The two  $^{13}\text{C}$  are much longer lived due to their weaker hyperfine couplings. Since the nuclear spin-flips are mostly a result of the laser illumination, it must be noted, that the number of 200 ns laser pulses per time depends on the duration of the nuclear spin controlled electron  $\pi$  - pulse. This duration for  $^{14}\text{N}$ ,  $^{13}\text{C}_1$  and  $^{13}\text{C}_2$  is 2  $\mu\text{s}$ , 5  $\mu\text{s}$ , 10  $\mu\text{s}$ , respectively.





## 1.9 The neutral electron charge state unraveled by single shot readout

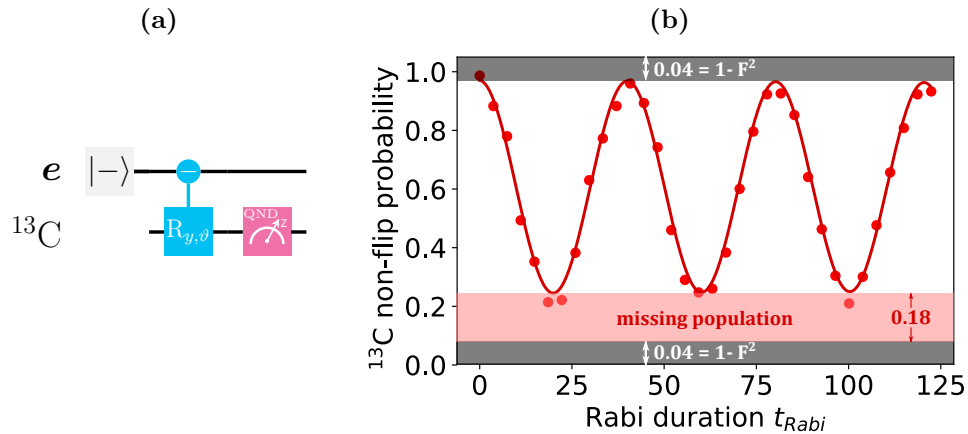


**Fig. 1.18: Rabi oscillations of  $^{13}\text{C}$  nuclear spin, read out with SSR.** The nuclear Rabi sequence (a) is performed with the electron spin being in  $m_s = -1$ . The SSR readout is performed with sequence Seq1.6. (b) The nuclear Rabi curve shows the  $^{13}\text{C}$  non-flip probability, which was fit to the function  $A \cos(2\pi(x - x_0)/T_{\text{Rabi}}) + c$ . Fitting parameters are  $T_{\text{Rabi}} = 40.1 \mu\text{s}$ ,  $A = 0.368$ ,  $c = 0.59$ . The overall visibility  $2A = 0.736$  is reduced due to the presence of the  $\text{NV}^0$  charge state and the SSR fidelity.

Figure 1.18b shows a nuclear spin Rabi experiment, which was performed on transition  $T[^{13}\text{C}(A_{zz} = 89 \text{ kHz}), -1]$  with sequence 1.18a. Therefore, amplitude and frequency of the RF driving field are fixed, while the duration  $t_{\text{Rabi}}$  is swept. The signal is the probability for the  $^{13}\text{C}$  not to be flipped by the resonant RF driving, which unlike the average photon number signal taken for the electron Rabi experiment figure 1.11c allows for the quantitative determination of the spin state. The QND measurement fidelity  $F_r$  can be deduced from the missing population at the top to approximately  $F_r^2 = 96\%$ . This fidelity reduces the maximum possible contrast by  $2(1 - F_r^2) = 0.08 = 8\%$ . The  $^{13}\text{C}$  nuclear Rabi frequency  $\Omega \approx 25 \text{ kHz}$  is three orders of magnitude lower than that of the electron spin due to the small  $\tilde{\gamma}_n$ .

**Missing population due to  $\text{NV}^0$**  Another major contribution to the reduced visibility in figure 1.18b is the existence of the  $\text{NV}^0$  charge state, which is also here prevalent with a probability of  $p_{\text{NV}^0} \approx 30\%$ . Interestingly, the missing population is less than 30%, as it would be the case for the  $^{14}\text{N}$  nuclear spin [78]. Instead, the presented Rabi experiment would imply a  $p_{\text{NV}^0} \approx 18.26\%$ . What first seems puzzling is straightforward to explain from the measurements of the  $^{13}\text{C}$  transition frequencies for the NV center being in  $\text{NV}$  or  $\text{NV}^0$  as shown in figure 1.19. The  $^{13}\text{C}_2$  hyperfine splitting in  $\text{NV}^0$  was determined to be

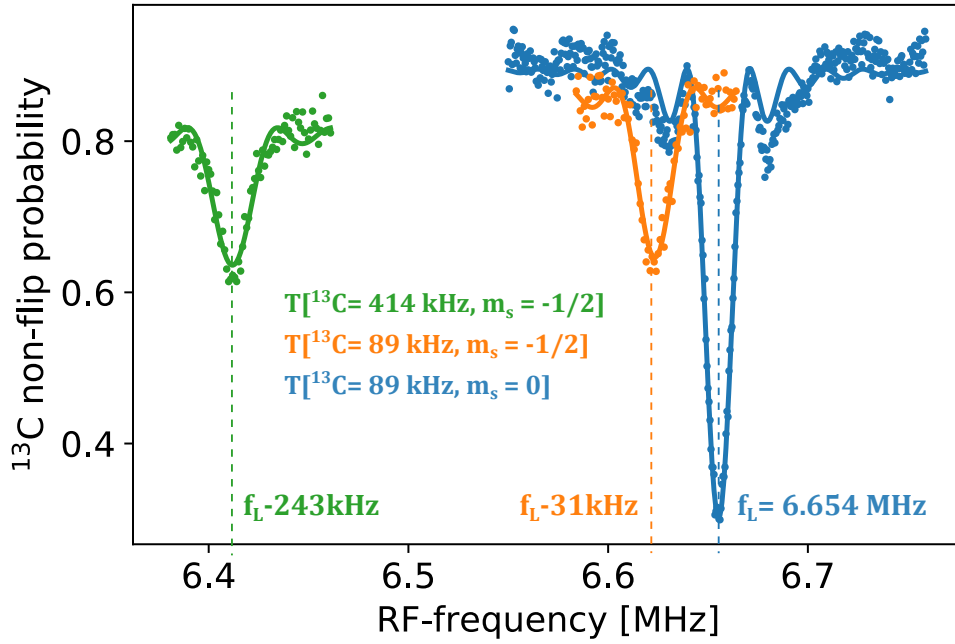


**Fig. 1.19:** Nuclear spin NMR spectra for determination of  $^{13}\text{C}_1$  and  $^{13}\text{C}_2$  hyperfine coupling for NV center charge state  $\text{NV}^0$ . When the electron is in  $\text{NV}^-$ , the respective hyperfine couplings are  $A_{zz} = 413\text{ kHz}$  and  $A_{zz} = 89\text{ kHz}$ . The blue curve shows the spectrum of transition  $T[^{13}\text{C}(A_{zz}=89\text{ kHz}), 0]$  (cf. section 1.6.4). Before measurement of the spectra for  $T_{\text{nvz}}[^{13}\text{C}(A_{zz}=414\text{ kHz}), -1/2]$  (green curve) and  $T_{\text{nvz}}[^{13}\text{C}(A_{zz}=89\text{ kHz}), -1/2]$  (orange curve), the NV center was pumped to charge state  $\text{NV}^0$  by a 0.5 ms red laser pulse. The resulting hyperfine frequencies are  $A_{zz}^{\text{nvz}} = 486\text{ kHz}$  and  $A_{zz}^{\text{nvz}} = 62\text{ kHz}$  for  $^{13}\text{C}_1$  and  $^{13}\text{C}_2$ , respectively.

$A_{zz}^{\text{nvz}} = 62$  kHz, however since in  $\text{NV}^0$  the electron spin is a doublet ( $S = 1/2$ ), the effective frequency shift compared to the  $^{13}\text{C}$  larmor frequency (transition  $\text{T}[^{13}\text{C}(A_{zz}=89\text{ kHz}), 0]$ ) is only 31 kHz. The effective frequency shift against the frequency of  $^{13}\text{C}$  transition  $\text{T}[^{13}\text{C}(A_{zz}=89\text{ kHz}), -1]$  is 58 kHz. Thereby, with the nuclear Rabi frequency of  $\approx 25$  kHz, both transitions  $\text{T}[^{13}\text{C}(A_{zz}=89\text{ kHz}), 0]$  and  $\text{T}[^{13}\text{C}(A_{zz}=89\text{ kHz}), -1]$  will be affected to a small degree by the Rabi driving, leading to a reduction in missing population compared to what would be expected from the actual  $\text{NV}^0$  probability. The crosstalk to transition  $\text{T}[^{13}\text{C}(A_{zz}=89\text{ kHz}), 0]$  is important, as the electron spin polarization is less than 100 %.

# 2

## Nuclear spin cooling

A key challenge in quantum technology is the initial state preparation of the used quantum systems. Fully mixed states are left unchanged by unitary operations and thus can neither be used in quantum information processing nor in quantum metrology. Huge efforts are made to improve quantum state initialization, in particular in NMR, where at magnetic fields of 1 T and temperatures of 300 K, the proton spin polarization is only  $\Delta p \sim 10^{-6}$  according to

$$\begin{aligned}\Delta p &= \tanh\left(\frac{\tilde{\gamma}hB_{0,z}}{2k_{\text{B}}T}\right) \\ &= \tanh\left(\frac{\Delta E}{2k_{\text{B}}T}\right)\end{aligned}\tag{2.1}$$

(cf. [137]). The polarization of  $^{13}\text{C}$  nuclear spins is more than a factor of three smaller due to their smaller reduced gyromagnetic ratio  $\tilde{\gamma}$ . Generally, there are two immediate paths to increase spin polarization: Higher energy splittings, achieved by larger magnetic fields, or lower temperatures. Both paths are technically challenging and may not be applicable to all kinds of samples. Even at the highest reachable magnetic fields, proton spin polarizations are far from unity ( $\sim 10^{-4}$  at 24 T and 300 K) [138]. At temperatures below 1 mK and magnetic fields of 1 T, proton spin polarization approaches unity. However, at the same time the longitudinal relaxation of the nuclear spins becomes impractically long.

Electron spins have a three orders of magnitude higher gyromagnetic ratio compared to  $^{13}\text{C}$  nuclear spins, leading to  $\Delta p \sim 10^{-3}$  at 1 T and 300 K. The NV center electron spin can be optically polarized to  $\Delta p = 0.98$ , making it an ideal candidate for polarization transfer to nuclear spins.

This chapter discusses the polarization of  $^{13}\text{C}$  nuclear spin in the diamond lattice.

Internal  $^{13}\text{C}$  nuclear spins on the one hand can serve as a well characterized testbed for the investigation of various polarization techniques, which then can be applied to other spin species and in particular to nuclear spins outside of the diamond. Therefore, near-surface NV centers are used to polarize nuclear spins brought in contact to the diamond surface for later use. On the other hand, nuclear spins are very well isolated from external noise sources. Their robustness in combination with efficient initialization and readout makes them ideal candidates for quantum information processing. In particular hybrid quantum systems such as the NV center are promising, in which one can benefit from the strengths of both electron and nuclear spins. One prominent example for such a hybrid system using nuclear spins of donor atoms in doped silicon for storage and polarized electron spins for logical operations is described in the Kane proposal [139].

The focus of this chapter lies on the implementation of Heat-bath algorithmic cooling (HBAC) [24, 140–142] on the hybrid four-spin system of NV center electron spin and the three nuclear spins  $^{14}\text{N}$ ,  $^{13}\text{C}_1$  and  $^{13}\text{C}_2$  introduced in section 2.3. Thereby, the electron spin serves as the heat bath and the two  $^{13}\text{C}$  nuclear spins as reset qubits. Among the known spin cooling techniques HBAC has a special place due to its thermodynamic perspective that allows for entropy compression in parts of the subsystem to a degree much higher than achievable by conventional schemes. While there is large theoretical research, earlier experiments (NMR based) have been limited to basic demonstrations of the scheme. One major reason is, that in NMR for large polarizations very low temperatures are required, for which the thermal equilibrium takes very long to reach. A key prediction of HBAC, the asymptotic cooling limit, had not yet been verified experimentally. Here, a novel variable degree nuclear spin polarization sequence is introduced, which allows for independent polarizations of the two reset qubits  $^{13}\text{C}_1$  and  $^{13}\text{C}_2$  from  $\Delta p = 0$  to  $> 0.5$ , which exceeds the available reset spin polarizations in common NMR systems by multiple orders of magnitude. The three used nuclear spins can be read out projectively and due to the exceptional control on the hybrid spin system, the HBAC algorithm can be repeated up to 23 times to reach saturation of the asymptotic limit of HBAC.

**Chapter outline** The four sections of this chapter cover three different classes of nuclear spin hyper-polarization techniques with very different working principles and strengths.

The first class polarizes by postselecting for wanted nuclear spin orientations and discarding all the others. This technique does not rely on the transfer of polarization from the NV center electron spin but uses the latter one for efficient nuclear spin readout (cf. section 1.8). The reached effective nuclear spin polarizations are superior to any other known technique due to the high SSR fidelities. The postselection technique is covered in section 2.1. Also it is used in all experiments in this work with the exception of section 2.3.

A second class of techniques directly generates the coupling needed for transfer with MW and RF. As an example this may be a swap gate, implemented via selective  $\pi$  -

pulses [143]. In section 2.2, a variable degree SWAP mechanism is introduced, which allows to partially polarize individual nuclear spins by polarization transfer from the electron spin. Section 2.3 then introduces an implementation of algorithmic cooling, which allows to redistribute the limited purity achieved with the variable degree SWAP mechanism, to get one highly polarized sub-ensemble, while another sub-ensemble is left in a less pure state. Thereby, the polarization of the sub-ensemble can be increased above the value of any spin of the original ensemble, which mimics the operation principle of a heat pump.

A third and very versatile nuclear spin polarization technique uses static magnetic or MW fields to leverage otherwise suppressed off-diagonal components of the hyperfine tensor describing the coupling between electron and nuclear spin (i.e.  $A_{zx}$  or  $A_{\perp}$ , cf. sections 1.4.1 and 1.4.2) [22, 144–146]. In Section 2.4, it is shown how a carefully designed pulse sequence can generate an artificial flip-flop Hamiltonian, very similar to that in equation 1.13. It is shown, how this technique is used for the polarization of weakly coupled nuclear spins with  $A_{zz}$  as low as the homogeneous broadening of the electron spin.

## 2.1 Cooling by postselection

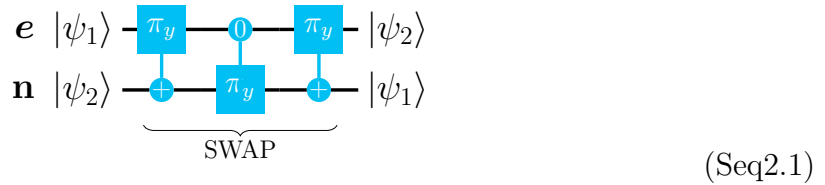
In quantum information processing, spin initialization by QND measurement with successive postselection is a viable approach. For the strongly coupled nuclear spins  $^{14}\text{N}$ ,  $^{13}\text{C}_1$  and  $^{13}\text{C}_2$ , this is possible. Therefore, the nuclear spin is read with a number of readout repetitions  $N_{\text{ssr}}$  far smaller than its lifetime under illumination. For very long-lived nuclear spins such as  $^{13}\text{C}_2$  with a lifetime  $T_{1\text{C}}^{\text{bright}}$  on the order of one million laser pulses,  $N_{\text{ssr}} = 5000$  is a good choice. Then the nuclear spin can be read with fidelities beyond  $F_r = 99\%$  and without inducing any significant nuclear spin decay. Therefore, when all experimental runs during which the nuclear spin state was not initialized are discarded as failed runs, in the successful runs the nuclear spin polarization is equal to the nuclear spin readout fidelity, i.e.  $\Delta p = 2F_r - 1$ . Even in the worst case of a fully mixed state, for a single qubit only half of the experimental runs need to be discarded. What remains is a polarized sub-ensemble. The advantages of this readout technique are the very high nuclear polarization or initialization fidelity. Unfortunately, for fully mixed states the number of successful runs decreases exponentially with increasing number of qubits to be initialized. Therefore, often a mixed approach is used, where the nuclear spin qubits are first actively purified and then read out for postselection. This approach is used in the majority of the here presented experiments, even though not always explicitly stated.

## 2.2 Full and partial polarization transfer

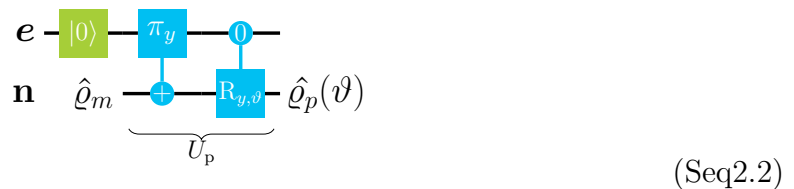
The NV center electron spin polarization can be transferred to a nuclear spin two-level system by the use of a SWAP gate, which writes the electron spin state to the nuclear spin and the nuclear spin state to the electron spin [114].

A SWAP gate can be composed of electron spin state selective nuclear spin  $\pi$  - pulses and nuclear spin state selective electron spin  $\pi$  - pulses as shown in sequence Seq2.1.

**From SWAP gate to spin transfer gate** Here, the non-local electron  $\pi$  - pulse is the crucial part, as it can only be implemented straight forwardly for strongly coupled nuclear spins with  $A_{zz} > T_{2e}^*$ , as described in section 1.6.6 on page 35. In this section, the polarization of strongly coupled nuclear spins via a SWAP operation is shown. In principle the technique can also be used for weakly coupled nuclear spins, if the nuclear spin controlled electron  $\pi$  - pulses are implemented with the technique introduced in chapter 3. Especially for a large number of weakly coupled nuclear spins the pulsed polarization technique introduced in section 2.4 showed better cooling performance compared to gate based SWAP operations.



This SWAP gate here is adapted, for the efficient generation of a variable degree of nuclear spin polarization. Firstly, the final electron spin state after application of the SWAP gate is irrelevant, as it only acts as source of polarization and can be easily repolarized with a green or red laser pulse into  $|m_s = 0\rangle$ . Therefore, the third controlled rotation is not required and the SWAP gate simplifies to two controlled spin rotations. Secondly, the second electron controlled nuclear rotation does not necessarily need to cover the full angle  $\vartheta = \pi$  but can be replaced by a rotation of variable angle,  $R_{y,\vartheta}$  as shown in sequence Seq2.2.



Here,  $U_p$  is an operation which (partially) transfers the electron spin state to the nuclear spin. The control states of the two non-local spin operations (here  $|+\rangle$  and  $|0\rangle$ ) determine

the state into which the nuclear spin is polarized. In the given example, the probability to find the nuclear spin in state  $|+\rangle$  is increased from 0.5 ( $\vartheta = 0$ ) to 1 ( $\vartheta = \pi$ ).

**Theoretical polarization transfer performance** When the nuclear spin initially is in a fully unpolarized state  $\hat{\rho}_m = 1/2 \sum_i |i\rangle\langle i|$  and the electron spin initially is in a fully polarized spin state  $|m_s = 0\rangle$ , application of the polarization transfer operation  $U_p$  results in the traced out nuclear spin state

$$\hat{\rho}_p(\vartheta) = \begin{pmatrix} 0.75 - 0.25 \cos(\vartheta) & -0.25 \sin(\vartheta) \\ -0.25 \sin(\vartheta) & 0.5 \cos\left(\frac{\vartheta}{2}\right)^2 \end{pmatrix} \quad (2.2)$$

with a polarization  $\Delta p$  of the two-level system

$$\begin{aligned} \Delta p &= \rho_{11} - \rho_{22} \\ &= 0.75 - 0.25 \cos(\vartheta) - 0.5 \cos\left(\frac{\vartheta}{2}\right)^2 \end{aligned} \quad (2.3)$$

For  $\vartheta = 0$ , no polarization is transferred and thus  $\hat{\rho}_p(\vartheta) = \hat{\rho}_m$  and  $\Delta p = 0$ . For  $\vartheta = \pi$ , the polarization transfer is maximal. Assuming a pure electron spin initial state  $|m_s = 0\rangle$  and perfect quantum gates, the nuclear spin will be in the fully polarized state

$$\begin{aligned} \hat{\rho}_p(\pi) &= \begin{pmatrix} 1 & 0 \\ 0 & 0 \end{pmatrix} \\ &\equiv |m_n = +\rangle \end{aligned} \quad (2.4)$$

with a polarization  $\Delta p = 1$ .

**Experimentally limiting factors** In the experiment, a variety of factors will reduce the polarization efficiency. Firstly, the transferable electron polarization is only 90% to 98% (cf. section 1.3 on page 14). Secondly, all gate operations involved in the spin transfer sequence have gate fidelities which are determined by spin decay during the gate duration and the spectral selectivity of the pulses (cf. sections 1.6.4 and 1.6.6). The electron spin gates required for the spin transfer sequence Seq2.2 need to be spectrally selective in a very dense electron hyperfine spectrum. This in particular for the  $^{13}\text{C}_2$  with  $A_{zz} = 90$  kHz sets a lower limit for the achievable gate fidelity (cf. figure 1.15). The electron spin controlled nuclear gates on the other hand are limited by the electron spin decay  $T_{1,e} = 5.7$  ms, which usually is two orders of magnitude larger than the gate duration and crosstalk to other transitions. This crosstalk is negligible for the most part by sensible choice of magnetic field  $B_{0,z}$  and pulse duration. Thirdly, the probability for the NV center to be in the  $\text{NV}^-$  charge state ( $p_{\text{NV}^-} \approx 70\%$ ) limits the success rate of the gates involving the NV

center electron spin to exactly this value, as the  $NV^-$  charge state has an electron triplet ( $S = 1$ ), while the  $NV^0$  charge state has an electron doublet ( $S = 1/2$ ), cf. section 1.2. For weakly coupled nuclear spin gates there can be exceptions, which however do not apply to the here presented polarization transfer method (cf. figures 1.18b and 1.19 on pages 46 and 47). Consequentially, only  $p_{NV^-} \approx 70\%$  of all polarization transfer attempts are successful, while the rest fails completely.

For multi-level systems of size  $M$  which are in a completely mixed state, the probability to polarize  $p_M$  into one particular sublevel is reduced by charge state effects alone to

$$p_M = \frac{1}{M} \sum_{i=0}^{M-1} (p_{NV^-})^i \quad (2.5)$$

For a qubit this corresponds to a maximal single-level occupation probability of  $p_2 = 0.85$  and for a qutrit to  $p_3 = 0.73$  corresponding to qubit and qutrit expectation values of and  $\langle \hat{I}_z \rangle = 0.35$  and  $\langle \hat{I}_z \rangle = 0.63$ , respectively.

### 2.2.1 Increasing the $^{14}\text{N}$ nuclear spin polarization

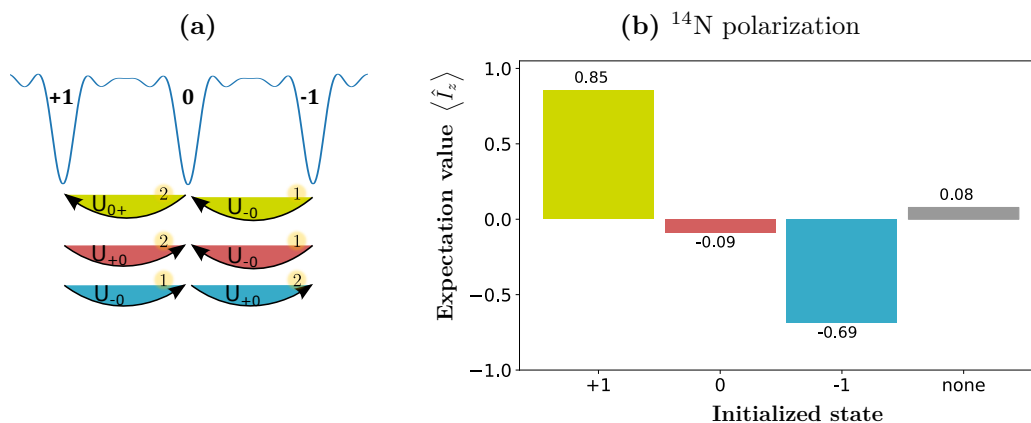
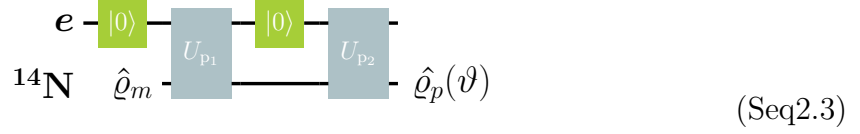


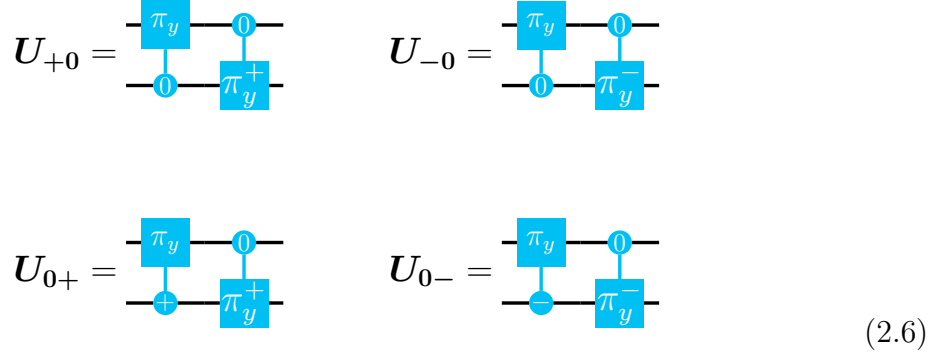
**Fig. 2.1: Performance of  $^{14}\text{N}$  SWAP gate polarization** into  $^{14}\text{N}$  states  $|+\rangle$  (green),  $|0\rangle$  (red) and  $|-\rangle$  (blue) after polarization transfer from the NV center electron spin. **(a)** Required gate order for polarization into  $|+\rangle$ ,  $|0\rangle$  and  $|-\rangle$  with sequence Seq2.3. Gates  $U_{ij}$  are taken from sequence 2.6. The yellow shaded numbers 1, 2 match the subscript numbers in  $U_{p_1}$  and  $U_{p_2}$ . **(b)**  $^{14}\text{N}$  nuclear spin state expectation value  $\langle \hat{I}_z \rangle$  after polarization into states  $|+\rangle$ ,  $|0\rangle$  and  $|-\rangle$  by the gate combinations shown in **(a)** or without polarization (“none”). Each of the four expectation values is averaged over 11997 runs of the  $^{14}\text{N}$  nuclear spin polarization sequence Seq2.3. Each run is followed by SSR via sequence Seq1.7 with  $N_{\text{SSR}} = 300$  to read out the qutrit spin state.

The  $^{14}\text{N}$  nuclear spin is a spin triplet with substates  $|+\rangle$ ,  $|0\rangle$  and  $|-\rangle$  (cf. section 1.4.3 on page 23) and thus requires two independent SWAP operations for maximal polarization,

as the two-level spin subspaces  $|+\rangle \leftrightarrow |0\rangle$  and  $|0\rangle \leftrightarrow |-\rangle$  need to be polarized sequentially. In a three-level system, full polarization is equivalent to finding the nuclear spin in one particular target polarization state  $|+1\rangle, |0\rangle, |-1\rangle$  with 100% probability. Therefore, two different polarization transfer gates  $U_{p_1}$  and  $U_{p_2}$  need to be performed together with two laser pulses which are required to repolarize the electron spin (cf. sequence Seq2.3).



Here, low intensity laser pulses of wavelength 637 nm were used due to their high efficiency for electron polarization (cf. section 1.3). Depending on the desired target polarization state, gates  $U_{p_1}$  and  $U_{p_2}$  in sequence Seq2.3 need to be replaced with different combinations of gates from sequence 2.6.



The combination of gates  $U_{p_1}$  and  $U_{p_2}$  used for polarization transfer into the particular  $^{14}\text{N}$  nuclear spin states  $|+1\rangle, |0\rangle, |-1\rangle$  can be taken from figure 2.1a. For example polarization into  $^{14}\text{N}$  nuclear spin state  $|+1\rangle$  is achieved with  $U_{p_1} = U_{-0}$  and  $U_{p_2} = U_{0+}$ . Gates  $U_{+0}, U_{-0}, U_{0+}, U_{0-}$  address the  $^{14}\text{N}$  nuclear spin two-level subspaces  $|+\rangle \leftrightarrow |0\rangle, |0\rangle \leftrightarrow |-\rangle, |+\rangle \leftrightarrow |0\rangle$  and  $|0\rangle \leftrightarrow |-\rangle$ . They polarize the addressed  $^{14}\text{N}$  two-level subspace into states  $|0\rangle, |0\rangle, |+\rangle, |-\rangle$ . Gates  $U_{+0}, U_{-0}, U_{0+}, U_{0-}$  differ by the  $^{14}\text{N}$  control state (0, +, -, small filled circles) of the electron  $\pi$ -pulses and the two-level subspace addressed by the  $^{14}\text{N}$   $\pi$ -pulse (+, -, superscript in blue boxes, cf. section 1.6.4 on page 32).

**Result and discussion** Figure 2.1b shows the resulting  $^{14}\text{N}$  expectation value  $\langle \hat{I}_z \rangle$  after running the polarization sequence Seq2.3. Polarization into spin state  $|+\rangle$  works significantly better than that into  $|-\rangle$ . Even when the  $^{14}\text{N}$  is not actively polarized, the expectation value is slightly positive. This is expected due to dynamics at the GSLAC and the ESLAC (cf. 1.4.1 on page 20). Here however the larger polarization of  $|+\rangle$  compared to  $|-\rangle$  probably additionally is affected by the different experimental gate fidelities of  $U_{+0}$ ,

$U_{-0}$ ,  $U_{0+}$  and  $U_{0-}$ . The  $^{14}\text{N}$  has a very large hyperfine coupling  $A_{zz} = -2.16$  MHz which allows for very fast, high fidelity gate operations.

Especially for polarization into spin state  $|+\rangle$ , with  $\langle \hat{I}_z \rangle = 0.85$  the qutrit expectation value is much larger than the theoretically expected value  $\langle \hat{I}_z \rangle = 0.63$  which is received when taking into account charge state effects. The nonetheless high  $^{14}\text{N}$  polarizations can be explained with the lack of depolarization mechanisms. In section 2.2.2,  $^{13}\text{C}$  nuclear spins are depolarized before polarization transfer from the electron spin and thus there the actual polarization efficiency of one or multiple repetitions can be determined.

### 2.2.2 Increasing the $^{13}\text{C}$ nuclear spin polarization

As  $^{13}\text{C}$  nuclear spins are spin doublets ( $I = \frac{1}{2}$ ) a single polarization transfer step can lead to full polarization. The general polarization transfer mechanism is equivalent to the one for  $^{14}\text{N}$  nuclear spin polarization, discussed in section 2.2.1. However, here the goal is a variable degree of polarization as discussed on page 53 (later required for the benchmarking of the algorithmic cooling section 2.3). Sequence Seq2.4 is the basic building block for variable degree spin transfer from electron spin to a  $^{13}\text{C}$  nuclear spin.

$$\begin{array}{c} \text{---} \\ \text{---} \\ \text{---} \end{array} \begin{array}{c} \times \\ \downarrow \\ \vartheta \end{array} = \begin{array}{c} e \\ \text{---} \\ \text{---} \\ \text{---} \end{array} \begin{array}{c} |0\rangle \\ \hat{Q}_m \\ U_{p_1} \\ \hat{Q}_p(\vartheta) \end{array} \quad (\text{Seq2.4})$$

The chosen representation of  $U_{p_1}$  depends on the state into which the target  $^{13}\text{C}$  should be polarized and can either be  $U_{-+}$  for polarization into  $^{13}\text{C}$  spin state  $|+\rangle$  or  $U_{+-}$  for polarization into  $|-\rangle$ .

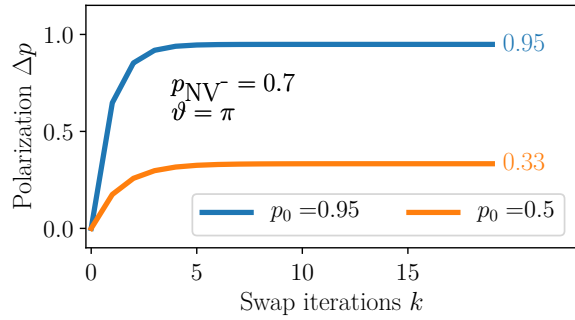
$$\begin{array}{c} U_{+-} = \\ \text{---} \\ \text{---} \end{array} \begin{array}{c} \pi_y \\ \oplus \\ R_{y,\vartheta} \end{array} \quad \begin{array}{c} U_{-+} = \\ \text{---} \\ \text{---} \end{array} \begin{array}{c} \pi_y \\ \oplus \\ R_{y,\vartheta} \end{array} \quad (2.7)$$

**Full sequence with depolarization and qubit SSR readout** To test the performance of variable degree  $^{13}\text{C}$  polarization with sequence Seq2.4, it is embedded in sequence Seq2.5 with  $U_{p_1} = U_{-+}$  and repeated for  $k$  iterations leading to sequence Seq2.5.

$$\begin{array}{c} e \\ \text{---} \\ \text{---} \\ \text{---} \end{array} \begin{array}{c} |0\rangle \\ \hat{Q}_m \\ \left( \begin{array}{c} |0\rangle \\ \pi_y \\ \oplus \\ R_{y,\vartheta} \\ U_{-+} \end{array} \right)^k \\ \text{---} \\ \text{---} \end{array} \begin{array}{c} \text{QND} \\ \otimes \end{array} \quad (\text{Seq2.5})$$

The actual polarization transfer part of the sequence consists of a 80  $\mu\text{s}$  red laser pulse for electron reset, a nuclear spin controlled electron  $\pi$  - pulse (6  $\mu\text{s}$ /20  $\mu\text{s}$  for  $^{13}\text{C}_1$ / $^{13}\text{C}_2$ ) and a electron spin controlled nuclear spin rotation of variable duration (0  $\mu\text{s}$  to 100  $\mu\text{s}$ ). To increase the nuclear spin polarization, the polarization transfer part can be repeated  $k$  times. Finally, the spin state is read out with SSR. The nuclear spin polarization is read out with the SSR sequence Seq1.8, which does not destroy the nuclear spin state. This is an important detail, as the lack of depolarization mechanisms allows for polarization buildup. Therefore, each measurement run needs to be prepended with a  $^{13}\text{C}$  nuclear spin  $\pi/2$  - pulse, which in combination with the in total  $N_{\text{SSR}}+k+1$  performed laser pulses prevents the accumulation of polarization.

**Fig. 2.2: Simulation of  $^{13}\text{C}$  polarization build-up.** during polarization sequence sequence Seq2.5 with optimal swap angle  $\vartheta = \pi$ . Two different electron polarizations  $p_0$  were considered. Already after  $k = 2$  iterations almost the full polarization is reached.



**Simulation of polarization build-up** For polarization buildup over multiple swap iterations  $k$ , two conditions must be fulfilled. A first condition is, that the nuclear spin must not be fully polarized within a single run. This is given here due to charge state  $\text{NV}^0$ , which prevents  $\approx 30\%$  of all polarization attempts. If for example the first polarization attempt fails, a second one can increase the success probability to  $1 - (p_{\text{NV}^-})^2$ . Please note, that this is different from limited fidelities of the polarization transfer gate  $U_{p_1}$ , in which case a second polarization step may even decrease the nuclear spin polarization or imperfect electron spin polarization, both in which cases additional swap iterations  $k$  will not further increase polarization. A second condition is the lack of depolarization mechanisms, which for immobile  $^{13}\text{C}$  spins is predominantly longitudinal relaxation due to interaction with the NV center electron spin. This process depends on the  $^{13}\text{C}$  hyperfine tensor describing the coupling between electron and nuclear spin  $\mathbf{A}$  and therefore can even be deactivated for special  $^{13}\text{C}$  locations within the diamond lattice section 1.8. The simulation shown in figure 2.2 considers the case of such  $^{13}\text{C}$  spins, which is a reasonable assumption in particular for  $^{13}\text{C}_1$  and  $^{13}\text{C}_2$ , with which the polarization sequence Seq2.5 is benchmarked. The polarization builds up over approximately  $k = 3$  iterations, whereby even after two iterations almost full polarization is reached. The initial electron spin polarization is given by population of electron spin state  $|0\rangle$  ( $m_s = 0$ ). This is important, as the electron spin is a triplet and polarization is not only reduced by population in  $|-\rangle$

but also in  $|+\rangle$ . Therefore, the achievable nuclear spin polarization is  $\Delta p < p_0$ .

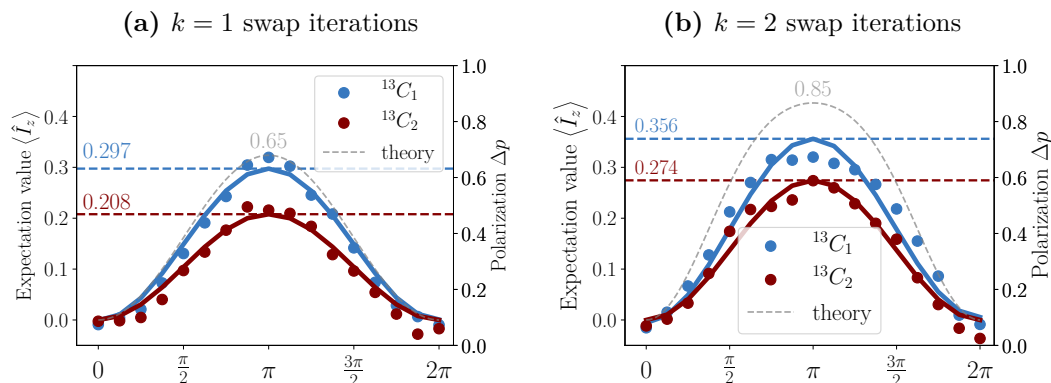


**Fig. 2.3: Variable degree polarization transfer from electron spin to the two nuclear spins  $^{13}\text{C}_1$  and  $^{13}\text{C}_2$ .** (a) shows the used pulse sequence. The electron initially is in state  $|m_s = 0\rangle$ , while the target  $^{13}\text{C}$  nuclear spin is in a fully mixed state. To remove any remaining polarization, before the polarization step, a  $50\ \mu\text{s}$   $\pi/2$ -pulse is performed on the nuclear spin. The experiment was performed for angles  $\vartheta$  between  $0$  and  $2\pi$  and for  $k = 1$  (b) and  $k = 2$  (c). The result is theoretically described by equation 2.2, which justifies to fit the data to function  $a \cdot \cos \vartheta$ . The polarization here can be read as  $\Delta p = 2 \langle \hat{I}_z \rangle$ . The theoretical curve is determined under the assumption of 30 %  $\text{NV}^0$  probability and 95 % probability for the NV center to be in spin state  $|m_s = 0\rangle$  after a laser pulse.

**Result and discussion** Figure 2.3a shows the  $\langle \hat{I}_z \rangle$  expectation value of the  $^{13}\text{C}$  nuclear spin after  $k = 1$  iterations of polarization sequence Seq2.4. The shape of the curve can be understood from equation 2.2 by taking into account the limited electron spin polarization efficiency and the limited probability for the presence of the  $\text{NV}^-$  charge state. Under the assumption of probabilities  $p_0 = 0.95$  to find the electron spin in spin state  $m_s = 0$  and  $p_{\text{NV}^-} = 0.7$  to find the electron spin in charge state  $\text{NV}^0$  after a laser pulse, the maximal theoretical  $^{13}\text{C}$  nuclear spin polarization is  $\Delta p = 0.65$ . For  $^{13}\text{C}_1$  and  $\vartheta = \pi$ , the experimentally determined polarization is  $\Delta p = 0.58$  (fit value) or  $\Delta p = 0.64$  (data point). For  $^{13}\text{C}_2$ , however, the values with  $\Delta p = 0.41$  ( $\Delta p = 0.43$ ) for fit value (data point) are far below the theoretically expected value. An explanation for this behavior is found in the limited fidelity of the nuclear controlled electron rotation used for the spin transfer operation  $U_{-+}$ . As discussed in section 1.6.6 on page 35, the maximal spectral selectivity of an electron gate is ultimately determined by the ratio of hyperfine coupling  $A_{zz}$  and the inhomogeneous broadening of the electron spin transition on one side and the gate duration on the other. Therefore, high fidelity nuclear spin selective electron  $\pi$ -pulses involving  $^{13}\text{C}_2$  with a hyperfine coupling  $A_{zz} = 90\ \text{kHz}$  require long gate durations and pulses, which are shaped via optimal control theory. Here, an unoptimized, rectangular

pulse of duration 20  $\mu\text{s}$  was used. For  $^{13}\text{C}_1$  with a hyperfine coupling of  $A_{zz} = 413$  kHz, an optimal control implemented pulse of duration 6  $\mu\text{s}$  was used, which had a fidelity above 95 %.

Figure 2.3b shows the  $\langle \hat{I}_z \rangle$  expectation value of the  $^{13}\text{C}$  nuclear spin after  $k = 2$  iterations of polarization sequence Seq2.4. Using the same assumptions as for  $k = 1$ , here a theoretical  $^{13}\text{C}$  polarization of  $\Delta p = 0.85$  would be expected. In the experiment, this second iteration brings an increase in  $^{13}\text{C}_2$  maximum polarization to  $\Delta p = 0.55$  ( $\Delta p = 0.55$ ) for fit (data point). For  $^{13}\text{C}_1$  the maximum polarization now is  $\Delta p = 0.64$  ( $\Delta p = 0.71$ ). Although this increase is significant, the additional polarization is lower than predicted by theory (cf. figure 2.3a) and a saturation behaviour already is apparent.

## 2.3 Heat-bath algorithmic cooling

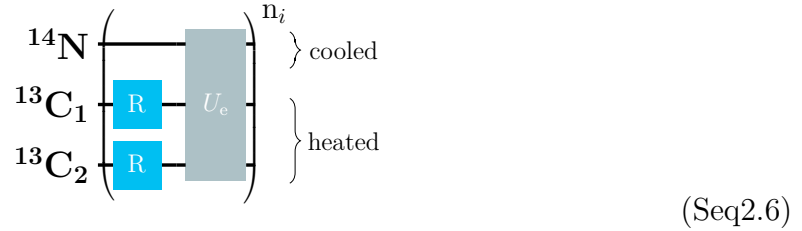
HBAC techniques provide ways to selectively enhance the polarization of a sub-ensemble of qubits at the expense of a bath, whose purity is decreased in the cooling process [24, 140, 142]. Thereby, the target sub-ensemble is cooled below the bath temperature, which means that the polarization of each cooled qubit can be larger than the initial polarization of any spin in the ensemble. This is particularly interesting, as for example in NMR the polarization of each spin achieved with standard cooling techniques such as increasing the energy gap often is very low, while the number of available bath spins is enormous.

Hyperfine coupled electron-nuclear spin systems like the NV center are a suitable testbed for HBAC in particular due to the variable degree of polarization that can be transferred to the nuclear spin ensemble via a partial swap operation. The total ensemble consists of three nuclear spins,  $^{14}\text{N}$ ,  $^{13}\text{C}_1$  and  $^{13}\text{C}_2$ , which can be polarized independently of each other, from  $\Delta p = 0$  to  $\Delta p > 0.4$  with one iteration of the partial swap operation (cf. section 2.2). The target spin, i.e. the spin whose polarization is increased by the HBAC algorithm here is chosen to be  $^{14}\text{N}$ . The initial polarization of the bath spins  $^{13}\text{C}_1$  and  $^{13}\text{C}_2$  can be freely and individually tuned from  $\Delta p = 0$  to  $\Delta p = 0.58$  and  $\Delta p = 0.41$  in a single spin transfer iteration  $k$ . In principle a fourth spin allowing for high fidelity local and non-local spin operations is available: the NV center electron spin. Unfortunately, the electron spin needs to serve as a mediator for the interaction between the nuclear spins, for which a pure electron spin state is a mandatory prerequisite. Therefore, it here can only act as an ancillary spin.

The physical system of one NV center and multiple nuclear spins in combination with SSR provide means to demonstrate a generic heat engine model for a quantum refrigerator with the electron spin as a working fluid. The electron spin could continuously extract heat from a cold bath and dump it into the heat bath [147].

### 2.3.1 Cooling principle and asymptotic limit

The basic operation principle of the here presented HBAC algorithm is shown in sequence Seq2.6. The bath spins  $^{13}\text{C}_1$  and  $^{13}\text{C}_2$  are reset before each application of the cooling gate  $U_e$ . The procedure is repeated for  $n_i$  iterations, whereby the target spin  $^{14}\text{N}$  is cooled and its polarization is asymptotically increased towards the cooling limit  $\Delta p_{\max}$ .



The thermal equilibrium state  $\rho$  of a qubit at temperature  $T$  with energy splitting  $\Delta E = \tilde{\gamma}hB_{0,z}$  is

$$\rho_{\text{eq}} = \frac{1}{e^\epsilon + e^{-\epsilon}} \begin{pmatrix} e^\epsilon & 0 \\ 0 & e^{-\epsilon} \end{pmatrix}, \quad (2.8)$$

with  $\epsilon = \Delta E/2k_B T$ . The reset operations are non-unitary operations and happen via polarization transfer from the central spin. The state of the two  $^{13}\text{C}$  spins after the reset operation is described by

$$\rho_{C_{1,2}} = \frac{1}{e^{\epsilon_{1,2}} + e^{-\epsilon_{1,2}}} \begin{pmatrix} e^{\epsilon_{1,2}} & 0 \\ 0 & e^{-\epsilon_{1,2}} \end{pmatrix}, \quad (2.9)$$

The  $^{13}\text{C}$  polarization in this description is  $\Delta p_{1,2} = \tanh \epsilon_{1,2}$ . The final asymptotic  $^{14}\text{N}$  state after  $n_i \rightarrow \infty$  iterations of the HBAC cooling procedure can be described by

$$\rho_f = \frac{1}{e^{\epsilon_{\max}} + e^{-\epsilon_{\max}}} \begin{pmatrix} e^{\epsilon_{\max}} & 0 \\ 0 & e^{-\epsilon_{\max}} \end{pmatrix}. \quad (2.10)$$

For the effective three-qubit system, the value  $\epsilon_{\max}$  can be calculated analytically. The limit of HBAC expresses that for reset polarizations given by  $\epsilon_{1,2}$  one has

$$\epsilon_{\max} \leq 2^{n-1}(\epsilon_1 + \epsilon_2) \quad (2.11)$$

with the number  $n$  of computation qubits ( $n = 1$  in this experiment). One can express  $\epsilon_{\max}$  in terms of polarization as

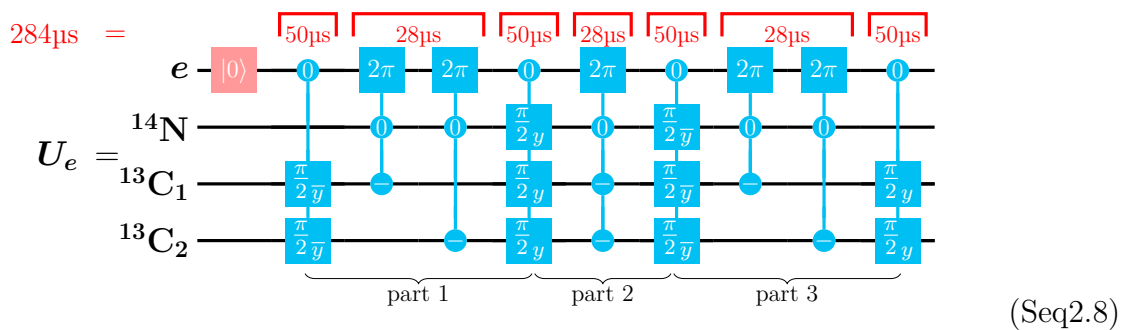
$$\Delta p_{\max} = p_0 - p_1 = \frac{e^{\epsilon_{\max}} - e^{-\epsilon_{\max}}}{e^{\epsilon_{\max}} + e^{-\epsilon_{\max}}} = \tanh(\epsilon_{\max}), \quad (2.12)$$



**HBAC operation as NMR gate** The qubit subspaces  $|0\rangle, |1\rangle$  are mapped to the nuclear spin subspaces  $|+\rangle, |0\rangle$  ( $^{14}\text{N}$ ) and  $|+\rangle, |-\rangle$  ( $^{13}\text{C}$ ). Then the HBAC gate operation is

$$|N, C_1, C_2\rangle = |0 + +\rangle \leftrightarrow |+ - -\rangle \quad (2.15)$$

sequence Seq2.7 is an effective gate representation, which can not be implemented straightforwardly in the hybrid NV center -  $^{13}\text{C}$  system. Firstly, there is no direct implementation of the required CNOT gates in NMR and secondly and more importantly, the missing interaction between the nuclear spins makes the direct non-local gates impossible to perform. Instead, sequence Seq2.7 needs to be dissected into multiple separated parts consisting of nuclear  $\pi/2$  - pulses as well as electron  $2\pi$ -rotations controlled by different nuclear spin states.



The total gate duration of  $U_e$  is  $284 \mu\text{s}$ . The nuclear  $\pi/2$  - pulses bring the nuclear spins to a coherent superposition state and from there also back to an eigenstate. Their duration of  $50 \mu\text{s}$  was chosen to omit heating of the sample due to the large RF power and to omit crosstalk to other nuclear spin transitions. For example transitions  $T [^{13}\text{C}, 0]$  and  $T [^{14}\text{N} = +1, 0]$  are as close as  $120 \text{ kHz}$  (cf. appendix C). The electron  $2\pi$ -rotations here act as controlled nuclear spin - nuclear spin phase gates, which do not change the state of the electron spin. Therefore, the electron spin state remains in state  $|m_s = 0\rangle$  during the long nuclear spin  $\pi/2$  - pulses and therefore, for the most part of the sequence the electron spin state decays on a timescale of  $T_{1e} = 5.7 \text{ ms}$ . During the  $2\pi$  - pulses with at total duration of  $84 \mu\text{s}$ , coherences are involved which decay on a timescale of  $T_{2,e}^{\text{Hahn}} = 395 \mu\text{s}$ . Here again, during each run the gate  $U_e$  only has a probability of  $70\%$  to have an effect. The other  $30\%$  of the runs the NV center is in charge state  $\text{NV}^0$ . The electron spin gates were optimized with help of the optimal control platform DYNAMO [148] to realize fast and robust gates despite electron decoherence on timescales of  $T_{2,e}^{\text{Hahn}}$  and a dense electron spin spectrum (cf. figure 1.13).

**Benchmarking the experimental performance of  $U_e$**  The performance of  $U_e$  in the experiment was benchmarked with sequence Seq2.9. First the three nuclear spins are initialized by

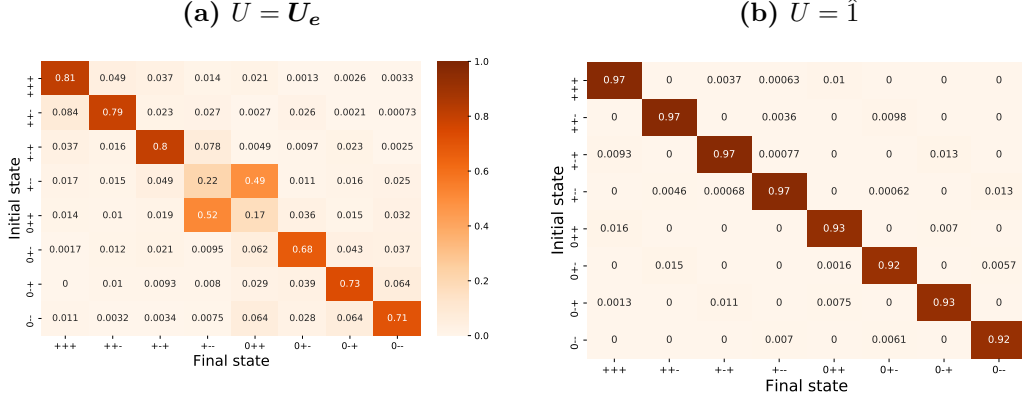
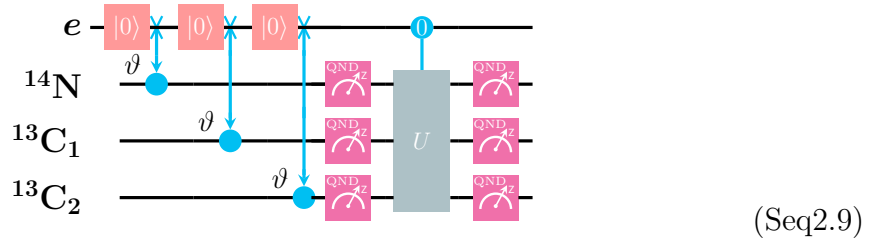


**Fig. 2.4: Benchmarking measurements for the cooling gate  $U_e$ , performed with sequence Seq2.9.** The three nuclear spins are polarized with three consecutive spin transfer gates into one of the eight possible initial states  $|m_N m_{C1} m_{C2}\rangle$ . Then either the gate  $U = U_e$  is performed and the resulting spin state is read out with SSR. The result is presented in (a). To be able to tell apart gate fidelity from readout fidelity, in (b) the equivalent measurement results are shown where  $U$  is the identity operation  $U = \hat{1}$ . The measurements give an overview of the performance of the gate  $U_e$  and the signature transformation  $|0 + +\rangle = |100\rangle \leftrightarrow |011\rangle = |+ - -\rangle$  is clearly visible.

polarization transfer from the electron spin with a subsequent SSR measurement. Then  $U_e$  is performed and finally the three nuclear spins are read out again with SSR.

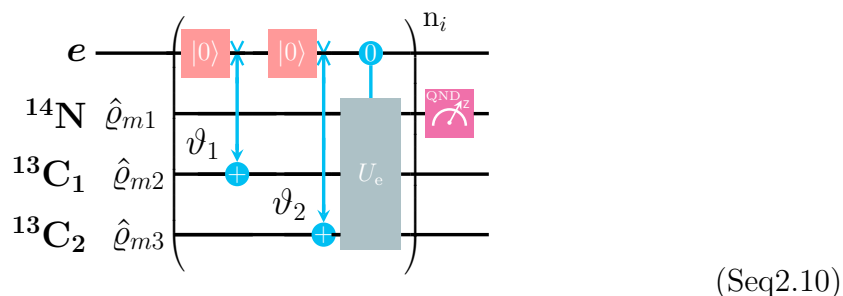


Initialization and readout is performed into all eight eigenstates  $|m_N m_{C1} m_{C2}\rangle$  of the three-qubit register. The result for  $U = U_e$  is shown in figure 2.4a. The signature of the operation  $|0 + +\rangle \leftrightarrow |+ - -\rangle$  is clearly visible as the central part of the matrix. However, two things here should be pointed out. First, like any other electron spin gate, it works only 70% of all runs due to charge state  $NV^0$  and unity fidelity will not be achieved under otherwise perfect conditions. Secondly, even the diagonal elements, i.e., those elements which are not affected by  $NV^0$ , are below unity. To exclude imperfect readout as a reason, the measurement was repeated with  $U = \hat{1}$  and the result is shown in figure 2.4b. By comparison of the two resulting matrices, the effect of the  $U_e$  can be told apart from the readout. It should be noted, that the population of  $^{14}\text{N}$  nuclear spin level  $|-\rangle$  was determined experimentally, however there was no significant crosstalk

between this level and the other eight levels used for the cooling algorithm. Thus, for the sake of brevity here only the relevant eight levels are presented.

### 2.3.3 HBAC scaling with iterations and bath polarization

The theoretical predictions of the asymptotic cooling limit and the scaling behavior with polarization of the bath spins made in section 2.3.1 are tested experimentally with the HBAC test sequence Seq2.10.



In this sequence, both the iterations  $n_i$  as well as the polarization transfer angles  $\vartheta_1$  and  $\vartheta_2$  are varied (cf. figure 2.3a). The two  $^{13}\text{C}$  spins are repeatedly reset into  $|+\rangle$  with red laser illumination followed by polarization transfer from the electron spin (cf. sequence Seq2.4). The polarization of the  $^{13}\text{C}$  is estimated from previous calibration in section 2.2.2, which was performed for  $k = 1$  and  $k = 2$  swap iterations. A direct readout of the  $^{13}\text{C}$  polarization and therefore also the loss of polarization due to loss of polarization to the  $^{14}\text{N}$  nuclear spin was not performed. Only the final polarization of the target spin  $^{14}\text{N}$  is read out with SSR.

**Polarization towards the asymptotic limit** In the first experiment, the two  $^{13}\text{C}$  nuclear spins are polarized with the same polarization transfer angles  $\vartheta = \vartheta_1 = \vartheta_2$  between 0 to  $\pi$ . Therefore, the polarizations  $\Delta p_1$  and  $\Delta p_2$  of these two reset spins are not the same but both increase monotonically with increasing  $\vartheta$  (cf. figure 2.3a and table 2.1). The cooling sequence is repeated up to  $n_i = 23$ , for varying reset polarization angles  $\vartheta$  and the data is presented in figure 2.5 and table 2.1. The predicted asymptotic behavior can be observed with a maximally  $^{14}\text{N}$  polarization  $\Delta p_N = 0.79$  for a swap angle  $\vartheta = \pi$ . At  $n_i = 5$ , the  $^{14}\text{N}$  polarization is almost saturated.

**Resimulation of the polarization curves with realistic parameters** The dashed lines shown in figure 2.5 were obtained by a full simulation of the polarization sequence Seq2.10, due to known constraints two additional assumptions had to be made. For once, it is known that during 70% of the iterations the polarization sequence has no effect at all due to

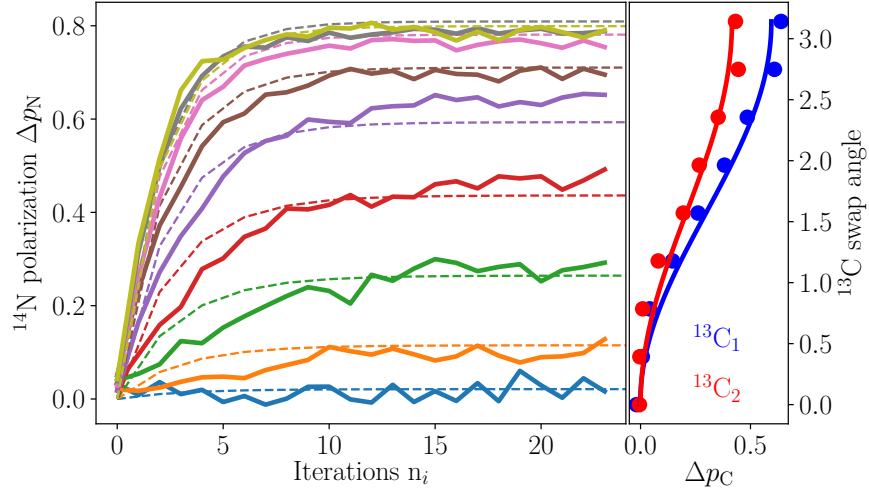


**Fig. 2.5: Hyperpolarization of the nitrogen nuclear spin via HBAC for 0 to 24 cooling iterations and varying reset polarizations.** The graph on the left shows the  $^{14}\text{N}$  polarization achieved through HBAC for different swap angles and  $^{13}\text{C}$  reset spin polarizations. Values are found in table 2.1. For a swap angle  $\pi$ , the reset polarizations of the two  $^{13}\text{C}$  spins reach their maximal values  $\Delta p_1 = 0.59$  and  $\Delta p_2 = 0.42$  and the  $^{14}\text{N}$  nuclear spin is polarized to a value of  $\Delta p_N = 0.79$  (yellow curve). The dashed lines show a resimulation of the data under the assumption that the gate  $U_e$  is active only during every second iteration (cf. figure 2.4a) and the swap angle is miscalibrated by  $22.3^\circ$  or  $+0.39$ .

$^{13}\text{C}$ swap angle [rad] $\vartheta$	0.00	0.39	0.79	1.18	1.57	1.96	2.36	2.75	3.14
$\Delta p_1$	0.00	0.02	0.09	0.18	0.30	0.41	0.51	0.57	0.59
$\Delta p_2$	0.00	0.02	0.06	0.13	0.21	0.29	0.35	0.40	0.42
$\Delta p_N$	0.02	0.13	0.29	0.49	0.65	0.70	0.75	0.79	0.79
$\Delta p_{N,\max}$	0.02	0.12	0.26	0.44	0.59	0.71	0.78	0.80	0.80

**Table 2.1:** Tabular summary of data from figure 2.5 for  $n_i = 24$  iterations of sequence Seq2.10. The column colors match the lines in the associated figure. The  $^{13}\text{C}$  swap angles are varied and thus polarizations  $\Delta p_1$  ( $\Delta p_2$ ) of  $^{13}\text{C}_1$  ( $^{13}\text{C}_2$ ) vary. The maximum polarization  $\Delta p_N$  achieved in the experiment and the theoretically expected maximum polarization  $\Delta p_{N,\max}$  are given.

charge state  $\text{NV}^0$ . Additionally, the gate fidelity of  $\mathbf{U}_e$  is certainly below 1, but a process tomography of such a large parameters space is very challenging to do. Therefore, a simple estimate is made from the data presented in figure 2.4a. There, the gate fidelity can be estimated to be smaller than 0.5 from the relevant four items in the central part. The most basic but still deduction to be made from this data is, that  $\mathbf{U}_e$  has a gate fidelity of 1 but is effective only during 50% of the iterations  $n_i$  and does nothing during the other 50%. Therefore, the  $x$ -axis is stretched for the simulated data for a factor of two compared to the experimentally obtained data. In other words, two iterations in the experiment correspond to one iteration in the dashed theory plot. The second assumption needs to be made on the  $^{13}\text{C}$  polarization, which does not necessarily coincide with the calibration data presented in figures 2.3a and 2.3b. Instead, due to the lack of  $^{13}\text{C}$  depolarization mechanisms, there may be polarization build-up between different iterations  $n_i$ . This fact is dealt with by assuming, that the swap angle  $\vartheta$  is miscalibrated by  $-22.3^\circ$  and thus the actual  $^{13}\text{C}$  polarization for each theory curve is received by assuming a  $+22.3^\circ$  larger swap angle and thus for the most part a slightly higher  $^{13}\text{C}$  polarization than what would be expected without this assumption. Here it must be emphasized, that the theory curves acquired under these assumptions are no more than educated guesses from incomplete experimental data. In particular the swap angle correction  $22.3^\circ$  was chosen, as it produced the best match between theory and experiment.

**Behavior for variable reset polarizations** The ability to vary the reset polarization of the two  $^{13}\text{C}$  reset spins independently over a wide range of possible polarizations from  $\Delta p_1 = 0$  to 0.59 and from  $\Delta p_2 = 0$  to 0.42 allows to analyze the HBAC algorithm in more detail. The number of iterations therefore is set to a large value of  $n_i = 23$ , which was shown to be in the asymptotic limit in figure 2.3a for multiple swap angles  $\vartheta$ . The two swap angles  $\vartheta_1$  and  $\vartheta_2$  then are varied independently.

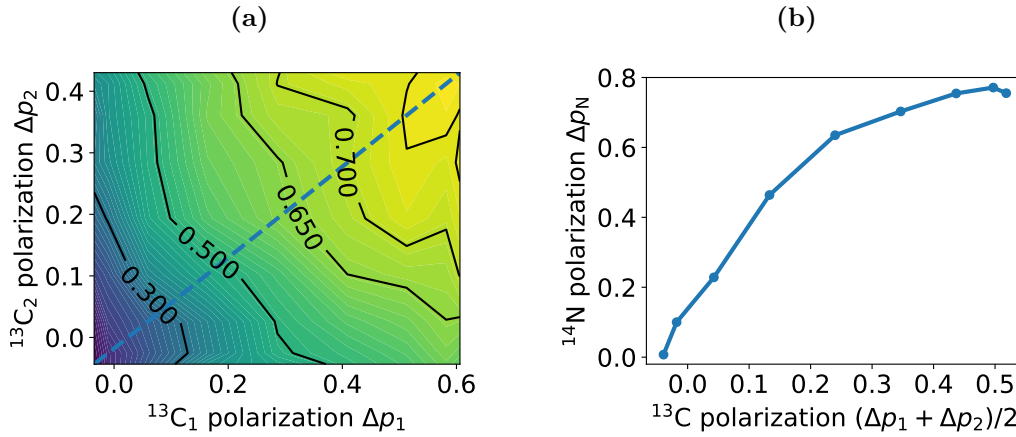


**Fig. 2.6:**  $^{13}\text{C}$  reset spin polarization dependent hyperpolarization of the  $^{14}\text{N}$  nuclear spin via HBAC for 23 cooling iterations and independently varied reset polarizations. The number of iterations  $n_i = 23$  is fixed, while the swap angles  $\vartheta_1$  and  $\vartheta_2$  which control the  $^{13}\text{C}$  reset polarization are swept. The x- and y-axes of plots (a) shows the effective polarization values calculated from calibration data figure 2.3b. (b) shows a diagonal cut through (a).

## 2.4 Pulsed polarization

Gate based approaches such as the ones introduced in sections 2.2 and 2.3 are not feasible for the hyper-polarization of weakly coupled nuclear spins, as the low interaction does not allow for non-local quantum gates to be performed with reasonable fidelities on timescales required for polarization build-up. One possible approach here is the NOVEL method, which uses resonant driving of the electron spin to bring it into a spin-locked state and thus allow for polarization transfer with the nuclear spin at a rate proportional to the hyperfine component  $A_{zx}$  [149]. However, the NOVEL method requires a very stable MW amplitude, as the Rabi driving frequency sets the resonance condition for the addressed nuclear spin transition. At the here applied external magnetic field of  $B_{0,z} = 0.65$  T, the electron Rabi driving frequency is  $\approx 7$  MHz and even fluctuations of 1% lead to fluctuations of the Rabi frequency large enough to stop the polarization transfer for weakly coupled nuclear spins with long polarization transfer times. Therefore, other techniques are required, which can address a large number of weakly coupled nuclear spins in the lowest possible time and still are robust against fluctuations of the MW amplitude. An idea on how such a technique could work is given by the diagonal hyperfine coupling tensor of the  $^{14}\text{N}$ , with its very large perpendicular hyperfine interaction terms  $A_{\perp}$  ( $\sim 60$  MHz section 1.4.1). These terms are directly leading to flip-flop terms in the

NV center Hamiltonian (cf. equation 1.13).

$$\hat{H}_{\text{flipflop}} = c \left( \hat{S}_+ \hat{I}_- + \hat{S}_- \hat{I}_+ \right) \quad (2.16)$$

with  $c = \frac{A_{\perp}}{2}$ . At the GSLAC and ESLAC, the prefactor  $c$  indeed gives the flip-flop - rate between electron spin and the coupled nuclear spin and allows for very high polarization efficiencies of the  $^{14}\text{N}$  nuclear spin due to its large values of  $A_{\perp}$  [145]. For high magnetic fields though, the flip-flop - rate is largely suppressed, which drastically reduces the polarization efficiency even for the  $^{14}\text{N}$  nuclear spin (cf. equation 1.35). Unfortunately, for  $^{13}\text{C}$  the perpendicular hyperfine components  $A_{xx}$ ,  $A_{yy}$  are comparable to  $A_{zz}$  and thus for weakly coupled  $^{13}\text{C}$ ,  $A_{\perp}$  is three orders of magnitude lower compared to  $^{14}\text{N}$  (cf. figure 1.7e). These low values of  $A_{\perp}$  are not sufficient for polarization transfer, particularly at high magnetic fields. Average Hamiltonian theory can help to generate flip-flop terms with large prefactors  $c$  which are not suppressed and thus  $c$  directly translates into the flip-flop rate at any magnetic field.

### 2.4.1 Using average Hamiltonian theory for the generation of a flip-flop Hamiltonian

Here, average Hamiltonian theory is used to generate an effective flip-flop Hamiltonian  $\hat{H}_{\text{flipflop}}$ , whose amplitude  $c$  is proportional to the  $^{13}\text{C}$  hyperfine component  $A_{zx}$  [150, 151]. The used polarization sequence is constructed with the PulsePol framework introduced by Schwartz et al. [152]. The basic building block of the polarization sequence is sequence Seq2.11, which essentially consists of two independent DD sequences, both of duration  $\tau_{\text{DD}}$ .

$$e \quad |0\rangle \text{---} \underbrace{\left[ \frac{\pi}{2} \text{ }_x \quad \frac{\tau}{2} \quad \text{XY}_4 \quad \frac{\tau}{2} \quad \frac{\pi}{2} \text{ }_x \right]}_{U_{xx} = e^{i\alpha A_{zx} S_x I_x}} \text{---} \underbrace{\left[ \frac{\pi}{2} \text{ }_y \quad \frac{\tau}{2} \quad \text{XY}_4 \quad \frac{\tau}{2} \quad \frac{\pi}{2} \text{ }_y \right]}_{U_{yy} = e^{i\alpha A_{zx} S_y I_y}} \text{---} \quad (Seq2.11)$$

Here  $\tau = \tau_{\text{DD}}/N_{\pi}$ . As DD sequence, here the XY-4 with  $N_{\pi} = 4 \pi$  - pulses was chosen due to the increased coherence time compared to a Hahn-Echo sequence. Then, the total waiting time per XY-4 sequence needs to be

$$\tau_{\text{DD}} = \left( \frac{1}{2f_L + A_{zz}} - \frac{1}{4\Omega} \right) (N_{\pi} + 0.25) \quad (2.17)$$

with the Larmor frequency  $f_L$  and the hyperfine component  $A_{zz}$  of the addressed nuclear spin as well as the electron Rabi frequency  $\Omega$ . Please note, that when the  $\pi$  - pulse duration is on the order of the interpulse distance  $\tau$ , then correction factors for  $\tau_{\text{DD}}$  need

to be added in equation 2.17, which can be determined experimentally (cf. figures 2.9a and 2.9b on page 72). The selectivity to an individual nuclear spin here is given through  $A_{zz}$ , which makes polarization transfer to selected, isolated nuclear spins possible.

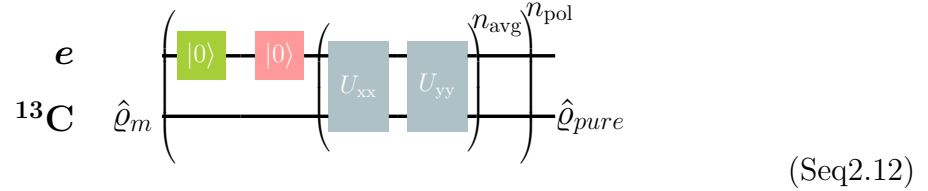
During the two DD sequences, the coupled system of electron spin and nuclear spin evolves unitarily according to  $U_{xx} = e^{i\alpha A_{zx} S_x I_x}$  and  $U_{yy} = e^{i\alpha A_{zx} S_y I_y}$ , respectively. Averaging Hamiltonian theory states that by rapid alternation of  $U_{xx}$  and  $U_{yy}$  on timescales smaller than the inverse nuclear Larmor frequency the individual components are averaged to the flip-flop term

$$\hat{H}_{\text{flipflop}} = -\alpha \frac{A_{zx}}{4} (\hat{S}_+ \hat{I}_- + \hat{S}_- \hat{I}_+) \quad (2.18)$$

Sequence Seq2.11 is repeated  $n_{\text{avg}}$  times up to a total time  $T_{\text{avg}} = 2n_{\text{avg}}\tau_{DD}$  during which the coupled nuclear spin electron spin system coherently evolves according to  $\hat{H}_{\text{flipflop}}$ . A flip-flop (i.e. transfer of polarization) is completed after

$$n_{\text{avg}} = \frac{2}{\alpha A_{zx}} \quad (2.19)$$

This relation allows for the experimental determination of  $\alpha$ , when  $A_{zx}$  is known. When a single iteration of the sequence does not suffice due to weak hyperfine coupling of the nuclear spin, the electron spin can be repolarized by laser illumination before an additional polarization transfer attempt. With increasing number  $n_{\text{pol}}$ , the nuclear spin polarization is increased towards its maximal value.



Generally, weak red laser illumination can result in a very high electron polarization. However, red laser illumination also does not provide a back-channel from  $\text{NV}^0$  [74]. Thus, each red laser pulse is prepended by a green one, which pumps back from  $\text{NV}^0$ . The pulse durations of red and green are  $0.3 \mu\text{s}$  and  $70 \mu\text{s}$ .

### 2.4.2 Experimental determination of the coupling constant

The coupling constant  $\alpha$  can be determined from equation 2.19, when both  $A_{zx}$  and  $A_{zz}$  of a nuclear spin are known and  $A_{zx}$  is not too small, such that polarization can be transferred to and from the nuclear spin multiple times. Figure 2.7 shows the dynamics for a single electron repolarization  $n_{\text{pol}}$  but increasing number  $n_{\text{avg}}$  and thus increasing

interaction time  $T_{\text{avg}}$ . For this experiment  $^{13}\text{C}_1$  was chosen as the target spin, due to its large hyperfine couplings  $A_{zz} = 413\text{ kHz}$  and  $A_{zx} = 67.4\text{ kHz}$  (determined in section 4.2). The  $\pi$  - pulse duration was 50 ns. The interpulse distance was calculated according to equation 2.17. The polarization transfer is completed after  $n_{\text{avg}} = 17$ , thus according to equation 2.19,  $\alpha = 1.78$  for the polarization sequence Seq2.11.

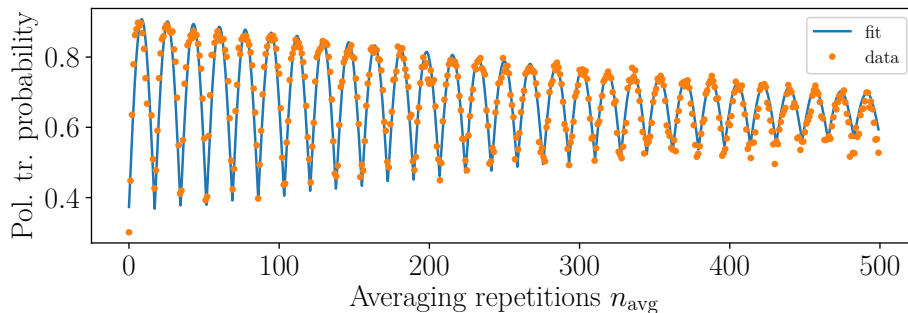


**Fig. 2.7: Polarization transfer probability from electron spin to a  $^{13}\text{C}$  nuclear spin.** with hyperfine components  $A_{zz} = 413\text{ kHz}$  and  $A_{zx} = 67.4\text{ kHz}$ . The nuclear spin starts initialized and the averaging Hamiltonian equation 2.18 generated by sequence Seq2.12 transfers the electron spin state to and from the nuclear spin. The oscillation period is  $n_{\text{avg}} = 34$ . The nuclear spin state is read out with SSR readout with a fidelity of 94 %.

### 2.4.3 Polarization measurements

In this chapter, the polarization efficiency of sequence Seq2.12 for two different weakly coupled  $^{13}\text{C}$  spins with  $A_{zz} = 12.3\text{ kHz}$  ( $A_{zx} = 2.6\text{ kHz}$ ) and  $A_{zz} = 5.8\text{ kHz}$  ( $A_{zx} = 15.3\text{ kHz}$ ) is shown. Therefore, the addressed nuclear spin is first polarized with  $n_{\text{pol}}$  laser pulses and  $n_{\text{avg}}$  repetitions of the polarization sequence. The  $^{13}\text{C}$  nuclear spin Larmor frequency was 7.1 MHz and the  $\pi$  - pulse duration was 50 ns. The interpulse distance was calculated according to equation 2.17 for a nuclear spin with zero hyperfine coupling ( $A_{zz} = 0\text{ kHz}$ ).

The effective magnetization is read out with the coherent stimulated echo technique, which can measure magnetic fields with precision limited by  $T_{1e}$  (cf. section 3.2.1 on page 89). The measurement results are shown in figures 2.8a and 2.8b. For both nuclear spins, the polarization saturates for the maximal value  $n_{\text{avg}} = 40$  at  $n_{\text{pol}} = 100$  laser pulses. This behaviour is somewhat surprising, as the  $A_{zx}$  couplings are much smaller for  $^{13}\text{C}$  with  $A_{zz} = 12.3\text{ kHz}$ . A possible explanation could be found in the better isolation of this  $^{13}\text{C}$  in the  $A_{zz}$  spectrum. For clarification, further analysis would be necessary. The polarization sequence has a duration of 30 ms for  $n_{\text{avg}} = 40$  at  $n_{\text{pol}} = 100$  and both

nuclear spins are polarized to

$$\Delta p = p_{|+\rangle} - p_{|-\rangle} > 90 \% \quad (2.20)$$

This probability is limited by the electron spin polarization and the efficiency of the polarization sequence. The electron spin polarization for these measurements was  $\approx 95\%$ . The probability to find the polarized  $^{13}\text{C}$  in spin state  $|+\rangle$  therefore also is larger than 99%.

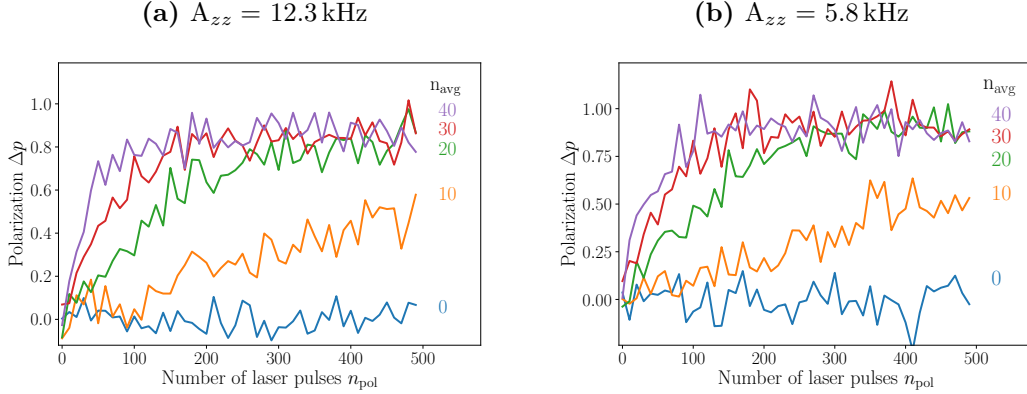


**Fig. 2.8: Polarization transfer to two weakly coupled nuclear spins using the Pulse-Pol sequence Seq2.12.** Both nuclear spins reach polarizations very close to one. The polarization values  $\Delta p$  are normalized to the maximal readout contrast of 0.52 in (a) and 0.43 in (b), both determined in sensing experiments on the two nuclear spins.

#### 2.4.4 Effective interpulse distance for long microwave pulses

The exact value of  $\tau_{DD}$  is crucial for the successful nuclear spin polarization by sequence Seq2.12. Unfortunately, equation 2.17 only gives a (very good) estimate for  $\tau_{DD}$ , which needs to be calibrated for different Rabi frequencies  $\Omega$ . The calculated value of  $\tau_{DD}$  for the polarization of a  $^{13}\text{C}$  nuclear spin with zero hyperfine coupling ( $A_{zz} = 0 \text{ kHz}$ ) at a magnetic field  $B_{0,z} = 0.65 \text{ T}$  is  $\tau_{DD} \approx 200 \text{ ns}$  and thus the interpulse distance is  $\tau = 47 \text{ ns}$ . This value needs to be corrected for

$$\Delta\tau = -\frac{0.0887}{\Omega} + 0.00383 \quad (2.21)$$

The calibration was performed by sweeping the interpulse distance  $\tau$  for different Rabi frequencies  $\Omega$  and thereby measuring the magnetization of the  $^{13}\text{C}$  with  $A_{zz} = 12.3 \text{ kHz}$ . With increasing Rabi period  $T_{\text{Rabi}}$  both the polarization efficiency as well as the interpulse distance are lowered. When the duration of the MW  $\pi$ -pulses takes up more and more time of the total sequence  $\tau_{DD}$ , the formula is not correct anymore.

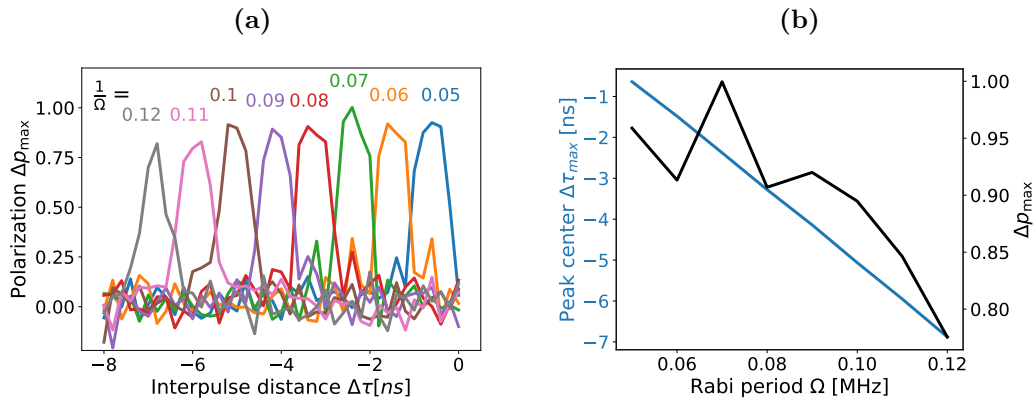


**Fig. 2.9: Maximal magnetization and interpulse distance offset  $\Delta\tau$  for different Rabi periods  $T_{\text{Rabi}}$ .** Sequence Seq2.12 was performed with  $n_{\text{pol}} = 300$  and  $n_{\text{avg}} = 30$  while polarization of the  $^{13}\text{C}$  with  $A_{zz} = 12.3$  kHz was measured. As the Rabi period increases, the interpulse distance offset  $\Delta\tau$  for which the polarization is maximal decreases linearly as well as the contrast.

## 2.5 Summary and outlook

This chapter focuses on the polarization of  $^{13}\text{C}$  nuclear spins in the diamond lattice. For the sake of completeness, first the well known and in this work regularly used technique of cooling by postselection is briefly discussed. It allows for nuclear spin polarizations beyond 99 % by discarding measurement runs with unfitting nuclear spin states. Then, as a preparatory work for the actual highlight of this chapter, the demonstration of heat-bath algorithmic cooling, variable degree polarization transfer from NV center electron spin to two rather strongly coupled  $^{13}\text{C}$  nuclear spins is demonstrated. Thereby, in a single run of the polarization sequence, the polarization could be freely varied between  $\Delta p = 0$  and  $\Delta p = 0.416$  for the weaker coupled and  $\Delta p = 0.594$  for the stronger coupled of the two  $^{13}\text{C}$  nuclear spins.

This high degree of control over the polarization of two individual nuclear spin qubits was then used, to investigate the heat-bath algorithmic cooling technique over a wide range of parameters. The two  $^{13}\text{C}$  spins were used as reset qubits and a two-level subspace of the  $^{14}\text{N}$  nuclear spin was used as target qubit. Hereby, the electron spin is to be seen as heat-bath, which allows to dispose of entropy on the reset qubits. The temperature of the bath limits the possible polarization of the reset qubits. Repeated repolarization of the reset qubits with subsequent application of a specially designed cooling operation polarizes the  $^{14}\text{N}$  nuclear spin qubit subspace more and more with every iteration. As many as  $n_i = 23$  cooling iterations were performed, and saturation of the asymptotic heat-bath algorithmic cooling bound could be observed already around  $n_i = 5$  to 10 iterations. For the above mentioned maximal reset spin polarizations

of  $\Delta p = 0.416$  and  $\Delta p = 0.594$ , the  $^{14}\text{N}$  qubit could be polarized to  $\Delta p_N = 0.79$  at  $n_i = 23$  iterations. This observation already makes the strength of heat-bath algorithmic cooling apparent: The target qubit(s) can be polarized to a higher degree than would be allowed straightforwardly from the temperature of the heat-bath. For lower reset spin polarizations the qualitative behavior remains the same, however, with a lower heat-bath algorithmic cooling bound. The heat-bath algorithmic cooling bound is reached within a similar number of iterations independent of the reset spin polarizations. In the asymptotic limit of  $n_i = 23$  cooling iterations, the achievable target spin polarization is depicted for a 2D - map of reset spin polarizations. The here presented heat-bath algorithmic cooling experiments could enable further studies on exploring and controllably benchmarking the role of correlations on heat exchange processes in the quantum limit. By extending the used reset qubits to weakly coupled nuclear spins, a further increase in the number of reset qubits would be possible. This potentially may lead to faster convergence or a higher cooling limit for the same reset spin polarization (i.e. bath temperature). To reach this goal, the fidelities of the quantum gates would have to be improved by going to lower temperatures, where the coherence times are longer.

In the last section, the carefully designed pulse sequence allows to generate an artificial flip-flop Hamiltonian for the polarization of weakly coupled  $^{13}\text{C}$  nuclear spins. Nuclear spins with couplings of  $A_{zz} = 12.3\text{ kHz}$  and  $A_{zz} = 5.8\text{ kHz}$  could both be polarized to  $\Delta p > 90\%$ .



# 3

## Quantum enhanced correlation spectroscopy

High precision quantum metrology relies on most accurate measurements of quantum phases. However, numerous susceptibilities to environmental noise make quantum states fragile, resulting in limited sensitivity. Therefore, the acquisition of a large phase is a central challenge [153–157]. Typically, two strategies are used to enhance quantum sensing: One way is multi-particle entanglement of sensing qubits which results in rapid phase accumulation, but is often counterbalanced by faster dephasing [158–161]. Entanglement however, pays off, if fluctuations of the quantity to be measured have a shorter correlation time than the single sensor coherence time. A long-lived memory is another way which is advantageous when the quantity to be measured has a longer correlation time than the sensor's coherence time [162–165]. The quantum memory approach is particularly suited in hybrid sensor systems where the sensing qubit strongly interacts with the quantity to be measured while the storage qubit is well isolated from environmental influences except for its coupling to the sensor. Typically, highest sensitivity is reached when the available coherence time of the sensing qubit is most effectively used [166–168]. Further enhancement is gained if the quantum state of the sensing qubit is at least partially stored for a later feedback, and thereby exploiting the observable's longer correlation time [162, 163, 165].

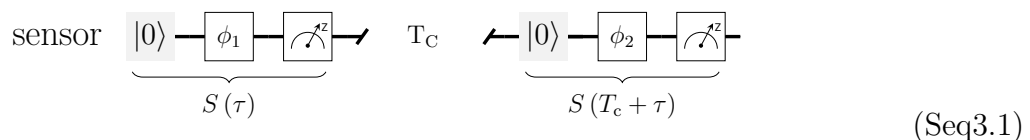
In this chapter, the  $^{14}\text{N}$  nuclear spin is utilized as a quantum memory for full storage of the sensor's quantum state leading to enhanced sensitivity. Entanglement between the quantum memory and the sensing qubit during the phase accumulation process makes efficient use of the available resources. The enhanced sensing time due to use of the quantum memory improves spectral resolution. The quantum memory enhanced sequence is used for the detection of weakly coupled magnetic fields with a frequency resolution of 210 Hz. A further benefit of the phase estimation-type [169] protocol is the added ability to perform high-fidelity non-local gate operations between quantum memory and

a strongly or weakly coupled sample spin. The investigated sensor- quantum memory method is compatible with other recently developed classical correlation methods [170–172]. The results in this chapter are published in [173].

**Chapter outline** This chapter is subdivided in four sections. In section 3.1, the quantum enhanced sensing protocol which uses a quantum memory is compared to a conventional correlation measurement with a classical memory. The transition from fully classical to fully quantum memory is experimentally demonstrated. A two-fold higher sensitivity of the quantum enhanced sensing protocol is shown. Section 3.2 demonstrates several applications of the quantum enhanced sensor-memory hybrid system to detect and interact with  $^{13}\text{C}$  nuclear spins. Weakly coupled nuclear spins are detected and quantum operations between the memory spin and a weakly coupled  $^{13}\text{C}$  nuclear spin are shown, which can ultimately lead to entanglement. Section 3.3 then finally uses the quantum memory enhanced sensing protocol to detect a time-varying field produced by  $^{13}\text{C}$  nuclear spins with hyperfine couplings  $\pm 50$  kHz. Section 3.4 summarizes the observations and gives a brief outlook.

### 3.1 Measurement protocol with and without quantum memory

If the correlation time of the measured quantity (e.g. a magnetic field) is longer than the coherence time of the sensor, this coherence time limits the frequency resolution of the measurement and makes recording of dynamics challenging. To recover dynamics and increase spectral resolution, subsequently measured quantities  $S$  can be correlated (i.e.  $\langle S(\tau) S(T_c + 2\tau) \rangle$ ).

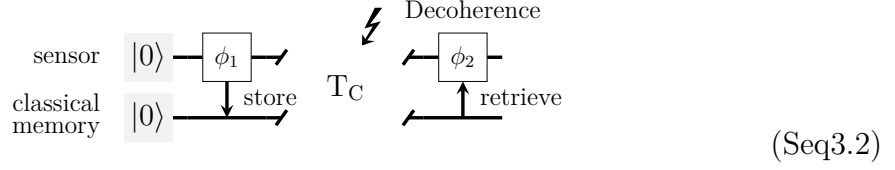


However, in any realistic scenario the measurement exhibits a limited visibility  $A < 1$  (cf. figure 1.18b on page 46) of the measurement signal  $S$ , which leads to a reduced visibility  $A < S$  and thus the visibility of the correlation measurement sequence Seq3.1 decreases as  $\propto A^2$ .

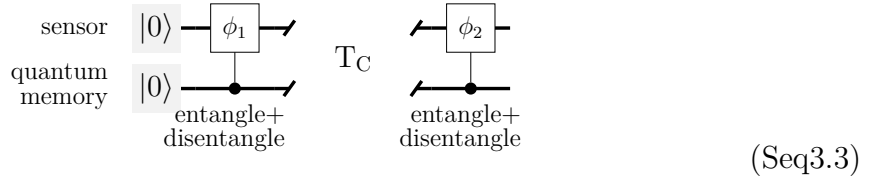
One solution are classical correlation measurements [162, 163, 174–180], where a long-lived memory stores the phase information for later use (e.g. the phase  $\varphi_1$ ) and thereby removes the necessity for an intermediate readout. Existing schemes use a classical

### 3.1 Measurement protocol with and without quantum memory

memory for storage.



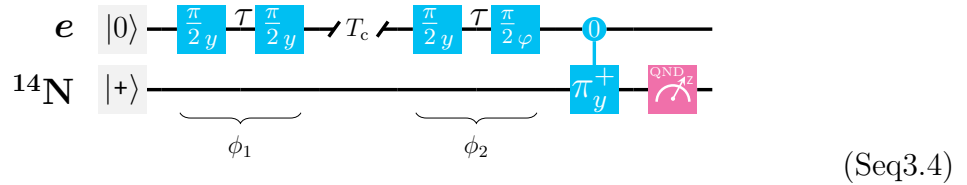
Due to decoherence, a classical memory can not store the full information acquired by the quantum sensor. Instead, only the population along one direction is preserved and thus half of the signal amplitude  $A$  is lost. The full measurement contrast  $A$  can be retained by use of a quantum memory, which is entangled with the NV center electron sensor during the phase accumulation times and disentangled thereafter. Thereby, the phase information is entirely stored on the quantum memory, while the sensor resides in an eigenstate during the long correlation time  $T_c$  and is not affected by decoherence.



If the signal is produced by another quantum system, the state of this quantum system directly influences the phase on the quantum memory and thus non-local gates become possible with this technique.

#### 3.1.1 Entanglement free correlation measurement with classical memory

The conventional, classical correlation sequence Seq3.2 can be implemented on the electron spin alone, which then acquires a phase during the sensing times  $\tau$  and also stores parts of the phase information during the correlation time  $T_c$ . The used electron spin subspace here again is  $|0\rangle, |-\rangle$ . In this simplified scheme, neither the storage nor the retrieval process are necessary, as memory and sensor are a single entity.



For faster readout, the sensor information is transferred to a nuclear spin which allows for SSR [18]. In this scheme, the  $^{14}\text{N}$  nuclear spin is exclusively used to increase the readout efficiency and not as a memory of any kind. The used  $^{14}\text{N}$  subspace is  $|+\rangle, |0\rangle$ .

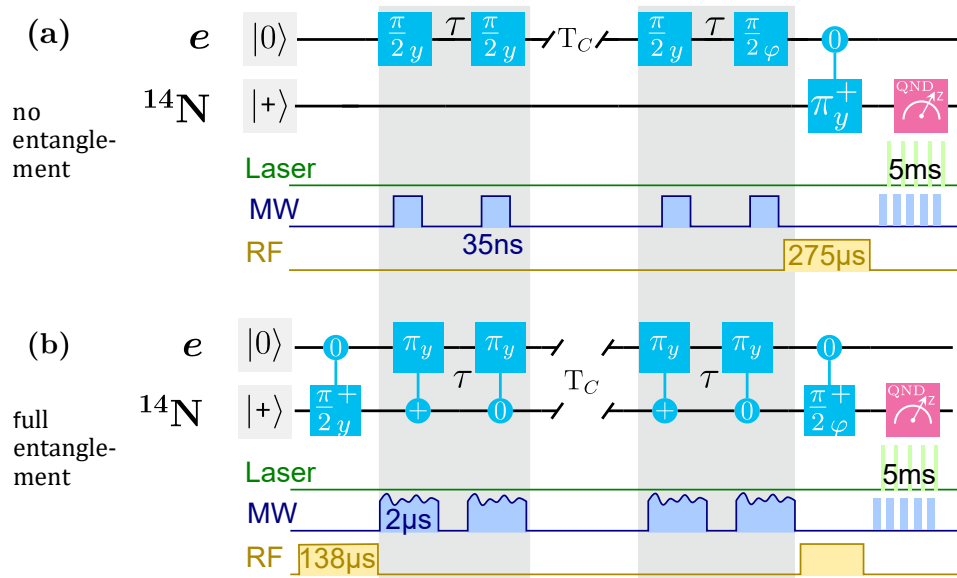


**Fig. 3.1: Comparison of sequence durations of conventional and entanglement enhanced sequence.** Sequences in (a) and (b) are identical to sequences Seq3.4 and Seq3.5 on pages 77 and 81. (a) The conventional correlation sequence is performed entirely on the electron spin, and only for enhanced readout the phase information after the sequence is mapped to the  $^{14}\text{N}$  nuclear spin. The four electron spin  $\pi/2$  - pulses are not selective to the  $^{14}\text{N}$  nuclear spin state and thus can be performed within only 35 ns. (b) the quantum enhanced correlation sequence uses entanglement between electron and nuclear spin, which is switched on and off by electron  $\pi$  - pulses that are selective to either  $^{14}\text{N}$  nuclear spin states  $|+\rangle$  or  $|0\rangle$ . Each of these four  $\pi$  - pulses has a duration of 2  $\mu\text{s}$ . The readout in both conventional and quantum enhanced case takes 5.275 ms. Therefore, the sequences have a duration of  $5.275 \text{ ms} + 2\tau + T_C$  differing only by the readout duration of 0.14  $\mu\text{s}$  (a) and 8  $\mu\text{s}$  (b).

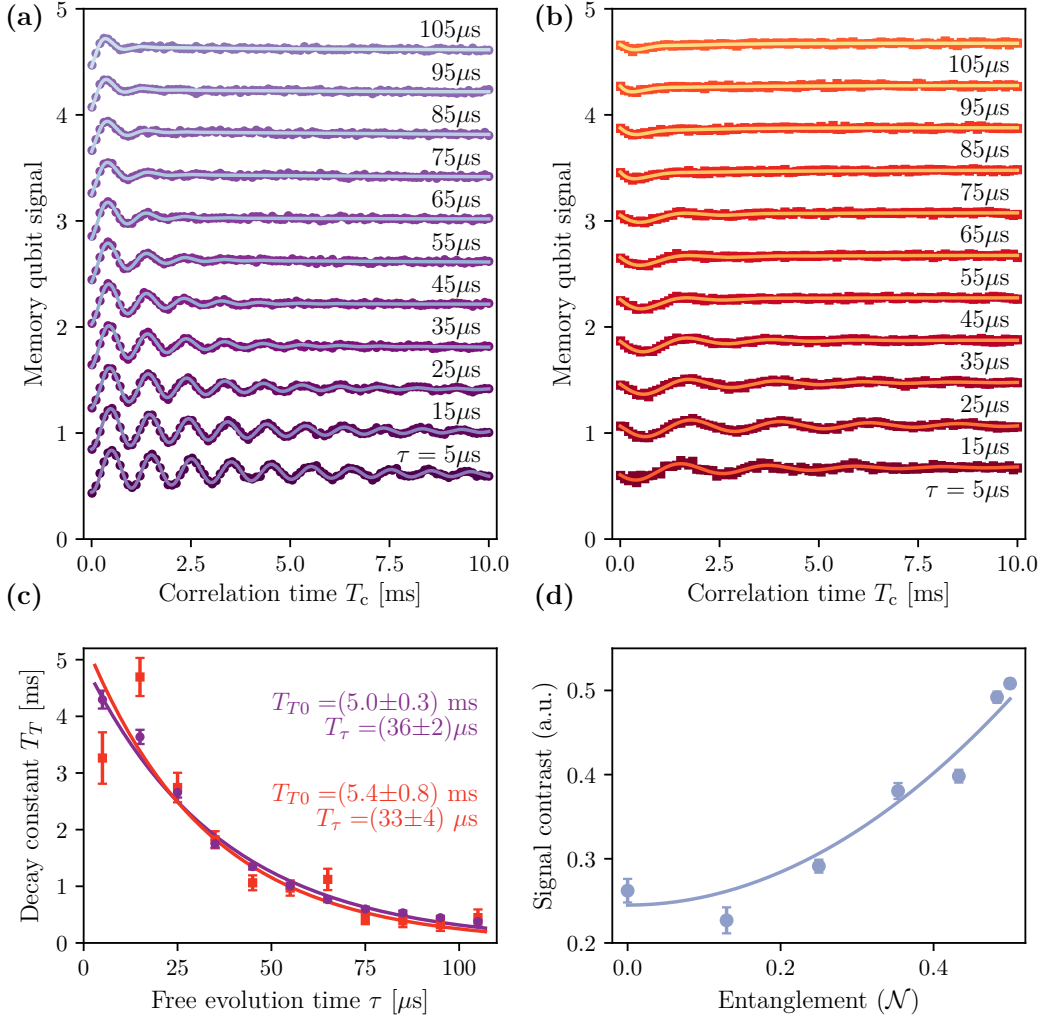


**Fig. 3.2: Comparison of enhanced and conventional correlation measurements.** (a), (b) Stacks of correlation measurements for full (a,  $\eta = 1$ ) and no entanglement (b,  $\eta = 0$ ) between sensor and memory qubit for various sensing times  $\tau$  as stacking parameter. Associated measurement sequences are given in sequences Seq3.5 and Seq3.4. The memory readout signal (i.e. the probability of detecting state  $|1\rangle$ ) is plotted against the correlation time  $T_c$  (stack-offset  $n \cdot 0.4, n \in \{0, 1, \dots, 10\}$ ). Oscillations on the signal are introduced artificially by a phase offset  $\varphi = 2\pi \cdot T_c \cdot f_T$ ,  $f_T = 1\text{kHz}$  (a) and  $f_T = 0.5\text{kHz}$  (b) to sample the stored quantum phase (see equation 3.8 and equation 3.2). All data sets are fit by  $y = y_0 + (A_0/2) \exp\{-T_c/T_T\} \cos(\varphi + \varphi_0) + A_1 \exp\{-T_c/T_1\}$ . (c) Fit values for decay constant  $T_T$  over  $\tau$  for no (squares, orange) and full (circles, purple) entanglement of sensor and memory. The function  $T_T = T_{T0} \exp\{-\tau/T_\tau\}$  is fit to the weighted data and the corresponding parameters are displayed. (d) Signal contrast  $A_0$  for  $T_c = 0$  over entanglement between sensor and memory qubit given as negativity  $\mathcal{N}$ . All error bars give standard errors taken from the used least square fit.

The electron pulses (here  $\pi/2$ ) are local gates and thus can be performed very rapidly, here  $T_\pi = 35$  ns. The RF pulses used for nuclear spin manipulation take  $275 \mu\text{s}$ , while the readout takes  $5$  ms (cf. figure 3.1a). In essence, sequence Seq3.4 is a classical stimulated echo sequence as it is known from EPR and optics [179, 181]. For  $T_c = 0$  it is identical to a Hahn-echo sequence introduced as sequence Seq1.4 and therefore will decouple from all static magnetic fields. For the common case of  $T_c \gg \tau$ , all magnetic field frequencies with exception of  $f = 1/T_c$  will lead to a phase difference  $\Delta\phi \neq 0$  (cf. sequence Seq1.5) with

$$\Delta\phi = \phi_1 - \phi_2 \quad (3.1)$$

Any changes in local magnetic field during correlation time  $T_c$  lead to a phase difference  $\Delta\phi$  which remains on the memory qubit and constitutes the metrology information. During the correlation time  $T_c$ , the electron spin sensor is not in a superposition state and thus not sensitive to noise. Nonetheless, larger correlation times  $T_c$  greatly influence the effective coherence time  $T_{2e}$ , as for longer  $T_c$  also slowly varying noise sources have an impact (cf. figure 3.2).

**Half signal visibility** The final SSR readout yields the probability  $S_{\text{conv}}$  to find the electron spin in spin state  $|m_s = -1\rangle$  [182].

$$\begin{aligned} S_{\text{conv}} &= \frac{1+c}{2} - A \frac{\langle \cos^2\phi - \cos\phi \sin\phi \rangle \cos(\Delta\phi - \varphi)}{2} \\ &= \frac{1+c}{2} - \frac{A \cos(\Delta\phi - \varphi)}{2} \end{aligned} \quad (3.2)$$

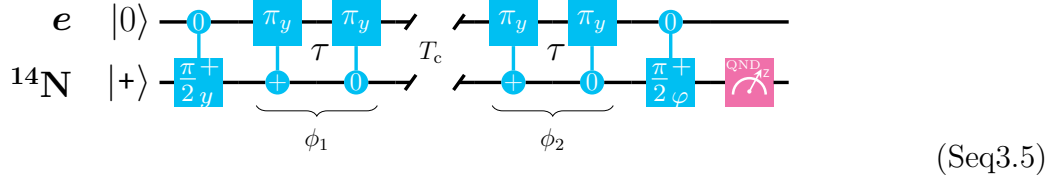
with the phase  $\varphi$  of the final electron  $\pi/2$  - pulse. The decay of residual coherence for  $T_c > T_{2e}$  on the sensor after the first  $\tau$  enters by averaging over a range of  $\phi$  larger than  $2\pi$ , which leads to factor  $1/2$  in equation 3.2. This factor  $1/2$  is lost due to the classicality of the used memory and can be regained by use of a quantum memory. Imperfect initialization and readout of the sensor and memory system result in finite signal contrast  $A < 1$  and a signal shift  $c \approx 0.2$  ( $0 \leq S \leq 1$ ). The main reason for this signal shift is the  $\text{NV}^0$  charge state [78].

### 3.1.2 Quantum memory enabled by sensor-memory entanglement

A fully featured quantum memory can regain the signal contrast which is lost when using a classical memory (cf. equation 3.2). An implementation of the entanglement assisted sensing scheme sequence Seq3.3 is shown in sequence Seq3.5. It consists of an electron spin quantum sensor and a  $^{14}\text{N}$  nuclear spin quantum memory. Here, electron spin subspace  $|0\rangle, |-\rangle$  and  $^{14}\text{N}$  nuclear spin subspace  $|+\rangle, |0\rangle$  are used as sensor and

### 3.1 Measurement protocol with and without quantum memory

memory qubit.



Sequence Seq3.5 consists of two phase accumulation steps separated by the correlation time  $T_c$  with the electron spin as sensing/processing qubit and the  $^{14}\text{N}$  nuclear spin as storage qubit. Each phase accumulation step comprises a pair of entangling and disentangling gates separated by a sensing time  $\tau$ . During  $T_c$ , the phase which is acquired by the sensing qubit, remains stored in the memory. The electron pulses (here  $\pi$ ) are controlled gates of duration  $2\ \mu\text{s}$ , which flip the electron spin conditionally to  $^{14}\text{N}$  states  $|m_N = +1\rangle$  or  $|0\rangle$ . Due to the complexity of the electron spin spectrum for the used NV center, (cf. section 1.5.1 and figure 1.12 on pages 23 and 31), they are implemented as amplitude and phase modulated fields, optimized for maximum fidelity and robustness against detunings of the MW frequency [18, 183]. The optimization was performed with the optimal control platform DYNAMO [148]. The two RF  $\pi/2$  - pulses each take  $138\ \mu\text{s}$  and here are also selective to the electron spin state  $|0\rangle$ . This is not necessary, however, single frequency RF pulses are controlled operations (cf. section 1.6.4), and for truly local gates, two or more RF pulses would be needed. The initial controlled gate on the memory excludes cases where the electron spin was not properly initialized, so its application is justified. Assuming high fidelity nuclear spin controlled electron  $\pi$ -gates ( $\text{C}_n\text{Pi}_e$ -gates), the second controlled gate on the memory again eliminates only cases of wrong initial sensor states. The readout of the memory spin takes  $5\ \text{ms}$  (cf. figure 3.1b).

**Dynamics on coupled sensor-memory system** Before sequence Seq3.5, the electron sensor qubit is polarized via a green laser pulse and the  $^{14}\text{N}$  memory spin is prepared in a superposition state.

$$|\Psi_i\rangle = |0\rangle \otimes (|+\rangle + |0\rangle) \quad (3.3)$$

This quantum state essentially does not acquire any phase because of the weak nuclear magnetic moment. Next, a fully entangled state is prepared by applying a  $\text{C}_n\text{Pi}_e$ - gate.

$$|\Psi_0\rangle = |0+\rangle + |-0\rangle \quad (3.4)$$

During a free evolution time  $\tau$ , a phase  $\phi_1$  is accumulated leading to  $|0+\rangle + e^{i\phi_1} |10\rangle$  with  $\phi_1 = -\tilde{\gamma}_e B_{0,z}\tau$ . The subsequently applied  $\text{C}_n\text{Pi}_e$ - gate disentangles the sensor and memory spins.

$$|\Psi_1\rangle = |-\rangle \otimes (|+\rangle + e^{i\phi_1} |0\rangle) \quad (3.5)$$

Now, the accumulated phase is stored in the memory, while no phase information remains on the sensing qubit. Note that the first and second  $C_n\text{Pi}_e$ -gates are controlled by the  $|+\rangle$ - and  $|0\rangle$ -state, respectively. Therefore, the electron spin state is  $|m_s = -1\rangle$  after the second gate. This fact becomes particularly important in section 3.2.

During the following correlation time  $T_c$ , changes in external parameters like magnetic field do not change the stored phase. Any detuning  $\Delta\omega$  of the RF field used for nuclear spin driving versus the memory spin energy splitting leads to an additional phase against which the sequence is not robust.

$$|\Psi_2\rangle = |-\rangle \otimes \left( |+\rangle + e^{i(\phi_1 + \Delta\omega T_c)} |0\rangle \right) \quad (3.6)$$

If  $\Delta\omega$  is known, it can be compensated for. The classical memory does not store coherences during  $T_c$  and thus the detuning  $\Delta\omega$  remains without effect.

After the correlation time  $T_c$ , the pair of  $C_n\text{Pi}_e$ -gates is repeated and the system is found in state

$$|\Psi_f\rangle = |0\rangle \otimes \left( |+\rangle + e^{i(\Delta\phi + \Delta\omega T_c)} |0\rangle \right). \quad (3.7)$$

with  $\Delta\phi = \phi_1 - \phi_2$ . The particular order of  $|+\rangle$  - and  $|0\rangle$  - controlled  $C_n\text{Pi}_e$ -gates ultimately refocuses any quasi static magnetic fields. Any change in local magnetic field during  $T_c$ , however, leads to a phase difference  $\Delta\phi$  in the second  $\tau$  period, which remains on the memory qubit and constitutes the metrology information.

**Full signal visibility** The final SSR readout yields the probability  $S_{\text{enh}}$  to find the nuclear spin memory in spin state  $|m_N = 0\rangle \equiv |1\rangle$  [18, 182],

$$S_{\text{enh}} = \frac{1 + c}{2} - A \frac{\cos(\Delta\omega T_c + \Delta\phi - \varphi)}{2} \quad (3.8)$$

with the phase  $\varphi$  of the final nuclear  $\pi/2$  - pulse.

The oscillation amplitude is a factor two larger compared to the case of a classical memory (cf. equation 3.2) directly leading to a two-fold increased sensitivity. The nuclear spin memory here is chosen to be the  $^{14}\text{N}$  nuclear spin due to its large hyperfine component of  $A_{zz} = -2.16$  MHz which allows for fast entangling and disentangling operations. In principle any strongly coupled nuclear spin such as  $^{13}\text{C}_1$  and  $^{13}\text{C}_2$  are valid choices of memories. Here, the gate duration is  $2\ \mu\text{s}$ , which renders the enhanced sequence in total  $8\ \mu\text{s}$  longer than the conventional sequence Seq3.4 [170–172]. Compared to a total sequence duration of more than 5 ms (due to the readout), this additional time is negligible and thus the two-fold increase in sensitivity comes at practically no cost.

### 3.1.3 Performance comparison of quantum and classical memory

As a figure of merit for the comparison of conventional and quantum enhanced correlation sequence, the phase information stored on the memory is measured. According to

### 3.1 Measurement protocol with and without quantum memory

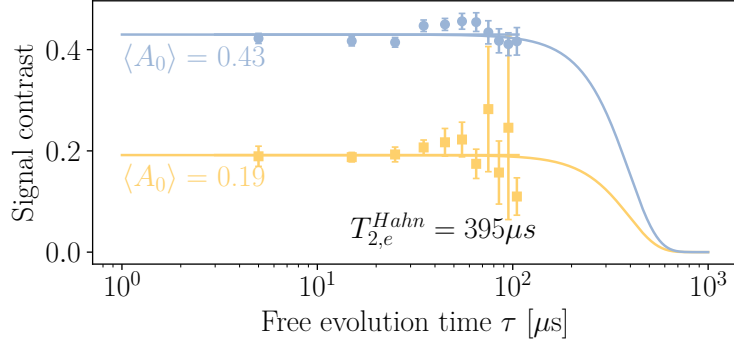


**Fig. 3.3: Amount of stored information for conventional and enhanced method.** The initial signal contrast  $A_0$  (amplitude for  $T_c = 0$ ) taken from fits to figures 3.2a, b on page 79 is plotted for increasing sensing time  $\tau$  for enhanced and conventional measurement sequence. The two solid lines represent Hahn-echo decay curves with  $T_{2e} = 395 \mu\text{s}$ ,  $p = 3$  and amplitude  $\langle A_0 \rangle$  as the weighted average of the data points (cf. figure 1.16b). Error bars give standard errors taken from the used least square fit.

equations 3.2 and 3.8, this quantity can be expressed by the signal contrasts  $A_{\text{enh}}$  and  $A_{\text{conv}}$  where the signal is the probability to find the memory qubit in state  $|0\rangle$ . Figures 3.2a and b show the memory signals for enhanced and conventional sequences, respectively. The stored phase  $\Delta\phi$  is visualized on the memory qubit by increasing the phase  $\varphi$  of the final memory  $\pi/2$  - pulse according to

$$\Delta\phi = \varphi = \Delta f T_c \quad (3.9)$$

with  $\Delta f = 1 \text{ kHz}$  and  $0.5 \text{ kHz}$  for enhanced and conventional measurement, respectively. The resulting oscillating signals have contrasts  $A_{\text{enh}}$  and  $A_{\text{conv}}$  which decays with time constants  $T_T$ , when the correlation times  $T_c$  is increased. This decay has multiple origins:

- The electron spin is in the eigenstate  $|m_s = -1\rangle$  during  $T_c$  which is subject to longitudinal relaxation ( $T_{1,e} = 5.7 \text{ ms}$ ).
- The nuclear spin memory is in a superposition state during  $T_c$  which is subject to decoherence ( $T_{2n} = 8.5 \text{ ms}$ ).
- The electron spin is in a superposition state during  $\tau$  and thus there is subject to decoherence. For larger correlation times, the magnetic environment has more time to change and thus can not be decoupled from.

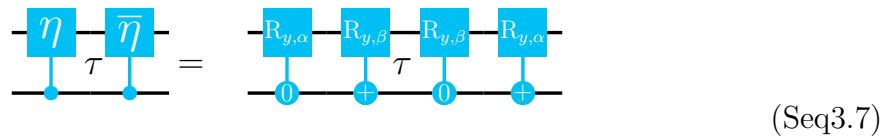
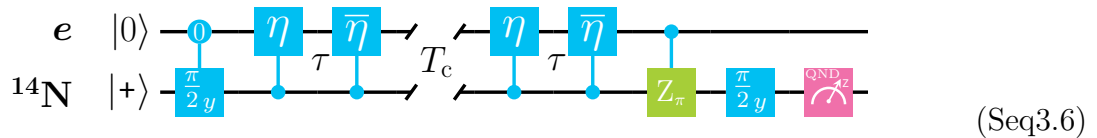
Longitudinal relaxation on the electron spin as well as decoherence on the memory spin are both intrinsic effects of the NV center (cf. section 1.7). Only during the sensing times  $\tau$ , the coupled sensor-memory system is sensitive to the magnetic environment and

decay can be induced by external noise sources. From figure 3.2a,b the amount of phase information  $A_0$  for zero correlation time  $T_c$  but varying sensing time  $\tau$  can be extracted. It is shown in figure 3.3. With increasing  $\tau$  the sensor spin decoheres on timescales of  $T_{2,e}^{\text{Hahn}} = 395 \mu\text{s}$  to good approximation due to the long  $T_{1,e}$  and  $T_{2n}$  times. The decay constant is the same for conventional and quantum enhanced sequence. The decay is that of a Hahn-echo experiment, which has an exponent  $p = 3$ , characteristic for a slowly fluctuating spin bath [130, 184]. Therefore, the initial signal contrast  $A_0$  is almost constant for  $\tau = 5 \mu\text{s}$  to  $105 \mu\text{s}$  (figure 3.3) but twice as large with quantum memory compared to the classical memory. Please note, that for times  $T_c \ll T_{2,n}^{\text{Hahn}}$ , the electron spin memory here referred to as ‘‘classical memory’’ in fact is a fully featured quantum memory, too. Therefore, the factor two in the initial signal contrast only emerges for larger  $T_c$ , when the residual coherence is gone. The experimental data presented in figure 3.2b, shows sine oscillations with a period of 2 ms and no phase offset, which allows to effectively neglect this residual coherence.

Summarizing, entangling the sensor and the memory qubit does not deteriorate the relaxation times intrinsic to the sensor qubit and yields the benefit of a doubled signal. Both classical as well as quantum mechanical memory increase the frequency resolution by a factor of  $T_{1,e}/T_{2,e}^{\text{Hahn}} \approx 15$ .

### 3.1.4 Transition between classical and quantum memory

Classical and quantum enhanced sequences Seq3.4 and Seq3.5 can be combined into the unified sequence Seq3.6, which allows for a continuous transition between the two cases corresponding to a fully classical and fully quantum memory via the parameter  $\eta$ . With increasing  $\eta$ , the degree of entanglement is increased and thereby more phase information previously stored on the classical electron memory is stored on the nuclear spin quantum memory.



Hereby the rotation angles  $\alpha$  and  $\beta$  are connected to the entanglement parameter  $\eta$  by

$$\alpha = \frac{\pi}{2} (1 + \eta) \quad \beta = \frac{\pi}{2} (1 - \eta) \quad (3.10)$$

### 3.1 Measurement protocol with and without quantum memory

with  $0 \leq \eta \leq 1$ .

For the creation of variable entanglement between sensor and memory, first the state  $|\Psi_i\rangle = |0\rangle \otimes (|+\rangle + |0\rangle)$  is generated. Therefore a  $\pi/2$  - pulse is performed on the memory spin to create an equal superposition state; this part is not entangling, as the sensor qubit is in an eigenstate. Then, for memory state  $|0\rangle$  the sensor qubit is rotated around the  $y$ -axis by an angle  $\alpha$ , and for  $|+\rangle$  by an angle  $\beta$ . The latter part is dependent on the memory state and creates entanglement for  $\eta \neq 0$ . The  $\bar{\eta}$ -gate is designed such that for no phase accumulation during  $\tau$  the sensor state is finally  $|0\rangle$  regardless of the memory state. After the second phase accumulation step, the information stored on the classical electron spin memory needs to be added to that already stored on the nuclear spin quantum memory. This is achieved with a controlled phase-flip gate, which adds a phase of  $\pi$  to the nuclear spin memory, if the electron spin memory is in state  $|-\rangle$ . The negativity  $\mathcal{N}$  of the entangled state is an entanglement measure that ranges from  $\mathcal{N} = 0$  for no entanglement (equivalent to sequence Seq3.4) to  $\mathcal{N} = 0.5$  for an electron spin - nuclear memory spin Bell state (equivalent to sequence Seq3.5)[185, 186].

For the initial state  $|\Psi_i\rangle$ , the value of  $\mathcal{N}$  can be calculated in dependence of  $\eta$  as

$$\mathcal{N} = \frac{\sin\left(\eta\frac{\pi}{2}\right)}{2} \quad (3.11)$$

The amount of stored information (i.e. the expected signal contrast) can be calculated in dependence of  $\eta$ . Therefore, for each degree of entanglement  $\mathcal{N}$ , the initial state  $|\Psi_i\rangle\langle\Psi_i|$  is propagated through the entire sequence Seq3.6. During the correlation time  $T_c$  complete sensor spin decoherence is emulated by deleting all coherences between different electron spin projections in the total density matrix  $\rho$ . As a result, the probability  $P$  to find the  $^{14}\text{N}$  memory spin in spin state  $|+\rangle$  is obtained.

$$\begin{aligned} P(\Delta\phi) &= \frac{1 + \cos^2(\eta \cdot \pi/2)}{2} \frac{\cos \Delta\phi}{2} \\ &= f(\mathcal{N}) \cdot \frac{\cos \Delta\phi}{2} \end{aligned} \quad (3.12)$$

$$f(\mathcal{N}) = \left(\frac{1}{2} + 2\mathcal{N}^2\right) \quad (3.13)$$

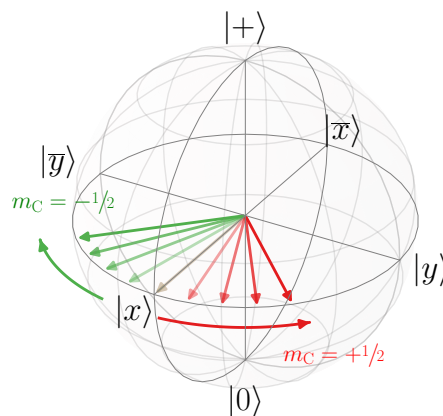
The function value of equation 3.12 oscillates with  $\Delta\phi$ . The prefactor in equation 3.12 can be expressed with the negativity  $\mathcal{N}$  by substituting  $\eta$  using equation 3.11 leading to equation 3.13.

Experimentally, the stored phase  $\Delta\phi$  again is visualized by increasing the phase  $\varphi$  of the final memory spin  $\pi/2$  - pulse. The sensing time  $\tau$  is chosen to be  $5\ \mu\text{s}$ . In the limit of maximal and no entanglement, the measurement results are presented as the most

bottom curve in figures 3.2a,b, showing a contrast of  $A_0 = 0.19$  and  $A_0 = 0.43$ . These measurements were here repeated with highly optimized pulses resulting in  $A_0 = 0.25$  and  $A_0 = 0.49$ . Figure 3.2d shows the signal contrast in dependence of  $\mathcal{N}$ . The quadratic dependence predicted by theory is found in the experiment and the fit to equation 3.13 is in good agreement with the data.

## 3.2 Applications of the quantum enhanced correlation spectroscopy sequence to carbon nuclear spins

**Fig. 3.4: Memory spin phase for two different sample spin orientations.** Sign and magnitude of the acquired phase  $\phi$  depend on the orientation and gyromagnetic ratio of the target nuclear spin. Red (green) refers to positive (negative) phase accumulation on the memory spin due to the sample spin being in state  $|+\rangle$  ( $|-\rangle$ ).



In this section, the quantum enhanced correlation sequence is used to interact with individual weakly coupled nuclear spins.  $^{13}\text{C}$  nuclear spins can be initialized, coherently controlled and read out. Therefore, they can serve as well characterized sample quantum systems and deterministic sources of magnetic fields. In addition,  $^{13}\text{C}$  spins have very long  $T_1$  relaxation times and therefore the corresponding magnetic field at the sensor position shows a particularly long correlation time with a time constant beyond seconds. Their eigenstates are  $|+\rangle, |-\rangle$  with associated quantum number  $m_C = +1/2, -1/2$  (cf. section 1.4.3 on page 23). After the first memory  $\pi/2$  - pulse in sequence Seq3.5, the memory spin state is  $|x\rangle = |+\rangle + |0\rangle$  (cf. equation 3.3). During the first sensing time  $\tau$  in sequence Seq3.5, the  $^{14}\text{N}$  nuclear spin acquires a phase

$$\phi_1 = 2\pi m_C A_{zz} \tau \quad (3.14)$$

whose sign depends on the  $^{13}\text{C}$  nuclear spin quantum number  $m_C$  (cf. figure 3.4). Without any further experimental effort, the phases  $\phi_1$  and  $\phi_2$  accumulated during the first and the second sensing time are equal, leading to a net phase  $\Delta\phi = 0$ . Therefore, the nuclear spin needs to be manipulated during  $T_c$ , or it will not have any effect on the hybrid quantum sensor. This principle is illustrated in figure 3.5 for the example of a magnetic field produced by either a nuclear spin or a classical oscillating magnetic field source.

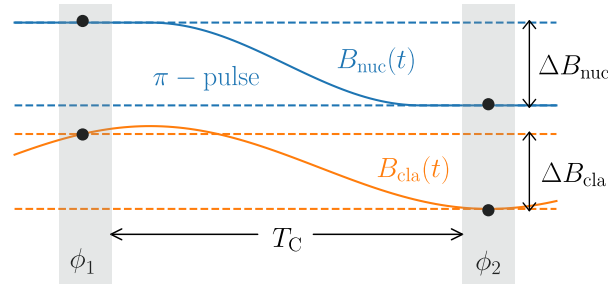
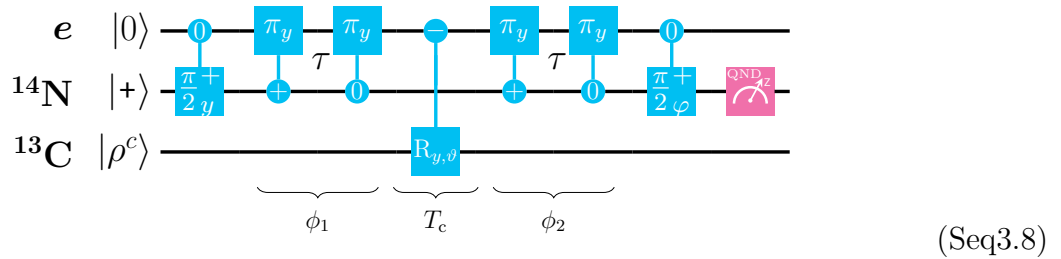


**Fig. 3.5: Phase information acquired due to time dependent magnetic fields.** The magnetic field  $B(t)$  evolves during  $T_C$ , which leads to different sensing phases  $\phi_1$  and  $\phi_2$  acquired during the first and the second phase accumulation time. The actual sensing information is the phase difference  $\Delta\phi = \gamma_e \Delta B \tau$ .  $B_{\text{nuc}}$  is generated by a long-lived nuclear spin, which is deterministically flipped by a  $\pi$ -pulse during  $T_C$ .  $B_{\text{cla}}$  is generated by a classical oscillating magnetic field source.

**Switching the field orientation** In the simplest case, nuclear spin manipulation is performed with a rectangular RF pulse of frequency  $\nu$  resonant to the nuclear spin transition, which flips the  $^{13}\text{C}$  by an angle  $\vartheta$  [187] (cf. section 1.6). Therefore, the quantum correlation sequence Seq3.5 is extended by a nuclear spin rotation  $R_{y,\vartheta}$  to become sequence Seq3.8.



During the nuclear spin rotation, the electron spin is in state  $|-\rangle$  and a  $^{13}\text{C}$  nuclear spin with hyperfine coupling constant  $A_{zz}$  has then the transition frequency

$$f_C = f_{\text{Larmor}} - A_{zz} \quad (3.15)$$

according to section 1.6.4. This relation makes  $A_{zz}$  frequency selective  $^{13}\text{C}$  manipulation possible. For  $\vartheta = 0$ , the sample spin state is not altered during  $T_C$  and memory and sample spin are uncorrelated after the second sensing time. For  $\vartheta = \pi$ , however,  $^{13}\text{C}$  nuclear spin state  $|+\rangle$  is changed to  $|-\rangle$  and vice versa. The phase on the  $^{14}\text{N}$  memory spin after the total phase accumulation time  $2\tau$  is

$$\Delta\phi = 4\pi m_C A_{zz} \tau \quad (3.16)$$

when the  $^{13}\text{C}$  is in the eigenstate with quantum number  $m_C$  before the sequence. After the second sensing step but before the final  $\pi/2$ -rotation in sequence Seq3.5, the memory

spin is found in state

$$\rho_{+/-}^N = \frac{1}{2} \begin{bmatrix} 1 & \cos\left(\frac{\vartheta}{2}\right)^2 + e^{-i\Delta\phi} \sin\left(\frac{\vartheta}{2}\right)^2 \\ \cos\left(\frac{\vartheta}{2}\right)^2 + e^{i\Delta\phi} \sin\left(\frac{\vartheta}{2}\right)^2 & 1 \end{bmatrix} \quad (3.17)$$

for a pure initial sample spin state (i.e. either  $|+\rangle$  or  $|-\rangle$ ) and

$$\rho_{\text{mix}}^N = \frac{1}{2} \begin{bmatrix} 1 & \cos\left(\frac{\vartheta}{2}\right)^2 + \cos(\Delta\phi) \sin\left(\frac{\vartheta}{2}\right)^2 \\ \cos\left(\frac{\vartheta}{2}\right)^2 + \cos(\Delta\phi) \sin\left(\frac{\vartheta}{2}\right)^2 & 1 \end{bmatrix} \quad (3.18)$$

for the sample spin initially being in a fully mixed state, i.e. an equal statistical superposition of  $|+\rangle$  and  $|-\rangle$ .

**Reading in-phase and quadrature component of the sensing phase  $\phi$**  Figure 3.4 on page 86 shows a representation of the memory spin state for the quantum correlation sequence Seq3.5 before the second  $\pi/2$  - pulse. For  $\vartheta = \pi$ , the memory spin state given by equation 3.17 can be written as the pure state

$$|\psi_m\rangle = \cos(\Delta\phi) |x\rangle + \sin(\Delta\phi) |y\rangle \quad (3.19)$$

with the equatorial basis states  $|x\rangle$ ,  $|y\rangle$  given in figure 3.4. The phase  $\varphi$  of the second  $\pi/2$  - pulse in sequence Seq3.5 allows to choose the component of  $|\psi_m\rangle$  which should be read out. These components are shown in table 3.1. The components  $\cos(\Delta\phi)$  and

angle $\varphi$	0	$+\pi/2$	$\pi$	$-\pi/2$
phase component of $\Delta\phi$	$\cos(\Delta\phi)$	$\sin(\Delta\phi)$	$-\cos(\Delta\phi)$	$-\sin(\Delta\phi)$
projected basis state	$ x\rangle$	$ y\rangle$	$ \bar{x}\rangle$	$ \bar{y}\rangle$

**Table 3.1: Read out memory phase components for different values of  $\varphi$**  The angle  $\varphi$  of the final  $\pi/2$  - pulse determines the phase component of the sensing phase  $\Delta\phi$  which is transferred to the readout basis.

$\sin(\Delta\phi)$  are commonly referred to as the in-phase and the quadrature component of  $\Delta\phi$ . Since  $\cos(\Delta\phi)$  is symmetrical in the sign of  $\Delta\phi$ , for  $\varphi = 0$  or  $\varphi = \pi$  no statement about the sign of  $\Delta\phi$  can be made. For  $\varphi = \pm\pi/2$ , the opposite is true. The phase information though is not always needed and can even invalidate the signal, namely when the sample spin is unpolarized. Then, the two sample spin states  $|+\rangle$  and  $|-\rangle$  appear with equal probability, and thus the memory qubit signal averages to zero. In the same case, however, the in-phase component gives full information about the unpolarized sample spin. As a consequence, the in-phase component is used for spin detection and the quadrature component is used for detection of spin or signal field orientation.

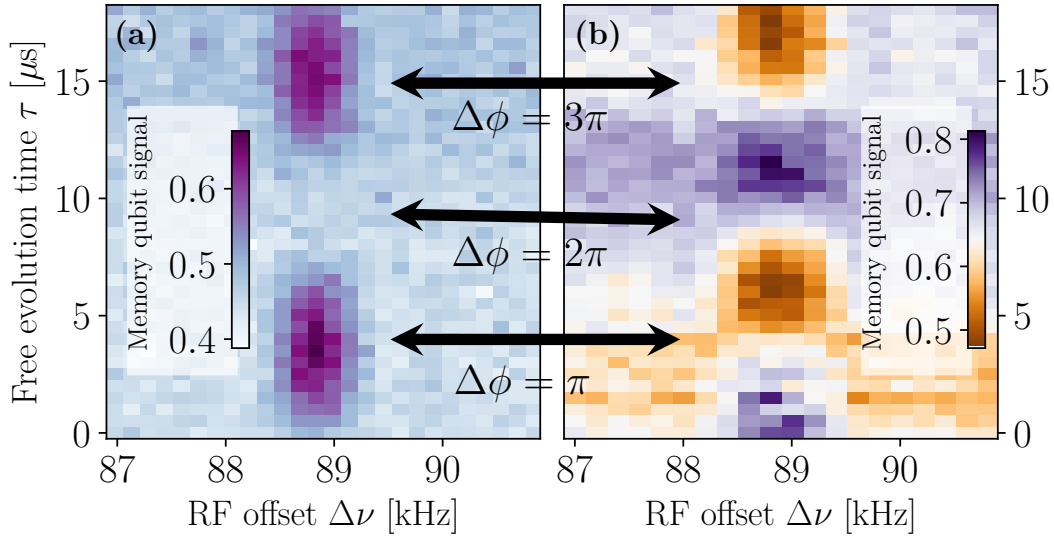


**Fig. 3.6: Memory qubit signal for different detunings  $\Delta\nu$  and sensing times  $\tau$ .** Shown is the color coded probability of detecting  $^{14}\text{N}$  memory qubit state  $|-\rangle$  after performing the quantum enhanced correlation sequence Seq3.5 with (a)  $\varphi = 0$  and (b)  $\varphi = \pi/2$ . During  $T_c = 1$  ms, a RF pulse was performed, which is equivalent to a  $\pi$ -pulse on  $^{13}\text{C}_2$  with  $A_{zz} \approx 89$  kHz when  $A_{zz} = \Delta\nu$ . Then,  $\Delta\phi = -2\pi A_{zz}(\tau + \tau_0)$  ( $\tau_0 \approx 2$   $\mu\text{s}$ , see main text and appendix D). (a) and (b) show  $\cos \Delta\phi$  and  $\sin \Delta\phi$ , respectively due to the choice of  $\varphi$ . The non-zero contrast in (b) is achieved only by initializing the sample spin  $^{13}\text{C}_2$  to  $|-\rangle$  before running the sequence.

### 3.2.1 Quantum correlations between memory qubit and sample spin

To demonstrate enhanced sensing by the quantum memory, sequence Seq3.5 is used to establish quantum correlations between the strongly coupled  $^{14}\text{N}$  nuclear spin and a  $^{13}\text{C}$  nuclear spin. For full entanglement, flip-angle and acquired sensing phase need to be  $\vartheta = \pi$  and  $\Delta\phi = \pm\frac{\pi}{2}$ , respectively. According to equation 3.17, depending on the initial sample spin state being  $|+\rangle$  or  $|-\rangle$ , the memory spin is then found in spin state  $|x\rangle$  or  $|\bar{x}\rangle$ , respectively (cf. figure 3.4). Therefore, this operation represents a non-local nuclear spin-nuclear spin gate, which is capable of generating a fully entangled state. Since nuclear spin readout is performed in the  $|+\rangle, |-\rangle$ -basis, the final  $\pi/2$ -rotation needs to be performed around the  $\bar{x}$ - instead of the  $y$ -axis to transfer states  $|y\rangle$  and  $|\bar{y}\rangle$  to states  $|0\rangle$  and  $|+\rangle$ , respectively (cf. sequence Seq3.5). This is achieved for  $\varphi = \pi/2$ . Analogously, for  $\varphi = 0$ , states  $|x\rangle$  and  $|\bar{x}\rangle$  are transferred to states  $|0\rangle$  and  $|+\rangle$ , respectively.

**Sweeping  $\Delta\phi$  by sweeping  $\tau$**  Here, the easy to control and easy to read out nuclear spin  $^{13}\text{C}_2$  with  $A_{zz} = 89$  kHz was initialized in spin state  $|-\rangle$ . The sensing time  $\tau$  is swept from 0  $\mu\text{s}$  to 18  $\mu\text{s}$  and the detuning  $\Delta\nu$  of the RF field is swept around the hyperfine

coupling  $A_{zz} \approx 89$  kHz. For  $\Delta\nu = A_{zz}$ , a  $\pi$  - pulse is performed on the target nuclear spin, the addressed transition thereby is  $T[^{13}\text{C}(A_{zz}=89\text{ kHz}), -1]$  (cf. section 1.6.4). The phase  $\varphi$  of the RF field is set to  $\varphi = 0$  (figure 3.6a) and  $\varphi = \pi/2$  (figure 3.6b) to measure  $\cos(\Delta\phi)$  and  $\sin(\Delta\phi)$  of the memory's phase  $\Delta\phi(\tau)$  (cf. equation 3.8). It is particularly important to note, that  $\Delta\phi = 0$  does not correspond to  $\tau = 0$ . Instead, equation 3.16 needs to be corrected for the finite  $C_n\text{Pi}_e$ - gate duration, which adds an offset  $\tau_0 \approx 2\ \mu\text{s}$  leading to

$$\Delta\phi = 4\pi m_C A_{zz} \underbrace{(\tau + \tau_0)}_{\tau_{\text{eff}}} \quad (3.20)$$

For further details on the implementation of the  $C_n\text{Pi}_e$ -gates, their robustness and the effective sensing time  $\tau_{\text{eff}}$ , see appendix D. The signal oscillates for increasing  $\tau$  when the radio-frequency is in resonance. In the  $\cos(\Delta\phi)$  case no distinction can be made between initial  $^{13}\text{C}$  sample spin state  $|+\rangle$  and  $|-\rangle$ , as the signal is independent of the sign of  $\Delta\phi$ . In the  $\sin(\Delta\phi)$  case, however, the initial sample spin state can be determined. While a signal sign-independent scheme is convenient for the detection of nuclear spins (cf. section 3.2.2), the signal sign-dependent scheme allows for the determination of magnetic field orientation. When the field is produced by a sample spin (or any quantum system), setting  $\varphi = \pi/2$  allows for entanglement between memory spin and that sample spin. If the sample spin in figure 3.6b would not be initialized in  $|-\rangle$  but e.g. in the superposition state  $|+\rangle + |-\rangle$ , memory and sample spin would end up in a maximally entangled state for  $\Delta\nu \approx 89$  kHz and  $\tau = 4.8\ \mu\text{s}$ . Then, the memory spin - sample spin system would be in spin state

$$\psi_{\text{ent}} = |0-\rangle + |++\rangle \quad (3.21)$$

after sequence Seq3.5. Note that the spectral window of coherent interaction in figures 3.6a and 3.6b has a width of approximately 1 kHz. This is compatible with the RF  $\pi$  - pulse duration of 1 ms which is much longer than the sensor's coherence time  $T_{2,\text{sensor}}$ .

**Sweeping the sample spin flip angle  $\vartheta$**  Here the quantum enhanced correlation sequence Seq3.5 is used to measure Rabi oscillations of the sample spin  $^{13}\text{C}_2$  by variable amplitude RF driving during the correlation time  $T_c = 1$  ms. The sample spin is initialized to  $|-\rangle$  before the sequence and the RF driving field is set to resonance ( $\Delta\nu \approx 89$  kHz). According to equation 3.17, the acquired phase  $\Delta\phi$  on the memory spin not only depends on the sensing time  $\tau$ , but also on the flip-angle  $\vartheta$  of the sample spin. Therefore, the RF driving amplitude is increased, and the  $^{14}\text{N}$  memory qubit signal is measured. Figures 3.7a and b show the in-phase and quadrature components of  $\Delta\phi$ , respectively. Figure 3.7a (b) show the cases of  $\varphi = 0$  ( $\varphi = \pm\pi/2$ ) and  $\tau_{\text{eff}} = 1/2A_{zz} \approx 5.5\ \mu\text{s}$  ( $\tau_{\text{eff}} = 1/4A_{zz} \approx 2.8\ \mu\text{s}$ ). The corresponding effective sensing times  $\tau$  have been extracted

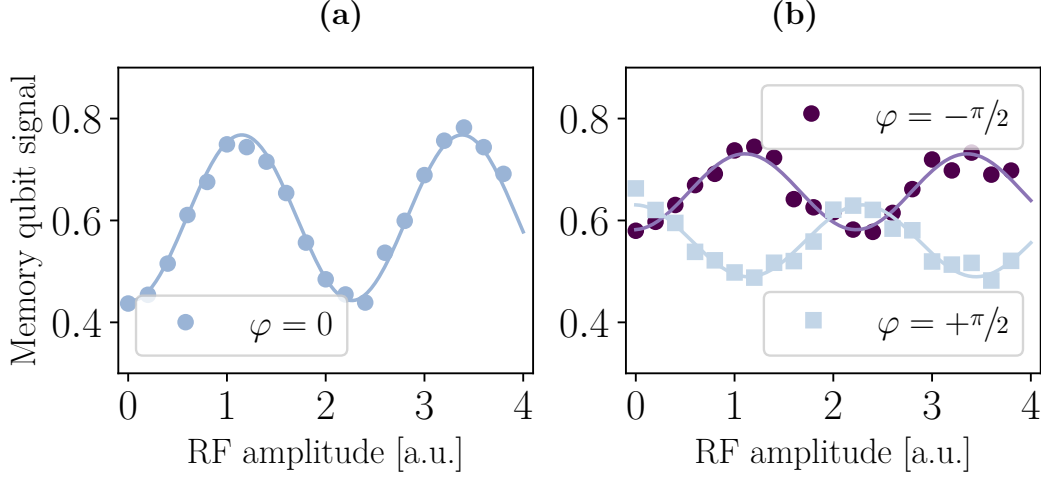


**Fig. 3.7: Effect of nuclear Rabi oscillations performed during  $T_c$  on in-phase and quadrature components of sensing phase  $\Delta\phi$ .** The sample spin flip angle  $\vartheta$  is proportional to the RF amplitude. For (a) and (b), the in-phase ( $\varphi = 0$ ) and quadrature components ( $\varphi = \pm\pi/2$ ) are transferred to the memory spin readout basis. The effective sensing time is (a)  $\tau_{\text{eff}} = 1/2A_{zz} \approx 5.5 \mu\text{s}$  and (b)  $\tau_{\text{eff}} = 1/4A_{zz} \approx 2.8 \mu\text{s}$ .

from figure 3.6a (b) for the phases  $\Delta\phi = \pi$  ( $\Delta\phi = \pi/2$ ). Here, again for  $\varphi = 0$ , the memory signal oscillates as  $\cos(\Delta\phi)$ , while for  $\varphi = \pm\pi/2$  it oscillates as  $\pm\sin(\Delta\phi)$ . Interestingly, for  $\varphi = 0$  and RF amplitude around 0.5 ( $\vartheta = \pi/2$ ) the memory spin and the sample spin are entangled, again resulting in

$$\psi_{\text{ent}} = |0-\rangle + |++\rangle \quad (3.22)$$

Thus both variation in  $\tau$  and  $\vartheta$  can lead to memory-nuclear spin entanglement. Therefore, the novel sensing sequence Seq3.5 can establish coherent interactions among memory and sample spins with high spectral selectivity on the sample spins frequency.

### 3.2.2 Enhanced high resolution correlation spectroscopy

Here, the measurement sequence Seq3.5 is used for the detection of weakly coupled  $^{13}\text{C}$  spins. Therefore, parameters  $\vartheta = \pi$  and  $\varphi = 0$  are chosen. The exact value of  $\tau$  is not decisive, however nuclear spins with  $A_{zz} = n/\tau$  will result in  $\Delta\phi = n \cdot 2\pi$  with  $n \in \mathbb{N}$  and thus can not be detected. Here, the sensing time is adjusted to the expected hyperfine coupling  $A_{zz} = \Delta\nu$  according to  $\tau \approx (2A_{zz})^{-1}$  to  $\tau = 40 \mu\text{s}$ . The RF frequency offset  $\Delta\nu$  is swept around the bare  $^{13}\text{C}$  Larmor frequency  $f_L$ .

For a coarse spectrum a correlation time of  $T_c = 500 \mu\text{s}$  is chosen. The resulting spectrum in figure 3.8a at  $\Delta\nu = 89 \text{ kHz}$  reveals the already known  $^{13}\text{C}_2$ . Additional nuclear spins are found around  $\Delta\nu = 0$ , which are barely resolvable. A higher spectral

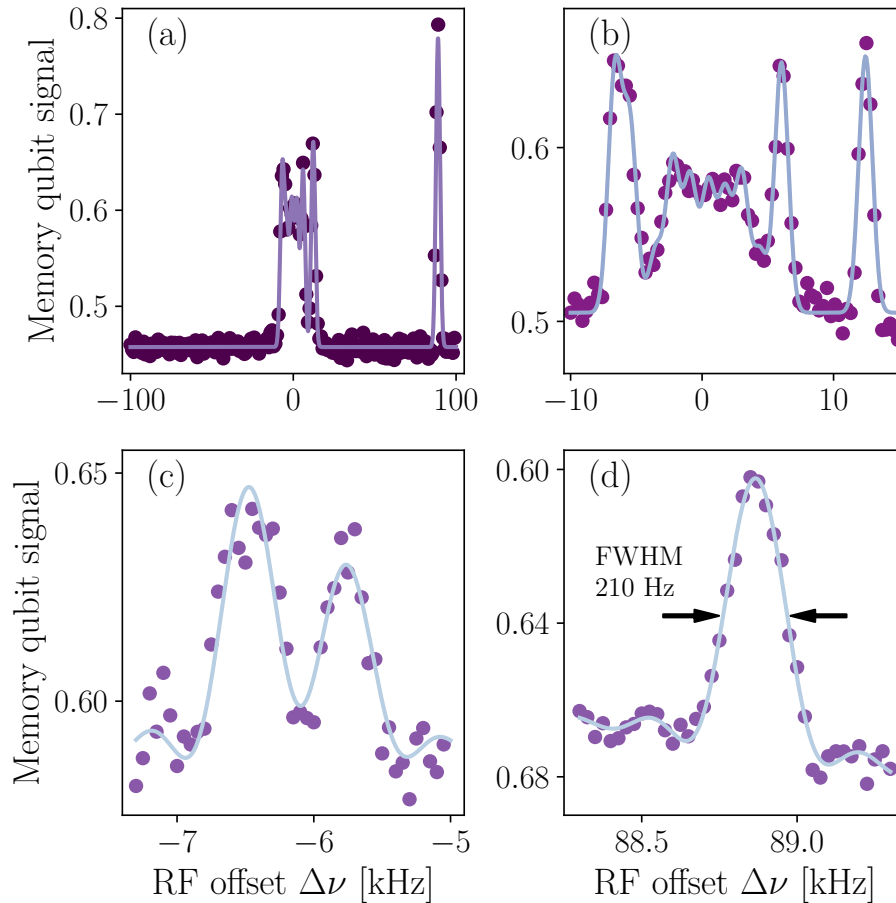


**Fig. 3.8: Resolving nuclear spins at the strong coupling limit.** (a–d), Enhanced Mims ENDOR spectra of hyperfine-coupled  $^{13}\text{C}$  spins. During the entire correlation period  $T_c$  the RF pulse is switched on. The duration of the correlation time  $T_c$  is set to 0.5 ms (a), 1 ms (b), 2 ms (c) and 4.3 ms (d). The amplitudes of the  $^{13}\text{C}$  RF pulses during  $T_c$  had gaussian (a,b) or rectangular (c,d) envelope functions, thus peaks were fit with Gaussian or sinc- functions, respectively. Spectral resolution increases with  $T_c$ . For the unresolved resonances found at  $-4\text{kHz}$  to  $4\text{kHz}$  an empirically determined number of peaks is fit. (d) The best frequency resolution of 210 Hz was achieved for  $T_c = 4.3\text{ms}$ .

resolution is obtained in figure 3.8b where  $T_c$  is set to 1 ms. When  $T_c$  is set to 2 ms two formerly unresolved  $^{13}\text{C}$  spins around  $-6$  kHz coupling are now distinguishable (figure 3.8c). The best spectral resolution of 210 Hz (full width half maximum (FWHM)) is obtained for a correlation time of 4.3 ms (cf. figure 3.8d).

### 3.3 Fixed sensing scheme for the detection of variable fields at high resolution

The resolution of the spectra in figure 3.8 is inversely proportional to  $T_c$ . Here, a different scheme is presented, which also relies on the correlation sequence Seq3.5, but whose frequency resolution is exclusively determined by the resolution with which a target field can be prepared. All parameters of sequence Seq3.5 therefore are fixed and the target field is altered, which is a more favorable setup for a sensor device. This target field here again is produced by  $^{13}\text{C}$  nuclear spins with hyperfine couplings  $A_{zz}^{(i)}$ . They need to be polarized into spin state  $|+\rangle$  or  $|-\rangle$ , with quantum numbers  $m_C \in \pm 1/2$ . This polarization here is performed with the pulsed polarization technique introduced in section 2.4. The field of the  $^{13}\text{C}$  is additive and the electron spin transition  $|0\rangle \leftrightarrow |-\rangle$  experiences a total shift

$$f_{\text{Ctot}} = \sum_i m_{C_i} A_{zz}^{(i)} \quad (3.23)$$

For strongly coupled nuclear spins, the same effect can be observed in the ODMR spectrum shown in figure 1.13 on page 32. Here, however, the interest lies in the detection of weakly coupled nuclear spins and it is their combined hyperfine field  $f_{\text{Ctot}}$ , which shall be measured. The maximum electron frequency shift is

$$f_{\text{Ctot,max}} = \sum_i |A_{zz}^{(i)} / 2| \quad (3.24)$$

for which there is one particular set of  $m_{C_i}$ . An upper bound for  $f_{\text{Ctot,max}}$  is set by the inhomogeneous broadening of the electron spin, for which the major source is known to be the  $^{13}\text{C}$  bath [188]. From the electron coherence time  $T_{2,e}^*$ , one expects  $f_{\text{Ctot,max}} \approx 30$  kHz.

For the detection of  $f_{\text{Ctot}}$ , in this section again sequence Seq3.5 is used with  $\varphi = \pi/2$  as angle of the second memory spin  $\pi/2$  - pulse. Therefore, the memory signal is

$$S \propto \sin(2\pi f_{\text{Ctot,max}} \tau) \quad (3.25)$$

analogous to equation 3.16.

**Setting the field  $f_{\text{Ctot}}$**  The selectivity of the  $^{13}\text{C}$  detection here is given by the frequency resolution with which the frequency superposition  $f_{\text{Ctot}}$  (i.e.  $\{m_{C_i}\}$ ) can be set. With

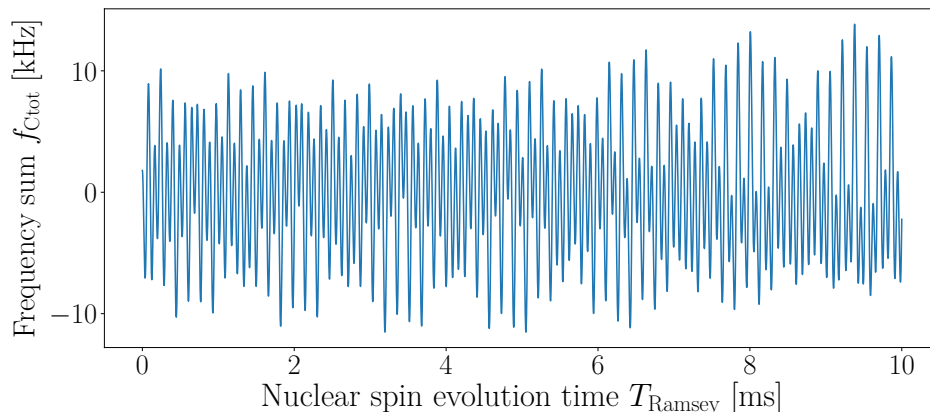


**Fig. 3.9: Superposition field produced by multiple carbon nuclear spins during a nuclear Ramsey experiment.** As initial value of this simulation, all  $^{13}\text{C}$  nuclear spins are in spin state  $|+\rangle$  and produce a field of 1.9 kHz due to the superposition of their hyperfine couplings  $A_{zz}^{(i)} \in \{-5.9 \text{ kHz}, -6.5 \text{ kHz}, -2.2 \text{ kHz}, 5.9 \text{ kHz}, 12.4 \text{ kHz}\}$ . When the free evolution time  $T_R$  is increased, the effective field produced by the nuclear spins evolves up to a maximum value  $\sum_i |A_{zz}^{(i)}|/2$  (cf. sequence Seq3.9). The final  $\pi/2$ -pulse is performed around an axis  $\nu = \pi/2$ .

the Ramsey sequence Seq3.9, this frequency resolution is inversely proportional to the free evolution time  $T_R$ , which decays on timescales of  $T_{2,C}^* \approx 8.5 \text{ ms}$ .

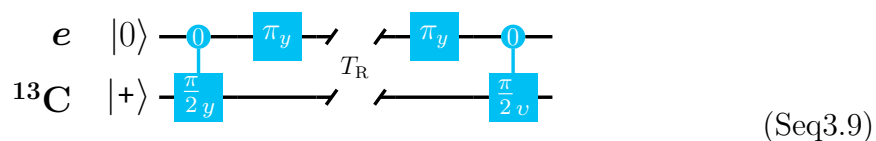


Figure 3.9 shows a simulation of sequence Seq3.9 with  $A_{zz}^{(i)} \in \{-5.9 \text{ kHz}, -6.5 \text{ kHz}, -2.2 \text{ kHz}, 5.9 \text{ kHz}, 12.4 \text{ kHz}\}$  and all five  $^{13}\text{C}$  initially polarized in  $|+\rangle$ . The initial field produced by the  $^{13}\text{C}$  is no larger than 1.9 kHz according to equation 3.23. For increasing free evolution time  $T_R$ , the effective field produced by the nuclear spins evolves according to

$$f_{\text{Ctot}} = \sum_i \frac{A_{zz}^{(i)}}{2} \cos(2\pi A_{zz}^{(i)} T_R) \quad (3.26)$$

Within the nuclear spin coherence time  $T_{2,C}^* \approx 8.5 \text{ ms}$ , the maximum field for these settings is  $f_{\text{Ctot}} \approx 10 \text{ kHz}$  due to the unfavorable values  $A_{zz}^{(i)}$ , which are very close to or multiples of each other.

**Making the correlation sequence selective to a single carbon nuclear spin** After the field  $f_{\text{Ctot}}$  has been set with sequence Seq3.9, it can be detected with the correlation sequence Seq3.5.

### 3.3 Fixed sensing scheme for the detection of variable fields at high resolution

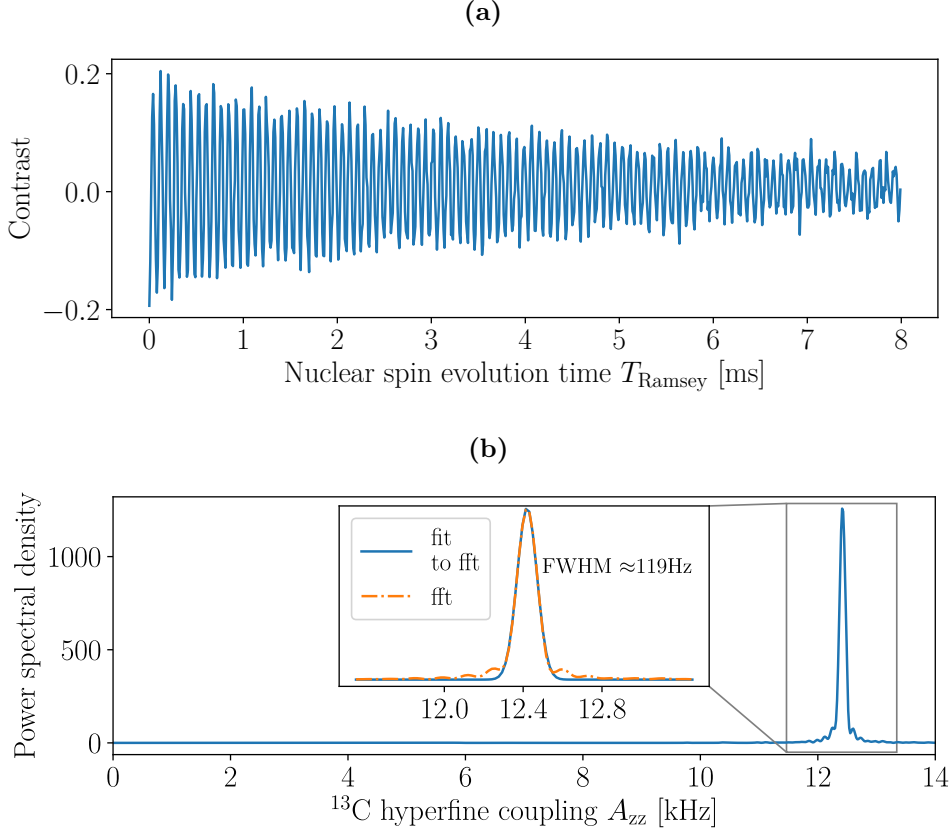


**Fig. 3.10: Time and frequency domain signals of a single carbon spin Ramsey experiment.** (a) shows Ramsey oscillations of a single  $^{13}\text{C}$  with  $A_{zz} = 12.42$  kHz, taken with sampling frequency 100 kHz. (b) A single peak appears in the Fourier spectrum with a FWHM of 119 Hz (Gaussian).

The frequency of the RF  $\pi$  - pulse during  $T_c$  allows to coarsely select ranges of hyperfine frequencies  $A_{zz}$ . As a first example,  $T_c$  is set to 500  $\mu\text{s}$ . This value of  $T_c$  allows, to selectively apply the sample spin  $\pi$  - pulse only to the hyperfine frequency 12.4 kHz with width  $\approx 2$  kHz. Nuclear spins outside that range are barely detectable. From the spectra shown in figure 3.8, the  $^{13}\text{C}$  nuclear spin found at this  $A_{zz}$  value is known to be rather isolated. Maximum sensitivity is achieved for  $\Delta\phi = \pi$  and thus for the detection of this nuclear spin  $\tau = (2A_{zz})^{-1} \approx 40$   $\mu\text{s}$ . Equations 3.25 and 3.26 together yield the expected signal

$$S(T_R) \propto \sin\left(\frac{\pi}{2} \cos(2\pi A_{zz} T_R)\right) \quad (3.27)$$

Figure 3.10a shows the resulting oscillation for  $T_R = 0$  ms to 10 ms. Although the shape of the actual signal equation 3.26 is altered by the detection function equation 3.25, the periodicity remains unaltered, which is illustrated in appendix E. The Fourier transform of the data with respect to  $T_R$  reveals the expected nuclear spin coupling

$A_{zz} = 12.420(51)$  kHz, whereby  $\sigma = 51$  Hz is the standard deviation determined from the fit. The FWHM of the peak is 122 Hz, which is very well compatible with the nuclear spin coherence time  $T_{2,C}^* \approx 8.5$  ms.

**Detecting the field produced by all carbon nuclear spins at once** To measure the field produced by all carbon spins at once, here  $T_c = 15 \mu\text{s}$  is chosen, as it is the shortest possible  $^{13}\text{C}$   $\pi$  - pulse duration. Additionally, the selectivities of the four  $\text{C}_n\text{Pi}_e$ -gates in the correlation sequence Seq3.5 were changed from memory spin states  $|+\rangle, |0\rangle, |+\rangle, |0\rangle$  to  $|0\rangle, |0\rangle, |+\rangle, |+\rangle$ , such that the electron spin is in state  $|0\rangle$  during  $T_c$ . This way, all  $^{13}\text{C}$  nuclear spins have the same frequency and can be flipped at once, when the  $\pi$  - pulse is applied at the  $^{13}\text{C}$  - Larmor frequency. Again, first the Ramsey sequence Seq3.9 is performed and afterwards the superposition of all hyperfine frequencies  $A_{zz}^{(i)}$ , namely  $f_{\text{Ctot}}$ , is measured with the quantum enhanced correlation sequence Seq3.5. This experiment allows to determine the spectrum of the  $^{13}\text{C}$  hyperfine couplings  $A_{zz}$  with very high frequency resolution. The spectrum including sign and absolute values of  $A_{zz}$  can only be determined, when both the in-phase as well as the quadrature component of the Ramsey phase after the free evolution time  $T_R$  are measured. Therefore, the Ramsey sequence Seq3.9 is performed for  $\nu = 0$  and  $\nu = \pi/2$ . The detection function here for the sake of brevity is assumed to be linear instead of the actual behaviour according to equation 3.16. Thereby, the periodicity is not altered (cf. appendix E) and the discussion is simplified. In-phase and quadrature components of

$$\Delta\phi = 2\pi\tau f_{\text{Ctot}}(T_R) \quad (3.28)$$

are shown in figure 3.11a. With the simplification of a linear detection function, the signals are  $S_i \propto \cos\phi_R$  (in-phase) and  $S_q \propto \sin\phi_R$  (quadrature). Combining the information of both measurements yields

$$\begin{aligned} S &= S_i - iS_q \\ &= \cos\Delta\phi - i\sin\Delta\phi \\ &= e^{-i\Delta\phi} \end{aligned} \quad (3.29)$$

Figure 3.11b shows the Fourier transformation of the combined measurement signals, to yield a full  $^{13}\text{C}$  spectrum in a window  $-50$  kHz to  $50$  kHz due to a sampling frequency of  $100$  kHz. The increased resolution compared to the previous measurements reveals two additional  $^{13}\text{C}$  nuclear spins with couplings  $-2.3$  kHz and  $-2.1$  kHz. Here it is important to note, that the decoupling nature of the correlation sequence Seq3.5 against the  $^{13}\text{C}$  nuclear spins is removed, as they are flipped during  $T_c$ . Thereby, in the sensing times, the signal decays on timescales of  $T_{2,e}^* \approx 30 \mu\text{s}$ . This effect could be removed, if a shaped pulse would flip all  $^{13}\text{C}$  nuclear spins except for those with hyperfine couplings very close to zero. Alternatively, a cluster of nuclear spins with very similar hyperfine frequencies

### 3.3 Fixed sensing scheme for the detection of variable fields at high resolution

$A_{zz}$  which are not at the Larmor frequency could be resolved without having to flip the  $^{13}\text{C}$  bath and thus keeping the longer coherence times.

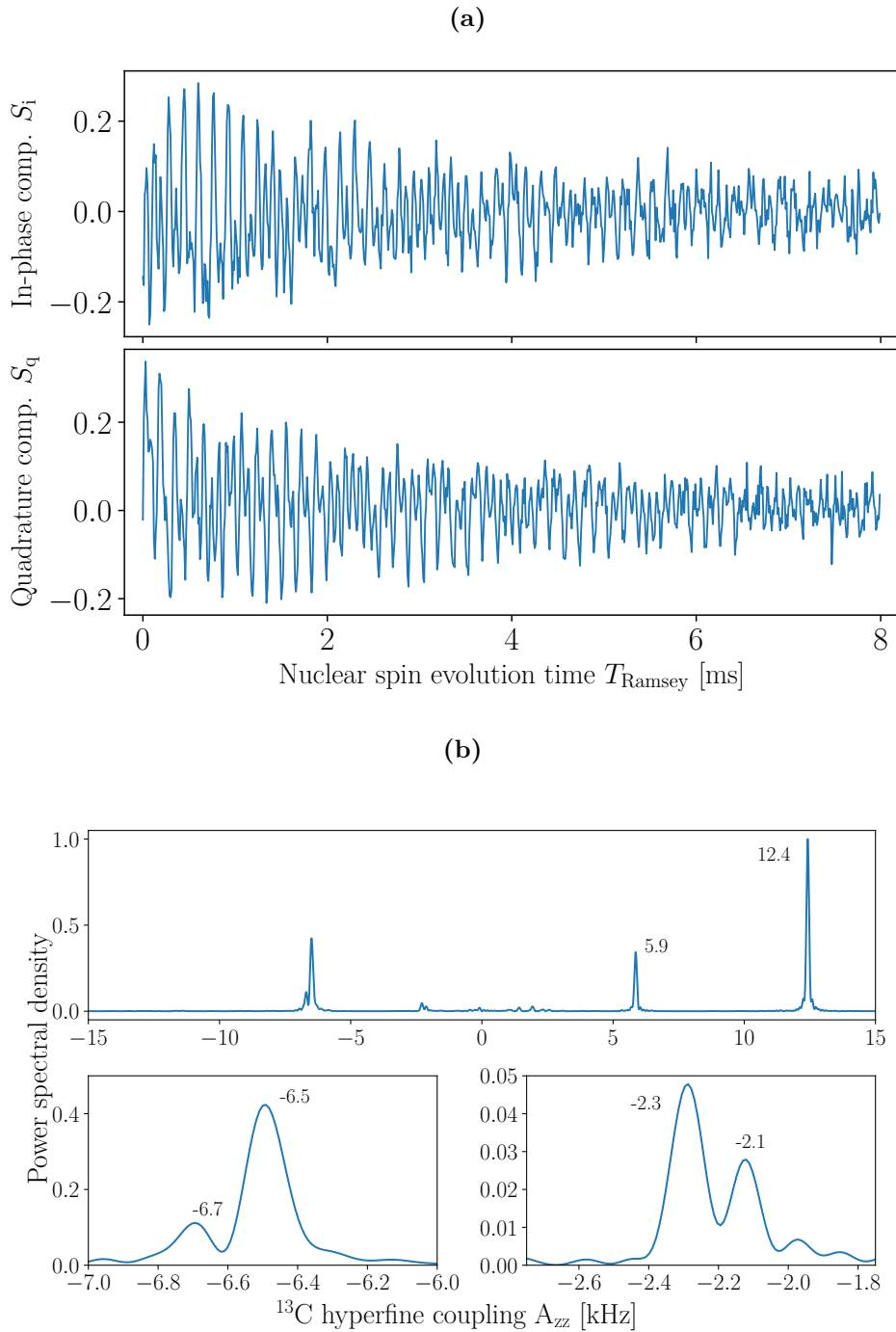


**Fig. 3.11: Time and frequency domain signals of a multi carbon spin Ramsey experiment.** (a) Ramsey oscillations of multiple  $^{13}\text{C}$ , measured with sampling frequency 100 kHz. The Ramsey oscillations were done according to sequence Seq3.9 with  $\nu = 0$  (top, in-phase component) and  $\nu = \pi/2$  (bottom, quadrature component). (b) Fourier transform of combined signals from (a) with zero padding. Multiple nuclear spin peaks appear at their respective hyperfine couplings  $A_{zz}$ .

### 3.4 Summary and outlook

In this chapter, an entangled hybrid quantum sensor-memory pair is implemented for improved correlation spectroscopy, which outperforms the sole sensor by a factor of two in measurement signal and hence by a factor of four in measurement time needed to reach an identical signal to noise ratio. Storing the full quantum state not only allows for improved detection of weakly coupled qubits, but also enables coherent interaction and non-local gates between memory and distinct weakly coupled qubits. The experimental overhead thereby is negligible, for the measurement with highest resolution the total measurement time is increased by 0.083 % from 9.575 ms to 9.583 ms. The relation between sensing time  $\tau$  and memory storage time  $T_T$  is analyzed. Both for classical and quantum memory, the storage time decays exponentially with  $\tau$  and the decay constant is  $T_T \approx 35 \mu\text{s}$ . An explanation for this coupled behaviour is found in the increased accumulation of noise information on the memory for larger  $\tau$  and an increased chance for the noise environment to change (and thus not being able to be decoupled from) for larger correlation times  $T_c$ .

A sample application of the quantum memory enhanced correlation sequence is found in the detection and correlation with weakly coupled  $^{13}\text{C}$  nuclear spins. As the quantum enhanced correlation sequence is designed to decouple from most magnetic field sources, a RF pulse with very high frequency sensitivity during the correlation time  $T_c$  is used to recouple individual  $^{13}\text{C}$  nuclear spins. The effect of this pulse is analyzed and an optimal point is found when a  $\pi$  - pulse is performed during  $T_c$ . Phase information about individual  $^{13}\text{C}$  nuclear spins is collected and the in-phase and quadrature components are individually investigated and an application is found for each. The in-phase component is not sensitive to the sign of the field produced by the  $^{13}\text{C}$  nuclear spin and thus can be non-zero, independently of the  $^{13}\text{C}$  polarization. Therefore, the in-phase component is suitable for detection of individual, weakly coupled  $^{13}\text{C}$  nuclear spins with very high frequency resolution at a full-width half maximum of 210 Hz. The quadrature component of the sensing phase on the other hand allows for the design of controlled quantum operations between the memory nuclear spin and a (weakly coupled)  $^{13}\text{C}$  nuclear spin. Therefore, the sensing time  $\tau$  is set such, that the  $^{14}\text{N}$  memory spin is found in orthogonal basis states for the two  $^{13}\text{C}$  spin eigenstates  $|+\rangle$  and  $|-\rangle$ , respectively. When the  $^{13}\text{C}$  sample spin is put in a superposition state before the sequence, it will be in a maximally entangled state with the memory spin afterwards. Thereby, entanglement is possible with a frequency resolution of 210 Hz, meaning that controlled quantum operations are possible in a very dense spectrum. This frequency resolution is more than a factor of ten improvement to the case where no nuclear spin quantum memory is used.

Finally, the time varying magnetic field produced by all  $^{13}\text{C}$  nuclear spins which are coupled to the NV center with hyperfine frequencies in a window of  $A_{zz} = -50 \text{ kHz}$  to  $50 \text{ kHz}$  around the bare  $^{13}\text{C}$  larmor frequency are detected. Hereby, the frequency resolution is limited by the sample spin coherence time of 8.5 ms and thus a frequency resolution

of FWHM= 119 Hz is possible, revealing two additional nuclear spins previously not detectable. Their hyperfine coupling frequencies  $A_{zz}$  are  $-2.3$  kHz and  $-2.1$  kHz. The frequency resolution here is no more limited by the available correlation time  $T_c$ , but by the frequency resolution with which the time varying  $^{13}\text{C}$  sample spin field can be set. Therefore, the sensor sensitivity no longer is lowered by the necessity to increase the correlation time  $T_c$  for maximum frequency resolution and thereby decreasing the available sensing time  $\tau$ .

The presented method allows for various applications, for example chemical-shift detection with high spatial resolution [20], or it might improve proposals where an ancillary nuclear spin memory should be utilized for improved spatial resolution of sample spins [50]. The demonstrated coherent interaction with weakly coupled qubits facilitated by the quantum memory is particularly interesting for preparation, steering and readout of larger scale quantum simulators as proposed in [34]. Most importantly, the approach is complementary to others exploiting entanglement, as for example GHZ states or spin squeezed states of multiple sensors. In the first case, the quantum phase might be stored on a single memory as presented in this chapter, whereas in the latter case each sensor participating in the squeezed state needs a separate memory. An interesting test system for the latter would be an ensemble of NV centers [38], where each center intrinsically comprises a sensor and a memory. For this system, the beneficial implementation of squeezing has been proposed [189]. Furthermore, the application of quantum-error-correction protocols [17, 35, 190] may extend the nuclear spin's storage time beyond the  $T_1$  time of the electron spin. Another alternative would be the storage into weakly coupled memory spins which could potentially be completely decoupled from the electron spin [191] reaching storage times of seconds and corresponding spectral resolutions below one Hz. As a final remark, the quantum enhanced correlation measurement resembles Kitaev's phase estimation algorithm using just a single phase accumulation step [192, 193]. More efficient phase estimation can be achieved by increasing the number of memory qubits and performing a final inverse quantum Fourier transformation.

# 4

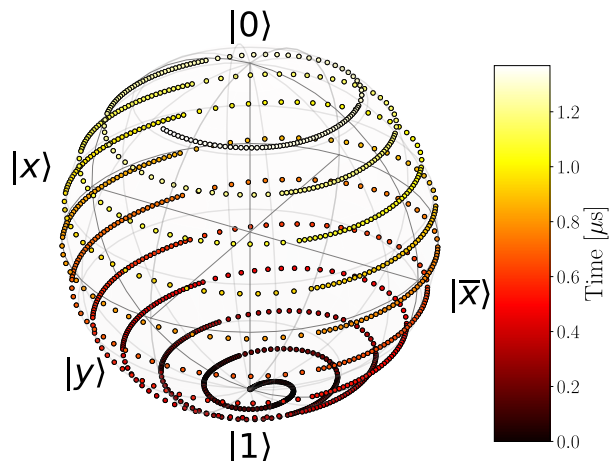
## High resolution hyperfine tensor analysis

The highly precise addressing and control over individual spin qubits is a key requirement for the upscaling of NV center based quantum computing. Nuclear spins are a valuable, highly abundant resource. In the previous chapter, techniques were discussed, which address individual  $^{13}\text{C}$  nuclear spins found around a single NV center, selective to their hyperfine component  $A_{zz}$ . Thereby, several weakly coupled nuclear spin qubits were identified. In particular the two nuclear spins found around  $A_{zz} \approx -6.6$  kHz (cf. figure 3.8) provide an interesting example for the application of the technique presented in this chapter. In the  $A_{zz}$  spectrum, they are very close and hard to resolve and one can imagine, that when spins spectrally get even closer to each other, they will not be resolvable with previously presented techniques. Here, the  $A_{zx}$  hyperfine coupling component comes into play to make them resolvable. Methods which are sensitive to  $A_{zx}$  allow for additional means of control over nuclear spins, potentially leading to a drastic increase in the number of accessible nuclear spin qubits around an NV center. A technique not only sensitive to  $A_{zz}$  but also to  $A_{zx}$  allows to address individual nuclear spins even if two nuclear spins have identical values of  $A_{zz}$  or  $A_{zx}$ . Such a technique was introduced by Taminiau et al. [25] for the use at low magnetic fields ( $B_{0,z} \approx 0.04$  T), which uses a dynamical decoupling sequence performed on the electron spin to control multiple individual weakly coupled nuclear spins. With an appropriate DD sequence such as the KDD sequence, electron spin coherence times of  $\approx 3$  ms can be reached, which allows for a precision  $\approx 0.3$  kHz (cf. section 1.7). The here presented technique combines the coherent stimulated echo method introduced in chapter 3 with the lock-in detection method by Taminiau et al., to allow for nuclear spin detection on timescales of  $T_{1,e}$  and therefore possible frequency resolutions both for the determination of  $A_{zz}$  and  $A_{zx}$  better than 0.2 kHz.

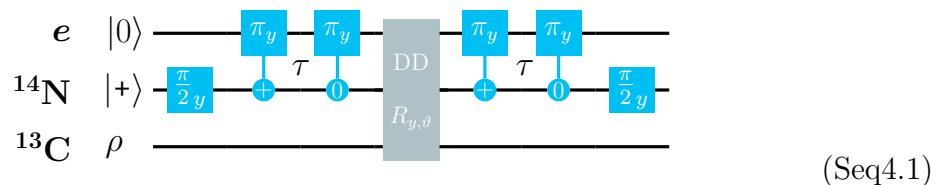
**Chapter outline** In section 4.1, the quantum enhanced correlation spectroscopy method is combined with a dynamical decoupling sequence. The resulting sequence is analyzed in detail. In section 4.2 the new technique is applied to individual  $^{13}\text{C}$  nuclear spins with well resolved hyperfine peaks  $A_{zz}$ . In section 4.3, the two nuclear spins  $A_{zz} = -6.6$  kHz are analyzed and a path for their individual addressing is presented.

## 4.1 Quantum enhanced correlation spectroscopy combined with a dynamical decoupling sequence

**Fig. 4.1: Simulation of nuclear spin evolution during dynamical decoupling sequence Seq4.2 on the Bloch sphere.** The nuclear spin qubit starts in spin state  $|1\rangle$  and then spirals towards state  $|0\rangle$ , for which it would need  $N_\pi = 24$   $\pi$  - pulses. Parameters:  $\Omega = 10$  MHz,  $A_{zx} = 1$  MHz,  $A_{zz} = 500$  kHz,  $\tau_k = 43$  ns.



Here, the basic equation Seq4.1 is introduced, which is a modified form of sequence Seq3.8. The nuclear spin manipulation  $R_{y,\vartheta}$ , which is performed during  $T_c$  here is performed by a DD sequence.



Whereby in the previous chapter the properties of  $R_{y,\vartheta}$  were described only by oscillation frequency and amplitude of the RF pulse, here a third component, the  $A_{zx}$  coupling of the addressed nuclear spin is added. The method is an improved version of the weakly coupled nuclear spin detection and manipulation method introduced in [25]. The general principle as well as the relevant equations remain valid for the here presented method. The general building block is the DD sequence Seq4.2 involving  $N$  individual  $\pi$  - pulses

#### 4.1 Quantum enhanced correlation spectroscopy combined with a dynamical decoupling sequence

separated by the interpulse distance  $\tau$ .

$$\text{---} \boxed{R_{y,\theta}} \text{---} = \text{---} \boxed{\pi_{\alpha_1}} \text{---} \tau_k \text{---} \boxed{\pi_{\alpha_2}} \text{---} \dots \text{---} \boxed{\pi_{\alpha_N}} \text{---} \frac{\tau_k}{2} \quad (\text{Seq4.2})$$

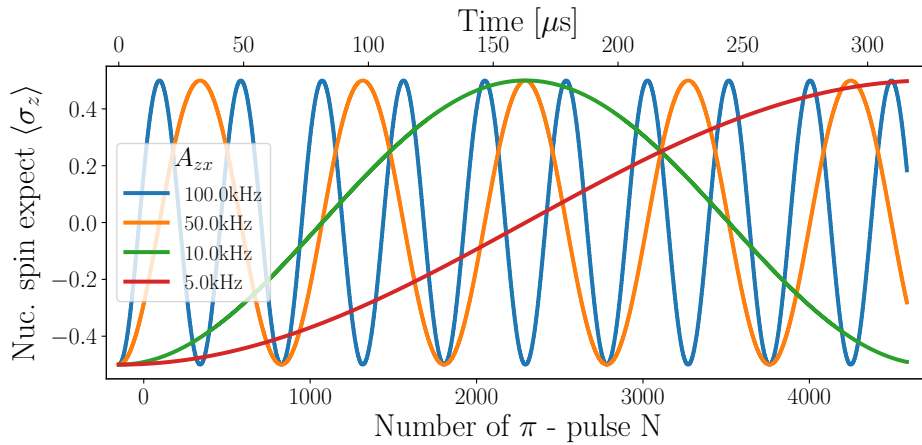
The dynamics can be described by three parameters: The hyperfine components  $A_{zz}$ ,  $A_{zx}$  and the number of  $\pi$  - pulses  $N$ . Resonances appear for the interpulse distance  $\tau_k$ , described by the equation 4.1

$$\tau_k = \frac{(2k - 1)}{2f_L + A_{zz}} - \frac{1}{\Omega} \quad (4.1)$$

with the resonance order  $k = 1, 2, 3, \dots$ . The Rabi frequency  $\Omega$  here is mostly limited by the requirement  $\tau_k \geq 0$ . For these values of  $\tau_k$ , a  $\pi$  - pulse is performed on the target nuclear spin with hyperfine components  $A_{zz}$ ,  $A_{zx}$ , if sequence Seq4.2 is performed with a number of

$$N_\pi = \frac{\pi}{m_x} \quad \text{with } m_x = \frac{A_{zx}}{\sqrt{(A_{zz} + f_L)^2 + A_{zx}^2}} \quad (4.2)$$

individual  $\pi$  - pulses.



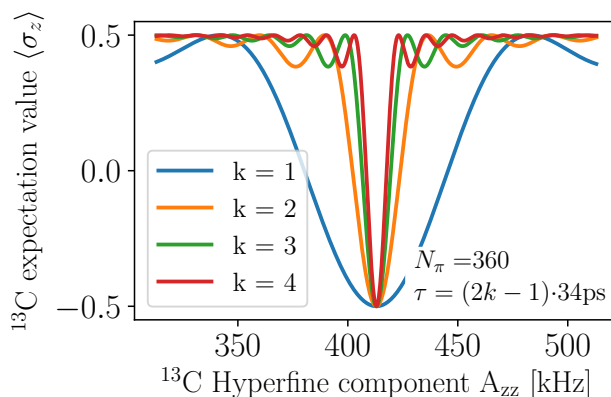
**Fig. 4.2: Nuclear spin  $\langle \sigma_z \rangle$  - expectation value during dynamical decoupling for varying  $A_{zx}$**  For all four curves, the hyperfine coupling  $A_{zz}$  is 50 kHz. With increasing  $A_{zx}$ , the oscillation gets faster according to equations 4.2 and 4.3. When  $A_{zz}$  and the Larmor frequency of a  $^{13}\text{C}$  nuclear spin are known,  $A_{zx}$  can be determined from the oscillation period.

Figure 4.1 shows the trajectory on the Bloch sphere, that a  $^{13}\text{C}$  with an assumed hyperfine coupling  $A_{zx} = 1 \text{ MHz}$  and  $A_{zz} = 500 \text{ kHz}$  undergoes during sequence Seq4.2

for  $\tau_k$  according to equation 4.1 and  $k = 1$ . Please note, that for these values, equation 4.2 becomes inaccurate. After  $N_\pi = 24$ , the nuclear spin qubit is transferred from  $|1\rangle$  to  $|0\rangle$  by an effective  $\pi$  - pulse ( $\vartheta = \pi$ ). The total required duration to perform a  $\pi$  - pulse is a little larger than  $1 \mu\text{s}$ , which can be expected from  $A_{zx} = 1 \text{ MHz}$ . The nuclear spin expectation value  $\langle\sigma_z\rangle$  during this time oscillates with the number of  $\pi$  - pulses  $N$  as

$$\langle\sigma_z\rangle(N) = \frac{1}{2} \cos\left(\pi \frac{N}{N_\pi}\right) \quad (4.3)$$

This oscillatory behaviour is shown in figure 4.2 for four nuclear spins with  $A_{zz} = 50 \text{ kHz}$  and four different values of  $A_{zx}$ . For smaller  $A_{zx}$ , the time and thereby number of  $\pi$  - pulses  $N_\pi$  required to perform a  $\pi$  - pulse, increases. Please note the similarities between these oscillations and the Rabi oscillations performed with a rectangular shaped RF pulse in figure 3.7. One question that arises is, how selective sequence Seq4.2 is with respect to  $A_{zz}$ . Figure 4.2 shows the  $^{13}\text{C}$  nuclear spin expectation value  $\langle\sigma_z\rangle$  for parameters  $\tau_k$  and  $N_\pi$  calculated to perform a  $\pi$  - pulse for a nuclear spin with  $A_{zz} = 413 \text{ kHz}$  and  $A_{zx} = 66 \text{ kHz}$ . With increasing order  $k$ , the selectivity as well as the sequence duration increases, and the dip width can be calculated from  $m_x / [(2k + 1)\pi]$  [25]. Another way to increase the selectivity is to keep low at  $k = 1$  but perform a number of 3, 5, 7, .. times  $N_\pi \pi$  - pulses.



**Fig. 4.3: Frequency selectivity of sequence Seq4.2 for increasing order  $k$ .** With increasing  $k$ , the total sequence duration and at the same time the frequency selectivity increases. Parameters:  $A_{zx} = 413 \text{ kHz}$ ,  $A_{zz} = 66 \text{ kHz}$

## 4.2 Determination of hyperfine component $A_{zx}$

The here presented technique does not rely on the electron spin being in a superposition state during  $T_c$ . As discussed in section 3.1.2 on page 80, after the first sensing step and before  $T_c$ , the electron spin starts in the eigenstate  $|-\rangle$  and is in a superposition state only during the  $\pi$  - pulses of the DD - sequence. The duration of these  $\pi$  - pulses is only limited by the available MW driving amplitude and thus by the technical equipment and is typically on the order of ns. Therefore, the hyperfine coupling component  $A_{zx}$  can

### 4.3 Resolving $^{13}\text{C}$ nuclear spins by their $A_{zx}$ coupling.

be determined with a precision on timescales of  $T_{1,e}$  by measurement of the oscillations described by equation 4.3. These measurements have been performed for four nuclear spins whose  $A_{zz}$ -coupling is well resolved, i.e. no other nuclear spin has a similar hyperfine coupling  $A_{zz}$ . The results are presented in figures 4.4a to 4.4d. The four nuclear spins were already investigated in figure 3.8 or even are found in the ODMR spectrum with  $A_{zz} = 414\text{ kHz}$ ,  $A_{zz} = 89\text{ kHz}$ ,  $A_{zz} = 12.4\text{ kHz}$  and  $A_{zz} = 5.9\text{ kHz}$ . For each of these four nuclear spins, now additional knowledge has been acquired, as their hyperfine components  $A_{zx}$  have been determined to  $A_{zx} = 65\text{ kHz}$ ,  $A_{zx} = 19\text{ kHz}$ ,  $A_{zx} = 2.6\text{ kHz}$  and  $A_{zx} = 15.3\text{ kHz}$ , respectively.

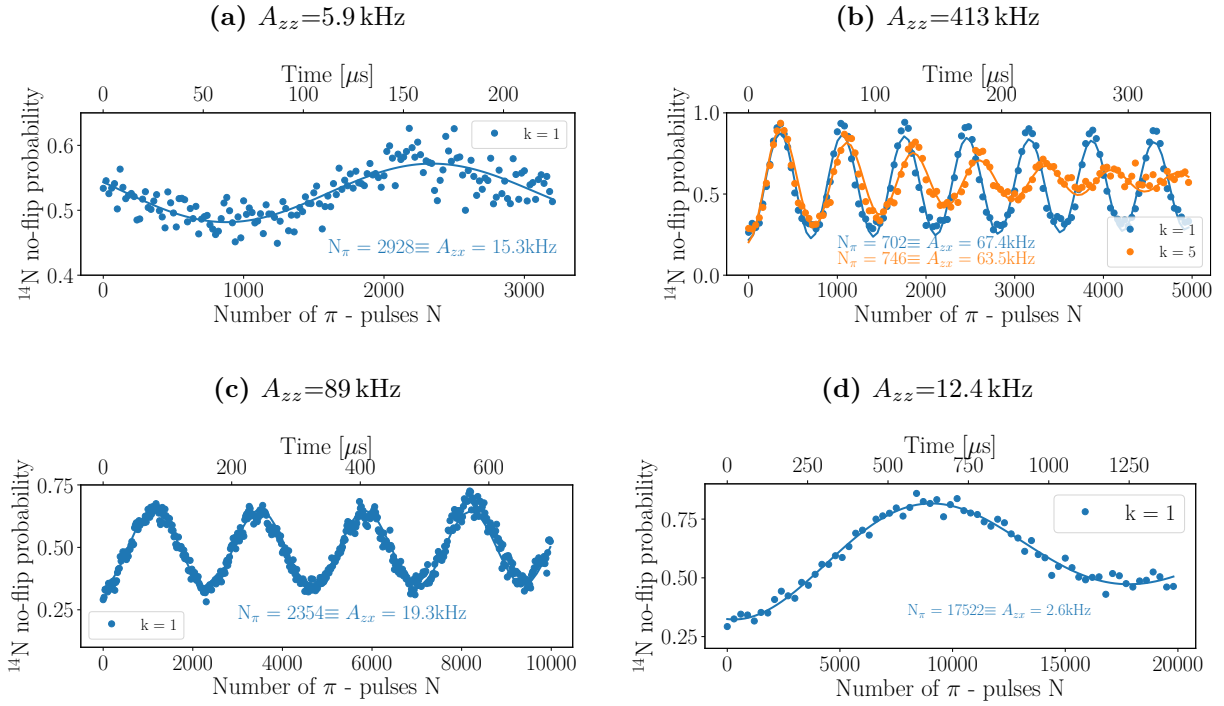


**Fig. 4.4: Hyperfine components  $A_{zz}$  and  $A_{zx}$  for four carbon nuclei.** The number  $N_\pi$  ( $A_{zx}$ ) of  $\pi$ -pulses in sequence Seq4.2 required for a flip of the  $^{13}\text{C}$  nuclear spins with hyperfine component  $A_{zz}$  allows to determine the hyperfine component  $A_{zx}$ .

### 4.3 Resolving $^{13}\text{C}$ nuclear spins by their $A_{zx}$ coupling

In this section, finally the two barely resolvable nuclear spins found in figure 3.8c are investigated. Therefore, a hyperfine coupling  $A_{zz} \approx 6.56\text{ kHz}$  was assumed and the interpulse distance  $\tau_k$  was determined by equation 4.1. Then, as previously described, ?? was performed with the DD sequence Seq4.2 during  $T_c$ . The frequency selectivity of the sequence with respect to  $A_{zz}$  is not high enough to resolve the two nuclear spins. As

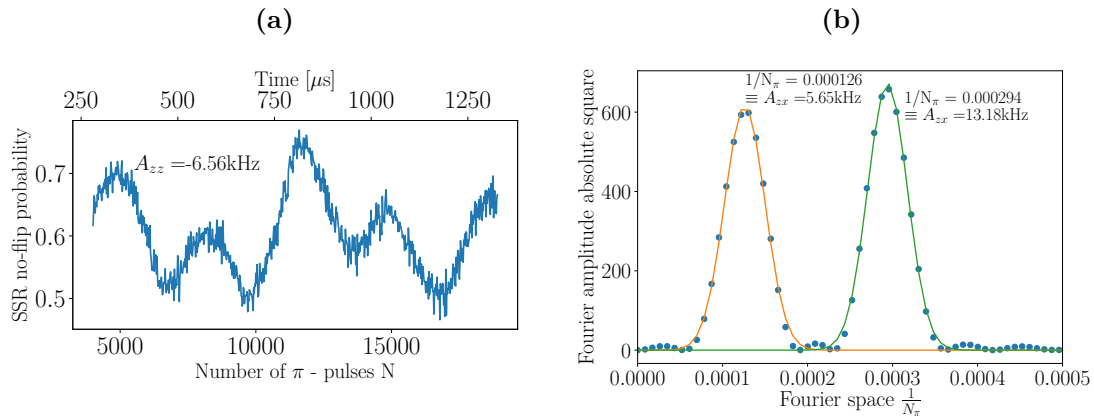


**Fig. 4.5: Two-nuclear spin oscillation by spin-lock sequence.** The measurement was performed with ??, where the sample nuclear spin rotation  $R_{y,\theta}$  is performed with the DD sequence Seq4.2. (a) The interpulse distance  $\tau_k$  is calculated with  $A_{zz} = 6.56$  kHz. With increasing number of  $\pi$ -pulses,  $N$ , the signal oscillates as the sum of two cosines. (b) From the oscillation frequency with respect to  $N$ , the nuclear spin hyperfine couplings  $A_{zx}$  can be determined. Therefore, a Fourier transform of the signal in (a) was performed. The two nuclear spins found near  $A_{zz} = 6.56$  kHz have  $A_{zx}$  couplings 5.65 kHz and 13.18 kHz.

shown in figure 4.5a, however, this is not true for  $A_{zx}$ . The signal oscillates not with one but with the sum of two cosines (cf. equation 4.3). From the Fourier transformation of the signal, the number of  $\pi$ -pulses  $N_\pi$  required of a flip of the two individual nuclear spins and therefrom their hyperfine coupling  $A_{zx}$  can be determined. The values are  $A_{zx} = 5.65$  kHz and  $A_{zx} = 13.18$  kHz. This observation is particularly interesting in terms of individual addressing of the two spins. The measurement shows, that no selectivity due to  $A_{zz}$  is given, since otherwise no two but only one oscillation would be present. Still, it is possible to selectively perform a  $\pi$ -pulse on one nuclear spin but not on the other one. After  $N_\pi \approx 8000$  and  $N_\pi \approx 3400$   $\pi$ -pulses in the DD sequence Seq4.2, a  $\pi$ -pulse is performed on the two nuclear spins, respectively. A reasonably good selectivity is already given at  $N = 7500$ , where on one of the two nuclear spins almost a  $\pi$ -pulse has been performed, while on the other one it is a little bit more than  $2\pi$ , which is equal to performing no operation at all. For  $N = 136000$ , an exact  $10\pi$  rotation is performed on the first nuclear spin and a  $17\pi$  rotation is performed on the second one.

## 4.4 Summary and outlook

In this chapter, a technique was presented, which uses the quantum enhanced correlation spectroscopy method as basis and performs a DD sequence during the correlation time  $T_c$ . This DD sequence performs a nuclear spin rotation which depends both on hyperfine

components  $A_{zx}$  and  $A_{zz}$ . While the general technique of performing a DD sequence to address nuclear spins with these two hyperfine components has been presented in [25], here the frequency resolution is increased from being limited by the coherence time to being limited by the larger longitudinal relaxation time  $T_{1,e}$  of the NV center electron spin. This is achieved by the fact, that due to use of the nuclear spin quantum memory (e.g. a  $^{14}\text{N}$ ), the electron spin no more is required to be in a superposition state. Instead, during  $T_c$  it resides in an eigenstate and only during the, potentially infinitesimally short, electron  $\pi$  - pulses, it is in a superposition state. The described technique allowed to determine the  $A_{zx}$  couplings of a total of 6 nuclear spins. Four of these nuclear spins are well resolved in the  $A_{zz}$  spectrum, meaning there are no other nuclei with similar  $A_{zz}$  couplings. The hyperfine coupling values  $A_{zx}(A_{zz})$  are  $A_{zx} = 414 \text{ kHz}$  ( $A_{zz} = 65 \text{ kHz}$ ),  $A_{zx} = 89 \text{ kHz}$  ( $A_{zz} = 19 \text{ kHz}$ ),  $A_{zx} = 12.4 \text{ kHz}$  ( $A_{zz} = 2.6 \text{ kHz}$ ) and  $A_{zx} = 5.9 \text{ kHz}$  ( $A_{zz} = 15.3 \text{ kHz}$ ). The technique shows its full potential, when two not well resolved spins are investigated. Here, two spins at  $-6 \text{ kHz}$  and a frequency separation  $A_{zz}$  well below  $1 \text{ kHz}$  are found, whose  $A_{zx}$  values could be determined to be  $A_{zx} = 5.65 \text{ kHz}$  and  $A_{zx} = 13.18 \text{ kHz}$ . With the presented technique, these formerly barely resolvable spins now can be individually flipped, where for  $N = 136000$   $\pi$  - pulses one nuclear spin performs a  $10\pi$  - rotation (equal to zero) and the other performs a  $17\pi$  - rotation. It is important to note, that these operations can be performed conditionally on the memory state and therefore allows e.g. for entanglement with it.

The presented technique allows not only to determine the  $A_{zx}$  hyperfine component but with a given reference frame also the  $A_{zy}$  component of each  $^{13}\text{C}$  nuclear spin can be determined. Thereby, the relative position of NV center and  $^{13}\text{C}$  nuclear spins can be determined with the help of further simulations connecting position and hyperfine tensor. During the preparation of the presented work, such a technique was published as [194] and thus no further efforts were made in this direction.



# 5

## The quantum Fourier transform in a hybrid qudit quantum phase estimation algorithm

The accurate and precise determination of quantum phases lies both at the heart of quantum metrology and quantum computing. Often, the target quantity is an energy shift which causes a phase evolution during a well known time. Applications like chemical structure analysis require spectral resolutions on the order of Hz and below, which is unreachable within the NV center electron spin coherence time [20]. Therefore, correlation type sequences such as that introduced in sequence Seq3.5 on page 81 are required, which use long lived memories [14, 173]. On one hand, a quantum correlation type sequence benefits from the long correlation time which results in a high spectral resolution. On the other hand, during the correlation time information is only stored and no additional information about the target quantity is acquired. The long correlation time therefore is most efficiently used, if as much information as possible is acquired and stored during the phase accumulation steps. This phase information must be stored in a quantum register. The amount of retrievable phase information from a quantum register is fundamentally limited to  $\log_2(N)$  bits per energy level, which is known as Holevo's Bound [195]. For one qubit, exactly one bit of classical information can be extracted, while for two qubits (with four energy levels) it is already two bits of information. Therefore, the quantum register should have the highest possible number of energy levels. Besides increasing the number of qubits, the register size can also be increased if its constituents are not qubits but entities with higher multiplicities, so called qudits [196, 197]. Highest flexibility is reached, when qudits of different multiplicities together can form a quantum register, on which the quantum phase estimation algorithm is performed. So far, neither the quantum phase estimation algorithm nor the QFT have been performed on a real hybrid qudit spin system. There has, however, been an implementation which emulates a hybrid qudit

system [26]. In this chapter, existing theories are extended to this more general case, to enable for the implementation of the quantum phase estimation algorithm on a system of a single electron spin as a quantum sensor supported by a hybrid qudit memory register of one  $^{14}\text{N}$  qutrit and two  $^{13}\text{C}$  qubits.

**Chapter outline** In this chapter, the quantum phase estimation algorithm and its implementation on a hybrid qudit system of one  $^{14}\text{N}$  qutrit and two  $^{13}\text{C}$  nuclear spins is presented. In section 5.1, some basic principles of quantum phase estimation are introduced, which allow to see the quantum phase estimation algorithm in the more general context of quantum metrology. Then, in section 5.2 a mathematical description of the hybrid qudit QFT is derived in analogy to existing descriptions for qubits and qudits. Two examples for the derived theory are given at the end of the section. Starting from this very general description of the QFT, the quantum phase estimation algorithm performed on hybrid qudits is introduced in section 5.3. In the last two main sections, the quantum phase estimation algorithm is experimentally demonstrated. First, on a qutrit register in the context of quantum correlation spectroscopy in section 5.4, where quantum phase estimation of the magnetic field is produced by a  $^{13}\text{C}$  sample spin. Then, on a register of one qutrit and two qubits with an artificially generated phase in section 5.5. In section 5.6, the chapter is summarized and an outlook is given.

## 5.1 Basic principles of quantum phase estimation

The basic principles of quantum phase estimation are best understood from the example of a Ramsey interferometry experiment performed on a two-level system which initially is prepared in a superposition state  $|\psi_0\rangle = |0\rangle + |1\rangle$ . When a magnetic field  $B$  induces a frequency shift  $\omega = \tilde{\gamma}B$ , the state evolves during a time  $\tau$  as

$$|\psi\rangle = |0\rangle + e^{-i\Delta\phi} |1\rangle \quad (5.1)$$

with  $\Delta\phi = \omega\tau$ . A  $\pi/2$  - pulse then converts the sensing information from a phase to a probability

$$p = (1 + \cos \Delta\phi) / 2 \quad (5.2)$$

for finding the two-level system in the computational basis state  $|1\rangle$ . When only the inevitable quantum projection noise is considered and the interferometer is operated around a point of highest slope (i.e.  $p = 0.5$ ), the precision  $\delta\omega$  scales as

$$\delta\omega = \frac{1}{\tau\sqrt{N_m}} \quad (5.3)$$

with  $N_m$  repetitions of the measurement [198, 199]. This scaling behavior for example was used by Balasubramanian et al. to determine the magnetic field amplitude  $\delta B = \delta\omega/\tilde{\gamma}$  with an uncertainty of  $\delta B = 4$  nT within one second of measurement time as a result of a long sensing time  $\tau$ . At the same time, however, the maximum detectable field was reduced to  $B_{\max} = 31$  nT. This reduction is a result of the oscillatory behavior of equation 5.2 which introduces ambiguities for phases  $|\Delta\phi| > \pm\pi/2$  and thereby limits the maximally detectable frequency to  $\omega_{\max} < \pi/2\tau$ . When only small changes around a previously well known working point are expected, a sensor protocol designed with uncompromising focus on optimal sensitivity can be the right choice. Generally, this will not be the case. Strategies involving different phase accumulation times  $\tau_i$  use the available resources to increase the sensor sensitivity while also preserving sensor bandwidth [182, 200]. A common idea is to use multiple separate sensing steps of duration  $\tau_i$ , in which different phases  $\Delta\phi_i = \tau_i\omega$  are acquired. While the absolute measurement uncertainty then is dominated by the measurement with maximal  $n_i$ , ambiguities are removed by the measurements yielding smaller phases.

The quantum phase estimation algorithm achieves this by use of a quantum register to which the phase information obtained in the individual sensing steps is transferred. In the simple case of multiple qubits, the sensing time doubles for every next sensing step. The collective phase information is processed with the iQFT before read out in the computational basis [201]. An approach using multiple memories which store more information compared to a single qubit memory is particularly useful in correlation spectroscopy measurements. Then, the phase estimation algorithm can be performed in a single run, which is efficient as the total measurement duration is dominated by the long correlation time and not by the actual sensing time.

## 5.2 The hybrid qudit quantum Fourier transform

The QFT is the quantum analogon to the discrete Fourier transform. It unitarily transforms from the computational basis  $|0\rangle, |1\rangle, \dots, |N-1\rangle$  into the Fourier basis according to

$$QFT |j\rangle = \frac{1}{\sqrt{N}} \sum_{k=0}^{N-1} e^{2\pi jk/N} |k\rangle \quad (5.4)$$

with integers  $N$ ,  $j = 0, 1, 2, \dots, N-1$ . The Fourier basis states are equally weighted superpositions of the  $N$  computational basis states. For a physical implementation, the actual composition of the used memory register can be chosen freely. The natural choice in quantum information science is to use a number of  $n = \log_2 N$  qubits, however, also the use of  $n = \log_d N$  memory qudits of multiplicity  $d$  is mentioned in literature [201–203]. In this section the existing theory is extended to the case of hybrid qudit

memory registers of multiplicities

$$d = \{d_1 d_2 \dots d_n\} \quad (5.5)$$

which includes the qubit and qudit QFT. In the last two paragraphs of this section, examples are given for  $d = \{3\}$  (a qutrit memory) and  $\{322\}$  (a memory register constituted of one qutrit and two qubits).

**Theoretical foundation** Equation 5.4, the definition of the QFT, does not give insight into the construction of a gate sequence to perform the *QFT* gate on a hybrid qudit register with multiplicities  $d = \{d_1 d_2 \dots d_n\}$ . With some algebra, the right side of equation 5.4 can be written as product state of the individual qudit states. This representation is given in equation 5.10e. The required theory is derived in analogy to the derivation for the qubit case given in [201]. The interested reader may want to first get a full understanding of the qubit QFT before advancing to the more general hybrid qudit case which is derived here.

Given are  $n$  systems with multiplicities  $d$  and a total system size  $N = \prod_{l=1}^n d_l$ . First, some definitions and expressions are given to simplify the actual deduction of the product representation of the QFT, which is given in equation 5.10.

- An integer  $k = 0, \dots, N - 1$  then can be given in a hybrid base digital representation as

$$\begin{aligned} k &= k_n + \sum_{l=1}^{n-1} k_l \prod_{m=l+1}^n d_m \\ &= \{k_1 k_2 \dots k_n\} \end{aligned} \quad (5.6)$$

with  $k_l = 0, 1, \dots, d_l - 1$ . The base of the digital representation is  $d = \{d_1 d_2 \dots d_n\}$ . As an example, for the case  $d = \{22 \dots 2\}$ , equation 5.6 shows the common binary representation  $k = 2^{n-1} k_1 + 2^{n-2} k_2 + \dots + k_1$ .

- The expression

$$\begin{aligned} \frac{k}{N} &= k_n \prod_{m=1}^n d_m^{-1} + \sum_{l=1}^{n-1} k_l \prod_{m=l+1}^n d_m \prod_{o=1}^l d_o^{-1} \\ &= \sum_{l=1}^n k_l \prod_{m=1}^l d_m^{-1} \end{aligned} \quad (5.7)$$

is useful to understand the step from equation 5.10a to equation 5.10b

- The integer number  $j = 0 \dots N - 1$  is given in the hybrid digital representation

$$\boxed{j = j_1 + \sum_{l=2}^n j_l \prod_{m=1}^{l-1} d_m} \quad (5.8)$$

## 5.2 The hybrid qudit quantum Fourier transform

Please note, that  $j$  is given in the reversed base  $\{d_n \dots d_2 d_1\}$ , as opposed to  $k$ . This is necessary, as QFT (and iQFT) reverse the order of the qudits.

- With  $e^{2\pi i x} = 1$ ,  $x \in \mathbb{Z}$ , the transformation

$$\exp\left(2\pi i \left[ j \prod_{m=1}^l d_m^{-1} \right]\right) = \exp\left(2\pi i \left[ j_1 \prod_{m=1}^l d_m^{-1} + \underbrace{\sum_{p=2}^n j_p \prod_{o=1}^{p-1} d_o \prod_{m=1}^l d_m^{-1}}_{\in \mathbb{Z} \text{ for } p-1 \geq l} \right]\right) \quad (5.9a)$$

$$= \exp\left(2\pi i \left[ j_1 \prod_{m=1}^l d_m^{-1} + \sum_{p=2}^l j_p \prod_{o=1}^{p-1} d_o \prod_{m=1}^l d_m^{-1} \right]\right) \quad (5.9b)$$

$$= \exp\left(2\pi i \left[ j_1 \prod_{m=1}^l d_m^{-1} + \sum_{p=2}^l j_p \prod_{m=p}^l d_m^{-1} \right]\right) \quad (5.9c)$$

$$= \exp\left(2\pi i \left[ \sum_{p=1}^l j_p \prod_{m=p}^l d_m^{-1} \right]\right) \quad (5.9d)$$

$$(5.9e)$$

is valid, which allows to understand the step from equation 5.10d to equation 5.10e.

With these prerequisites, the transformation from the definition of the QFT, equation 5.10a to its product representation, equation 5.10e, can be performed:

$$QFT |j\rangle = \frac{1}{\sqrt{N}} \sum_{k=0}^{N-1} e^{2\pi i j k / N} |k\rangle \quad (5.10a)$$

$$= \frac{1}{\sqrt{N}} \sum_{k_1=0}^{d_1-1} \dots \sum_{k_n=0}^{d_n-1} e^{2\pi i j \left( \sum_{l=1}^n k_l \prod_{m=1}^l d_m^{-1} \right)} |k_1 \dots k_n\rangle \quad (5.10b)$$

$$= \frac{1}{\sqrt{N}} \sum_{k_1=0}^{d_1-1} \dots \sum_{k_n=0}^{d_n-1} \bigotimes_{l=1}^n e^{2\pi i j k_l \prod_{m=1}^l d_m^{-1}} |k_l\rangle \quad (5.10c)$$

$$= \frac{1}{\sqrt{N}} \bigotimes_{l=1}^n \sum_{k_l=0}^{d_l-1} e^{2\pi i k_l j \prod_{m=1}^l d_m^{-1}} |k_l\rangle \quad (5.10d)$$

$$\boxed{= \frac{1}{\sqrt{N}} \bigotimes_{l=1}^n \sum_{k_l=0}^{d_l-1} e^{2\pi i k_l \sum_{p=1}^l j_p \prod_{m=p}^l d_m^{-1}} |k_l\rangle} \quad (5.10e)$$

$$= \frac{1}{\sqrt{N}} \bigotimes_{l=1}^n \sum_{k_l=0}^{d_l-1} e^{2\pi i k_l 0 \cdot j_1 \dots j_2 j_l} |k_l\rangle \quad (5.10f)$$

For the last equivalence of equation 5.10e and equation 5.10f, the hybrid digital fraction

is defined as

$$0.j_l..j_2j_1 = \frac{j_l}{d_1} + \dots + \frac{j_2}{d_1..d_{l-1}} + \frac{j_1}{d_1..d_l} \quad (5.11)$$

with  $l = 1, 2, \dots, n$  in analogy to the digital fraction [201].

While the actual definition of the QFT (cf. equation 5.4) gives a general description, no information on the actual system composition is given. This changes with the product representation equation 5.10e, which thereby makes it possible to derive an efficient quantum circuit on an  $N$  level memory system of any qudit composition  $d = \{d_1 d_2 .. d_n\}$ . Therefore, only two kinds of quantum gates are required:

- The extension of the Hadamard gate for a qudit system with multiplicity  $d_i$ , which is a local gate. Equivalent gates like  $\pi/2$  - pulses (for qubits) are valid replacements.
- Bipartite controlled phase gates which induce a phase on state  $|j_b\rangle$  of a first qudit, if the state of a second qudit is in state  $|j_a\rangle$ .

Since the QFT can be constructed by these two kinds of unitary gates, it must be unitary itself.

The qutrit equivalent of the Hadamard gate (or  $\pi/2$  - pulse) is the Chrestenson gate

$$C = \frac{1}{\sqrt{3}} \begin{pmatrix} 1 & 1 & 1 \\ 1 & e^{\frac{2\pi i}{3}} & e^{\frac{4\pi i}{3}} \\ 1 & e^{\frac{4\pi i}{3}} & e^{\frac{2\pi i}{3}} \end{pmatrix} \quad (5.12)$$

It is discussed in appendix F and a two-frequency optimal control pulse is given which was used for its implementation on the  $^{14}\text{N}$  nuclear spin qutrit.

**QFT on a qutrit** From the QFT product representation given in equation 5.10e, the QFT for the single qutrit case can be derived ( $n = 1$  and  $d = \{3\}$ ).

$$\begin{aligned} QFT_{\{3\}} |j\rangle &= \frac{1}{\sqrt{3}} \left[ |0\rangle + e^{\frac{2\pi i j_1}{3}} |1\rangle + e^{\frac{4\pi i j_1}{3}} |2\rangle \right] \\ &= C |j\rangle \end{aligned} \quad (5.13)$$

with the Chrestenson gate  $C$ , which is given in equation 5.12. The Chrestenson gate is the equivalent of the Hadamard gate for qutrits. For the implementation of this single qudit QFT, naturally only one local gate and no controlled phase gates are required.

**Twelve level QFT on one qutrit and two qubits** The QFT can also be derived and later implemented for  $n = 3$  individual particles with  $d = \{322\}$  (one qutrit with  $d_1 = 3$  two qubits with  $d_2 = d_3 = 2$ ). In digital representation (cf. equation 5.8),  $j$  can be written as

$$j = j_1 + 3j_2 + 6j_3 \quad (5.14)$$

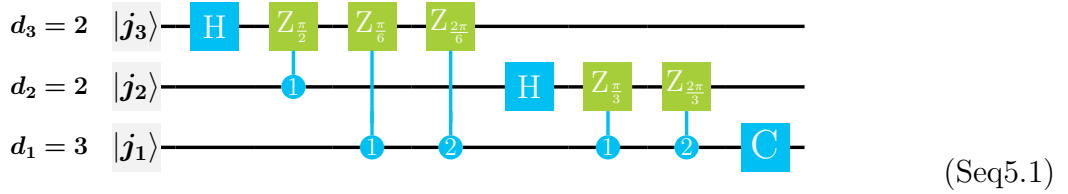
The QFT product representation, equation 5.10e, for this case yields

$$\begin{aligned}
 QFT_{\{322\}} |j\rangle &= \frac{1}{\sqrt{12}} \bigotimes_{l=1}^3 \sum_{k_l=0}^{d_l-1} e^{2\pi i k_l \sum_{p=1}^l j_p \prod_{m=p}^l d_m^{-1}} |k_l\rangle \\
 &= \frac{1}{\sqrt{3}} \left( |0\rangle + e^{2\pi i [\frac{j_1}{3}]} |1\rangle + e^{2\pi i [\frac{2j_1}{3}]} |2\rangle \right) \\
 &\quad \otimes \frac{1}{\sqrt{2}} \left( |0\rangle + e^{2\pi i [\frac{j_1}{6} + \frac{j_2}{2}]} |1\rangle \right) \\
 &\quad \otimes \frac{1}{\sqrt{2}} \left( |0\rangle + e^{2\pi i [\frac{j_1}{12} + \frac{j_2}{4} + \frac{j_3}{2}]} |1\rangle \right)
 \end{aligned} \tag{5.15}$$

The sequence is performed in reverse order, i.e. the state  $|j_3\rangle$  is manipulated first. Ultimately, it needs to acquire the phase  $2\pi i [\frac{j_1}{12} + \frac{j_2}{4} + \frac{j_3}{2}]$ . The Hadamard gate creates the state

$$\begin{aligned}
 |\psi_3\rangle &= H |j_3\rangle \\
 &= \frac{1}{\sqrt{2}} \left( |0\rangle + e^{2\pi i [\frac{j_3}{2}]} |1\rangle \right)
 \end{aligned} \tag{5.16}$$

Then, a controlled phase gate  $Z_{\frac{\pi}{2}}$  adds a phase  $\pi/2$ , if the second memory qudit ( $d_2 = 2$ ) is in state  $|j_2 = 1\rangle$ . Finally, two controlled phase gates add a phase  $\pi/6$  if the first spin is in state  $|j_1 = 1\rangle$  and a phase of  $2\pi/6$  if the first spin is in state  $|j_1 = 2\rangle$  [204]. For the second qubit, the procedure is analogous. The operation on the first memory qudit with state  $|j_1\rangle$  does not rely on the state of the other two spins and thus analogously to the single qutrit case ( $d = \{3\}$ ), the Chrestenson gate is performed. The full QFT is shown in sequence Seq5.1.



Please note, that gates conditional to multiple levels of the same spin (i.e. the qutrit) can be efficiently implemented as a single gate and are only here shown as two separate gates for better comprehensibility.

### 5.3 The quantum phase estimation algorithm

The general goal of the quantum phase estimation algorithm is, to find the unknown eigenvalue  $e^{i\Delta\phi}$  of a unitary operator  $U$ . What first seems like a very abstract formulation

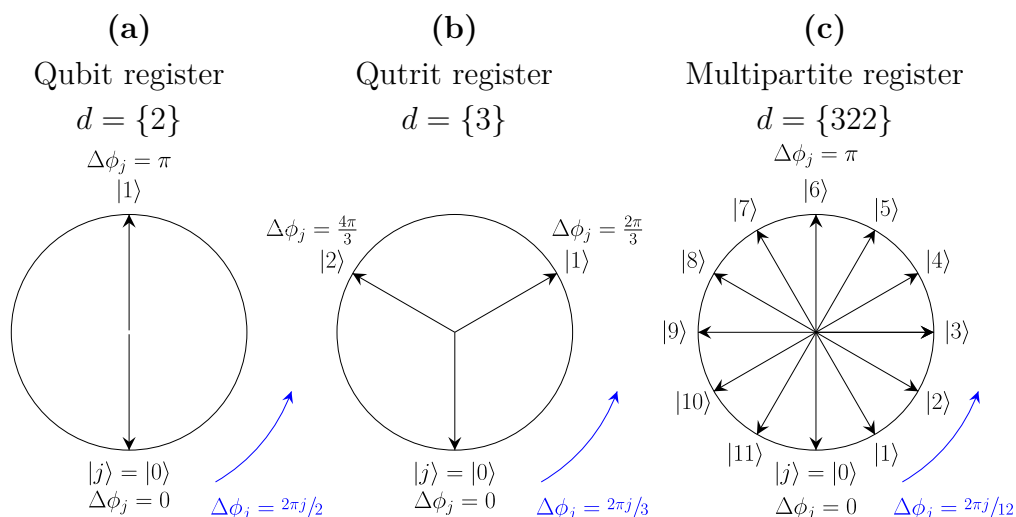


**Fig. 5.1: Sensing phases  $\Delta\phi_j$  and their associated computational basis states**

The iQFT maps a state  $|\Delta\phi_j\rangle$  with the associated phase  $\Delta\phi_j$  to a computational basis state  $|j\rangle$ . This state  $|j\rangle$  can be read out to yield a digital representation of  $\Delta\phi_j$  (cf. equation 5.18).

(a) A qubit register only can represent binary 0 and 1, which allows to map the phases 0 ( $\pi$ ) to the computational basis states  $|0\rangle$  ( $|1\rangle$ ). (b) A qutrit memory has three computational basis eigenstates to which the phases 0,  $2\pi/3$ ,  $4\pi/3$  are mapped. (c) With a multipartite register with multiplicities  $d = \{322\}$  twelve phases  $\Delta\phi_j$  can be mapped to the twelve different computational basis states. For example, the state  $|j = 8\rangle = |j_3 j_2 j_1\rangle = |102\rangle$  (cf. equation 5.14) corresponds to a phase  $\Delta\phi_j = 2\pi 8/12$  (cf. equation 5.4).

in the context of quantum metrology becomes clear, when one rewrites the output state of the Ramsey sensing sequence, equation 5.1, as

$$\begin{aligned}
 |\psi\rangle &= \frac{1}{\sqrt{2}} (|0\rangle + e^{i\Delta\phi} |1\rangle) \\
 &= \underbrace{\begin{pmatrix} 1 & 0 \\ 0 & e^{i\Delta\phi} \end{pmatrix}}_{U_{\text{Ramsey}}} \frac{1}{\sqrt{2}} (|0\rangle + |1\rangle)
 \end{aligned} \tag{5.17}$$

The Ramsey sequence implements the gate unitary operation  $U_{\text{Ramsey}}$ , whose eigenvalue  $\Delta\phi$  gives us the desired information about the measured quantity. Please note, that the sign of  $\Delta\phi$  was inverted, which does not change the working principle.

The key ingredient of the quantum phase estimation algorithm is the inverse quantum Fourier transform  $\text{iQFT} = \text{QFT}^\dagger$ , which can be straightforwardly constructed by inverting the sequence obtained for the QFT. The operational principle can be illustrated with the definition of the QFT, which is rewritten with the sensing phase  $\Delta\phi_j = 2\pi j/N$  to become equation 5.18.

$$\begin{aligned}
 QFT |j\rangle &= \frac{1}{\sqrt{N}} \sum_{k=0}^{N-1} e^{ik\Delta\phi_j} |k\rangle \\
 &= \frac{1}{\sqrt{N}} \left[ |0\rangle + e^{i\Delta\phi_j} |1\rangle + e^{2i\Delta\phi_j} |2\rangle + \dots + e^{(N-1)i\Delta\phi_j} |N-1\rangle \right] \\
 &\equiv |\Delta\phi_j\rangle
 \end{aligned} \tag{5.18}$$

For  $\Delta\phi_j < 2\pi$ , the QFT bijectively connects the state  $|\Delta\phi_j\rangle$  (and thereby the sensing phase  $\Delta\phi_j$ ) in the Fourier basis to the state  $|j\rangle$  in the computational basis (cf. figure 5.1), which is guaranteed by the unitarity of the QFT. This observation gives the idea of the quantum phase estimation algorithm: If the state  $|\Delta\phi_j\rangle$  can be generated by some sensing algorithm, the iQFT efficiently transforms it into an eigenstate of the computational basis and the computational basis state  $|j\rangle$  represents the phase  $\Delta\phi$  with a resolution of  $2\pi/N$ .

**Quantum phase estimation algorithm** The quantum phase estimation algorithm uses the following procedure to obtain an approximation of  $\Delta\phi$ :

1. Create an equal superposition state of the memory register

$$|\psi_0\rangle = |0\rangle + |1\rangle + |2\rangle \dots + |N-1\rangle \tag{5.19}$$

2. Use a quantum sensor to imprint a phase  $\Delta\phi$  onto the memory register, resulting in the state

$$|\psi_{\Delta\phi_j}\rangle = |0\rangle + e^{i\Delta\phi_j} |1\rangle + e^{i2\Delta\phi_j} |2\rangle + \dots + e^{i(N-1)\Delta\phi_j} |N-1\rangle \tag{5.20}$$

The procedure of writing a phase  $\Delta\phi$  to a multipartite quantum register is discussed in more detail in one of the next paragraphs.

3. Apply the iQFT to transform from the Fourier basis into the computational basis. For

$$\begin{aligned}
 \Delta\phi &= \Delta\phi_j \\
 &= \frac{2\pi}{N} j
 \end{aligned} \tag{5.21}$$

the result is the computational basis state  $|j\rangle$ . For  $\Delta\phi \neq \Delta\phi_j$ , a superposition state is obtained.

4. Read out the memory register in the computational basis.

**Behavior for phases  $\Delta\phi \neq \Delta\phi_j$**  So far, the quantum phase estimation algorithm was only discussed in the context of written phases  $\Delta\phi_j = \frac{2\pi}{N}j$  (step 2). This was necessary, as they are, in the context of the derivation of the quantum phase estimation algorithm, the result of the application of the QFT to the quantum state  $|j\rangle$ . However, as the quantum phase estimation procedure no more generates the phases  $\Delta\phi$  by application of the QFT, this restriction is no more appropriate. In the context of the quantum phase estimation procedure, the restriction must be loosened to  $\Delta\phi \in \mathbb{R}$ , as any real number phase can in principle be imprinted on the quantum register by a quantum sensor. Figures 5.2a to 5.2c show the probabilities  $p_j(\Delta\phi)$  to find registers of different sizes  $N$  in a state  $|j\rangle$ , when a phase  $\Delta\phi$  was imprinted on them. The probabilities  $p_j(\Delta\phi)$  are given by

$$p_j(\Delta\phi) = |\langle j | iQFT | \psi_{\Delta\phi} \rangle|^2 \quad (5.22)$$

with  $\Delta\phi$  according to equation 5.20. Figures 5.2a to 5.2c that phases between  $\Delta\phi_j$  and  $\Delta\phi_{j+1}$  are mapped to superposition states of  $|j\rangle$  and  $|j+1\rangle$  with a very high probability and thus, the quantum phase estimation algorithm also allows for detection of phases  $\Delta\phi \neq \Delta\phi_j$ .

**Writing a phase  $\Delta\phi$  to a multipartite register** Step 2 of the quantum phase estimation procedure requires to write the sensing phase  $\Delta\phi_j$  into the memory register to obtain the state

$$|\psi_{\Delta\phi_j}\rangle = |0\rangle + e^{i\Delta\phi_j} |1\rangle + e^{i2\Delta\phi_j} |2\rangle + \dots + e^{i(N-1)\Delta\phi_j} |N-1\rangle \quad (5.23)$$

For the quantum phase estimation algorithm it is important to know, how the sensing resources (i.e. the number of applications of  $U = e^{i\Delta\phi_j}$ ) have to be assigned to the individual qudit states such that the state equation 5.23 is generated. With equation 5.10d, the state of the  $l$ -th qubit can be written as

$$|\psi_l\rangle = \frac{1}{\sqrt{d_l}} \sum_{k_l=0}^{d_l-1} e^{ik_l\Delta\phi_j^{(l)}} \quad (5.24)$$

with  $\Delta\phi_j^{(l)} = j \prod_{m=1}^l d_m^{-1}$ . Therefore, the sensing phases for  $k_l = 1$  have a ratio

$$\frac{\Delta\phi_j^{(l-1)}}{\Delta\phi_j^{(l)}} = d^{(l)} \quad (5.25)$$

Without loss of generality, the phase  $\Delta\phi_j^{(n)} = \Delta\phi_j$  can be assigned to the  $n$ -th qubit. This assignment is equivalent to a single application of  $U$  to the state  $|j_n = 1\rangle$  of the  $n$ -th qubit. The sensing resources are the total required applications of  $U$  or a total sum

of phases written to the memory register of

$$\begin{aligned}
 \Delta\phi_{j,\text{tot}} &= \sum_{l=1}^n (d_l - 1) \Delta\phi_j^{(l)} \\
 &= \Delta\phi_j [(d_n - 1) + (d_{n-1} - 1) d_n + \dots + (d_1 - 1) d_n d_{n-1} \dots d_2] \\
 &= \Delta\phi_j \left[ d_n - 1 + \sum_{l=1}^{n-1} (d_l - 1) \prod_{m=l+1}^n d_m \right] \\
 &= (N - 1) \Delta\phi_j
 \end{aligned} \tag{5.26}$$

This may be surprising, as one would now expect the total sensing time to be the sum of the phases which were acquired by each individual state. However, the different states belonging to one qudit can (unlike the states of different qudits) simultaneously acquire a phase. Thus the  $d_l$  states of the  $l$ -th qudit require only  $(d_l - 1) \Delta\phi^{(l)}$  applications of  $U$ .  $U$  shall be applied to the qudit states a total of  $N - 1$  times, such that the total accumulated phase is  $(N - 1) \Delta\phi$ . An example of this behavior is found in the phase acquisition of the  $^{14}\text{N}$  qutrit memory, which is detailedly discussed in appendix G. Equations 5.21 and 5.26 together result in

$$\Delta\phi_{j,\text{tot}} = 2\pi \frac{N - 1}{N} j \tag{5.27}$$

and with  $j_{\text{max}} = N - 1$  in

$$\begin{aligned}
 \Delta\phi_{\text{tot, max}} &= 2\pi \frac{(N - 1)^2}{N} \\
 &= 2\pi \left( N + \frac{1}{N} - 2 \right)
 \end{aligned} \tag{5.28}$$

In the following two paragraphs, the phases for the two important examples of a single qutrit memory and a memory register consisting of one qutrit and two qubits are discussed.

**Writing phases to a single qutrit register** For the example of a single qudit  $d = \{3\}$  with  $n = 1$  and  $N = 3$ , the sensing phase is  $\Delta\phi_j^{(1)} = \Delta\phi_j$  leading to the state (cf. equations 5.24 and 5.25)

$$|\psi\rangle = \frac{1}{\sqrt{3}} \left( |0\rangle + e^{i\Delta\phi_j} |1\rangle + e^{2i\Delta\phi_j} |2\rangle \right) \tag{5.29}$$

The total written phase is  $\Delta\phi_{j,\text{tot}} = 2\Delta\phi_j$  (cf. equation 5.26). Please note, that for a single qudit of multiplicity ( $d = \{d_1\}$ ) with  $j = j_1$ , the definition of the QFT suffices to determine the sensing phases that must be acquired by each individual level.

**Writing phases to a twelve level register of one qutrit and two qubits** For the example of a memory register of one qutrit ( $d_1 = 3$ ) and two qubits ( $d_2 = d_3 = 2$ ,  $d = \{322\}$ ) with  $n = 3$ ,  $N = 12$ , the sensing phases that need to be written to the individual qudit states are (cf. equation 5.25)

$$\begin{aligned}
 \Delta\phi_j^{(3)} &= \Delta\phi_j \\
 \Delta\phi_j^{(2)} &= d_3\Delta\phi_j \\
 &= 2\Delta\phi_j \\
 \Delta\phi_j^{(1)} &= d_3d_2\Delta\phi_j \\
 &= 4\Delta\phi_j
 \end{aligned} \tag{5.30}$$

leading to the product state (cf. equations 5.24 and 5.25)

$$\begin{aligned}
 |\psi\rangle &= \frac{1}{\sqrt{3}} \left( |0\rangle + e^{4i\Delta\phi_j} |1\rangle + e^{8i\Delta\phi_j} |2\rangle \right) \\
 &\otimes \frac{1}{\sqrt{2}} \left( |0\rangle + e^{2i\Delta\phi_j} |1\rangle \right) \\
 &\otimes \frac{1}{\sqrt{2}} \left( |0\rangle + e^{i\Delta\phi_j} |1\rangle \right)
 \end{aligned} \tag{5.31}$$

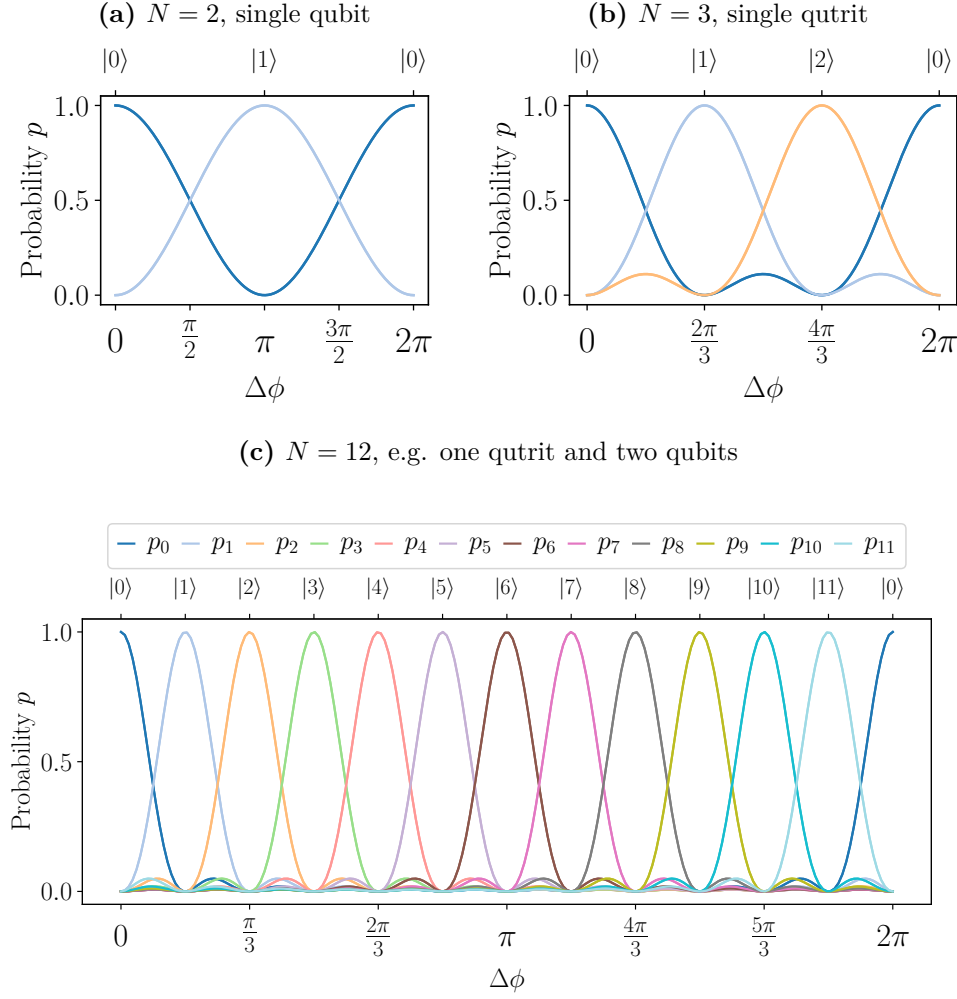


**Fig. 5.2: Phase estimation of arbitrary phases  $\Delta\phi$  on different memory register sizes.** For different register sizes  $N$ , the imprinted phase  $\Delta\phi$  is swept and the probabilities to find the register in computational basis state  $|j\rangle$  after performing the iQFT is plotted. For the phases  $\Delta\phi = 2\pi j/N$ , the eigenstates  $|j\rangle$  are found, while for all other phases one finds superposition states. **(a)** For  $N = 2$ , only the phases 0 and  $\pi$  are mapped to basis states, while the phases  $\Delta\phi_j = \frac{\pi}{2}$  and  $\frac{3\pi}{2}$  are both mapped to a superposition of the two basis states and hence can not be distinguished. **(b)** For  $N = 3$ , the phases  $\Delta\phi_j = 0, \frac{2\pi}{3}$  and  $\frac{4\pi}{3}$  are mapped to eigenstates. Interestingly, also for phases  $\Delta\phi \neq \Delta\phi_j$  the occupation probabilities  $p_j$  allow to find good estimates for  $\Delta\phi$ . For example for  $\Delta\phi = \frac{\Delta\phi_0 + \Delta\phi_1}{2} = \frac{\pi}{3}$ , the probability  $p_2$  to find the qutrit in state  $|2\rangle$  is very low, while there is a very high probability  $p_0 = p_1 \approx 0.5$  to find the memory in states  $|0\rangle, |1\rangle$ . **(c)** For a memory register composed of e.g. one qutrit and two qubits,  $N = 12$  different phases  $\Delta\phi_j$  can be mapped to computational basis states  $|j\rangle$ .

## 5.4 Experimental three level quantum phase estimation with quantum correlation spectroscopy

In this section, the experimental implementation of the quantum phase estimation algorithm with the  $^{14}\text{N}$  qutrit as a three level quantum register is presented. Therefore, a quantum correlation measurement sequence analogously to sequence Seq3.5 is used, to allow for high measurement precision (cf. chapter 3) and make best use of the increased storage capacity of the qutrit memory compared to the previously used qubit memory. For this section, the  $^{14}\text{N}$  qutrit memory register states are mapped to the logical states according to  $|-\rangle = |0\rangle$ ,  $|0\rangle = |1\rangle$  and  $|+\rangle = |2\rangle$ . For the construction of the sequence which use these states as memory levels, three ingredients are necessary:

- The Chrestenson gate  $C$  as the three level equivalent of the Hadamard gate to generate a superposition state.

$$\begin{aligned} |\psi_0\rangle &= C |0\rangle \\ &= \frac{1}{\sqrt{3}} (|-\rangle + |0\rangle + |+\rangle) \end{aligned} \quad (5.32)$$

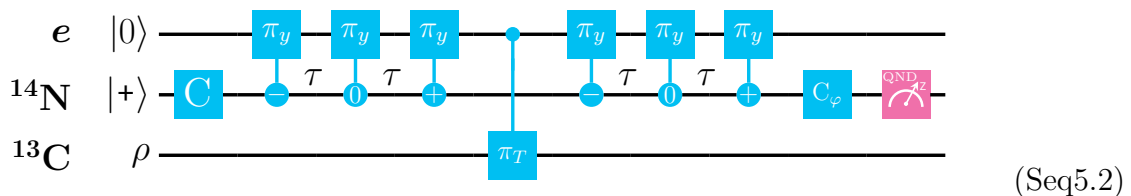
A discussion of the Chrestenson gate is found in appendix F

- A sensing part, which maps the electron sensor frequency shift  $\Delta f \propto \Delta\phi$  to the state

$$|\psi\rangle(\Delta\phi) = \frac{1}{\sqrt{3}} (|-\rangle + e^{i\Delta\phi_j} |0\rangle + e^{2i\Delta\phi_j} |+\rangle) \quad (5.33)$$

- An implementation of the iQFT for the given register size. According to section 5.2, for a single qutrit memory with a register of size  $n = 1$  and  $N = 3$  the iQFT can be implemented by a single Chrestenson gate.

**Sensing the phase  $\Delta\phi$**  One possible realization is given in sequence Seq5.2, which is designed for the detection and manipulation of single  $^{13}\text{C}$  nuclear spins with very high frequency precision. The main characteristics are analogous to sequence Seq3.8 on page 87. However, due to the increased size of the quantum register, a phase must not be written to one but two memory spin levels. Therefore, the two sensing times each involve three nuclear spin controlled electron  $\pi$  - pulses  $C_n\text{Pi}_e$ .



During  $T_c$ , the target  $^{13}\text{C}$  nuclear spin is flipped with a  $\pi$  - pulse. To avoid confusion it is important to note, that for technical reasons the order of the  $C_n\text{Pi}_e$  is reverted compared to the qubit sequence Seq3.8 on page 87. There, the  $C_n\text{Pi}_e$  gates were first performed selective to  $^{14}\text{N}$  memory spin states  $|+\rangle$  and then on  $|0\rangle$ , while here the order is  $|-\rangle$ ,  $|0\rangle$ ,  $|+\rangle$ .

According to equation 3.14, per sensing time  $\tau$  of sequence Seq5.2 a phase

$$\phi_\tau = 2\pi m_C A_{zz} \tau \quad (5.34)$$

is written to the nuclear spins with  $m_C$  being the  $^{13}\text{C}$  quantum number ( $m_C = +1/2, -1/2$ ). Therefore, before the final Chrestenson gate (i.e. the iQFT), the state is

$$\psi_{\Delta\phi} = \frac{1}{\sqrt{3}} \left( |-\rangle + e^{i\Delta\phi} |0\rangle + e^{2i\Delta\phi} |+\rangle \right) \quad (5.35)$$

$\Delta\phi = 2\phi_\tau$ . The state evolution during sequence Seq5.2, which leads to equation 5.35 is discussed in more depth in appendix G.

$^{13}\text{C}$ in mixed state	
$p_{-, \text{mixed}}$	$\frac{1}{9}(1 + 2\cos(2\pi A_{zz} \tau))^2$
$p_{0, \text{mixed}}$	$\frac{4}{9}(2 + \cos(2\pi A_{zz}\tau))\sin(2\pi A_{zz}\tau)^2$
$p_{+, \text{mixed}}$	$\frac{4}{9}(2 + \cos(2\pi A_{zz}\tau))\sin(2\pi A_{zz}\tau)^2$

**Table 5.1: Dependence of  $^{14}\text{N}$  qutrit probabilities on the sensing phase for a mixed state target spin.** When the target nuclear spin is in an equal superposition of its eigenstates  $|+\rangle$  and  $|-\rangle$ , it produces positive and negative fields with the same probabilities. Then the probability to measure memory spin states  $p_0$  and  $p_+$  become identical and no information about the sign of the target spin hyperfine coupling  $A_{zz}$  can be deduced. For a polarized target spin, this is possible.

**State occupation probabilities in the computational basis** The phase information is read out as probabilities

$$p_j(\Delta\phi) = |\langle j | iQFT | \psi_{\Delta\phi} \rangle|^2 \quad (5.36)$$

to find the  $^{14}\text{N}$  qutrit memory in one of the computational basis states  $|j\rangle = |+\rangle, |0\rangle, |-\rangle$  (cf. equation 5.36) after the iQFT. These probabilities can be expressed as

$$\begin{aligned} p_- &= \frac{1}{9}(1 + 2\cos(\Delta\phi))^2 \\ p_0 &= \frac{4}{9}\sin^2\left(\frac{\Delta\phi}{2}\right) \left(2 + \sqrt{3}\sin(\Delta\phi) + \cos(\Delta\phi)\right) \\ p_+ &= \frac{4}{9}\sin^2\left(\frac{\Delta\phi}{2}\right) \left(2 - \sqrt{3}\sin(\Delta\phi) + \cos(\Delta\phi)\right) \end{aligned} \quad (5.37)$$

with  $\Delta\phi = 4\pi m_C A_{zz} \tau$ . Table 5.1 lists the probabilities  $p(\tau)$  for an unpolarized nuclear target spin with hyperfine coupling  $A_{zz}$ . In this case, the sign of  $\Delta\phi$  is undetermined for any measurement run, and thus positive and negative sensing phases are equally probable. The  $^{14}\text{N}$  probabilities  $p_0$  and  $p_+$  therefore become

$$p_{0,\text{mixed}} = p_{+,\text{mixed}} = \frac{p_0 + p_+}{2} \quad (5.38)$$

Figure 5.3b shows the experimentally determined  $^{14}\text{N}$  probabilities for the unpolarized target nuclear spin  $^{13}\text{C}_2$  with hyperfine coupling  $A_{zz} \approx 90$  kHz in dependence of the phase accumulation time  $\tau$ . Figures 5.3a and 5.3c, show the same experiment but with  $^{13}\text{C}_2$  fully polarized into spin states  $|-\rangle$  and  $|+\rangle$ , respectively.

**Comparison with two level memory** To understand, why a three-level system is useful, a comparison to the two-level case is made. A two-level system can give a binary result in a single run of the experiment. An example for the respective observable can be: “Is there a spin present with hyperfine coupling  $A_{zz}$ ?” or if one already knows that there exists a spin with coupling  $A_{zz}$ , one may ask “Is the spin with coupling  $A_{zz}$  in spin state  $|+\rangle$  or in state  $|-\rangle$ ?”. If both questions should be answered at the same time, a third level is necessary. Then a single experiment can answer the ternary question “Is the spin with coupling  $A_{zz}$  in spin state  $|+\rangle$  or is it in state  $|-\rangle$  or does it not exist?”. Each of the three results is mapped to one of the three readout basis states  $|+\rangle$ ,  $|0\rangle$  or  $|-\rangle$ . In the here presented experiments, each result is associated with one possible sensing phase  $\Delta\phi$ .

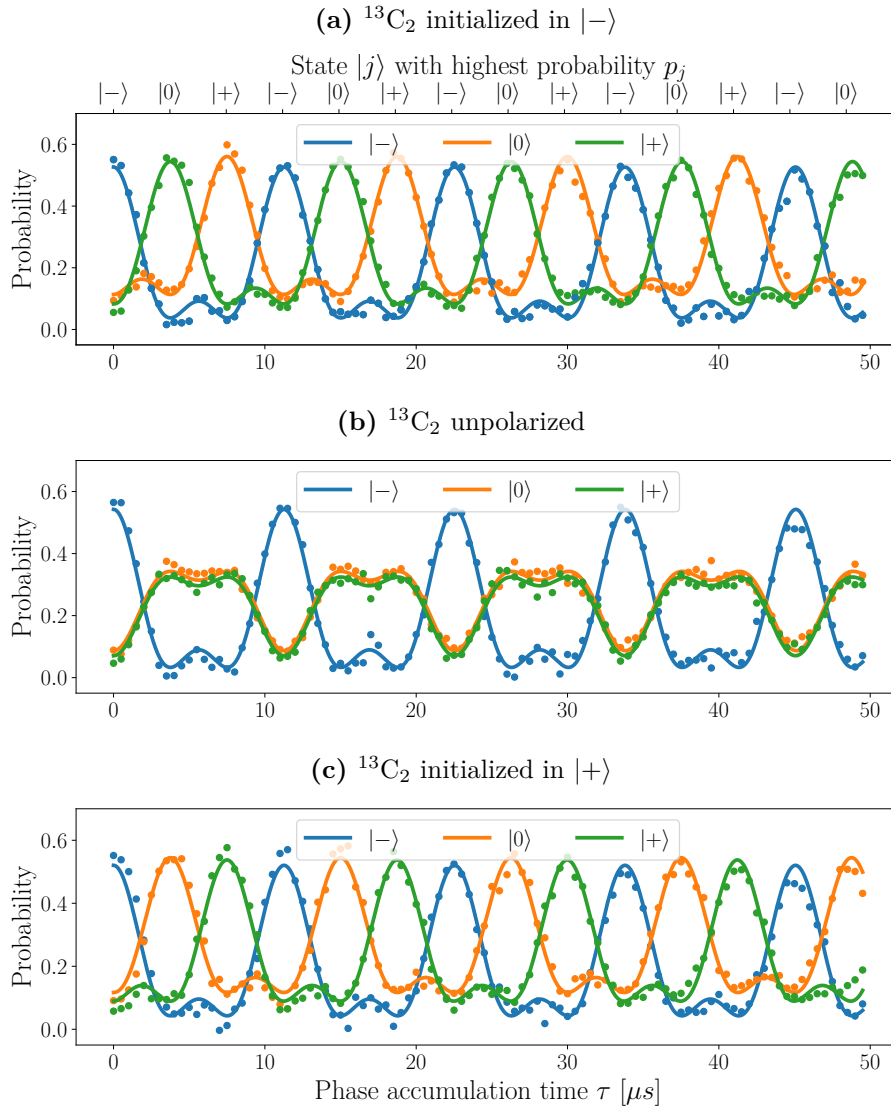


**Fig. 5.3: Experimental three level quantum phase estimation performed with quantum correlation spectroscopy.** The quantum phase estimation algorithm is experimentally implemented with a quantum correlation spectroscopy sequence used for phase accumulation and the sensing time  $\tau$  is swept (cf. sequence Seq5.2). The target nuclear spin is  $^{13}\text{C}_2$  with a hyperfine coupling strength  $A_{zz} \approx 90$  kHz. When the target nuclear spin is initialized in state  $|+\rangle$  ( $|-\rangle$ ), the sensing phase  $\Delta\phi$  which is accumulated by the  $^{14}\text{N}$  nuclear spin memory is positive (negative). For an unpolarized target spin, the  $^{14}\text{N}$  occupation probabilities of states  $|+\rangle$  and  $|-\rangle$  are averaged values.

## 5.5 Experimental implementation of the quantum phase estimation algorithm on a twelve level register

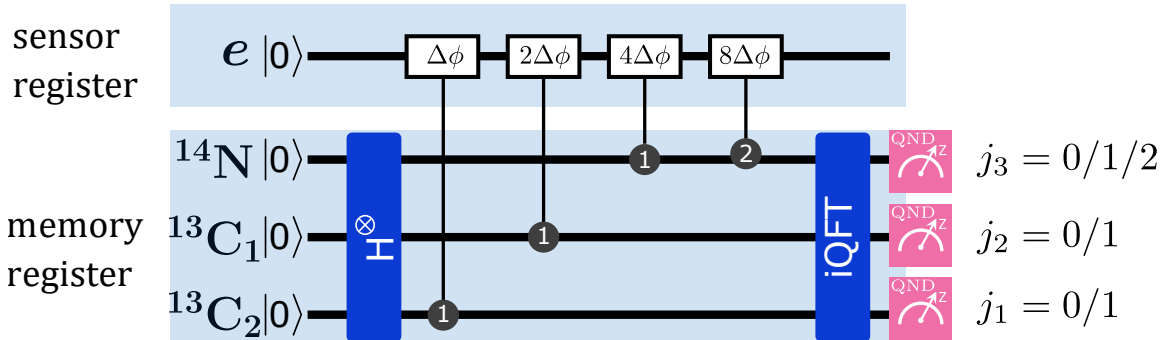


**Fig. 5.4: Schematics of quantum phase estimation algorithm on one qutrit and two qubits.** First, the nuclear spin memory register is initialized in  $|000\rangle$  and brought into an equal superposition state by generalized Hadamard gates. Then, the phases  $n\Delta\phi$  are written to the levels of the individual qudits. Finally, the phase information is processed by the iQFT gate and transformed to classical information via the readout.

In this section, the experimental implementation of the quantum phase estimation algorithm performed on a memory register of one qutrit and two qubits is shown. The QFT for this register size ( $n = 3$ ,  $d = \{322\}$ ,  $N = 12$ ) has already been derived as shown in sequence Seq5.1 and the iQFT can be obtained straightforwardly by reverting the QFT circuit and conjugating each involved quantum gate. The phases that need to be written to the individual qudit states are known from equation 5.31 on page 120. The general idea of this quantum phase estimation algorithm, which was already discussed in the previous sections of this chapter, is summarized in figure 5.4. A generalized Hadamard gate brings each involved qudit into a superposition state, which sets also the memory register into an equal superposition state of all  $N$  levels. Then a sensor device (in this case the NV center electron spin) imprints phases  $\Delta\phi$  on each of the qudit states, whose ratio is given by the quantum phase estimation algorithm (cf. section 5.3). After the phases have been imprinted, the iQFT is applied to the register, to efficiently transform the obtained phases into a computational basis state, which is then read out. Sequence Seq5.3 was used for the experimental implementation of the twelve-level quantum phase estimation

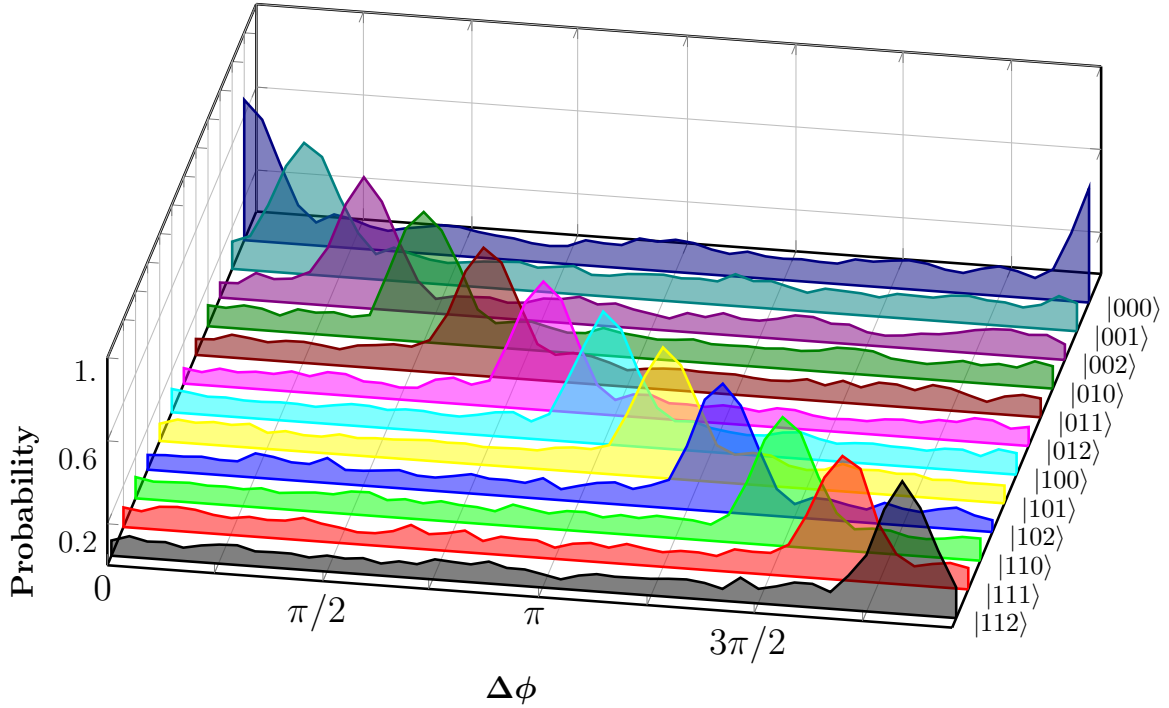
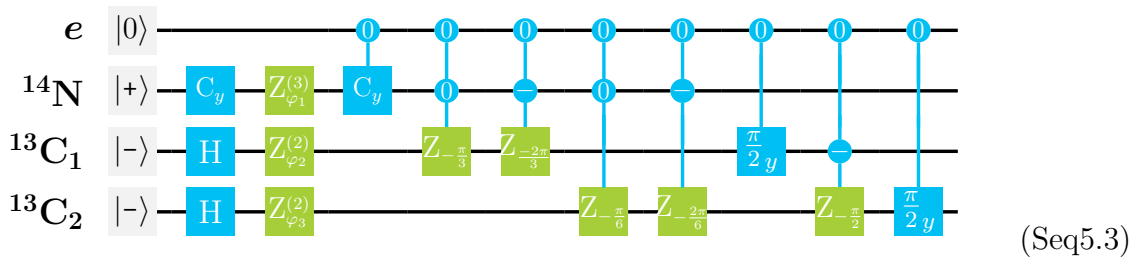


**Fig. 5.5: Experimental implementation of the twelve level quantum phase estimation algorithm.** A Hadamard gate brings the twelve-level memory register into an equal superposition state by resonantly applied RF driving. Then, a phase  $\Delta\phi$  is imprinted on the nuclear spin register according to equation 5.31. Finally, the phase information on the nuclear spin register is processed by the iQFT gate which efficiently transforms it into the computational basis. In this basis, the phase information is read out via nuclear spin SSR. With increasing sensing phase  $\Delta\phi$  which is written to the memory register, the probability to find the quantum register in higher states  $|j\rangle = |j_3j_2j_1\rangle$  is increased. It should be noted, that the maximally measured probabilities are lowered by  $\approx 30\%$  due to charge state  $NV^0$ . For better readability, the measured probability offset of state  $|000\rangle$ , which is also  $\approx 30\%$  due  $NV^0$  was removed.

algorithm.



The NV center electron spin serves as a mediator to allow for the implementation of the controlled phase gates between the otherwise non-interacting memory register nuclear spins. In this experimental realization, the phases are imprinted on the memory register by sweeping the phase of the RF driving field which is used for local gates on the nuclear spins. Thereby, a sensing sequence is emulated to show the operation principle of the quantum phase estimation circuit. For the experimental demonstration of the twelve-level quantum phase estimation algorithm, the sensing phase  $\Delta\phi$  is swept from zero to  $2\pi$  and the probability  $p_j$  to measure each of the twelve register states

$$\begin{aligned}
 |j = 0\rangle &= |000\rangle \\
 |1\rangle &= |001\rangle \\
 |2\rangle &= |002\rangle \\
 |3\rangle &= |010\rangle \\
 |4\rangle &= |011\rangle \\
 &\vdots
 \end{aligned} \tag{5.39}$$

is monitored. The experimental data is shown in figure 5.5 (cf. figure 5.2c for the equivalent simulated data). With increasing phase  $\Delta\phi$ , the probability to measure higher states  $|j\rangle$  increases. Most importantly, also for states

$$\Delta\phi \neq \frac{2\pi j}{N} \tag{5.40}$$

the probability distributions  $p_j$  allow for a reliable approximation of  $\Delta\phi$ .

## 5.6 Summary and outlook

In this chapter, the quantum phase estimation algorithm was experimentally implemented on a sensor-memory system of a single electron spin sensor and a hybrid qudit memory register of up to twelve levels. The quantum phase information is acquired by the electron spin sensor and written to the memory register, where it is processed by the inverse

quantum Fourier transform (iQFT) before it is converted to classical information by readout of the computational basis states.

To be able to accomplish this task, a general and instructive theory for construction of the quantum Fourier transform (QFT) and the quantum phase estimation algorithm on hybrid multiplicity quantum systems is given. Existing theories for memory registers which are composed of qudits of equal multiplicities are extended for the implementation of the QFT to memory registers which are composed of qudits of arbitrary multiplicities  $d = \{d_1 d_2 \dots d_n\}$ . As a first result, a gate sequence for the experimental implementation of the QFT a register of a one qutrit and two qubits is found. The QFT on a single qutrit was identified as the Chrestenson gate. A corresponding gate sequence for the implementation of the iQFT can be straightforwardly obtained by reverting the sequence for the QFT and conjugating each involved quantum gate. As a second result, a procedure was found for the determination of the sensing phases  $\Delta\phi^{(l)}$  that need to be written to each qudit. Only when this procedure is followed, the quantum phase estimation algorithm can find a meaningful approximation of an arbitrary sensing phase  $\Delta\phi$ . For a register of one qutrit and two qubits, the written phases must have ratios of 1 and 2, 1 and 4, and 1 and 8.

For the experimental implementation of the quantum phase estimation algorithm, firstly a qutrit memory register is used, to which a sensing phase  $\Delta\phi$  is written by a single electron spin sensor. Therefore, the electron spin sensor detects the magnetic field which is produced by single  $^{13}\text{C}$  nuclear spin with hyperfine coupling  $A_{zz} \approx 90$  kHz. This is achieved by a quantum correlation measurement, where two phase acquisition steps are separated by a long correlation time  $T_c$ . The combination of the quantum phase estimation algorithm with the quantum correlation spectroscopy allows to perform measurements which have high frequency precision due to long  $T_c$  and at the same time allow for determination of the signal amplitude with high precision and also high bandwidth. A three level memory increases the information content by a factor  $\log_2 3 \approx 1.58$  compared to a commonly used two-level memory. The qutrit sensing sequence is used to determine the amplitude and sign of the magnetization of a single  $^{13}\text{C}$  nuclear spin.

Secondly, the quantum phase estimation algorithm is experimentally implemented for the first time on a native hybrid spin system register consisting of a qutrit and two qubits (cf. [26], where a qutrit is emulated by two qubits). A twelve-level memory can obtain a factor of  $\log_2 12 \approx 3.58$  more phase information than a two-level memory and thus for example increase the bandwidth of an amplitude measurement by this factor.

In future experiments, the size of the memory register can be increased by the use of weakly coupled nuclear spins. Therefore, it may be necessary to go to lower temperatures, where the longitudinal relaxation time of the NV center electron spin is longer. The quantum phase estimation algorithms can be performed on the register of size  $N = 12$  to measure external magnetic fields or to improve the detection and coherent coupling to nuclear spins within the diamond. Proof of principle quantum algorithms such as Shor's

algorithm may be also an interesting application. In particular on the evolving field of quantum machine learning, new potential applications for the QFT are arising [205].

## Calibration of electron Rabi oscillations

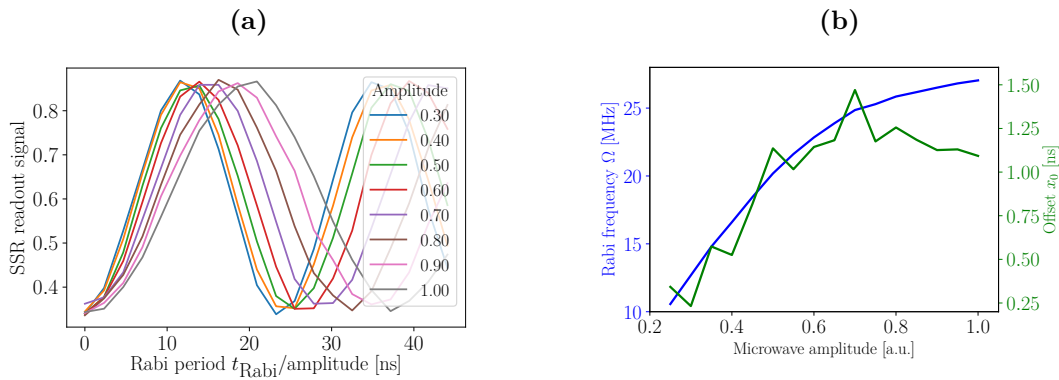


**Fig. A.1: Electron Rabi oscillations for different AWG amplitudes.** (a) For each curve, the  $x$  - axis is scaled by one over the amplitude. For perfectly linear amplitude - Rabi frequency behaviour, all curves would coincide. Instead, for larger amplitudes the Rabi frequency saturates and the increase is sub-linear. The curves were fitted to the function  $a \cos 2\pi\Omega(x - x_0) + c$  and the fit parameters  $\Omega$  and  $x_0$  are shown in (b).

Figure A.1a shows one set of Electron Rabi calibration measurements. The maximum Rabi frequency is  $\Omega \approx 27$  MHz. For larger amplitudes, the MW amplifier saturates and the Rabi frequency does no more increase linearly with the amplitude. Interestingly, there is an increasing offset  $x_0$ , which leads to an effective increase of the  $\pi$  - pulse duration by that value. For amplitude 0.8, the Rabi frequency is  $\Omega \approx 25$  MHz and the offset is  $x_0 \approx 1.25$  ns, which corresponds to a relative change in  $\pi$  - pulse duration of 5%. When high fidelity quantum operations are required, often even 1% Rabi miscalibration can be too much and this offset  $x_0$  needs to be taken into account.

# B

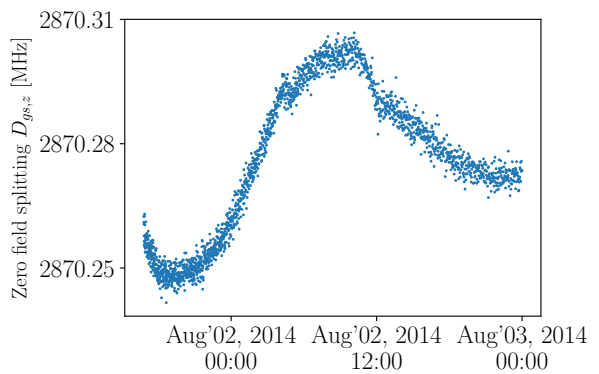
## Temperature tracking via the NV center electron spin double quantum transition

The ZFS of the electron spin triplet in the NV center optical ground state allows for the determination of temperature drifts with a gradient of [43]

$$\frac{\partial}{\partial T} D_{\text{es},z} = -74.2 \frac{\text{kHz}}{\text{K}} \quad (\text{B.1})$$

This effect here is used, to determine (undesired) temperature changes in the laboratory. Therefore, electron spin transitions  $m_s = 0 \leftrightarrow -1$  and  $m_s = 0 \leftrightarrow +1$  were measured directly after one another, while one measurement took less than 10s. The total drift corresponds to approximately 1 K.

**Fig. B.1: Temperature tracking with the NV center zero-field splitting.** The ZFS The data was taken between Aug 1st, 2014 at 4pm and Aug 3rd, 2014 at 12pm. The signal oscillates over the course of the day due to temperature fluctuations.



# C

## Additional experimental parameters

To give the reader a better overview about the experimental conditions under which the experiments were performed, here a full set of spin calibration data is shown. The magnetic field at the time of calibration was  $B_{0,z} = 0.67$  T. The NV center electron spin transition frequency  $m_s = 0 \leftrightarrow -1$  was 15 792.161 kHz. The electron ZFS could not be determined, as therefore the electron transition  $m_s = +1 \leftrightarrow 0$  would have to be measured, which has an approximate frequency of 21 532 MHz at this magnetic field. The maximum driving frequency for electron spin transition  $m_s = 0 \leftrightarrow -1$  was  $\approx 23$  MHz at a amplifier power of  $\approx 2.5$  W. For some experiments lower powers were used for technical reasons. Unfortunately, the technical equipment allows only to generate MW fields up to 18 GHz. Thus, all details given about  $m_s = +1$  have been calibrated at lower fields. Where no reliable statement about values can be made, no value is given.

Name	[MHz]	[kHz]
T [ $^{14}\text{N} = +1, +1$ ]	-9.1587	
T [ $^{14}\text{N} = -1, +1$ ]	0.7331	
T [ $^{13}\text{C} (A_{zz}=413 \text{ kHz}), +1$ ]	-6.7151	
T [ $^{13}\text{C} (A_{zz}=89 \text{ kHz}), +1$ ]	-7.0391	
T [ $^{14}\text{N} = +1, 0$ ]	-6.9939	19.67
T [ $^{14}\text{N} = -1, 0$ ]	2.8977	10.41
T [ $^{13}\text{C}, 0$ ]	-7.1278	34.33
T [ $^{14}\text{N} = +1, -1$ ]	-4.8285	6.45
T [ $^{14}\text{N} = -1, -1$ ]	5.0626	6.56
T [ $^{13}\text{C} (A_{zz}=413 \text{ kHz}), -1$ ]	-7.5405	36.42
T [ $^{13}\text{C} (A_{zz}=89 \text{ kHz}), -1$ ]	-7.2165	35.40

**Table C.1: Experimentally determined nuclear spin parameters for one nitrogen and multiple  $^{13}\text{C}$  nuclear spins.** Transition names are explained in figures 1.14a and 1.14b on page 33 and the external magnetic field during the measurement was  $B_{0,z} = 0.67 \text{ T}$ . Due to their three times larger gyromagnetic ratio, the  $^{13}\text{C}$  transition have significantly larger Rabi frequencies compared to the  $^{14}\text{N}$  transitions. Different Rabi frequencies for transitions of the same nuclear spin species are explained by hyperfine enhancement.

# D

## Effective sensing time for quantum enhanced stimulated echo

The MW - pulses used in the quantum enhanced sequence Seq3.4 (also cf. figure 3.1) are controlled gates. The electron spin spectrum is crowded, when many nuclear spins are hyperfine coupled to it and the electron spin resonance lines also are broadened by magnetic field drifts [17, 117] (cf. figure 1.15). Hence, the  $C_n\text{Pi}_e$ -gates, which are applied in the correlation sequence and the SSR measurements, are optimized for robustness against magnetic field drift and fluctuation of the MW field strength and to avoid spectral crosstalk [148]. While a  $C_n\text{Pi}_e$ - gate might be implemented by a rectangular time-domain pulse of Rabi frequency  $\Omega \approx 1.25$  MHz and duration  $t_p \approx 0.4$   $\mu\text{s}$ , the pulse has modulated amplitude and phase and takes  $t_p = 2$   $\mu\text{s}$  (see figure 3.1b).

During the novel quantum enhanced correlation sequence, four of these pulses were applied sequentially. A full correlation sequence is simulated in figure D.1 for  $\tau = 0$ ,  $T_c = 0$  and varying detuning. The comparably long duration of these pulses leads to phase accumulation on the memory spin even for sensing time  $\tau = 0$  as illustrated in figure D.1b. Apparently, over a spectral range of approximately 0.5 MHz the quantum state of the memory spin shows almost full phase contrast and hence good fidelity. An effective sensing time  $\tau_{\text{eff}} = \tau_0 + \tau$  has been introduced, where  $\tau_0$  accommodates for phase accumulation during  $C_n\text{Pi}_e$ - gate operations. The value of  $\tau_0$  is estimated as follows.

When the magnetic field stays constant during  $T_c$  also these finite length pulses do not lead to total phase accumulation. Hence, a nuclear spin with hyperfine coupling  $A_{zz} = 500$  kHz has been considered, which is flipped in  $T_c$ . During the first two  $C_n\text{Pi}_e$ -gates it may be in state  $|+\rangle$  exhibiting an initial shift of 250 kHz. Thus it exhibits a shift of  $-250$  kHz during the second sensing step  $\tau$  performed between the second two  $C_n\text{Pi}_e$ -gates. According to the pulse analysis displayed in figure D.1b this leads to a total

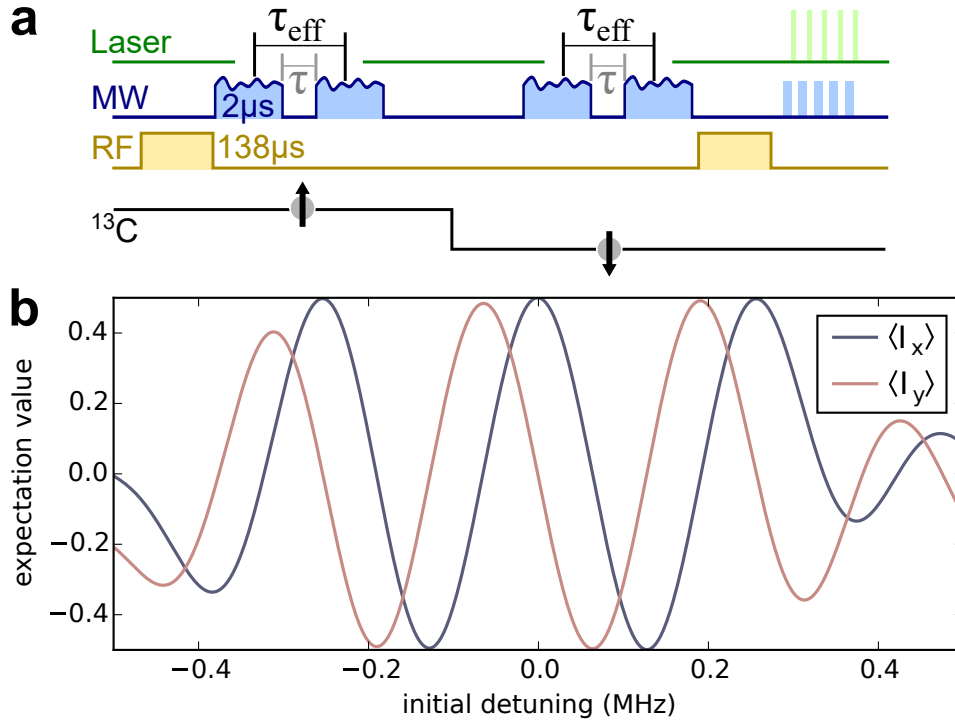


**Fig. D.1: Effective sensing time  $\tau_{\text{eff}}$ .** (a), Illustration of effective sensing time  $\tau_{\text{eff}}$  and actual  $C_n\text{Pi}_e$ - gate separation  $\tau$  during the sensing intervals of the correlation spectroscopy sequence (cf. figure 3.1) due to finite pulse length. A  $^{13}\text{C}$  sample spin (spin state is indicated by lower (black) line and arrow) adds an initial detuning to the sensor spin in the first sensing time  $\tau_{\text{eff}}$ , is flipped during  $T_c$  and then adds the negative of the initial detuning to the sensor spin during the second  $\tau_{\text{eff}}$ . (b), Simulated phase of the memory spin after the second phase accumulation period as displayed in (a) for  $\tau = 0$  depending on the initial detuning created by the sample spin. The phase is depicted as  $x$  and  $y$  quadratures of the memory spin,  $\langle I_x \rangle$  and  $\langle I_y \rangle$  respectively. This phase is attributed to an accumulation time  $\tau_0 = \tau_{\text{eff}} - \tau$  during the  $C_n\text{Pi}_e$ - gate duration. Over a spectral range of approximately 0.5 MHz the expectation values show almost full contrast.

phase accumulation of  $\Delta\phi = 2\pi A_{zz}\tau_0 \approx 2\pi$  and hence,  $\tau_0 \approx 2\ \mu\text{s}$  can be estimated.

# E

## Trigonometrical similarities: $\sin(\sin)$ and $\sin(\cos)$

Although there exists no trigonometrical identity, the functions  $\sin(x)$  and  $\sin(\sin(x))$  as well as  $\cos(x)$  and  $\sin(\cos(x))$  are very similar functions up to a factor 0.84 in amplitude. The very good pair wise agreement between the respective functions is shown in figure E.1.

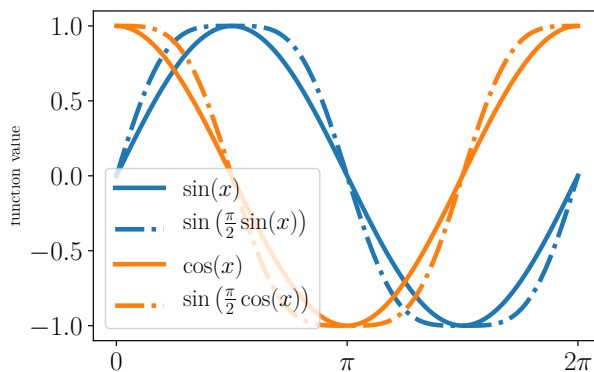


**Fig. E.1:** Illustration of similarities between nested trigonometrical functions sine and cosine. This plot shows the functions  $f_1 = \sin x$ ,  $f_2 = \cos x$  as well as  $\sin f_1$  and  $\sin f_2$ .

## The Chrestenson gate implemented on the nuclear spin qutrit

The quantum phase estimation algorithm introduced in section 5.3 requires the generation of an equal superposition state on each qudit of the memory register. In chapter 3, the  $^{14}\text{N}$  qubit subspace  $|+\rangle$ ,  $|0\rangle$  was put into a superposition state by a  $\pi/2$  - pulse, transferring initial state  $|+\rangle$  to state

$$|\psi\rangle_{\text{N}} = \frac{1}{\sqrt{2}} (|+\rangle + |0\rangle) \quad (\text{F.1})$$

For the sake of completeness, it should be noted, that a Hadamard gate would have performed this task equally well. One equivalent operation to a  $\pi/2$  - pulse for a qutrit system is the Chrestenson gate [206], which is given by equation F.2.

$$C = \frac{1}{\sqrt{3}} \begin{pmatrix} 1 & 1 & 1 \\ 1 & e^{\frac{2\pi i}{3}} & e^{\frac{4\pi i}{3}} \\ 1 & e^{\frac{4\pi i}{3}} & e^{\frac{2\pi i}{3}} \end{pmatrix} \quad (\text{F.2})$$

which when applied to the state  $|+\rangle$  results in spin state

$$|\psi\rangle_{\text{N}} = \frac{1}{\sqrt{3}} (|+\rangle + |0\rangle + |-\rangle) \quad (\text{F.3})$$

When the Chrestenson gate is applied twice, every eigenstate of the computational basis is again transferred to an eigenstate of the computational basis.

$$C^2 = \begin{pmatrix} 1 & 0 & 0 \\ 0 & 0 & 1 \\ 0 & 1 & 0 \end{pmatrix} \quad (\text{F.4})$$

Only the  $|+\rangle$  state remains unchanged by two sequential applications of  $C$ . Therefore, unlike the Hadamard gate, the Chrestenson gate is not its own inverse.

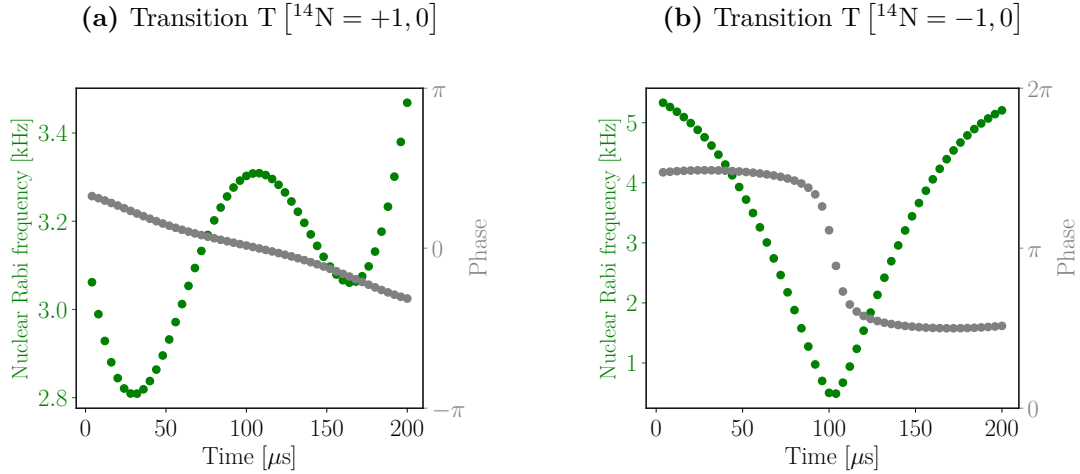


**Fig. F.1: Chrestenson gate implementation via amplitude and phase modulated RF pulses.** (a) and (b) show amplitudes and phases of the RF driving for the implementation of a Chrestenson gate. The pulse is subdivided in 50 time-slices of 4  $\mu\text{s}$  duration, each.

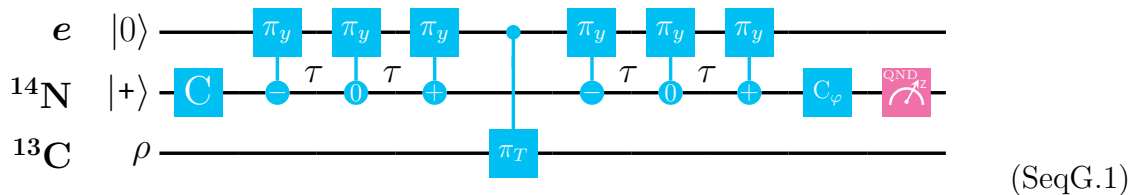
**Experimental implementation of the Chrestenson gate via two-frequency driving** A two-level system can be manipulated with Rabi driving on a single RF frequency, as discussed in section 1.6.4. In principle, the same is true for a multi-level system, if the driving frequency is large compared to the frequency separation of the individual levels. Here, this is not the case, and for the manipulation of the  $^{14}\text{N}$  three-level system, two independent frequencies are required for the frequency selective, separate manipulation of the two transitions T [ $^{14}\text{N} = +1, 0$ ] and T [ $^{14}\text{N} = -1, 0$ ] (cf. figure 1.14b, further experimental parameters are found in table C.1) [204]. Please note, that the electron spin is chosen to be in  $m_s = 0$ , which is convenient but in principle works equally well as any of the other two states  $m_s = \pm 1$ .

The Chrestenson gate is experimentally implemented as amplitude and phase modulated pulse, which was optimized with the optimal control platform DYNAMO [148]. Used amplitudes and phases are shown for T [ $^{14}\text{N} = +1, 0$ ] in figure F.1a and for T [ $^{14}\text{N} = -1, 0$ ] in figure F.1b.

# G

## State evolution during quantum phase estimation on a qutrit memory

The quantum enhanced correlation spectroscopy sequence Seq3.8, which is capable of detecting and interacting with individual  $^{13}\text{C}$  nuclear spins, is extended to use all three instead of only two  $^{14}\text{N}$  nuclear spin eigenstates as memory states. Therefore, a third  $\text{C}_n\text{Pi}_e$ -gate, which is selective to  $^{14}\text{N}$  memory spin state  $|-\rangle$  and a second sensing time  $\tau$  are added to both the first and the second sensing step. The resulting sequence SeqG.1 implements the quantum phase estimation algorithm (cf. section 5.3) on a single three level quantum register ( $N = 3, n = 1$ ).



During  $T_c$ , the sample spin is flipped with a  $\pi$  - pulse.

Here, the evolution during sequence SeqG.1 (which is equivalent to sequence Seq5.2 of the main text) is discussed. Thereby, the previously used notation ( $|\psi_e\rangle = |0\rangle, |-\rangle$ ) for the states of the electron spin subspace and ( $|\psi_n\rangle = |+\rangle, |0\rangle, |-\rangle$ ) for the states of the  $^{14}\text{N}$  nuclear spin qutrit is retained. When the  $\text{C}_n\text{Pi}_e$ -gates are assumed to be infinitesimally short, after the first Chrestenson gate the spin state is

$$\begin{aligned}
 |\psi_0\rangle &= |\psi_{e,0}\rangle \otimes |\psi_{n,0}\rangle \\
 &= |0\rangle \otimes (|+\rangle + |0\rangle + |-\rangle) \\
 &= | +0\rangle + |00\rangle + | -1\rangle
 \end{aligned}
 \tag{G.1}$$

Then, during the first sensing time, the memory state  $|-\rangle$  acquires a phase  $\phi$  due to the field produced by the sample spin (or by any other signal which should be sensed) and an additional phase  $\alpha_-$  due to the evolution of the memory spin in the hyperfine field of the electron spin. The resulting state is

$$|\psi_1\rangle = |0+\rangle + |00\rangle + e^{-i\phi-i\alpha_-} |--\rangle \quad (\text{G.2})$$

During the second sensing time, state  $|-\rangle$  again acquires the same phase as it did during the first sensing time. Additionally, state  $|0\rangle$  acquires a phase. The state is

$$\begin{aligned} |\psi_2\rangle = & \quad |-\rangle \\ & + e^{-i\phi-i\alpha_0} |0\rangle \\ & + e^{-2i\phi-2i\alpha_-} |--\rangle \end{aligned} \quad (\text{G.3})$$

Then, during the correlation time  $T_c$ , the electron spin is in spin state  $|-\rangle$  and thus the memory spin state evolves in the hyperfine field of the electron spin resulting in additional phase shifts  $\nu_+$ ,  $\nu_0$  and  $\nu_-$ . After  $T_c$ , the state is

$$\begin{aligned} |\psi_3\rangle = & + e^{-i\nu_+T} |-\rangle \\ & + e^{-i\nu_0T-i\phi-i\alpha_0} |0\rangle \\ & + e^{-i\nu_-T-2i\phi-2i\alpha_-} |--\rangle \end{aligned} \quad (\text{G.4})$$

The sample field after the correlation time  $T_c$  may be different from that before  $T_c$ . Therefore, during the third sensing time the memory spin accumulates a sensing phase  $\tilde{\phi}$ , which is potentially different from  $\phi$ . After the third sensing time, the state is

$$\begin{aligned} |\psi_4\rangle = & + e^{-i\nu_+T-i\tilde{\phi}-i\alpha_+} |-\rangle \\ & + e^{-i\nu_0T-i\phi-i\tilde{\phi}-2i\alpha_0} |0\rangle \\ & - e^{-i\nu_-T-2i\phi-2i\alpha_-} |0-\rangle \end{aligned} \quad (\text{G.5})$$

Thereby, the “-” before  $|0-\rangle$  is introduced, as a full  $2\pi$  - pulse was performed on the electron spin [17]. Analogously, after the fourth sensing time and before the second Chrestenson gate, the state is

$$\begin{aligned} |\psi_f\rangle = & - e^{-i\nu_+T-2i\tilde{\phi}-2i\alpha_+} |0+\rangle \\ & - e^{-i\nu_0T-i\phi-i\tilde{\phi}-2i\alpha_0} |00\rangle \\ & - e^{-i\nu_-T-2i\phi-2i\alpha_-} |0-\rangle \end{aligned} \quad (\text{G.6})$$

**Simplifying the result** With the substitution  $\Delta\phi = \phi - \tilde{\phi}$ , the memory state before the second Chrestenson gate is

$$\begin{aligned} |\psi_f\rangle = & - e^{-i\nu_+T+i\Delta\phi-2i\alpha_+} |+\rangle \\ & - e^{-i\nu_0T-2i\alpha_0} |0\rangle \\ & - e^{-i\nu_-T-i\Delta\phi-2i\alpha_-} |-\rangle \end{aligned} \quad (\text{G.7})$$

Thereby, global phases are neglected. The individual terms in equation G.7 can be simplified with knowledge of the Hamiltonian describing the sensor-memory system. Due to the zero magnetic moment of  $^{14}\text{N}$  memory spin state  $|0\rangle$ ,  $\nu_0 = 0$ . To find  $\alpha_{\pm} = \nu_{\pm}\tau$ , one has to diagonalize the sensor-memory spin Hamiltonian to receive  $\nu_+$  and  $\nu_-$ . With  $A_{\perp} = 0$ , one would find  $\nu_+ = \nu_- = A_{zz}$  (cf. section 1.4). The found values differ from  $A_{\parallel}$  by approximately 250 Hz, which leads to significant offset phases  $\alpha_{\pm}$  for common values of  $T_c$ . The values  $\nu_+$  and  $\nu_-$  can be calculated from the difference of the  $^{14}\text{N}$  nuclear spin transition frequencies  $\Delta f$  in electron spin state  $|0\rangle$  and  $|-\rangle$ .

$$\begin{aligned} \nu_+ &= \Delta f_{\text{T}[^{14}\text{N}=+1,-]} - \Delta f_{\text{T}[^{14}\text{N}=+1,0]} \\ \nu_- &= \Delta f_{\text{T}[^{14}\text{N}=-1,-]} - \Delta f_{\text{T}[^{14}\text{N}=-1,0]} \end{aligned} \quad (\text{G.8})$$

In the experiment, the additional phases appearing due to  $\nu_+$  and  $\nu_-$  can be compensated for by a  $\tau$  and  $T_c$  dependent rotation of the phase  $\varphi$  of the final Chrestenson gate. Then, the state of the memory spin only depends on the sensing phase  $\Delta\phi$  and thus on the sample field. The memory spin state then evolves as

$$\begin{aligned} \psi_{\text{fc}} &= \psi_{\text{fc}}(\Delta\phi) \\ &= e^{+i\Delta\phi} |+\rangle + |0\rangle + e^{-i\Delta\phi} |-\rangle \end{aligned} \quad (\text{G.9})$$

which is equivalent to the state required for the quantum phase estimation algorithm before the iQFT (cf. equation 5.29). Please note, that the iQFT here is implemented by the second Chrestenson gate in sequence SeqG.1 (cf. appendix F and section 5.2).



## Bibliography

- [1] R. P. Feynman. “Simulating physics with computers”. *Int J Theor Phys* **21** (1982) (cit. on pp. ix, 1).
- [2] D. Deutsch and R. Jozsa. “Rapid Solution of Problems by Quantum Computation”. *Proc. R. Soc. Lond. A* **439** (1992) (cit. on pp. ix, 1).
- [3] L. K. Grover. “Quantum Mechanics Helps in Searching for a Needle in a Haystack”. *Physical Review Letters* **79** (1997) (cit. on pp. ix, 1).
- [4] P. W. Shor. “Polynomial-Time Algorithms for Prime Factorization and Discrete Logarithms on a Quantum Computer”. *SIAM Journal on Computing* **26** (1997) (cit. on pp. ix, 1).
- [5] B. Korzh, C. C. W. Lim, R. Houlmann, N. Gisin, M. J. Li, D. Nolan, B. Sanguinetti, R. Thew, and H. Zbinden. “Provably secure and practical quantum key distribution over 307 km of optical fibre”. *Nature Photonics* **9** (2015) (cit. on pp. ix, 1).
- [6] C. Monroe and J. Kim. “Scaling the Ion Trap Quantum Processor”. *Science* **339** (2013) (cit. on pp. ix, 1).
- [7] M. H. Devoret and R. J. Schoelkopf. “Superconducting Circuits for Quantum Information: An Outlook”. *Science* **339** (2013) (cit. on pp. ix, 1).
- [8] T. F. Watson, S. G. J. Philips, E. Kawakami, D. R. Ward, P. Scarlino, M. Veldhorst, D. E. Savage, M. G. Lagally, M. Friesen, S. N. Coppersmith, M. A. Eriksson, and L. M. K. Vandersypen. “A programmable two-qubit quantum processor in silicon”. *Nature* **555** (2018) (cit. on pp. ix, 1).
- [9] G. Tosi, F. A. Mohiyaddin, V. Schmitt, S. Tenberg, R. Rahman, G. Klimeck, and A. Morello. “Silicon quantum processor with robust long-distance qubit couplings”. *Nature Communications* **8** (2017) (cit. on pp. ix, 1).
- [10] E. Togan, Y. Chu, A. S. Trifonov, L. Jiang, J. Maze, L. Childress, M. V. G. Dutt, A. S. Sørensen, P. R. Hemmer, A. S. Zibrov, and M. D. Lukin. “Quantum entanglement between an optical photon and a solid-state spin qubit”. *Nature* **466** (2010) (cit. on pp. x, 2).

- [11] F. Dolde, I. Jakobi, B. Naydenov, N. Zhao, S. Pezzagna, C. Trautmann, J. Meijer, P. Neumann, F. Jelezko, and J. Wrachtrup. “Room-temperature entanglement between single defect spins in diamond”. *Nat Phys* **9** (2013) (cit. on pp. x, 2).
- [12] F. Dolde, H. Fedder, M. W. Doherty, T. Nöbauer, F. Rempp, G. Balasubramanian, T. Wolf, F. Reinhard, L. C. L. Hollenberg, F. Jelezko, and J. Wrachtrup. “Electric-field sensing using single diamond spins”. *Nat Phys* **7** (2011) (cit. on pp. x, 2, 9).
- [13] S. D. Bennett, N. Y. Yao, J. Otterbach, P. Zoller, P. Rabl, and M. D. Lukin. “Phonon-Induced Spin-Spin Interactions in Diamond Nanostructures: Application to Spin Squeezing”. *Physical Review Letters* **110** (2013) (cit. on pp. x, 2).
- [14] M. Pfender, N. Aslam, P. Simon, D. Antonov, G. Thiering, S. Burk, F. Fávvaro de Oliveira, A. Denisenko, H. Fedder, J. Meijer, J. A. Garrido, A. Gali, T. Teraji, J. Isoya, M. W. Doherty, A. Alkauskas, A. Gallo, A. Grüneis, P. Neumann, and J. Wrachtrup. “Protecting a Diamond Quantum Memory by Charge State Control”. *Nano letters* **17** (2017) (cit. on pp. x, 2, 9, 12, 39, 42, 109).
- [15] F. Jelezko, T. Gaebel, I. Popa, M. Domhan, A. Gruber, and J. Wrachtrup. “Observation of coherent oscillation of a single nuclear spin and realization of a two-qubit conditional quantum gate”. *Physical Review Letters* **93** (2004) (cit. on pp. x, 2, 27, 35, 44).
- [16] P. Neumann, R. Kolesov, B. Naydenov, J. Beck, F. Rempp, M. Steiner, V. Jacques, G. Balasubramanian, M. L. Markham, D. J. Twitchen, S. Pezzagna, J. Meijer, J. Twamley, F. Jelezko, and J. Wrachtrup. “Quantum register based on coupled electron spins in a room-temperature solid”. *Nat Phys* **6** (2010) (cit. on pp. x, 2, 9, 21).
- [17] G. Waldherr, Y. Wang, S. Zaiser, M. Jamali, T. Schulte-Herbrüggen, H. Abe, T. Ohshima, J. Isoya, J. F. Du, P. Neumann, and J. Wrachtrup. “Quantum error correction in a solid-state hybrid spin register”. *Nature* **506** (2014) (cit. on pp. x, 2, 9, 13, 25, 37, 44, 100, 135, 142).
- [18] P. Neumann, J. Beck, M. Steiner, F. Rempp, H. Fedder, P. R. Hemmer, J. Wrachtrup, and F. Jelezko. “Single-Shot Readout of a Single Nuclear Spin”. *Science* **329** (2010) (cit. on pp. x, 2, 27, 44, 77, 81, 82).
- [19] A. Dréau, P. Spinicelli, J. R. Maze, J.-F. Roch, and V. Jacques. “Single-Shot Readout of Multiple Nuclear Spin Qubits in Diamond under Ambient Conditions”. *Phys. Rev. Lett.* **110** (2013) (cit. on pp. x, 2, 44).

- [20] N. Aslam, M. Pfender, P. Neumann, R. Reuter, A. Zappe, F. F. d. Oliveira, A. Denisenko, H. Sumiya, S. Onoda, J. Isoya, and J. Wrachtrup. “Nanoscale nuclear magnetic resonance with chemical resolution”. *Science* (2017) (cit. on pp. xi, 3, 9, 100, 109).
- [21] P. J. Rayner, P. Norcott, K. M. Appleby, W. Iali, R. O. John, S. J. Hart, A. C. Whitwood, and S. B. Duckett. “Fine-tuning the efficiency of para- hydrogen-induced hyperpolarization by rational N -heterocyclic carbene design”. *Nature Communications* **9** (2018) (cit. on pp. xii, 3).
- [22] F. Shagieva, S. Zaiser, P. Neumann, D. B. R. Dasari, R. Stöhr, A. Denisenko, R. Reuter, C. A. Meriles, and J. Wrachtrup. “Microwave-Assisted Cross-Polarization of Nuclear Spin Ensembles from Optically Pumped Nitrogen-Vacancy Centers in Diamond”. *Nano letters* **18** (2018) (cit. on pp. xii, 3, 51).
- [23] D. A. Broadway, J.-P. Tetienne, A. Stacey, J. D. A. Wood, D. A. Simpson, L. T. Hall, and L. C. L. Hollenberg. “Quantum probe hyperpolarisation of molecular nuclear spins”. *Nature Communications* **9** (2018) (cit. on pp. xii, 3).
- [24] S. Raeisi and M. Mosca. “Asymptotic Bound for Heat-Bath Algorithmic Cooling”. *Physical Review Letters* **114** (2015) (cit. on pp. xii, 4, 50, 59, 61).
- [25] T. H. Taminiau, J. J. T. Wagenaar, T. van der Sar, F. Jelezko, V. V. Dobrovitski, and R. Hanson. “Detection and Control of Individual Nuclear Spins Using a Weakly Coupled Electron Spin”. *Phys. Rev. Lett.* **109** (2012) (cit. on pp. xiv, 5, 9, 37, 101, 102, 104, 107).
- [26] S. Dogra, Arvind, and K. Dorai. “Implementation of the quantum Fourier transform on a hybrid qubit-qutrit NMR quantum emulator”. arXiv:1503.06624 [quant-ph] (2015) (cit. on pp. xv, 6, 110, 129).
- [27] M. Leifgen, T. Schröder, F. Gädeke, R. Riemann, V. Métilion, E. Neu, C. Hepp, C. Arend, C. Becher, K. Lauritsen, and O. Benson. “Evaluation of nitrogen- and silicon-vacancy defect centres as single photon sources in quantum key distribution”. *New Journal of Physics* **16** (2014) (cit. on p. 9).
- [28] C. Kurtsiefer, S. Mayer, P. Zarda, and H. Weinfurter. “Stable Solid-State Source of Single Photons”. *Phys. Rev. Lett.* **85** (2000) (cit. on p. 9).
- [29] N. Lo Piparo, M. Razavi, and W. J. Munro. “Measurement-device-independent quantum key distribution with nitrogen vacancy centers in diamond”. *Phys. Rev. A* **95** (2017) (cit. on p. 9).
- [30] W. Pfaff, B. J. Hensen, H. Bernien, S. B. van Dam, M. S. Blok, T. H. Taminiau, M. J. Tiggelman, R. N. Schouten, M. Markham, D. J. Twitchen, and R. Hanson. “Unconditional quantum teleportation between distant solid-state quantum bits”. *Science* **345** (2014) (cit. on p. 9).

- [31] H. Bernien, B. Hensen, W. Pfaff, G. Koolstra, M. S. Blok, L. Robledo, T. H. Taminiau, M. Markham, D. J. Twitchen, L. Childress, and R. Hanson. “Heralded entanglement between solid-state qubits separated by three metres”. *Nature* **497** (2013) (cit. on p. 9).
- [32] K. Nemoto, M. Trupke, S. J. Devitt, B. Scharfenberger, K. Buczak, J. Schmiedmayer, and W. J. Munro. “Photonic Quantum Networks formed from NV-centers”. *Scientific Reports* **6** (2016) (cit. on p. 9).
- [33] L. Robledo, L. Childress, H. Bernien, B. Hensen, P. F. A. Alkemade, and R. Hanson. “High-fidelity projective read-out of a solid-state spin quantum register”. *Nature* **477** (2011) (cit. on pp. 9, 15).
- [34] J. Cai, A. Retzker, F. Jelezko, and M. B. Plenio. “A large-scale quantum simulator on a diamond surface at room temperature”. *Nat Phys* **9** (2013) (cit. on pp. 9, 100).
- [35] J. Cramer, N. Kalb, M. A. Rol, B. Hensen, M. S. Blok, M. Markham, D. J. Twitchen, R. Hanson, and T. H. Taminiau. “Repeated quantum error correction on a continuously encoded qubit by real-time feedback”. *Nature Communications* **7** (2016) (cit. on pp. 9, 100).
- [36] J. R. Maze, P. L. Stanwix, J. S. Hodges, S. Hong, J. M. Taylor, P. Cappellaro, L. Jiang, M. V. G. Dutt, E. Togan, A. S. Zibrov, A. Yacoby, R. L. Walsworth, and M. D. Lukin. “Nanoscale magnetic sensing with an individual electronic spin in diamond”. *Nature* **455** (2008) (cit. on p. 9).
- [37] S. Steinert, F. Dolde, P. Neumann, A. Aird, B. Naydenov, G. Balasubramanian, F. Jelezko, and J. Wrachtrup. “High sensitivity magnetic imaging using an array of spins in diamond”. *The Review of scientific instruments* **81** (2010) (cit. on p. 9).
- [38] T. Wolf, P. Neumann, K. Nakamura, H. Sumiya, T. Ohshima, J. Isoya, and J. Wrachtrup. “Subpicotesla Diamond Magnetometry”. *Phys. Rev. X* **5** (2015) (cit. on pp. 9, 100).
- [39] F. Dolde, M. W. Doherty, J. Michl, I. Jakobi, B. Naydenov, S. Pezzagna, J. Meijer, P. Neumann, F. Jelezko, N. B. Manson, and J. Wrachtrup. “Nanoscale Detection of a Single Fundamental Charge in Ambient Conditions Using the NV- Center in Diamond”. *Phys. Rev. Lett.* **112** (2014) (cit. on p. 9).
- [40] J. Michl, T. Teraji, S. Zaiser, I. Jakobi, G. Waldherr, F. Dolde, P. Neumann, M. W. Doherty, N. B. Manson, J. Isoya, and J. Wrachtrup. “Perfect alignment and preferential orientation of nitrogen-vacancy centers during chemical vapor deposition diamond growth on (111) surfaces”. *Applied Physics Letters* **104** (2014) (cit. on pp. 9, 12).

- [41] P. Neumann, I. Jakobi, F. Dolde, C. Burk, R. Reuter, G. Waldherr, J. Honert, T. Wolf, A. Brunner, J. H. Shim, D. Suter, H. Sumiya, J. Isoya, and J. Wrachtrup. “High-Precision Nanoscale Temperature Sensing Using Single Defects in Diamond”. *Nano Lett* **13** (2013) (cit. on pp. 9, 17).
- [42] V. Ivády, T. Simon, J. R. Maze, I. A. Abrikosov, and A. Gali. “Pressure and temperature dependence of the zero-field splitting in the ground state of NV centers in diamond: A first-principles study”. *Physical Review B* **90** (2014) (cit. on p. 9).
- [43] V. M. Acosta, E. Bauch, M. P. Ledbetter, A. Waxman, L.-S. Bouchard, and D. Budker. “Temperature Dependence of the Nitrogen-Vacancy Magnetic Resonance in Diamond”. *Phys. Rev. Lett.* **104** (2010) (cit. on pp. 9, 17, 132).
- [44] G. Kucsko, P. C. Maurer, N. Y. Yao, M. Kubo, H. J. Noh, P. K. Lo, H. Park, and M. D. Lukin. “Nanometre-scale thermometry in a living cell”. *Nature* **500** (2013) (cit. on p. 9).
- [45] S. Ali Momenzadeh, F. F. d. Oliveira, P. Neumann, D. D. Bhaktavatsala Rao, A. Denisenko, M. Amjadi, Z. Chu, S. Yang, N. B. Manson, M. W. Doherty, and J. Wrachtrup. “Thin Circular Diamond Membrane with Embedded Nitrogen-Vacancy Centers for Hybrid Spin-Mechanical Quantum Systems”. *Physical Review Applied* **6** (2016) (cit. on p. 9).
- [46] A. Ajoy and P. Cappellaro. “Stable three-axis nuclear-spin gyroscope in diamond”. *Phys. Rev. A* **86** (2012) (cit. on p. 9).
- [47] N. Zhao, J. Honert, B. Schmid, M. Klas, J. Isoya, M. Markham, D. Twitchen, F. Jelezko, R.-B. Liu, H. Fedder, and J. Wrachtrup. “Sensing single remote nuclear spins”. *Nat Nano* **7** (2012) (cit. on p. 9).
- [48] S. Kolkowitz, Q. P. Unterreithmeier, S. D. Bennett, and M. D. Lukin. “Sensing Distant Nuclear Spins with a Single Electron Spin”. *Phys. Rev. Lett.* **109** (2012) (cit. on pp. 9, 37).
- [49] T. Staudacher, F. Shi, S. Pezzagna, J. Meijer, J. Du, C. A. Meriles, F. Reinhard, and J. Wrachtrup. “Nuclear Magnetic Resonance Spectroscopy on a (5-Nanometer)<sup>3</sup> Sample Volume”. *Science* **339** (2013) (cit. on p. 9).
- [50] A. Ajoy, U. Bissbort, M. D. Lukin, R. L. Walsworth, and P. Cappellaro. “Atomic-Scale Nuclear Spin Imaging Using Quantum-Assisted Sensors in Diamond”. *Physical Review X* **5** (2015) (cit. on pp. 9, 100).
- [51] H. J. Mamin, M. Kim, M. H. Sherwood, C. T. Rettner, K. Ohno, D. D. Awschalom, and D. Rugar. “Nanoscale Nuclear Magnetic Resonance with a Nitrogen-Vacancy Spin Sensor”. *Science* **339** (2013) (cit. on p. 9).

- [52] T. Häberle, D. Schmid-Lorch, F. Reinhard, and J. Wrachtrup. “Nanoscale nuclear magnetic imaging with chemical contrast”. *Nat Nano* **10** (2015) (cit. on p. 9).
- [53] F. C. Ziem, N. S. Götz, A. Zappe, S. Steinert, and J. Wrachtrup. “Highly sensitive detection of physiological spins in a microfluidic device”. *Nano letters* **13** (2013) (cit. on p. 9).
- [54] W. H. Bragg and W. L. Bragg. “The Structure of the Diamond”. *Proc. R. Soc. Lond. A* **89** (1913) (cit. on p. 10).
- [55] A. C. Victor. “Heat Capacity of Diamond at High Temperatures”. *The Journal of Chemical Physics* **36** (1962) (cit. on p. 10).
- [56] S. Kumar, B. A. Reshi, and R. Varma. “Comparison of Silicon, Germanium, Gallium Nitride, and Diamond for using as a Detector Material in Experimental High Energy Physics”. *Results in Physics* (2018) (cit. on p. 10).
- [57] I. Aharonovich, A. D. Greentree, and S. Praver. “Diamond photonics”. *Nature Photonics* **5** (2011) (cit. on pp. 10, 15).
- [58] T. R. Anthony and W. F. Banholzer. “Properties of diamond with varying isotopic composition”. *Diamond and Related Materials* **1** (1992) (cit. on p. 10).
- [59] G. S. Gildenblat, S. A. Grot, and A. Badzian. “The electrical properties and device applications of homoepitaxial and polycrystalline diamond films”. *Proceedings of the IEEE* **79** (1991) (cit. on p. 10).
- [60] J. Walker. “Optical absorption and luminescence in diamond”. *Reports on Progress in Physics* **42** (1979) (cit. on p. 10).
- [61] A. M. Zaitsev. “Vibronic spectra of impurity-related optical centers in diamond”. *Physical Review B* **61** (2000) (cit. on p. 10).
- [62] D. J. Twitchen, M. E. Newton, J. M. Baker, T. R. Anthony, and W. F. Banholzer. “Electron-paramagnetic-resonance measurements on the divacancy defect center R4/W6 in diamond”. *Physical Review B* **59** (1999) (cit. on p. 11).
- [63] S. Onoda, K. Tatsumi, M. Haruyama, T. Teraji, J. Isoya, W. Kada, T. Ohshima, and O. Hanaizumi. “Diffusion of Vacancies Created by High-Energy Heavy Ion Strike Into Diamond”. *physica status solidi (a)* **214** (2017) (cit. on p. 11).
- [64] G. Davies and M. F. Hamer. “Optical Studies of the 1.945 eV Vibronic Band in Diamond”. *Proc. R. Soc. Lond. A* **348** (1976) (cit. on pp. 11, 12).
- [65] M. W. Doherty, N. B. Manson, P. Delaney, F. Jelezko, J. Wrachtrup, and L. C. L. Hollenberg. “The nitrogen-vacancy colour centre in diamond”. *Physics Reports* **528** (2013) (cit. on pp. 12, 14, 15, 19).

- [66] A. Gruber, A. Dräbenstedt, C. Tietz, L. Fleury, J. Wrachtrup, and C. von Borczyskowski. “Scanning Confocal Optical Microscopy and Magnetic Resonance on Single Defect Centers”. *Science* **276** (1997) (cit. on p. 12).
- [67] J. H. N. Loubser. “ESR studies of diamond powders”. *Solid State Communications* **22** (1977) (cit. on pp. 12, 15, 17, 21).
- [68] J. H. N. Loubser and J. A. van Wyk. “Electron spin resonance in the study of diamond”. *Rep. Prog. Phys.* **41** (1978) (cit. on pp. 12, 17, 21).
- [69] S. Felton, A. M. Edmonds, M. E. Newton, P. M. Martineau, D. Fisher, and D. J. Twitchen. “Electron paramagnetic resonance studies of the neutral nitrogen vacancy in diamond”. *Phys. Rev. B* **77** (2008) (cit. on pp. 12, 21).
- [70] N. Reddy, N. B. Manson, and E. R. Krausz. “Two-laser spectral hole burning in a colour centre in diamond”. *Journal of Luminescence* **38** (1987) (cit. on pp. 12, 15).
- [71] E. van Oort, N. B. Manson, and M. Glasbeek. “Optically detected spin coherence of the diamond N-V centre in its triplet ground state”. *Journal of Physics C: Solid State Physics* **21** (1988) (cit. on p. 12).
- [72] D. A. Redman, S. Brown, R. H. Sands, and S. C. Rand. “Spin dynamics and electronic states of N- V centers in diamond by EPR and four-wave-mixing spectroscopy”. *Physical Review Letters* **67** (1991) (cit. on p. 12).
- [73] M. V. Hauf, B. Grotz, B. Naydenov, M. Dankerl, S. Pezzagna, J. Meijer, F. Jelezko, J. Wrachtrup, M. Stutzmann, F. Reinhard, and J. A. Garrido. “Chemical control of the charge state of nitrogen-vacancy centers in diamond”. *Phys. Rev. B* **83** (2011) (cit. on p. 12).
- [74] N. Aslam, G. Waldherr, P. Neumann, F. Jelezko, and J. Wrachtrup. “Photo-induced ionization dynamics of the nitrogen vacancy defect in diamond investigated by single-shot charge state detection”. *New J. Phys.* **15** (2013) (cit. on pp. 12, 13, 15, 69).
- [75] M. Pfender, N. Aslam, G. Waldherr, P. Neumann, and J. Wrachtrup. “Single-spin stochastic optical reconstruction microscopy”. *Proceedings of the National Academy of Sciences of the United States of America* **111** (2014) (cit. on p. 13).
- [76] B. J. Shields, Q. P. Unterreithmeier, N. P. d. Leon, H. Park, and M. D. Lukin. “Efficient readout of a single spin state in diamond via spin-to-charge conversion”. *Physical Review Letters* **114** (2015) (cit. on p. 13).
- [77] Y. Doi, T. Fukui, H. Kato, T. Makino, S. Yamasaki, T. Tashima, H. Morishita, S. Miwa, F. Jelezko, Y. Suzuki, and N. Mizuochi. “Pure negatively charged state of the NV center in n -type diamond”. *Physical Review B* **93** (2016) (cit. on p. 13).

- [78] G. Waldherr, J. Beck, M. Steiner, P. Neumann, A. Gali, T. Frauenheim, F. Jelezko, and J. Wrachtrup. “Dark States of Single Nitrogen-Vacancy Centers in Diamond Unraveled by Single Shot NMR”. *Phys. Rev. Lett.* **106** (2011) (cit. on pp. 13, 40, 46, 80).
- [79] N. B. Manson, J. P. Harrison, and M. J. Sellars. “Nitrogen-vacancy center in diamond: Model of the electronic structure and associated dynamics”. *Phys. Rev. B* **74** (2006) (cit. on pp. 14, 15).
- [80] L. J. Rogers, R. L. McMurtrie, M. J. Sellars, and N. B. Manson. “Time-averaging within the excited state of the nitrogen-vacancy centre in diamond”. *New Journal of Physics* **11** (2009) (cit. on p. 14).
- [81] K. Mei, C. Santori, P. E. Barclay, L. J. Rogers, N. B. Manson, and R. G. Beausoleil. “Observation of the Dynamic Jahn-Teller Effect in the Excited States of Nitrogen-Vacancy Centers in Diamond”. *Physical Review Letters* **103** (2009) (cit. on p. 14).
- [82] J. R. Maze, A. Gali, E. Togan, Y. Chu, A. Trifonov, E. Kaxiras, and M. D. Lukin. “Properties of nitrogen-vacancy centers in diamond: the group theoretic approach”. *New J. Phys.* **13** (2011) (cit. on pp. 14, 15).
- [83] A. Batalov, C. Zierl, T. Gaebel, P. Neumann, I.-Y. Chan, G. Balasubramanian, P. R. Hemmer, F. Jelezko, and J. Wrachtrup. “Temporal Coherence of Photons Emitted by Single Nitrogen-Vacancy Defect Centers in Diamond Using Optical Rabi-Oscillations”. *Phys. Rev. Lett.* **100** (2008) (cit. on p. 15).
- [84] L. Robledo, H. Bernien, T. van der Sar, and R. Hanson. “Spin dynamics in the optical cycle of single nitrogen-vacancy centres in diamond”. *New Journal of Physics* **13** (2011) (cit. on p. 15).
- [85] C Santori, P E Barclay, K-M C Fu, R G Beausoleil, S Spillane, and M Fisch. “Nanophotonics for quantum optics using nitrogen-vacancy centers in diamond”. *Nanotechnology* **21** (2010) (cit. on p. 15).
- [86] V. M. Acosta, A. Jarmola, E. Bauch, and D. Budker. “Optical properties of the nitrogen-vacancy singlet levels in diamond”. *Phys. Rev. B* **82** (2010) (cit. on p. 15).
- [87] J. Harrison, M. J. Sellars, and N. B. Manson. “Optical spin polarisation of the N-V centre in diamond”. *Journal of Luminescence* **107** (2004) (cit. on p. 15).
- [88] M. Jamali, I. Gerhardt, M. Rezai, K. Frenner, H. Fedder, and J. Wrachtrup. “Microscopic diamond solid-immersion-lenses fabricated around single defect centers by focused ion beam milling”. *The Review of scientific instruments* **85** (2014) (cit. on p. 15).
- [89] J. A. Weil and J. R. Bolton. *Electron Paramagnetic Resonance: Elementary Theory and Practical Applications*. 2. Auflage. John Wiley & Sons, 2006 (cit. on p. 15).

- [90] G. D. Fuchs, V. V. Dobrovitski, R. Hanson, A. Batra, C. D. Weis, T. Schenkel, and D. D. Awschalom. “Excited-state spectroscopy using single spin manipulation in diamond”. *Physical Review Letters* **101** (2008) (cit. on pp. 15, 21).
- [91] A. Batalov, V. Jacques, F. Kaiser, P. Siyushev, P. Neumann, L. J. Rogers, R. L. McMurtrie, N. B. Manson, F. Jelezko, and J. Wrachtrup. “Low Temperature Studies of the Excited-State Structure of Negatively Charged Nitrogen-Vacancy Color Centers in Diamond”. *Phys. Rev. Lett.* **102** (2009) (cit. on p. 15).
- [92] X.-D. Chen, C.-H. Dong, F.-W. Sun, C.-L. Zou, J.-M. Cui, Z.-F. Han, and G.-C. Guo. “Temperature dependent energy level shifts of nitrogen-vacancy centers in diamond”. *Applied Physics Letters* **99** (2011) (cit. on p. 17).
- [93] D. M. Toyli, D. J. Christle, A. Alkauskas, B. B. Buckley, C. G. van de Walle, and D. D. Awschalom. “Measurement and Control of Single Nitrogen-Vacancy Center Spins above 600 K”. *Physical Review X* **2** (2012) (cit. on p. 17).
- [94] G. Audi, O. Bersillon, J. Blachot, and A. H. Wapstra. “The Nubase evaluation of nuclear and decay properties”. *Nuclear Physics A* **729** (2003) (cit. on p. 18).
- [95] M. Steiner, P. Neumann, J. Beck, F. Jelezko, and J. Wrachtrup. “Universal enhancement of the optical readout fidelity of single electron spins at nitrogen-vacancy centers in diamond”. *Physical Review B* **81** (2010) (cit. on p. 18).
- [96] A. Gali. “Hyperfine tensors of nitrogen-vacancy center in diamond from ab initio calculations”. arXiv:0905.1169 (2009) (cit. on pp. 19, 21).
- [97] N. Zhao, S.-W. Ho, and R.-B. Liu. “Decoherence and dynamical decoupling control of nitrogen vacancy center electron spins in nuclear spin baths”. *Physical Review B* **85** (2012) (cit. on p. 20).
- [98] D. Kielpinski. “A Decoherence-Free Quantum Memory Using Trapped Ions”. *Science* **291** (2001) (cit. on p. 20).
- [99] N. Zhao, J.-L. Hu, S.-W. Ho, J. T. K. Wan, and R. B. Liu. “Atomic-scale magnetometry of distant nuclear spin clusters via nitrogen-vacancy spin in diamond”. *Nature Nanotechnology* **6** (2011) (cit. on p. 20).
- [100] A. P. Nizovtsev, S. Y. Kilin, A. L. Pushkarchuk, V. A. Pushkarchuk, S. A. Kuten, O. A. Zhikol, S. Schmitt, T. Uden, and F. Jelezko. “Non-flipping  $^{13}\text{C}$  spins near an NV center in diamond: hyperfine and spatial characteristics by density functional theory simulation of the  $\text{C}_{510}[\text{NV}]\text{H}_{252}$  cluster”. *New Journal of Physics* **20** (2018) (cit. on p. 22).
- [101] G. Balasubramanian, P. Neumann, D. Twitchen, M. Markham, R. Kolesov, N. Mizuochi, J. Isoya, J. Achard, J. Beck, J. Tissler, V. Jacques, P. R. Hemmer, F. Jelezko, and J. Wrachtrup. “Ultralong spin coherence time in isotopically engineered diamond”. *Nature Materials* **8** (2009) (cit. on p. 23).

- [102] L. Marseglia, J. P. Hadden, A. C. Stanley-Clarke, J. P. Harrison, B. Patton, Y.-L. D. Ho, B. Naydenov, F. Jelezko, J. Meijer, P. R. Dolan, J. M. Smith, J. G. Rarity, and J. L. O'Brien. "Nanofabricated solid immersion lenses registered to single emitters in diamond". *Applied Physics Letters* **98** (2011) (cit. on p. 25).
- [103] N. Aslam, M. Pfender, R. Stöhr, P. Neumann, M. Scheffler, H. Sumiya, H. Abe, S. Onoda, T. Ohshima, J. Isoya, and J. Wrachtrup. "Single spin optically detected magnetic resonance with 60-90 GHz (E-band) microwave resonators". *The Review of scientific instruments* **86** (2015) (cit. on p. 26).
- [104] G. Burkard, V. O. Shkolnikov, and D. D. Awschalom. "Designing a cavity-mediated quantum cphase gate between NV spin qubits in diamond". *Physical Review B* **95** (2017) (cit. on p. 27).
- [105] Z. Y. Xu, Y. M. Hu, W. L. Yang, M. Feng, and J. F. Du. "Deterministically entangling distant nitrogen-vacancy centers by a nanomechanical cantilever". *Phys. Rev. A* **80** (2009) (cit. on p. 27).
- [106] A. Wickenbrock, H. Zheng, L. Bougas, N. Leefer, S. Afach, A. Jarmola, V. M. Acosta, and D. Budker. "Microwave-free magnetometry with nitrogen-vacancy centers in diamond". *Applied Physics Letters* **109** (2016) (cit. on p. 27).
- [107] S. E. Lillie, D. A. Broadway, J. D. A. Wood, D. A. Simpson, A. Stacey, J.-P. Tetienne, and L. C. L. Hollenberg. "Environmentally Mediated Coherent Control of a Spin Qubit in Diamond". *Phys. Rev. Lett.* **118** (2017) (cit. on p. 27).
- [108] I. I. Rabi. "On the Process of Space Quantization". *Physical Review* **49** (1936) (cit. on p. 27).
- [109] M. Fox. *Quantum Optics: An Introduction*. Oxford University Press, 2006 (cit. on p. 28).
- [110] J. Scheuer, X. Kong, R. S. Said, J. Chen, A. Kurz, L. Marseglia, J. Du, P. R. Hemmer, S. Montangero, T. Calarco, B. Naydenov, and F. Jelezko. "Precise qubit control beyond the rotating wave approximation". *New Journal of Physics* **16** (2014) (cit. on p. 28).
- [111] J. Wrachtrup, C. von Borczyskowski, J. Bernard, M. Orrit, and R. Brown. "Optically detected spin coherence of single molecules". *Phys. Rev. Lett.* **71** (1993) (cit. on p. 31).
- [112] L. Childress, M. V. G. Dutt, J. M. Taylor, A. S. Zibrov, F. Jelezko, J. Wrachtrup, P. R. Hemmer, and M. D. Lukin. "Coherent Dynamics of Coupled Electron and Nuclear Spin Qubits in Diamond". *Science* **314** (2006) (cit. on pp. 32, 40).
- [113] S. Sangtawesin, C. A. McLellan, B. A. Myers, A. C. B. Jayich, D. D. Awschalom, and J. R. Petta. "Hyperfine-enhanced gyromagnetic ratio of a nuclear spin in diamond". *New J. Phys.* **18** (2016) (cit. on p. 32).

- [114] M. V. G. Dutt, L. Childress, L. Jiang, E. Togan, J. Maze, F. Jelezko, A. S. Zibrov, P. R. Hemmer, and M. D. Lukin. “Quantum Register Based on Individual Electronic and Nuclear Spin Qubits in Diamond”. *Science* **316** (2007) (cit. on pp. 35, 52).
- [115] J. A. Jones, R. H. Hansen, and M. Mosca. “Quantum logic gates and nuclear magnetic resonance pulse sequences”. *Journal of Magnetic Resonance* **135** (1998) (cit. on p. 36).
- [116] R. Schmogrow, D. Hillerkuss, S. Wolf, B. Bäuerle, M. Winter, P. Kleinow, B. Nebendahl, T. Dippon, P. C. Schindler, C. Koos, W. Freude, and J. Leuthold. “512QAM Nyquist sinc-pulse transmission at 54 Gbit/s in an optical bandwidth of 3 GHz”. *Optics express* **20** (2012) (cit. on p. 36).
- [117] F. Dolde, V. Bergholm, Y. Wang, I. Jakobi, B. Naydenov, S. Pezzagna, J. Meijer, F. Jelezko, P. Neumann, T. Schulte-Herbrüggen, J. Biamonte, and J. Wrachtrup. “High-fidelity spin entanglement using optimal control”. *Nature Communications* **5** (2014) (cit. on pp. 36, 135).
- [118] S. Takahashi, R. Hanson, J. van Tol, M. S. Sherwin, and D. D. Awschalom. “Quenching Spin Decoherence in Diamond through Spin Bath Polarization”. *Physical Review Letters* **101** (2008) (cit. on p. 38).
- [119] G. Balasubramanian, P. Neumann, D. Twitchen, M. Markham, R. Kolesov, N. Mizuochi, J. Isoya, J. Achard, J. Beck, J. Tissler, V. Jacques, P. R. Hemmer, F. Jelezko, and J. Wrachtrup. “Ultralong spin coherence time in isotopically engineered diamond”. *Nat Mater* **8** (2009) (cit. on pp. 38, 111).
- [120] A. Gali. “Identification of individual C isotopes of nitrogen-vacancy center in diamond by combining the polarization studies of nuclear spins and first-principles calculations”. *Phys. Rev. B* **80** (2009) (cit. on p. 39).
- [121] A Gali and T Simon and J E Lowther. “An ab initio study of local vibration modes of the nitrogen-vacancy center in diamond”. *New J. Phys.* **13** (2011) (cit. on p. 39).
- [122] A. Jarmola, V. M. Acosta, K. Jensen, S. Chemerisov, and D. Budker. “Temperature- and Magnetic-Field-Dependent Longitudinal Spin Relaxation in Nitrogen-Vacancy Ensembles in Diamond”. *Phys. Rev. Lett.* **108** (2012) (cit. on p. 39).
- [123] T. Astner, J. Gugler, A. Angerer, S. Wald, S. Putz, N. J. Mauser, M. Trupke, H. Sumiya, S. Onoda, J. Isoya, J. Schmiedmayer, P. Mohn, and J. Majer. “Solid-state electron spin lifetime limited by phononic vacuum modes”. *Nature Materials* **17** (2018) (cit. on p. 40).

- [124] G.-Q. Liu, X.-Y. Pan, Z.-F. Jiang, N. Zhao, and R.-B. Liu. “Controllable effects of quantum fluctuations on spin free-induction decay at room temperature”. *Scientific Reports* **2** (2012) (cit. on p. 40).
- [125] P. Kehayias, M. Mrózek, V. M. Acosta, A. Jarmola, D. S. Rudnicki, R. Folman, W. Gawlik, and D. Budker. “Microwave saturation spectroscopy of nitrogen-vacancy ensembles in diamond”. *Physical Review B* **89** (2014) (cit. on p. 40).
- [126] Y. Rosenzweig, Y. Schlüssel, and R. Folman. “Probing the origins of inhomogeneous broadening in nitrogen-vacancy centers with Doppler-free-type spectroscopy”. *Physical Review B* **98** (2018) (cit. on p. 40).
- [127] B. Naydenov, F. Dolde, L. T. Hall, C. Shin, H. Fedder, L. C. L. Hollenberg, F. Jelezko, and J. Wrachtrup. “Dynamical decoupling of a single-electron spin at room temperature”. *Physical Review B* **83** (2011) (cit. on p. 41).
- [128] M. J. Biercuk, A. C. Doherty, and H. Uys. “Dynamical decoupling sequence construction as a filter-design problem”. *Journal of Physics B: Atomic, Molecular and Optical Physics* **44** (2011) (cit. on p. 41).
- [129] A.A Maudsley. “Modified Carr-Purcell-Meiboom-Gill sequence for NMR fourier imaging applications”. *Journal of Magnetic Resonance* (1969) **69** (1986) (cit. on p. 41).
- [130] G. d. Lange, Z. H. Wang, D. Ristè, V. V. Dobrovitski, and R. Hanson. “Universal Dynamical Decoupling of a Single Solid-State Spin from a Spin Bath”. *Science* **330** (2010) (cit. on pp. 41, 84).
- [131] A. M. Souza, G. A. Álvarez, and D. Suter. “Robust dynamical decoupling”. *Phil. Trans. R. Soc. A* **370** (2012) (cit. on p. 41).
- [132] A. M. Souza, G. A. Álvarez, and D. Suter. “Robust Dynamical Decoupling for Quantum Computing and Quantum Memory”. *Phys. Rev. Lett.* **106** (2011) (cit. on p. 41).
- [133] D. Hopper, H. Shulevitz, and L. Bassett. “Spin Readout Techniques of the Nitrogen-Vacancy Center in Diamond”. *Micromachines* **9** (2018) (cit. on p. 42).
- [134] L. Jiang, J. S. Hodges, J. R. Maze, P. Maurer, J. M. Taylor, D. G. Cory, P. R. Hemmer, R. L. Walsworth, A. Yacoby, A. S. Zibrov, and M. D. Lukin. “Repetitive Readout of a Single Electronic Spin via Quantum Logic with Nuclear Spin Ancillae”. *Science* **326** (2009) (cit. on p. 42).
- [135] M. Auzinsh, D. Budker, D. F. Kimball, S. M. Rochester, J. E. Stalnaker, A. O. Sushkov, and V. V. Yashchuk. “Can a Quantum Nondemolition Measurement Improve the Sensitivity of an Atomic Magnetometer?” *Phys. Rev. Lett.* **93** (2004) (cit. on p. 44).

- [136] F. Reinhard. “Diamond defects detect what lies beneath”. *Nature Electronics* **1** (2018) (cit. on p. 44).
- [137] J. H. Lee, Y. Okuno, and S. Cavagnero. “Sensitivity Enhancement in Solution NMR: Emerging Ideas and New Frontiers”. *Journal of magnetic resonance* (San Diego, Calif. : 1997) **241** (2014) (cit. on p. 49).
- [138] K. Hashi, S. Ohki, S. Matsumoto, G. Nishijima, A. Goto, K. Deguchi, K. Yamada, T. Noguchi, S. Sakai, M. Takahashi, Y. Yanagisawa, S. Iguchi, T. Yamazaki, H. Maeda, R. Tanaka, T. Nemoto, H. Suematsu, T. Miki, K. Saito, and T. Shimizu. “Achievement of 1020MHz NMR”. *Journal of magnetic resonance* (San Diego, Calif. : 1997) **256** (2015) (cit. on p. 49).
- [139] B. E. Kane. “A silicon-based nuclear spin quantum computer”. *Nature* **393** (1998) (cit. on p. 50).
- [140] P. O. Boykin, T. Mor, V. Roychowdhury, F. Vatan, and R. Vrijen. “Algorithmic cooling and scalable NMR quantum computers”. *Proceedings of the National Academy of Sciences* **99** (2002) (cit. on pp. 50, 59).
- [141] G. Brassard, Y. Elias, T. Mor, and Y. Weinstein. “Prospects and limitations of algorithmic cooling”. *The European Physical Journal Plus* **129** (2014) (cit. on p. 50).
- [142] J. M. Fernandez, S. Lloyd, T. Mor, and V. Roychowdhury. “Algorithmic Cooling of Spins: A Practicable Method for Increasing Polarization”. *International Journal of Quantum Information* **02** (2004) (cit. on pp. 50, 59).
- [143] R. Hanson and D. D. Awschalom. “Coherent manipulation of single spins in semiconductors”. *Nature* **453** (2008) (cit. on p. 51).
- [144] C. Belthangady, N. Bar-Gill, L. M. Pham, K. Arai, D. Le Sage, P. Cappellaro, and R. L. Walsworth. “Dressed-State Resonant Coupling between Bright and Dark Spins in Diamond”. *Phys. Rev. Lett.* **110** (2013) (cit. on p. 51).
- [145] V. Jacques, P. Neumann, J. Beck, M. Markham, D. Twitchen, J. Meijer, F. Kaiser, G. Balasubramanian, F. Jelezko, and J. Wrachtrup. “Dynamic Polarization of Single Nuclear Spins by Optical Pumping of Nitrogen-Vacancy Color Centers in Diamond at Room Temperature”. *Phys. Rev. Lett.* **102** (2009) (cit. on pp. 51, 68).
- [146] J. Scheuer, I. Schwartz, Q. Chen, D. Schulze-Süninghausen, P. Carl, Peter Höfer, A. Retzker, H. Sumiya, J. Isoya, B. Luy, M. B. Plenio, Boris Naydenov, and F. Jelezko. “Optically induced dynamic nuclear spin polarisation in diamond”. *New J. Phys.* **18** (2016) (cit. on p. 51).
- [147] D. Gelbwaser-Klimovsky, R. Alicki, and G. Kurizki. “Minimal universal quantum heat machine”. *Physical Review E* **87** (2013) (cit. on p. 59).

- [148] S. Machnes, U. Sander, S. J. Glaser, P. de Fouquieres, A. Gruslys, S. Schirmer, and T. Schulte-Herbrueggen. “Comparing, Optimising and Benchmarking Quantum Control Algorithms in a Unifying Programming Framework”. *Physical Review A* **84** (2011) (cit. on pp. 62, 81, 135, 140).
- [149] A. Henstra, P. Dirksen, J. Schmidt, and W. T. Wenckebach. “Nuclear spin orientation via electron spin locking (NOVEL)”. *Journal of Magnetic Resonance* (1969) **77** (1988) (cit. on p. 67).
- [150] S. A. Moiseev and V. A. Skrebnev. “Short-cycle pulse sequence for dynamical decoupling of local fields and dipole-dipole interactions”. *Physical Review A* **91** (2015) (cit. on p. 68).
- [151] A. Brinkmann. “Introduction to average Hamiltonian theory. I. Basics”. *Concepts in Magnetic Resonance Part A* **45A** (2017) (cit. on p. 68).
- [152] I. Schwartz, J. Scheuer, B. Tratzmiller, S. Müller, Q. Chen, I. Dhand, Z.-Y. Wang, C. Müller, B. Naydenov, F. Jelezko, and M. B. Plenio. “Robust optical polarization of nuclear spin baths using Hamiltonian engineering of nitrogen-vacancy center quantum dynamics”. *Science advances* **4** (2018) (cit. on p. 68).
- [153] T. Rosenband, D. B. Hume, P. O. Schmidt, C. W. Chou, A. Brusch, L. Lorini, W. H. Oskay, R. E. Drullinger, T. M. Fortier, J. E. Stalnaker, S. A. Diddams, W. C. Swann, N. R. Newbury, W. M. Itano, D. J. Wineland, and J. C. Bergquist. “Frequency Ratio of Al<sup>+</sup> and Hg<sup>+</sup> Single-Ion Optical Clocks; Metrology at the 17th Decimal Place”. *Science* **319** (2008) (cit. on p. 75).
- [154] D. Budker and M. Romalis. “Optical magnetometry”. *Nature Physics* **3** (2007) (cit. on p. 75).
- [155] G. Balasubramanian, I. Y. Chan, R. Kolesov, M. Al-Hmoud, J. Tisler, C. Shin, C. Kim, A. Wojcik, P. R. Hemmer, A. Krueger, T. Hanke, A. Leitenstorfer, R. Bratschitsch, F. Jelezko, and J. Wrachtrup. “Nanoscale imaging magnetometry with diamond spins under ambient conditions”. *Nature* **455** (2008) (cit. on p. 75).
- [156] J. R. Maze, P. L. Stanwix, J. S. Hodges, S. Hong, J. M. Taylor, P. Cappellaro, L. Jiang, M. V. G. Dutt, E. Togan, A. S. Zibrov, A. Yacoby, R. L. Walsworth, and M. D. Lukin. “Nanoscale magnetic sensing with an individual electronic spin in diamond”. *Nature* **455** (2008) (cit. on p. 75).
- [157] J. M. Taylor, P. Cappellaro, L. Childress, L. Jiang, D. Budker, P. R. Hemmer, A. Yacoby, R. Walsworth, and M. D. Lukin. “High-sensitivity diamond magnetometer with nanoscale resolution”. *Nature Physics* **4** (2008) (cit. on p. 75).
- [158] S. F. Huelga, C. Macchiavello, T. Pellizzari, A. K. Ekert, M. B. Plenio, and J. I. Cirac. “Improvement of Frequency Standards with Quantum Entanglement”. *Phys. Rev. Lett.* **79** (1997) (cit. on p. 75).

- [159] F. Wolfgramm, C. Vitelli, F. A. Beduini, N. Godbout, and M. W. Mitchell. “Entanglement-enhanced probing of a delicate material system”. *Nature Photonics* **7** (2013) (cit. on p. 75).
- [160] R. J. Sewell, M. Koschorreck, M. Napolitano, B. Dubost, N. Behbood, and M. W. Mitchell. “Magnetic Sensitivity Beyond the Projection Noise Limit by Spin Squeezing”. *Physical Review Letters* **109** (2012) (cit. on p. 75).
- [161] P. Neumann, R. Kolesov, B. Naydenov, J. Beck, F. Rempp, M. Steiner, V. Jacques, G. Balasubramanian, M. L. Markham, D. J. Twitchen, S. Pezzagna, J. Meijer, J. Twamley, F. Jelezko, and J. Wrachtrup. “Quantum register based on coupled electron spins in a room-temperature solid”. *Nature Physics* **6** (2010) (cit. on p. 75).
- [162] A. Laraoui, F. Dolde, C. Burk, F. Reinhard, J. Wrachtrup, and C. A. Meriles. “High-resolution correlation spectroscopy of  $^{13}\text{C}$  spins near a nitrogen-vacancy centre in diamond”. *Nature Communications* **4** (2013) (cit. on pp. 75, 76).
- [163] T. Staudacher, N. Raatz, S. Pezzagna, J. Meijer, F. Reinhard, C. A. Meriles, and J. Wrachtrup. “Probing molecular dynamics at the nanoscale via an individual paramagnetic centre”. *Nature Communications* **6** (2015) (cit. on pp. 75, 76).
- [164] X. Kong, A. Stark, J. Du, L. P. McGuinness, and F. Jelezko. “Towards Chemical Structure Resolution with Nanoscale Nuclear Magnetic Resonance Spectroscopy”. *Physical Review Applied* **4** (2015) (cit. on p. 75).
- [165] A. Ajoy, U. Bissbort, M. D. Lukin, R. L. Walsworth, and P. Cappellaro. “Atomic-Scale Nuclear Spin Imaging Using Quantum-Assisted Sensors in Diamond”. *Physical Review X* **5** (2015) (cit. on p. 75).
- [166] A. W. Chin, S. F. Huelga, and M. B. Plenio. “Quantum Metrology in Non-Markovian Environments”. *Physical Review Letters* **109** (2012) (cit. on p. 75).
- [167] G. Waldherr, J. Beck, P. Neumann, R. S. Said, M. Nitsche, M. L. Markham, D. J. Twitchen, J. Twamley, F. Jelezko, and J. Wrachtrup. “High-dynamic-range magnetometry with a single nuclear spin in diamond”. *Nature Nanotechnology* **7** (2011) (cit. on p. 75).
- [168] N. M. Nusran, M. U. Momeen, and M. V. G. Dutt. “High-dynamic-range magnetometry with a single electronic spin in diamond”. *Nature Nanotechnology* **7** (2012) (cit. on p. 75).
- [169] M. A. Nielsen and I. L. Chuang. *Quantum Computation and Quantum Information*. Cambridge University Press, 2000 (cit. on p. 75).
- [170] A. Laraoui, F. Dolde, C. Burk, F. Reinhard, J. Wrachtrup, and C. A. Meriles. “High-resolution correlation spectroscopy of  $^{13}\text{C}$  spins near a nitrogen-vacancy centre in diamond”. *Nat Commun* **4** (2013) (cit. on pp. 76, 82).

- [171] T. Staudacher, N. Raatz, S. Pezzagna, J. Meijer, F. Reinhard, C. A. Meriles, and J. Wrachtrup. “Probing molecular dynamics at the nanoscale via an individual paramagnetic centre”. *Nat Commun* **6** (2015) (cit. on pp. 76, 82).
- [172] X. Kong, A. Stark, J. Du, L. P. McGuinness, and F. Jelezko. “Towards Chemical Structure Resolution with Nanoscale Nuclear Magnetic Resonance Spectroscopy”. *Physical Review Applied* **4** (2015) (cit. on pp. 76, 82).
- [173] S. Zaiser, T. Rendler, I. Jakobi, T. Wolf, S.-Y. Lee, S. Wagner, V. Bergholm, T. Schulte-Herbrüggen, P. Neumann, and J. Wrachtrup. “Enhancing quantum sensing sensitivity by a quantum memory”. *Nature Communications* **7** (2016) (cit. on pp. 76, 109).
- [174] E. L. Hahn. “Spin Echoes”. *Phys. Rev.* **80** (1950) (cit. on p. 76).
- [175] W. B. Mims, K. Nassau, and J. D. McGee. “Spectral Diffusion in Electron Resonance Lines”. *Physical Review* **123** (1961) (cit. on p. 76).
- [176] W. P. Aue, E. Bartholdi, and R. R. Ernst. “Two-dimensional spectroscopy. Application to nuclear magnetic resonance”. *The Journal of Chemical Physics* **64** (1976) (cit. on p. 76).
- [177] T. Mossberg, A. Flusberg, R. Kachru, and S. R. Hartmann. “Total Scattering Cross Section for Na on He Measured by Stimulated Photon Echoes”. *Physical Review Letters* **42** (1979) (cit. on p. 76).
- [178] P. Hamm, M. Lim, and R. M. Hochstrasser. “Non-Markovian Dynamics of the Vibrations of Ions in Water from Femtosecond Infrared Three-Pulse Photon Echoes”. *Physical Review Letters* **81** (1998) (cit. on p. 76).
- [179] M. Mitsunaga and N. Uesugi. “248-Bit optical data storage in  $\text{Eu}^{3+}:\text{YAlO}_3$  by accumulated photon echoes”. *Optics Letters* **15** (1990) (cit. on pp. 76, 80).
- [180] J. Scheuer, A. Stark, M. Kost, M. B. Plenio, B. Naydenov, and F. Jelezko. “Accelerated 2D magnetic resonance spectroscopy of single spins using matrix completion”. *Scientific Reports* **5** (2015) (cit. on p. 76).
- [181] P. Hamm, M. Lim, and R. M. Hochstrasser. “Non-Markovian Dynamics of the Vibrations of Ions in Water from Femtosecond Infrared Three-Pulse Photon Echoes”. *Physical Review Letters* **81** (1998) (cit. on p. 80).
- [182] G. Waldherr, J. Beck, P. Neumann, R. S. Said, M. Nitsche, M. L. Markham, D. J. Twitchen, J. Twamley, F. Jelezko, and J. Wrachtrup. “High-dynamic-range magnetometry with a single nuclear spin in diamond”. *Nat Nano* **7** (2012) (cit. on pp. 80, 82, 111).

- [183] F. Jelezko, T. Gaebel, I. Popa, A. Gruber, and J. Wrachtrup. “Observation of Coherent Oscillations in a Single Electron Spin”. *Phys. Rev. Lett.* **92** (2004) (cit. on p. 81).
- [184] J. R. Klauder and P. W. Anderson. “Spectral Diffusion Decay in Spin Resonance Experiments”. *Physical Review* **125** (1962) (cit. on p. 84).
- [185] Peres. “Separability Criterion for Density Matrices”. *Physical Review Letters* **77** (1996) (cit. on p. 85).
- [186] G. Vidal and R. F. Werner. “Computable measure of entanglement”. *Physical Review A* **65** (2002) (cit. on p. 85).
- [187] W. B. Mims. “Pulsed Endor Experiments”. *Proc. R. Soc. Lond. A* **283** (1965) (cit. on p. 87).
- [188] G.-Q. Liu, Q.-Q. Jiang, Y.-C. Chang, D.-Q. Liu, W.-X. Li, C.-Z. Gu, H. Chun Po, W.-X. Zhang, N. Zhao, and X.-Y. Pan. “Protection of centre spin coherence by dynamic nuclear spin polarization in diamond”. *Nanoscale* **6** (2014) (cit. on p. 93).
- [189] P. Cappellaro and M. D. Lukin. “Quantum correlation in disordered spin systems: Applications to magnetic sensing”. *Phys. Rev. A* **80** (2009) (cit. on p. 100).
- [190] T. Unden, P. Balasubramanian, D. Louzon, Y. Vinkler, M. B. Plenio, M. Markham, D. Twitchen, A. Stacey, I. Lovchinsky, A. O. Sushkov, M. D. Lukin, A. Retzker, B. Naydenov, L. P. McGuinness, and F. Jelezko. “Quantum Metrology Enhanced by Repetitive Quantum Error Correction”. *Phys. Rev. Lett.* **116** (2016) (cit. on p. 100).
- [191] P. C. Maurer, G. Kucsko, C. Latta, L. Jiang, N. Y. Yao, S. D. Bennett, F. Pastawski, D. Hunger, N. Chisholm, M. Markham, D. J. Twitchen, J. I. Cirac, and M. D. Lukin. “Room-Temperature Quantum Bit Memory Exceeding One Second”. *Science* **336** (2012) (cit. on p. 100).
- [192] A. Y. Kitaev. “Quantum measurements and the Abelian Stabilizer Problem”. [arXiv:quant-ph/9511026](https://arxiv.org/abs/quant-ph/9511026) (1995) (cit. on p. 100).
- [193] T. Kaftal and R. Demkowicz-Dobrzański. “Usefulness of an enhanced Kitaev phase-estimation algorithm in quantum metrology and computation”. *Physical Review A* **90** (2014) (cit. on p. 100).
- [194] J. Zopes, K. Herb, K. S. Cujia, and C. L. Degen. “Three-Dimensional Nuclear Spin Positioning Using Coherent Radio-Frequency Control”. *Physical Review Letters* **121** (2018) (cit. on p. 107).
- [195] A. S. Holevo. “Bounds for the Quantity of Information Transmitted by a Quantum Communication Channel”. *Problems Inform. Transmission* (1973) (cit. on p. 109).

## Bibliography

- [196] A. Muthukrishnan and C. R. Stroud. “Multivalued logic gates for quantum computation”. *Physical Review A* **62** (2000) (cit. on p. 109).
- [197] A. Bocharov, M. Roetteler, and K. M. Svore. “Factoring with qutrits: Shor’s algorithm on ternary and metaplectic quantum architectures”. *Physical Review A* **96** (2017) (cit. on p. 109).
- [198] V. Giovannetti, S. Lloyd, and L. Maccone. “Quantum-Enhanced Measurements: Beating the Standard Quantum Limit”. *Science* **306** (2004) (cit. on p. 111).
- [199] V. Giovannetti, S. Lloyd, and L. Maccone. “Quantum Metrology”. *Phys. Rev. Lett.* **96** (2006) (cit. on p. 111).
- [200] N. M. Nusran, M. U. Momeen, and M. V. G. Dutt. “High-dynamic-range magnetometry with a single electronic spin in diamond”. *Nature Nanotechnology* **7** (2012) (cit. on p. 111).
- [201] M. A. Nielsen and I. L. Chuang. *Quantum computation and quantum information*. Cambridge university press, 2010 (cit. on pp. 111, 112, 114).
- [202] Stroud, Ashok Muthukrishnan C. R. “Quantum fast Fourier transform using multilevel atoms”. *Journal of Modern Optics* **49** (2002) (cit. on p. 111).
- [203] Y. Cao, S.-G. Peng, C. Zheng, and G.-L. Long. “Quantum Fourier Transform and Phase Estimation in Qudit System”. *Communications in Theoretical Physics* **55** (2011) (cit. on p. 111).
- [204] Y.-M. Di and H.-R. Wei. “Elementary gates for ternary quantum logic circuit”. arXiv:1105.5485 [quant-ph] (2011) (cit. on pp. 115, 140).
- [205] M. V. Altaisky. “Quantum neural network”. arXiv:quant-ph/0107012 (2001) (cit. on p. 130).
- [206] A. Al-Rabadi, L. Casperson, M. Perkowski, and X. Song. “Multiple-Valued Quantum Logic” (2002) (cit. on p. 139).

## **Eidesstattliche Erklärung**

Hiermit erkläre ich an Eides statt, dass ich die vorliegende Arbeit selbst verfasst habe und keine anderen als die angegebenen Quellen und Hilfsmittel benutzt habe.  
Stuttgart, den